KAUNAS UNIVERSITY OF TECHNOLOGY

DEIMANTĖ VAITUKAITYTĖ

MOLECULAR ENGINEERING OF ENAMINE-BASED HOLE TRANSPORTING MATERIALS FOR PEROVSKITE SOLAR CELLS

Doctoral dissertation
Natural Sciences, Chemistry (N 003)

2023, Kaunas

KAUNO TECHNOLOGIJOS UNIVERSITETAS

DEIMANTĖ VAITUKAITYTĖ

ENAMINO FRAGMENTĄ TURINČIŲ SKYLES TRANSPORTUOJANČIŲ MEDŽIAGŲ MOLEKULINĖ INŽINERIJA IR JŲ PRITAIKYMAS PEROVSKITINIAMS SAULĖS ELEMENTAMS

Daktaro disertacija
Gamtos mokslai, chemija (N 003)

2023, Kaunas

Disertacija rengta 2019–2023 metais Kauno technologijos universiteto Cheminės technologijos fakultete, Organinės chemijos katedroje. Mokslinius tyrimus rėmė Lietuvos mokslo taryba.

Mokslinis vadovas:
prof. dr. Vytautas GETAUTIS (Kauno technologijos universitetas, gamtos mokslai, chemija, N 003).

Redagavo: anglų kalbos redaktorė Brigita Brasienė (leidykla „Technologija"), lietuvių kalbos redaktorė Rozita Znamenskaitė (leidykla „Technologija").

Chemijos mokslo krypties disertacijos gynimo taryba:
prof. dr. Saulius GRIGALEVIČIUS (Kauno technologijos universitetas, gamtos mokslai, chemija, N 003) – **pirmininkas**;
doc. dr. Eglė ARBAČIAUSKIENĖ (Kauno technologijos universitetas, gamtos mokslai, chemija, N 003);
prof. dr. Vytas MARTYNAITIS (Kauno technologijos universitetas, gamtos mokslai, chemija, N 003);
prof. dr. Edvinas ORENTAS (Vilniaus universitetas, gamtos mokslai, chemija, N 003);
doc. dr. Cyril ROUSSEAU (Artua universitetas, Prancūzija, gamtos mokslai, chemija, N 003).

Disertacija bus ginama viešame Chemijos mokslo krypties disertacijos gynimo tarybos posėdyje 2023 m. rugsėjo 29 d., 10 val., Kauno technologijos universiteto Rektorato salėje.

Adresas: K. Donelaičio g. 73-402, Kaunas, LT-44249, Lietuva
Tel. (+370) 608 28 527; el. paštas doktorantura@ktu.lt

Disertacija išsiųsta 2023 m. rugpjūčio 29 d.
Su disertacija galima susipažinti interneto svetainėje http://ktu.edu ir Kauno technologijos universiteto bibliotekoje (K. Donelaičio g. 20, Kaunas, LT-44239, Lietuva).

TABLE OF CONTENTS

LIST OF ABBREVIATIONS

3D – three-dimensional;
4Br-SFX – 2,2′,7,7′-tetrabromospiro[fluorene-9,9′-xanthene];
a.u. – arbitrary unit;
AcOH – acetic acid;
AM1.5G – reference solar spectral irradiance according to ASTM G173-03;
aq – aqueous solution;
Ar – argon;
BCP – bathocuproine;
BDT – benzo[1,2-b:4,5:b′]dithiophene;
BzN(Et)$_3$Cl – benzyltriethylammonium chloride;
CB – conduction band;
CSA – camphor sulfonic acid;
DME – dimethoxyethane;
DMF – *N,N*-dimethylformamide;
DMSO – dimethylsulfoxide;
DSC – differential scanning calorimetry;
DSSC – dye-sensitized solar cells;
E_{ea} – electron affinity;
E_g – electronic/optical bandgap;
E*J* – exajoules;
ETL – electron transport layer;
ETM – electron transporting material;
eV – electronvolt;
EXO – exothermic process;
FA – formamidinium;
FDT – 2′,7′-bis(bis(4-methoxyphenyl)amino)spiro[cyclopenta[2,1-b:3,4-b′]dithiophene-4,9′-fluorene];
FF – fill factor;
FK209 – tris(2-(1*H*-pyrazol-1-yl)-4-*tert*-butylpyridine)cobalt(III) tri[bis(trifluoromethane)sulfonimide];
FTIR – Fourier-transform infrared spectroscopy;
FTO – fluorine-doped tin oxide;
HOMO – highest occupied molecular orbital;
HTL – hole transport layer;
HTM – hole transporting material;
i – intrinsic;
I_P – ionization potential;
ITO – indium doped tin oxide;
J_{max} – maximum photocurrent;
J_{sc} – short-circuit photocurrent density;
J-V – photocurrent-voltage;
LED – light-emitting diode;
LiTFSI – lithium bis(trifluoromethane)sulfonimide;

LUMO – lowest unoccupied molecular orbital;

MA – methylammonium;

mA – milliampere;

MALDI – matrix-assisted laser desorption/ionization;

Me – methyl;

MS – mass spectrometry;

m-TiO$_2$ – mesoporous titanium dioxide;

n – negative;

NDI – naphthalene diimide;

NMR – nuclear magnetic resonance;

OC – open-circuit;

p- – *para*-;

p – positive;

P3CT – poly[3-(4-carboxybutyl)thiophene-2,5-diyl];

P3HT – poly(3-hexylthiophene);

PCBM – [6,6]-phenyl-C$_{61}$-butyric acid methyl ester;

PCE – power conversion efficiency;

PDI – perylene diimide;

PEDOT:PSS – poly(3,4-ethylenedioxythiophene)-poly(styrenesulfonate);

PESA – photoelectron spectroscopy in air;

Ph – phenyl group;

P_{in} – power of the incident light;

PL – photoluminescence;

P_{max} – maximum power point;

ppm – parts per million;

PSC – perovskite solar cell;

PTAA – poly[bis(4-phenyl)(2,4,6-trimethylphenyl)amine];

*p*TSA – *para*-toluenesulfonic acid;

PV – photovoltaic;

r.t. – room temperature;

SAM – self-assembled monolayers;

SC – short-circuit;

SEM – scanning electron microscopy;

SFX – spiro[fluorene-9,9'-xanthene];

Spiro-OMeTAD – 2,2',7,7'-tetrakis[*N*,*N*-di(4-methoxyphenyl)amino]-9,9'-spirobifluorene;

SPO – stabilized power output;

SQ – Shockley–Queisser;

t- – tertiary;

*t*BP – 4-*tert*-butylpyridine;

T_c – crystallization temperature;

TCO – transparent conductive oxide;

T_{dec} – decomposition temperature;

TEA – triethylamine;

TEG – tetraethylene glycol;

8

TFA – trifluoroacetic acid;

TFSI – bis(trifluoromethane)sulfonimide;

T_g – glass transition temperature;

TGA – thermogravimetric analysis;

THF – tetrahydrofuran;

T_m – melting temperature;

T_p – polymerization temperature;

TPA – triphenylamine;

UV-vis – ultraviolet-visible;

VB – valence band;

V_{max} – maximum voltage;

V_{oc} – open-circuit voltage;

XTOF – xerographic time-of-flight;

Δ – heat;

λ – wavelength;

λ_{abs} – absorption maximum;

μ – hole drift mobility value at strong electric field;

μ_0 – hole drift mobility value at zero field strength.

1. INTRODUCTION

The Industrial Revolution, which began in the mid-18th century, led to several groundbreaking inventions, increased production and efficiency, migration to urban areas as well as improved working conditions and a better health care, which resulted in enormous growth of human population, being almost eight times larger today than it was a few hundred years ago. The industrialization and an increased number of inhabitants caused a vast consumption of fossil fuels and rising air pollution, which resulted in an energy and environmental crisis[1]. Therefore, the research on renewable energy is moving to the forefront in a variety of fields, owing to its increasing relevance in the modern world. Among various renewable energy technologies, solar energy is an incredibly abundant and extremely clean source; approximately 5×10^4 E*J* of easily harvestable energy reaches the Earth annually[2], while global energy consumption in 2021 was only 595 E*J*[3]. Therefore, the Sun is an inexhaustible free energy provider that has the potential to fulfill growing energy demand of the entire globe if appropriate technologies are used.

Silicon solar panels are the most employed photovoltaic (PV) technologies in the market for their well-known manufacturing procedure, abundance of silicon, and a lifespan of over 25 years. However, the production of traditional solar cells is an expensive and highly energy intensive process[4,5]. In addition, conventional solar cells have limited application possibilities due to their rigidity, brittleness, and heavy weight[6,7].

As the world transitions towards a carbon-free society, the necessity for more applicable technologies is inevitable. Over the past three decades, the development of thin and flexible PV technologies has captivated a significant amount of attention, demonstrating that emerging solar cells have immense potential for a low-cost and easy-processable fabrication technique with a minimum quantity of the used materials[8,9].

The most rapidly developing and one of the most promising PV technologies among other types is organic-inorganic hybrid perovskite solar cells (PSCs), which were reported in the literature for the first time in 2009 as light-energy converting devices[10]. One of the reasons for this attention is extraordinarily rapid improvement of power conversion efficiency (PCE) value, increasing from 3.8 % to almost 26 % in a little longer than a decade[10,11]. The astonishing performance of PSCs, which already exceeds those of the commercialized silicon solar panels, is based on the exceptional electrical and optical properties of halide perovskites[12,13].

Without a perovskite absorber layer, another crucial component for building efficient PSCs is the hole transport layer (HTL), which is responsible for the extraction in perovskite/hole transporting material (HTM) interface[14,15]. Organic synthesis supplies endless options to provide the necessary properties for the HTMs to successfully achieve the commercialization of efficient and stable PSCs.

The aim of the work is the design, synthesis, and characterization of novel cost-effective enamine-based hole transporting materials for perovskite solar cells.

The following objectives were outlined in order to achieve the aim of the dissertation:

1. To synthesize and investigate small organic molecules, containing aniline core and enamine-linked diphenyl branches, suitable for the application in the perovskite solar cells as hole transporting materials;

2. To synthesize and investigate thermal, optical, and photophysical properties of novel hole transporting materials based on spirobifluorene core with enamine-linked diphenyl branches and study their performance in perovskite solar cells;

3. To synthesize and characterize a new series of organic semiconductors with different central heteroatom cores and a varying number of enamine branches used for the hole transport in the perovskite solar cells;

4. To synthesize and characterize cross-linkable molecules that derived from fluorene and study the influence of thermal polymerization on the performance of perovskite solar cells;

5. To estimate the synthesis cost of synthesized hole transporting materials.

Scientific novelty and relevance of the work

In order to become commercially available, PSCs must conform to several requirements: reasonable price, high efficiency, and long-term stability. Although recently, a new PCE record of 25.7 % was certified[16], the lack of suitable HTMs circumscribes the performance of PSCs. The state-of-the-art benchmark for HTMs, called spiro-OMeTAD, was synthesized two decades ago; however, even nowadays, it is one of the most commonly used organic semiconductors for n-i-p structured devices. Thus, the synthesis of this HTM consists of six steps, which require inert conditions, and the usage of aggressive and sensitive reagents; furthermore, extensive purification procedures are mandatory. Such factors strongly influence the price of spiro-OMeTAD and limit its industrial applicability. Therefore, HTMs published in all four articles by the author of this dissertation were synthesized using a simple enamine synthesis chemistry, where metal catalysts and difficult purification procedures are not required, which results in a reduced final cost of the semiconductors.

A group of HTMs obtained from commercially available aniline via one-step procedure were presented in the first publication. PSCs containing such compounds as HTLs have demonstrated an efficiency of over 20 %, which at the time of the publication was a remarkable and promising result. Furthermore, the device containing an organic semiconductor with an enlarged π conjugated system endured 96 % of its original efficiency after storing it for 800 hours, while the efficiency of the reference device decreased to 42 %.

The second publication presented condensation-based spirobifluorene enamine family, where the same spirobifluorene core helped to improve the morphological stability and retain the electronic properties of connected π systems, as it did for spiro-OMeTAD. A different number of enamine arms in the central core as well plays an important role in the properties of semiconductors. A higher degree of substitution resulted in a higher glass transition temperature, hence improving morphological

11

properties as well as more stable amorphous state. As a result, the devices fabricated with spirobifluorene core based HTMs presented high PCE values exceeding 19 %, which are comparable to the efficiency of spiro-OMeTAD-based devices. Moreover, PSCs containing HTMs with one and two enamine arms demonstrated the best stability from the series, being more stable than the devices composed with a reference HTM.

The third publication as well focuses on the inexpensive and affordable straightforward synthesis of HTMs. In this publication, a new series of enamine-based organic semiconductors with a varied central heteroatom core (C, N, O, and S) and a different number of enamine arms was reported. The champion efficiency of PSCs containing HTM with nitrogen heteroatom exceeded 20 %, whereas the devices with spiro-OMeTAD showed identical PCE. Additionally, N- and C-cored HTMs allowed to reach a higher thermal stability of the PSCs compared to the reference-based devices. Such results indicate that logical molecular engineering of a simple condensation reaction can result in stable and high-performing solar cells.

The last publication focuses on low-cost and high efficiency and especially on the longevity of PSCs. In order to increase the electrical conductivity in organic semiconductors, chemical doping is used; however, due to the hygroscopic nature and chemical degradation, traditional dopants have a negative impact on the stability of devices. Therefore, in this publication, dopant-free HTMs were used for the fabrication of p-i-n structured devices. Thermal polymerization allowed to form solvent-resistant films, which led the efficiency of PSCs to exceed 18 %, thus making the proposed strategy an attractive approach for the further development of HTMs for PSCs.

Contribution of the author

The author has designed, synthesized, and purified four series of organic materials described in sub-chapters 2.1–2.4. The author has performed and analyzed the results of ultra-violet absorption, photoluminescence, and contact angle measurements. Moreover, the author has analyzed thermal, photophysical, and photovoltaic properties of the synthesized compounds. Dr. Zhiping Wang (Department of Physics, University of Oxford) fabricated and characterized the devices, performed stability tests, and analyzed the data. Assoc. Prof. Dr. Tadas Malinauskas (Department of Organic Chemistry, Kaunas University of Technology (KTU)) performed DFT calculations and analyzed the obtained data. Dr. Marytė Daškevičienė and Dr. Giedrė Bubnienė (Department of Organic Chemistry, KTU) advised and assisted with the synthesis of new compounds. Charge mobility and ionization potential measurements were performed by Dr. Vygintas Jankauskas and Dr. Jonas Nekrasovas (Institute of Chemical Physics, Vilnius University (VU)). Prof. Dr. Henry J. Snaith (Department of Physics, University of Oxford) advised with the preparation of the manuscript. Dr. Cristina Momblona and Dr. Bin Ding (Institute of Chemical Sciences and Engineering, École Polytechnique Fédérale de Lausanne (EPFL)) contributed to the film preparation, device fabrication, and testing. Dr. Kasparas Rakštys (Department of Organic Chemistry, KTU) advised on the synthesis approach and supervised the research. Dr. Cansu Igci (Institute of Chemical Sciences

and Engineering, EPFL) contributed to the conductivity measurements and analysis of the data. Dr. Albertus Adrian Sutanto (Institute of Chemical Sciences and Engineering, EPFL) contributed to the SEM measurements and analysis. Assoc. Prof. Dr. Alytis Gruodis (Institute of Chemical Physics, VU) performed computational simulations. Prof. Dr. Abdullah M. Asiri (Center of Excellence for Advanced Materials Research, King Abdulaziz University) and Prof. Dr. Paul J. Dyson (Institute of Chemical Sciences and Engineering, EPFL) helped by analyzing the data. Prof. Dr. Mohammad Khaja Nazeeruddin (Institute of Chemical Sciences and Engineering, EPFL) supervised the research and contributed to the writing and reviewing of the manuscript. Dr. Minh Anh Truong, Mr. Tsukasa Funasaki, and Dr. Takumi Yamada (Institute for Chemical Research, Kyoto University) fabricated and characterized the devices, performed stability tests, and analyzed the data. Dr. Richard Murdey, Prof. Dr. Yoshihiko Kanemitsu, and Prof. Dr. Atsushi Wakamiya (Institute for Chemical Research, Kyoto University) advised with the preparation of the manuscript. Dr. Amran Al-Ashouri (Young Investigator Group Perovskite Tandem Solar Cells, Helmholtz-Zentrum Berlin (HZB)) fabricated and characterized the devices, performed stability tests, and analyzed the data. Dr. Egidijus Kamarauskas (Institute of Chemical Physics, VU) performed ionization potential measurements. Dr. Artiom Magomedov advised and assisted with the synthesis and helped to prepare the manuscript. Prof. Dr. Steve Albrecht (Young Investigator Group Perovskite Tandem Solar Cells, HZB) advised with the preparation of the manuscript. Prof. Dr. Vytautas Getautis (Department of Organic Chemistry, KTU) advised on the design of new hole transporting materials and preparation of the manuscript.

List of scientific publications on the topic of the dissertation

1. **Vaitukaityte, Deimante**; Wang, Zhiping; Malinauskas, Tadas; Magomedov, Artiom; Bubniene, Giedre; Jankauskas, Vygintas; Getautis, Vytautas; Snaith, Henry J. Efficient and stable perovskite solar cells using low-cost aniline-based enamine hole-transporting materials // Advanced materials. ISSN 0935-9648. 2018, vol. 30, iss. 45, art. no. 1803735, p. 1-7. (Web of Science). DOI: 10.1002/adma.201803735. [IF: 25,809; Q1].

2. **Vaitukaitytė, Deimantė**; Al-Ashouri, Amran; Daškevičienė, Marytė; Kamarauskas, Egidijus; Nekrasovas, Jonas; Jankauskas, Vygintas; Magomedov, Artiom; Albrecht, Steve; Getautis, Vytautas. Enamine-based cross-linkable hole-transporting materials for perovskite solar cells // Solar RRL. ISSN 2367-198X. 2021, vol. 5, iss. 1, art. no. 2000597, p. 1-6. (Web of Science). DOI: 10.1002/solr.202000597. [IF: 9,173; Q1].

3. **Vaitukaityte, Deimante**; Momblona, Cristina; Rakstys, Kasparas; Sutanto, Albertus Adrian; Ding, Bin; Igci, Cansu; Jankauskas, Vygintas; Gruodis, Alytis; Malinauskas, Tadas; Asiri, Abdullah M.; Dyson, Paul J.; Getautis, Vytautas; Nazeeruddin, Mohammad Khaja. Cut from the same cloth: enamine-derived spirobifluorenes as hole transporters for Perovskite solar cells // Chemistry of materials. ISSN 0897-4756. 2021, vol. 33, iss. 15, p. 6059-6067. (Web of Science). DOI: 10.1021/acs.chemmater.1c01486. [IF: 10,508; Q1].

4. **Vaitukaityte, Deimante**; Truong, Minh Anh; Rakstys, Kasparas; Murdey, Richard; Funasaki, Tsukasa; Yamada, Takumi; Kanemitsu, Yoshihiko; Jankauskas, Vygintas; Getautis, Vytautas; Wakamiya, Atsushi. Molecular engineering of enamine-based hole-transporting materials for high-performing perovskite solar cells: influence of the central heteroatom // Solar RRL. ISSN 2367-198X. 2022, vol. 6, iss. 11, art. no. 2200590, p. 1-8. (Web of Science). DOI: 10.1002/solr.202200590. [IF: 9,173; Q1].

1.1. Perovskite solar cells

1.1.1. Hybrid organic-inorganic metal halides

German minerologist Gustav Rose discovered calcium titanium oxide ($CaTiO_3$), as well known as calcium titanate, in the Ural Mountains in 1839. Afterwards, this mineral was named perovskite in honor of Russian minerologist Lev A. Perovski[17]. Currently, the term 'perovskite' determines a class of compounds with a crystal structure similar to $CaTiO_3$. In general, the chemical formula of hybrid organic-inorganic halide perovskites, which are commonly used for photovoltaic applications, is ABX_3, where A represents a small monovalent organic cation (methylammonium $CH_3NH_3^+$ (MA) or formamidinium $NH_2=CH_3NH_2^+$ (FA)), B is a divalent metal cation (Pb^{2+} or Sn^{2+}), and X represents a monovalent halide anion (Cl^-, Br^-, or I^-). The idealized structure of perovskite has a cubic symmetry (Figure 1), where B-type cations coordinate with anions and form corner-sharing BX_6 octahedra, which define a cuboctahedral cavity for an A-type cation[18].
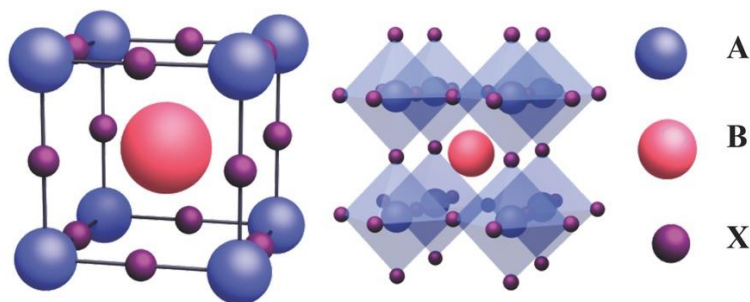
Figure 1. The ideal cubic structure of ABX_3 in a unit cell (left), and extended projection of the 3D crystal structure of perovskite (right); reproduced from ref. 19

Perovskites have been intensively studied not only for photovoltaic applications, but for light-emitting diodes (LEDs)[19–21] and photodetectors[22–24] as well. Such attention was attracted mainly because of their optical properties, including high absorption coefficients and tunable bandgaps, which are essential for light absorbers as well as light-emitting materials. $MAPbI_3$ perovskite absorber is known for a broad absorption range, which covers almost the entire visible spectrum, reaching the near infrared region (800 nm)[10]. Moreover, large absorption coefficient on the order of 10^5 cm^{-1} allows to use less material for the production of the perovskite layer; hence, it is an easy and less expensive manufacturing procedure[25]. The bandgap of perovskite can be adjusted from around 1.6 to 2.3 eV by choosing different cations or anions and

14

varying the ratio between them[26]. However, after years of optimization of the perovskite composition, triple cation perovskite mixture with the addition of an inorganic cesium cation became a standard for further research, showing improved reproducibility of the performance results and better stability[27].

1.1.2. Architectures and operating mechanism

The structure of hybrid organic-inorganic perovskite solar cell typically consists of five layers: transparent electrode, electron transporting material (ETM), light absorbing perovskite, hole transporting material, and metal electrode[28]. Since perovskites can be adjusted to n- or p-type conduction, several types of device architecture exist[29]. According to the structure of the electron transport layer, PSCs are separated into two categories, i.e., mesoscopic and planar[30], and both can be additionally divided into conventional (n-i-p) and inverted (p-i-n) configurations, depending on the position of charge extraction layers[31]. All four different types of device architecture can be seen in Figure 2.
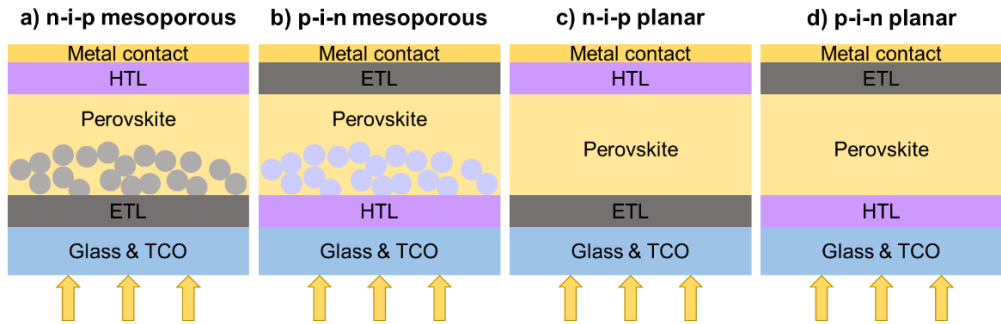
Figure 2. Schematic diagrams of PSCs in a) n-i-p mesoporous, b) p-i-n mesoporous, c) n-i-p planar, and d) p-i-n planar structures

Mesoscopic, as well known as mesoporous, solar cells were first introduced by Park et al. in 2012 when they reported a breakthrough in the PCE of devices by depositing perovskite onto mesoporous TiO_2 layer, which had HTM infiltrated pores[32]. Not long after, Snaith et al. presented a different device structure, where a compact layer of TiO_2 was followed by a mesoscopic scaffold of TiO_2 with infiltrated perovskite and a separate layer of perovskite[33]. This improvement led to achieve higher efficiency values of PSCs; therefore, such configuration was one of the most frequently used for a long time.

As an alternative, planar configuration, in which the mesoporous TiO_2 layer is eliminated, was investigated as well. In such structure, perovskite layer is deposited on top of the HTL after absorber layer follows electron transporting and blocking layer; thus, electron-hole pairs are separated more efficiently and rapidly[34,35].

As it is demonstrated in Figure 3, a photovoltaic process in a regular PSC begins when light passes through the transparent electrode; thus, photons excite the perovskite material, instantly photogenerating electron-hole pairs in the same layer. After the separation of electrons and holes (1), the electrons are injected from the conduction band (CB) of the perovskite to the electron transport layer (ETL) (2).

Simultaneously, photogenerated holes are injected from the valence band (VB) of the perovskite to the HOMO level of the hole transporting material (3). Afterwards, the charge carriers are transferred to the electrodes, where they are collected by external circuit, producing a photocurrent[36]. Unfortunately, such a mechanism is possible only under ideal conditions. In reality, several undesirable processes, such as back charge transfer recombination of the charge carriers (4–6) or non-radiative recombination (7), occur[37]. In order to fabricate high-efficiency PSCs, the processes of charge generation, separation, and extraction must occur more frequently than the charge recombination processes.
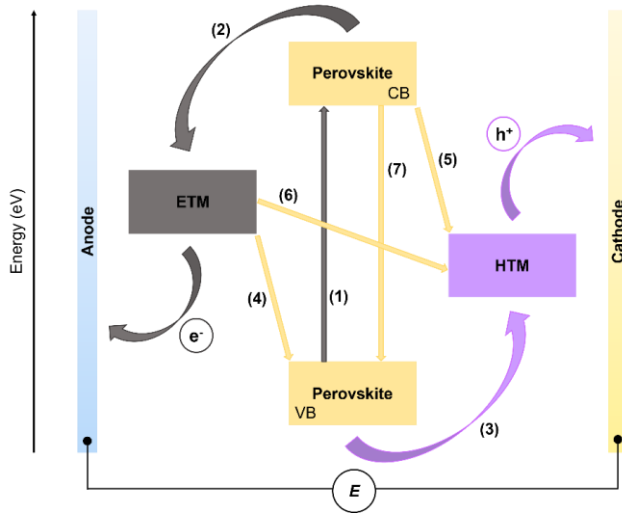
Figure 3. Schematic diagram of energy levels and charge transfer processes in conventional PSCs

1.1.3. Components of the structure

1.1.3.1. Transparent conductive oxide

Transparent conductive oxides (TCOs), as well known as working electrodes, usually have a wide bandgap ($E_g \geq 3.1$ eV); therefore, they can efficiently transmit light in the visible and near-infrared regions[38]. Other equally important characteristics of TCO materials are high conductivity and low resistivity[39]. Additionally, working electrodes must consist of low-cost materials to use them for the application in commercial solar cells. Although a variety of materials, such as tin oxide (SnO_2, SnO_2:F), indium oxide (In_2O_3), indium doped tin oxide (ITO), zinc oxide (ZnO), and others, are used as TCOs, only a few of them (ITO and FTO – fluorine-doped tin oxide) had application-specific properties and were chosen for the fabrication of PSCs of this dissertation.

1.1.3.2. Electron transport layer

The fundamental role of ETL is to ensure efficient extraction of photogenerated electrons from the perovskite light absorbing layer and transport to the contact

16

electrode. Another important function of ETM, greatly impacting the overall device performance, is the prevention of hole migration to the counter electrode. In order to implement such functions, this layer must meet several requirements. First, ETM should be able to form a dense uniform layer to prevent pinholes and shunting[40]. Second, the layer should be transparent because of the wide band gap to ensure efficient light harvesting. Third, ETM must have an appropriate band alignment with both the perovskite material to trigger electron transfer and the electrode to assure ohmic contact[28]. Fourth, high electron mobility is necessary to provide efficient charge transfer and reduce the charge accumulation[41]. Finally, ETM should be morphologically stable and have suitable layer preparation conditions, compatible with previous and following layers.

ETMs can be categorized into two groups, i.e., organic and inorganic. The organic category, which is more adapted for the fabrication of inverted PSCs, includes [6,6]-phenyl-C_{61}-butyric acid methyl ester (PCBM), buckminsterfullerene (C_{60}), and other fullerene derivatives[42]. However, several disadvantages, such as limited tunability of the LUMO level[43], insufficient morphological stability, costly synthesis, and purification procedures, limit the commercial applicability of fullerene ETMs[44]. Therefore, non-fullerene materials recently became an emerging topic of scientific interest. Perylene diimide (PDI)[45,46], naphthalene diimide (NDI)[47,48], and azaacene[49,50] derivatives preserve some fullerene properties and can propose some superiorities, such as easily tunable energy levels, good thermal and chemical stability, which show a great promise for the future applications. The inorganic category of ETMs, which includes titanium oxide (TiO_2)[51], tin (IV) oxide (SnO_2)[52], zinc oxide (ZnO)[53], zinc selenide (ZnSe)[54], cadmium sulfide (CdS)[55], etc., is more common for the application in regular PSCs. The most examined ETM for PSCs is TiO_2, which is known for its wide bandgap (~3.2 eV) and suitable CB energy (4.4 eV)[56], being marginally lower than that of the perovskite, thus guaranteeing an efficient electron injection. Despite publications about impressive device performance while using titanium oxide ETL, it has several disadvantages: a major one being the necessity of high temperature sintering at approximately 500 ºC for the deposition process[57]. As an alternative to TiO_2, tin (IV) oxide is a promising candidate, offering even lower CB energy level and a possibility to deposit this layer at relatively lower temperatures[58].

1.1.3.3.   Perovskite light-absorbing layer

Hybrid organic-inorganic halide perovskite plays the main role among the other components of PSCs and is essential for the absorption of light, photogeneration, and transportation of free carriers, demonstrating ambipolar behavior[59]. Great performance of devices can be attributed to the excellent optoelectronic properties of perovskite. The CB energy level of the well-known $MAPbI_3$ is around 5.2 eV, while the VB is approximately at 3.6 eV[60]; the numbers may vary depending on the material processing, which demonstrate perfect conditions for the electron injection from the CB of the perovskite into the CB of TiO_2 and the hole injection from the VB of the perovskite to the HOMO energy level of HTM. Furthermore, even though there are various deposition procedures for perovskite films, such as co-evaporation[61], sequential evaporation[62], or vapor-assisted solution method[63], the perovskite layer can

be formed as well by using a simple and economical technique, which is called solution deposition[64]. It can be performed as a one-step[65] or a two-step[66] procedure, where both precursors PbX_2 and MAX, dissolved in common organic solvents, such as dimethylsulfoxide (DMSO) or N,N-dimethylformamide (DMF), are either mixed into one solution, or both precursor solutions are prepared separately and thus deposited sequentially. Afterwards, the evaporation of a solvent at a suitable temperature induces the crystallization of the perovskite; hence, a light-absorbing layer is formed. Because of the simplicity and inexpensiveness of the solution-based procedure, it is particularly attractive for both industrial and academic researchers; therefore, only this method is used in this dissertation.

1.1.3.4. Hole transport layer

HTL is essential for the fabrication of highly efficient PSCs, being responsible for the processes of hole extraction at the perovskite/HTM interface and hole transportation to the metal electrode. Additionally, it helps to prevent unwanted charge recombination processes by acting as an energy barrier. In order to implement such functions, HTMs must have well-aligned energy levels; the HOMO level should be slightly higher in energy than the VB of the perovskite for efficient hole injection, whereas the LUMO level should be much higher in energy than the CB of the perovskite for the beneficial electron blocking. Other indispensable properties of HTMs are high hole mobility and sufficient conductivity, which ensure rapid hole transport to the contact before they recombine. Furthermore, in order to assure long-term device stability, HTMs should be thermally and photochemically stable, well soluble, and have good film-forming properties, because such layers have to protect oxygen and moisture sensitive perovskite layer from degradation[67]. Nonetheless, for PSCs to be commercially viable, a straightforward and cost-effective synthesis of HTMs should be considered.

Up till now, a considerable number of HTMs have been employed in PSCs and reported; all of them can be categorized into two types, i.e., organic and inorganic. There are several advantages of inorganic HTMs: simple fabrication procedures, low cost of production, good chemical stability, suitable energy levels, good transparency in a visible region, and high hole mobility[68,69]. The best performance of PSCs, containing inorganic HTLs, reportedly exceeds 20 % so far. Such PCE value was achieved in p-i-n configuration, where nickel oxide (NiO_x) doped with lithium (Li) and magnesium (Mg) was used as inorganic HTM, resulting in a highly stable device, maintaining over 85 % of its initial efficiency after 500 hours of operation[70]. A similar device performance of over 20 %, rapid charge extraction and transportation were demonstrated by copper thiocyanate (CuSCN), well known for its wide bandgap (3.9 eV), high conductivity, and suitable VB energy level (-5.3 eV)[71]. Another alternative is delafossite materials, such as copper gallium oxide ($CuGaO_2$), which, when coated on top of nickel oxide, yielded an inverted PSC with the efficiency of 20 % and maintained a great long-term stability[72]. Although inorganic HTMs have many favorable characteristics, which demonstrate their potential for the application in PSCs, the PCE has not been sufficiently optimized.

Organic HTMs can be divided into two categories, i.e., small molecules and polymers. In the category of small molecules, p-type semiconductor 2,2',7,7'-tetrakis[*N*,*N*-di(4-methoxyphenyl)amino]-9,9'-spirobifluorene (spiro-OMeTAD) has been selected as the state-of-the-art benchmark for HTMs in 1998, when it was first employed in solid-state dye-sensitized solar cells (DSSCs)[73], and it remains a reference HTM nowadays. Despite the high efficiency of PSCs, spiro-OMeTAD has several disadvantages, such as morphological instability of amorphous film, which has a negative impact on the long-term stability[74], and complicated multi-step synthesis (Scheme 1), which results in a high cost, hence smaller commercialization opportunities for wide application[75].
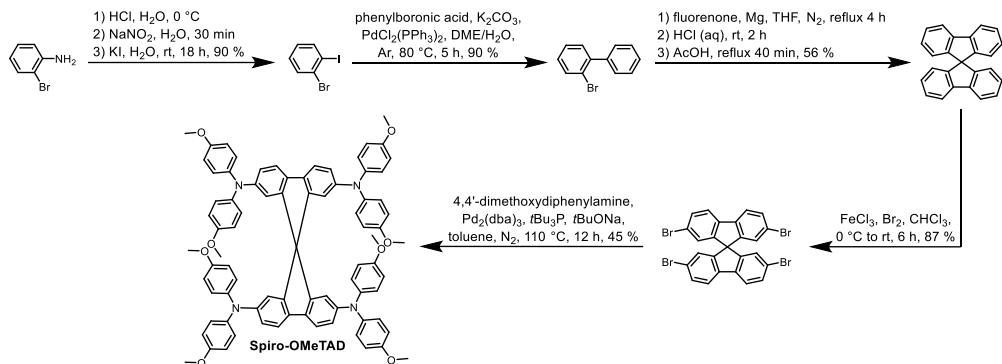
Scheme 1. An example of a possible synthesis route to obtain spiro-OMeTAD[76]

Moreover, spiro-OMeTAD, as the most organic semiconductor, has low conductivity and hole drift mobility; therefore, several dopants, such as lithium bis(trifluoromethane)sulfonimide (LiTFSI), tris(2-(1*H*-pyrazol-1-yl)-4-*tert*-butylpyridine)cobalt(III) tri[bis(trifluoromethane) sulfonimide] (FK209) and 4-*tert*-butylpyridine (*t*BP), are standardly added into the composition of HTL (Figure 4). The main role of oxidative additives is to remove electrons from the HOMO energy level of HTM, thus producing intrinsic holes, which lead to an enhanced charge carrier density, resulting in an improved film conductivity[77]. *t*BP helps to increase the solubility of LiTFSI and prevents aggregation of such salts, hence enhancing the quality of HTL[78]. Other sources state that it as well reduces charge recombination, significantly improving the performance of PSCs[79]. However, chemical doping can negatively influence the long-term stability of PSCs, since LiTFSI and *t*BP accelerate the chemical degradation of the perovskite due to their hygroscopic properties[80]. Alternatively, the use of dopant-free HTMs may help to improve the stability of PSCs.

LiTFSI
Lithium bis(trifluoromethane)sulfonimide

FK 209 Co(III) TFSI salt
tris(2-(1*H*-pyrazol-1-yl)-4-*tert*-butylpyridine)cobalt(III)
tri[bis(trifluoromethane)sulfonimide]

***t*BP**
4-*tert*-Butylpyridine
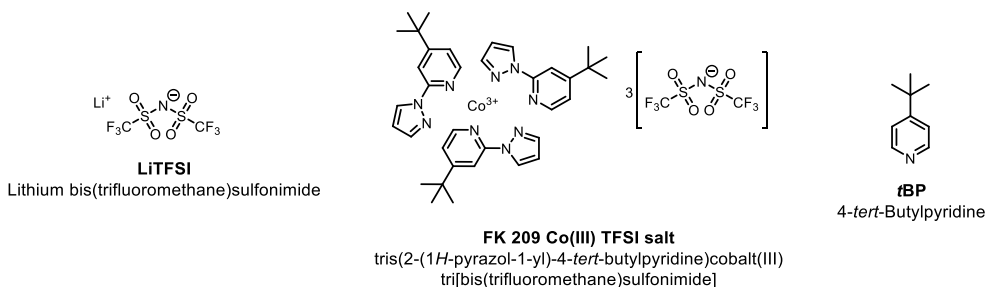
Figure 4. Chemical structures of the most common dopants for HTMs employed in PSCs[81]

Another major part of organic HTMs is classified as polymers, which are a more common choice for the inverted PSCs, since HTL has to withstand the deposition of a perovskite solution, containing polar solvents, such as DMF and DMSO. Polymeric materials are as well well-known for their exceptional charge carrier mobility, good film-forming properties, morphological stability, and hydrophobicity. In addition, a unique monomer feature that is called cross-linking allows for the formation of a 3D network, resulting in a dense solvent-resistant film, which acts as a protective layer for the perovskite, preserving it from moisture, hence potentially improving the stability of the device. One of the most efficient polymeric HTMs based on triphenylamine is poly[bis(4-phenyl)(2,4,6-trimethylphenyl)amine (PTAA), achieving the PCE of PSCs of around 22 %[82], which arises from an impressive hole mobility of 10^{-2}–10^{-3} cm^2/Vs. However, extremely high cost of over 3,000 €/g[83] limits its suitability for a large-scale commercial application. As an alternative, another well-known and cost-effective conductive polymer used in PSCs is poly(3,4-ethylenedioxythiophene)-poly(styrenesulfonate) (PEDOT:PSS). Nonetheless, the photovoltaic performance and stability of such devices are limited due to a significant energy barrier between PEDOT:PSS and the perovskite layer and intrinsically acidic properties of PEDOT:PSS[84]. The chemical structures of both PTAA and PEDOT:PSS can be found in Figure 5.

PTAA

PEDOT:PSS
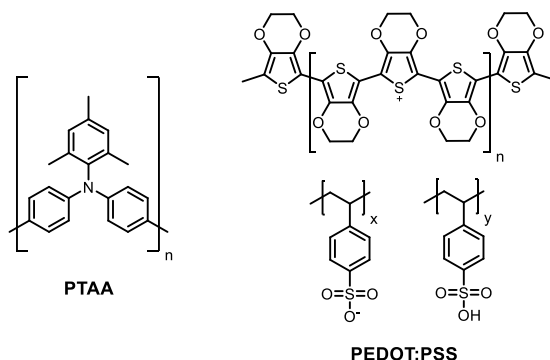
Figure 5. Chemical structures of several common polymeric HTMs[15]

In this dissertation, both types of organic HTMs have been used for the application in PSCs to examine the impact of different HTLs on the photovoltaic parameters of the device.

1.1.3.5. Counter electrode

The main role of counter electrode is to extract, transfer, and collect charges from charge transporting layer and generate current; therefore, naturally, it has a significant influence on the PCE and reliability of PSCs. In order to fabricate high-performing devices, the top electrode must comply with several requirements, such as good electrical conductivity, chemical and physical stability, simple deposition technique, and low-cost[85,86]. One of the most common counter electrodes used in PSCs is gold (Au), owning to its advantages, such as excellent conductivity, chemical inertness, and intrinsic stability[87]. However, Au has a few disadvantages as well: firstly, heat can influence its ion migration towards the perovskite layer through HTL, which can lead to a lower device performance and cause stability issues. Secondly, Au is an expensive material, and it might become an obstacle for large-scale applications in PSCs[88]. As an alternative, silver (Ag) with a higher conductivity and substantially lower price has been used as an electrode material. However, it is more reactive to the environment and prone to oxidation when compared to Au; hence, it could lead to rapid device degradation[89]. Despite the variety of metals, which have already been employed as effective top electrodes in PSCs, the research continues to explore alternative materials, such as carbon nanotubes and graphene, which have a potential to show even better stability and performance[90,91].

1.1.4. Photovoltaic characteristics

Photovoltaic parameters of PSC, such as open-circuit voltage (V_{OC}), short-circuit current density (J_{SC}), fill factor (FF), and power conversion efficiency (PCE), are usually extracted from a photocurrent-voltage (J-V) curve by measuring it with a solar simulator. The measurements are typically conducted under 1 sun illumination at standard AM1.5G solar spectrum[92] (Figure 6) by using an application of external potentials to the device and at the same time, measuring a corresponding current generation.
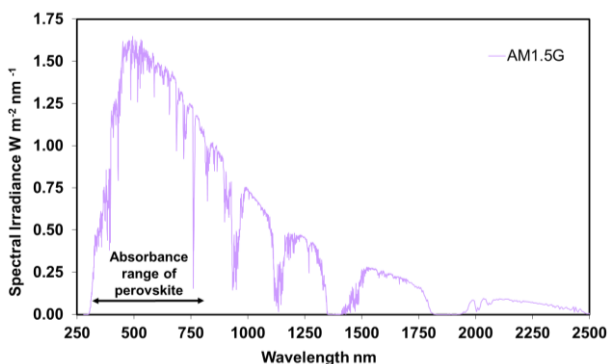
Figure 6. The AM1.5 Global spectrum of solar irradiation[92]

As shown in Figure 7, the V_{OC} is a characteristic obtained under open-circuit conditions when the photocurrent density is zero, whereas J_{SC} is a parameter obtained from a measured current at short-circuit as photovoltage equals zero. The maximum power point (P_{max}) can be determined as a value obtained by multiplying the photocurrent and voltage at their maximum values, J_{max} and V_{max}, respectively.
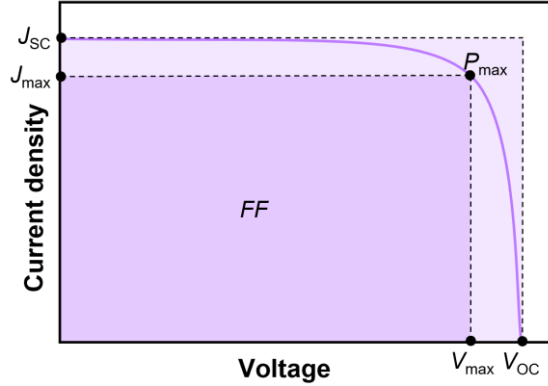
Figure 7. Typical *J-V* curve of a perovskite solar cell under constant illumination

The aforementioned parameters help to define the *FF*, which is a measure describing how closely a solar cell functions as an ideal source, expressed as a ratio of the P_{max} (represented by a dark purple rectangular in Figure 7) to the product of J_{SC} and V_{OC} (represented by a light purple rectangular):

$$FF = \frac{P_{max}}{J_{SC} \times V_{OC}} \tag{1}$$

When comparing the performance of different solar cells, the PCE is the most frequently used parameter, measuring the efficiency of a solar cell in converting incident light into electrical power, which is defined as a ratio of the maximum power output of a solar cell to the power of the incident light (P_{in}):

$$PCE = \frac{P_{max}}{P_{in}} = \frac{J_{SC} V_{OC} FF}{P_{in}} \tag{2}$$

The maximum efficiency of a solar cell is determined by the Shockley–Queisser (SQ) limit[93] (Figure 8). Assuming that the bandgap of a semiconductor is 1.34 eV for a single junction cell, the calculation places maximum PCE around 33.2 %[94]. However, the bandgap of $CH_3NH_3PbI_3$ is approximately 1.57 eV; therefore, the efficiency limit for PSCs is slightly lower, i.e., around 31 %[95].
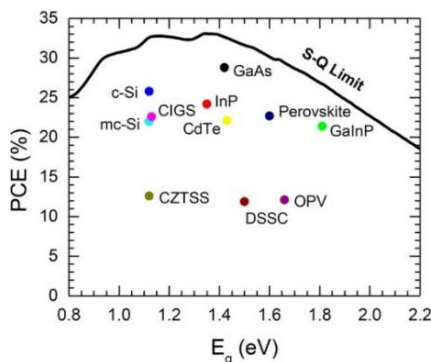
Figure 8. Shockley–Queisser limit: maximum PCE as a function of a bandgap energy; data points represent record efficiencies of laboratory solar cells[96]

The performance of PSCs is strongly influenced by the scan direction (forward and reverse), which leads to differential behavior of the *J-V* curve and is called hysteresis[97,98]. When a device is held at a forward bias voltage prior to measurement, the efficiency may be higher than when the device is at reverse biased, the maximum power point, or short-circuit. Furthermore, it has been observed that at the faster scan rate, hysteresis becomes more pronounced[99,100]. The causes of hysteresis in PSCs are still a subject of ongoing research; however, several reasons, such as ferroelectric polarization, unbalanced charge carrier transport, ion migration, and charge carrier trapping and detrapping, have been already proposed[101].

1.2. Molecular engineering of organic hole transporting materials for perovskite solar cells

Organic chemistry provides limitless possibilities for the synthesis of organic semiconductors and allows to adjust electronic properties, intermolecular interactions, and molecular functionality. Such an advantage enables the fulfillment of many requirements: high hole mobility and conductivity, good thermal as well as photochemical stability, and suitable energy level compatility, which are crucial features for high-performing HTMs in efficient PSCs. However, in order to manufacture affordable solar cells, the synthesis of HTMs has to be straightforward and low-priced; additionally, such compounds should have a simple purification procedure.

Since a tremendous number of HTMs has been synthesized to this day, only the selected examples of small organic molecules and polymeric compounds, their properties and performances are presented in this sub-section.

1.2.1. Small organic compounds as hole transporting materials

As mentioned in the sub-section 1.1.3.4., spiro-OMeTAD still prevails among other HTMs, and it is used as a reference molecule in PSCs. The reason for such an extraordinary performance lies in the chemical structure of the molecule, which consists of a 9,9'-spirobifluorene central core and four units of *p*-methoxydiphenylamine. A perpendicular arrangement of two electroactive

23

molecular fragments connected via a common *sp*³-hybridized carbon atom provides high morphological stability, while optoelectronic properties retain the original[75]. However, in order to obtain such spiro-centered core, it is necessary to use a complex multi-step synthetic procedure, which usually involves sensitive or aggressive reagents as well as harsh reaction conditions, such as very low temperatures. In addition, the remaining part of the molecule is equally important, especially to the electronic properties, since the prebrominated spiro core is linked with diphenylamine, endowed with electron-rich methoxy groups. C−N bonds are formed during a cross-coupling reaction, which as well has severe requirements, such as expensive transition-metal catalysts and inert reaction conditions[102]. Furthermore, the tedious purification procedure of HTM is mandatory for the production of efficient devices, since the remains of metal catalysts act as charge carrier traps and negatively impact their intrinsic properties[103,104]. These requirements greatly impact the commercial cost of spiro-OMeTAD, which varies between 350 and 500 €/g. Despite all drawbacks, spiro-OMeTAD is the most well-known and most frequently cited HTM in the literature. The efficiencies of PSCs based on this compound routinely surpass 20 %[105]; therefore, many researchers are working on the structural modifications of spiro-OMeTAD.

At the same time, the researchers are looking for ways to simplify the synthesis of HTMs by avoiding the use of palladium catalysts. Although a variety of semiconductors, containing different central cores, such as carbazole[106,107], truxene[108,109], thiophene[110,111], pyrene[112,113], and triazine[114,115] derivatives, have been reported, most of them are functionalized with diphenylamine or triphenylamine fragments, which indicates that problematic metal catalysts were used for the synthesis. One of the ways to enlarge conjugation by using a metal-free synthetic route is to use condensation chemistry. Such reactions do not require complicated purification procedures because the only by-product is a small molecule, e.g., water or ethanol. Additionally, condensation reactions are usually performed under ambient conditions. The aforementioned factors result in a greatly reduced synthesis cost of HTMs, demonstrating the potential of a straightforward condensation chemistry for the PV applications.

1.2.1.1.   Hole transporting materials based on spiro-OMeTAD

A variety of publications have already demonstrated that small organic spiro-based HTMs can achieve similar to spiro-OMeTAD photovoltaic performance of PSCs or even exceed it, while reducing the synthesis cost. Some representative examples of such compounds are shown in Figure 9 and Figure 10. The photovoltaic characteristics of spiro-type HTMs are summarized in Table 1.

One of the first publications about structural modification of spiro-OMeTAD HTM was reported by Seok et al. in 2014[116], when they examined the influence of the position of methoxy groups. It is worth mentioning that such group is responsible for the tuning of the HOMO level of the molecule as well as enhancing the contact between HTL and perovskite. According to Hammett, electron-donating or withdrawing properties of the methoxy group depend on the substitution position in the aromatic ring, *para*-substitution or *meta*-substitution, while *ortho*-substitution

influences the steric effect[117]. The best efficiency of 16.7 % for PSCs was achieved with *o*-substituted *po*-spiro-OMeTAD, demonstrating the highest value to date, which can be explained by the increased *FF*.

Other interesting modifications of methoxy groups were presented in a publication by Huang et al.[118], where they synthesized three new HTMs, containing replaced *p*-substituents with methylsulfanyl (spiro-S), ethyl (spiro-E), and *N,N*-dimethylamino (spiro-N) groups. Spiro-S and spiro-E showed closer HOMO energy values of −4.92 and −4.81 eV, respectively, when compared to spiro-MeTAD (−4.76 eV), which perfectly align with the energy levels of $CH_3NH_3PbI_3$. Whereas spiro-N demonstrated a higher HOMO energy level (−4.42 eV) influenced by a stronger electron-donating ability of *N,N*-dimethylamino groups. Different substitution of heteroatoms had a great impact on the optoelectronic properties of HTMs and the performance of devices. The highest PCE values of 15.92 and 15.75 % were obtained for PSCs based on spiro-S and spiro-E.

Spiro-OMeTAD

po-spiro-OMeTAD: R$_1$ = OCH$_3$, R$_2$ = H, R$_3$ = H
pm-spiro-OMeTAD: R$_1$ = H, R$_2$ = OCH$_3$, R$_3$ = H
pp-spiro-OMeTAD: R$_1$ = H, R$_2$ = H, R$_3$ = OCH$_3$

Spiro-S   **Spiro-E**   **Spiro-N**

X60   **H11**
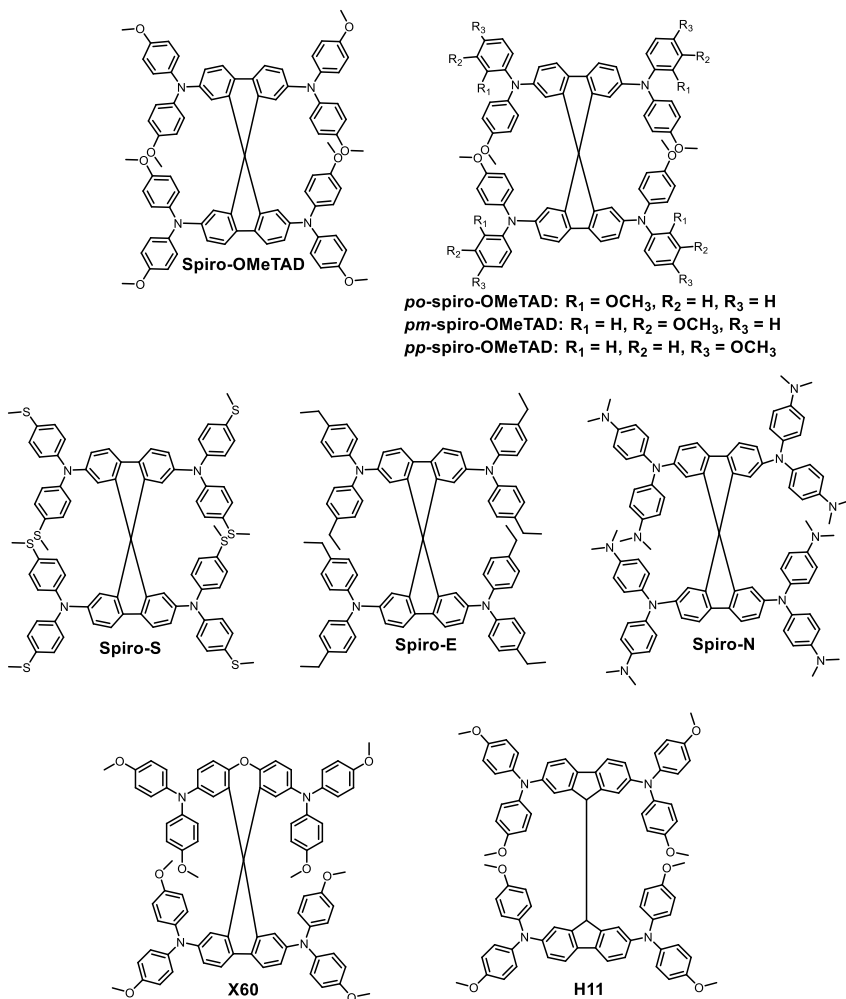
Figure 9. Chemical structures of spiro-OMeTAD and spiro-based HTMs[116-120]

One of the most frequently used methods to modify the structure of spiro-OMeTAD and make it more commercially available is to change the spirobifluorene central core. Sun et al. presented X60[119], containing an inserted oxygen bridge, which was synthesized via a simple two-step synthetic route. Low-cost raw materials, the one-pot approach to obtain the 2,2′,7,7′-tetrabromospiro[fluorene-9,9′-xanthene] (4Br-SFX) center, and the non-use of air-sensitive or corrosive reagents lead to a significantly reduced synthesis price. In addition, such a minimal change in the structure of HTM influenced an enhanced charge transfer, hence an incredible device PCE of 19.8 %. Equally high photovoltaic performance was reached by Hagfeldt et al.[120], who replaced the central spiro-linkage with a C−C bond, resulting in H11. The synthesis of this HTM as well contains only two steps; therefore, H11 as well as X60 show a great potential for large-scale applications in PSCs.
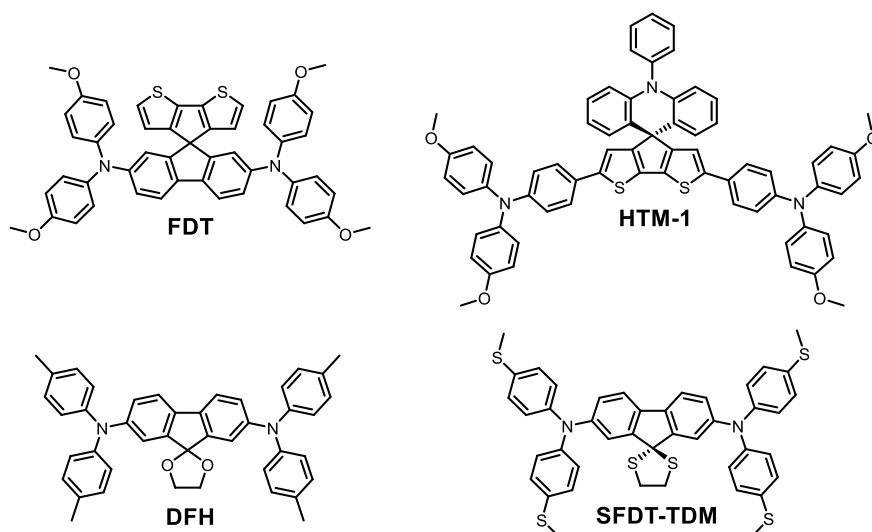
Figure 10. Chemical structures of spiro-based HTMs: FDT, HTM-1, DFH and SFDT-TDM[121-124]

As mentioned above, heteroatoms play a significant role in the performance of PSCs; therefore, in order to enhance hole transfer at the HTM/perovskite interface, the tiophene-iodine interaction was used. A novel spiro-cyclopentadithiophene central core, substituted by *N,N*-di-*p*-methoxyphenylamine donor groups, was molecularly engineered by Nazeeruddin et al.[121]. Such HTM, called FDT, employed in a conventional PSC architecture showed a remarkable performance, exceeding 20 % efficiency, and outperformed spiro-OMeTAD. Moreover, the synthesis cost of FDT (~60 $/g) was calculated to be eight times lower than of the purified reference material (~500 $/g). A similar approach was used in a publication by Grätzel et al.[122], where they presented a hole conductor HTM-1, comprising a central core of spiro-acridine-cyclopentadithiophene substituted by triarylamine moieties. Owing to its high hole drift mobility at low electric field, HTM-1 containing devices yielded a PCE of almost 21 %, exhibiting an excellent long-term operational stability after aging for 400 h. A

very similar efficiency of inverted PSCs was achieved by Berlinguette et al.[123], who reported a preferable dopant-free HTM (called DFH) containing two fluorene-bridged triphenylamine moieties connected to a 1,3-dioxolane group through a spiro carbon center. Such an excellent performance can be explained by the strong intermolecular interactions between dioxane groups, which lead to a high hole mobility value of 1×10^{-3} cm^2/Vs, and an improved morphology of the perovskite layer. Furthermore, DFH was obtained using a two-step synthetic procedure from inexpensive commercially available reagents at a cost of 3 \$/g. Recently, Zhu et al. reached a record PCE (21.7 %) among spiro-based dopant-free HTM based PSCs, introducing rationally designed spirofluorene-dithiolane based hole conductor named as SFDT-TDM[124]. The involvement of methylthio groups, which act as Lewis bases, led to the passivation of defects on the perovskite surface, improving charge extraction at the perovskite/HTM interface.

Table 1. Photovoltaic characteristics of PSCs employed with spiro-based HTMs

HTM	V_{OC} (V)	J_{SC} (mA/cm^2)	FF	PCE (%)	Reference PCE (%)[a]
po-spiro-OMeTAD[d]	1.02	21.2	0.78	16.7	15.2
pm-spiro-OMeTAD[d]	1.01	21.1	0.65	13.9	15.2
pp-spiro-OMeTAD[d]	1.00	20.7	0.71	14.9	15.2
Spiro-S[b,c]	1.06	19.15	0.78	15.92	11.55
Spiro-E[b,c]	1.07	18.24	0.80	15.75	11.55
Spiro-N[b,c]	0.96	16.55	0.75	11.92	11.55
X60[d]	1.14	24.15	0.70	19.55	-
H11[d]	1.15	24.2	0.71	19.8	18.9
FDT[d]	1.148	22.7	0.76	20.2	19.7
HTM-1[d]	1.10	24.74	0.77	20.95	21.09
DFH[b,c]	1.08	22.0	0.81	20.6	19.2
SFDT-TDM[b,d]	1.13	24.1	0.80	21.7	20.3

[a]Spiro-OMeTAD or PTAA was used as a reference HTM, [b]dopant-free composition, [c]p-i-n device structure, [d]n-i-p device structure.

1.2.1.2. Hole transporting materials based on the condensation chemistry

As a result of a facile, low-cost, organometallic-catalyst-free condensation chemistry, a new emerging group of materials demonstrate promising performance results in PSCs, competing even with a reference spiro-OMeTAD. Some examples of HTMs obtained via condensation reactions are shown in Schemes 2–4. The photovoltaic parameters of such compounds are summarized in Table 2.
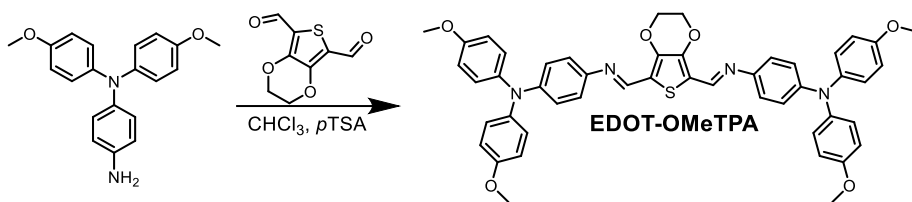
Scheme 2. Synthetic route and molecular structure of HTM EDOT-OMeTPA based on the condensation chemistry[125]

Docampo et al. have pioneered the utilization of small molecules obtained via condensation chemistry as HTMs for PSCs in 2015[125], when they introduced an azomethine-based compound EDOT-OMeTPA. It was synthesized by a simple one-step Schiff base condensation reaction (Scheme 2), which had only one by-product, i.e., water, hence an uncomplicated workup procedure. Regularly structured PSCs employed with EDOT-OMeTPA resulted in PCE exceeding 11 %, which at the time was in comparison with the state-of-the-art compound spiro-OMeTAD.
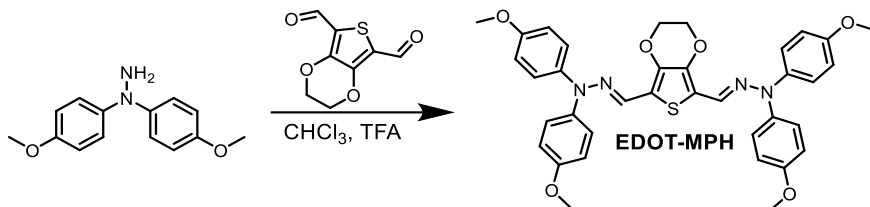
Scheme 3. Synthetic route and molecular structure of HTM EDOT-MPH based on the condensation chemistry[126]

Several years later, the same authors extended their research and presented a small molecule based on hydrazone, named EDOT-MPH, obtained via the hydrazine condensation reaction with aromatic aldehyde (Scheme 3)[126]. An application of such HTM in PSCs resulted in an average PCE of 15.8 %, which can be explained by a lower V_{OC} value, most likely originating from the unoptimized energy levels and interfacial recombination.
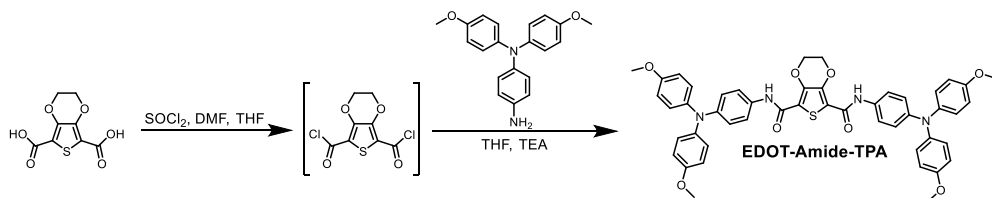
Scheme 4. Synthetic route and molecular structure of HTM EDOT-Amide-TPA based on the condensation chemistry[127]

One of the highest efficiencies for HTMs in PSCs at the time was reported by Petrus et al.[127], introducing the first hole conductor with an amide-based backbone named EDOT-Amide-TPA (Scheme 4). An outstanding PCE value of 20.3 %, outperforming spiro-OMeTAD-based devices (19.7 %), resulted from an effective

charge transfer at the perovskite/HTM interface, which is a consequence of intrinsic properties of amide group and passivation of the perovskite surface.
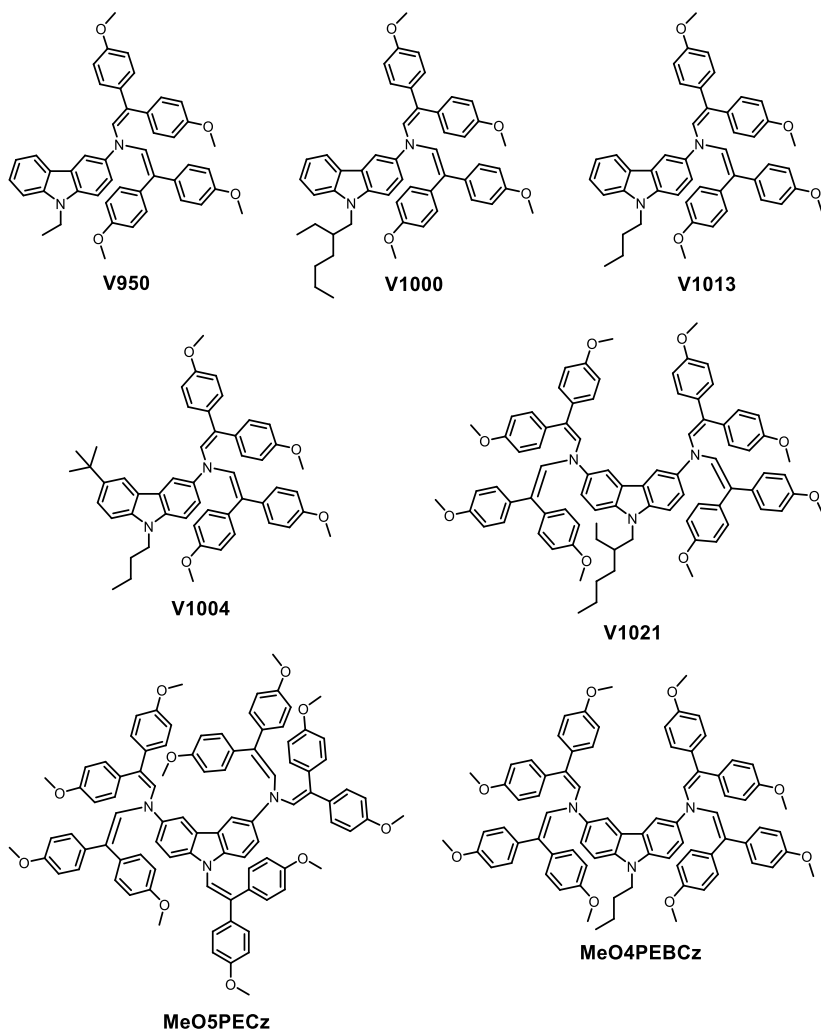
Figure 11. Chemical structures of HTMs based on condensation chemistry[128-130]

Previous studies gave a fresh start to a new class of compounds called enamines, containing diphenylethenyl fragments, by showing a cost-effective and more environmentally friendly route towards scaled-up synthesis of HTMs. Daskeviciene et al. reported a promising PCE value of the devices, reaching almost 18 %[128]. Such performance was demonstrated by mesoporous PSCs, employed with a *p*-type semiconductor V950, which was obtained via enamine condensation reaction between the aromatic amine and aromatic aldehyde, without the need for column chromatography or sublimation purification of the product. In the following publication, Daskeviciene et al. introduced a new series of enamines based on V950, conducting a more detailed investigation about the influence of aliphatic chains on the

properties of carbazole-based HTMs[129]. According to the research, the incorporation of longer alkyl chains (V1000, V1013) resulted in slightly decreased PCE values, whereas additional substitution with the *tert*-butyl group at the 6th position of the carbazole fragment (V1004) led to an increase in efficiency, reaching 18.6 %. However, the highest performance of PSCs from the series was achieved when the number of enamine fragments was doubled (V1021), and the devices employed with such HTM showed PCE exceeding 19 %, which coincides with the highest hole mobility value. Recently, a similar approach, using differently *N*-substituted carbazole derivatives, was reported by Snaith et al.[130]. MeO5PECz *N*-substituted with an additional diphenylethenyl group and MeO4PEBCz containing a butyl chain in the aforementioned position were used as dopant-free HTMs for n-i-p type devices. Champion PSCs fabricated with MeO4PEBCz achieved the efficiency of 16.4 %, while MeO5PECz reached almost 17 %, which shows a performance comparable to the devices employed with doped spiro-OMeTAD (18.1 %). Moreover, the removal of oxidizing additives considerably improved the stability of the devices by maintaining more than 80 % of their original efficiency after 1,000 h, whereas PSCs containing doped spiro-OMeTAD degraded rapidly within the first 24 h.

Table 2. Photovoltaic characteristics of PSCs employed with HTMs based on the condensation chemistry

HTM	V_{OC} (V)	J_{SC} (mA/cm^2)	*FF*	PCE (%)	Reference PCE (%)[a]
EDOT-OMeTPA[d]	0.95	18.9	0.61	11.0	11.9
EDOT-MPH[d]	1.06	20.1	0.73	15.8	17.2
EDOT-Amide-TPA[d]	1.16	22.7	0.77	20.3	19.7
V950[d]	1.07	22.5	0.74	17.8	18.6
V1000[d]	1.036	22.46	0.71	16.51	19.10
V1013[d]	1.022	22.39	0.75	17.09	19.10
V1004[d]	1.093	22.49	0.76	18.61	19.10
V1021[d]	1.118	22.62	0.75	19.01	19.10
MeO5PECz[b,d]	1.06	22.2	0.72	16.9	15.1[b]
MeO4PEBCz[b,d]	1.02	21.9	0.74	16.4	15.1[b]

[a]Spiro-OMeTAD or PTAA was used as a reference HTM, [b]dopant-free composition, [c]p-i-n device structure, [d]n-i-p device structure.

1.2.2. Polymeric compounds as hole transporting materials

As briefly mentioned in the sub-section 1.1.3.4., in addition to small organic molecules, polymers have attracted an increased amount of attention from researchers during recent years. Such interest mainly arose because of a few alluring properties of polymeric compounds: exceptional thermal stability, mechanical flexibility, good film forming ability, hydrophobicity, tunable energy levels, and rapid charge transport.

Despite previously mentioned polymeric compounds, such as PTAA[82], often used as a reference, or PEDOT:PSS[131], a variety of other polymers have been employed in PSCs as hole conductors. Based on the basic structure, polymers can be classified into two types, i.e., non-crosslinked (linear) and cross-linked (network) polymers.

1.2.2.1. Non-crosslinked polymers as hole transporting materials

Linear polymers are composed of repeated monomers, which are arranged in a straight line and tend to have end-to-end links. These polymers are usually held together by weak van der Waals forces or hydrogen bonding, whereas cross-linked polymers mainly have strong covalent bonds between monomeric units. Some examples of non-crosslinked polymeric compounds are shown in Figure 12. The photovoltaic parameters of such HTMs are summarized in Table 3.
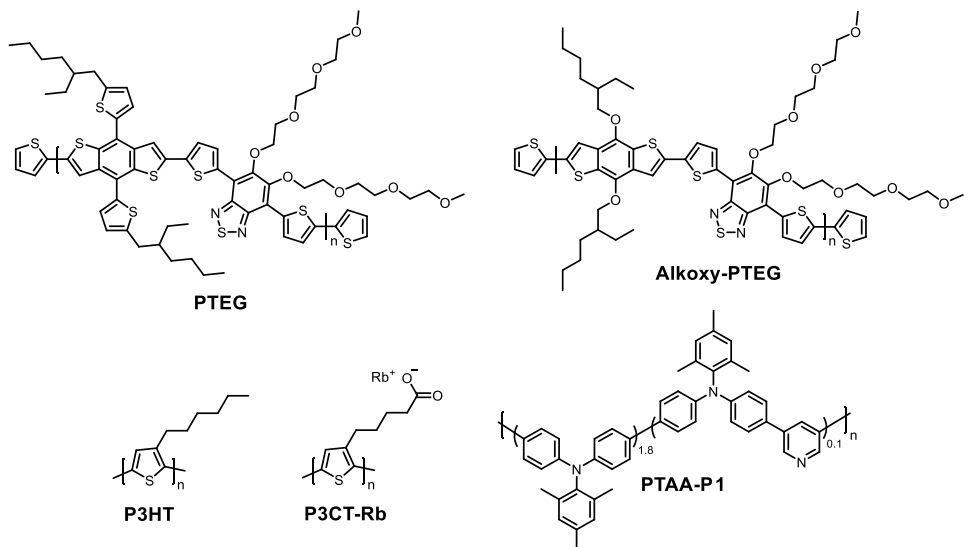
Figure 12. Chemical structures of HTMs based on non-crosslinked polymeric compounds[132-137]

A well-known polymer poly(3-hexylthiophene) (P3HT) presented only mediocre performance (10.3 %) when used without dopants in a regular PSC[132], which can be explained by low conductivity; however, after a few years, Carlo et al. demonstrated that the same HTM doped with regular additives can show a remarkable enhancement in device efficiency, reaching 19.25 %[133]. Similarly structured polymer named P3CT doped with alkali metal Rb^+ ions helped to achieve even higher efficiency (20.52 %) for inverted PSCs[134]. Such an improvement presented by Wu et al. is based on the enhanced conductivity and well-aligned work function of P3CT-Rb, corresponding with the VB of the perovskite, which as well resulted in a remarkable V_{OC} value and high FF. Another interesting enhancement of the efficiency of regularly structured PSCs was noticed after the incorporation of an undoped polymer-based HTM, named PTEG. Park et al., who presented such conductive polymer with incorporated flexible tetraethylene glycol (TEG) groups, which improve

solubility and contact with the perovskite layer, exhibited a successful performance of devices reaching 19.8 %[135]. However, the same authors later demonstrated that the PCE of devices containing PTEG derivative alkoxy-PTEG can be enhanced even further[136]. The replacement of tiophene groups with alkoxy groups in the backbone of BDT (benzo[1,2-b:4,5:b′]dithiophene) significantly improved the solubility of the HTM, even in non-aromatic green solvents, such as 3-methylcyclohexanone. Moreover, it has been found that TEG groups can prevent potential lead leakage by chelating lead ions. PSCs based on a dopant-free polymer alkoxy-PTEG exhibited a PCE of 21.2 %. Recently, a new molecular engineering strategy was used by Zhu et al. to improve the PCE of dopant-free PTAA-based p-i-n devices[137]. The incorporation of pyridine units into the PTAA backbone resulted in an extraordinary PV performance, reaching almost 25 %, which is one of the highest values for inverted PSCs reported to date. Additionally, these devices demonstrated superior long-term stability, maintaining more than 93 % of their initial efficiency after 800 h. Outstanding PV parameters can be explained by the interaction of pyridine units with the perovskite layer through the coordination with Pb^{2+} ions, positively affecting the interface of the perovskite film and the molecular conformation of HTM (PTAA-P1), providing favorable regularity and uniformity.

However, there are several issues limiting the scalable application of polymers in the PSCs. The most important disadvantages are the tedious synthesis schemes, low batch-to-batch reproducibility, and complicated purification procedures. Moreover, such non-crosslinked HTLs can be partially dissolved or etched by DMSO or DMF solvents, which are used for the subsequent fabrication step in p-i-n structured devices. In order to solve these issues, several different strategies, such as self-assembled monolayers[138] (SAMs) or the change of solvent for perovskite precursor[139], have been employed; however, another promising alternative called cross-linking has been reported recently.

Table 3. Photovoltaic parameters of PSCs employed with non-crosslinked polymer-based HTMs

HTM	V_{OC} (V)	J_{SC} (mA/cm^2)	*FF*	PCE (%)	Reference PCE (%)[a]
PEDOT:PSS[c]	1.03	22.57	0.81	18.8	-
P3HT[b,d]	0.96	19.5	0.55	10.3	-
P3HT[d]	1.09	23.86	0.74	19.25	-
P3CT-Rb[c]	1.144	21.67	0.83	20.52	-
PTEG[b,d]	1.14	22.5	0.77	19.8	-
Alkoxy-PTEG[b,d]	1.14	23.2	0.80	21.2	-
PTAA-P1[b,c]	1.17	25.50	0.83	24.89	22.85

[a]PTAA was used as a reference HTM, or compounds were compared with each other; [b]dopant-free composition, [c]p-i-n device structure, [d]n-i-p device structure.

1.2.2.2. Cross-linked polymers as hole transporting materials

Insufficiently researched cross-linkable compounds demonstrate excellent potential as HTMs for perovskite devices, since they have a combination of properties, which are common for both small-organic molecules and polymers. Firstly, such compounds can be synthesized via a simple low-cost synthetic route with ensured repeatability of reactions and without any extensive purification procedures, which is mainly attributed to small-organic materials. Secondly, cross-linkable compounds are known for their remarkable thermal and morphological stability, good film-forming properties, which are inherent characteristics of polymeric materials. Finally, the cross-linking of monomers that contain vinyl groups allows to form insoluble 3D networks, which are resistant to the solvents that are used for the perovskite precursor solution. Some representative examples of cross-linkable compounds are shown in Figure 13. The photovoltaic characteristics of such HTMs are summarized in Table 4.
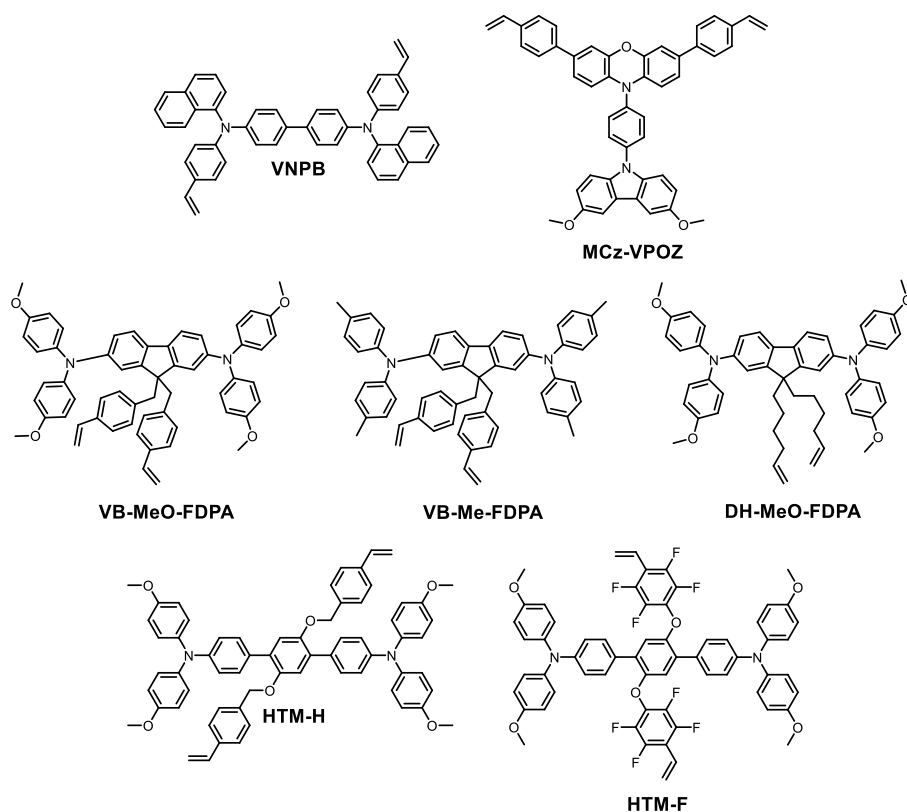
Figure 13. Chemical structures of cross-linkable HTMs[140-143]

Sargent et al. were among the first ones to report this new methodology for hole extraction, when in 2016 they presented a novel cross-linkable arylamine derivative, named VNPB, and employed it in a regular PSC architecture (PCE=16.5 %)[140]. VNPB was deposited on top of the perovskite layer by spin-coating; afterwards, it was thermally cross-linked, forming a protective 3D network, which enhanced the device

resistance to moisture, heat, and both polar and non-polar solvents. In addition, VNPB-based devices demonstrated impeccable stability results under heat and moisture after 30 days, which proved that cross-linked HTL provides exceptional physical protection to the perovskite.
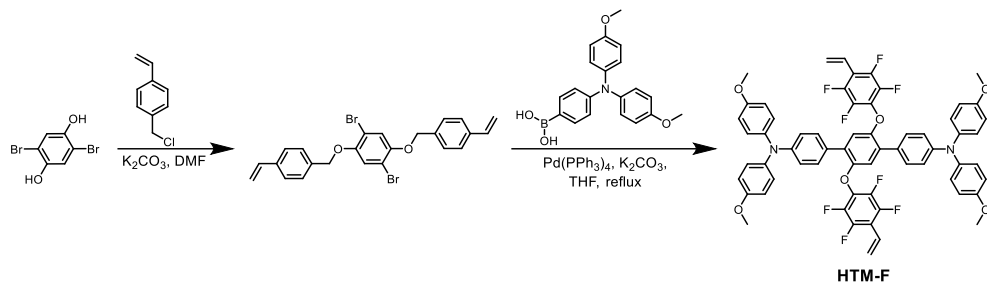
Scheme 5. The synthetic route of HTM-F[141]

Other HTMs containing triphenylamine moieties and cross-linkable groups of tetrafluorovinylic (the synthetic route is shown in Scheme 5) or vinylphenyl were introduced by Xu et al.[141]. The fabrication of inverted PSCs using dopant-free HTLs with fluorine units (HTM-F) and without fluorine units (HTM-H) resulted in high PV performance values of 20.51 and 19.07 %, respectively. Since fluorine atom, organic cations, and lead are capable of forming strong interactions, the inclusion of fluorine greatly improved the quality of the perovskite film by passivating the perovskite layer. More importantly, the incorporation of cross-linkable groups had a tremendous positive effect on the stability of devices, PSCs with HTM-F retaining 90 % of the efficiency after 2,000 h in ambient air. The thermal polymerization reaction of HTM-F and a schematic illustration of the formation of a cross-linked 3D polymer network are demonstrated in Figure 14.
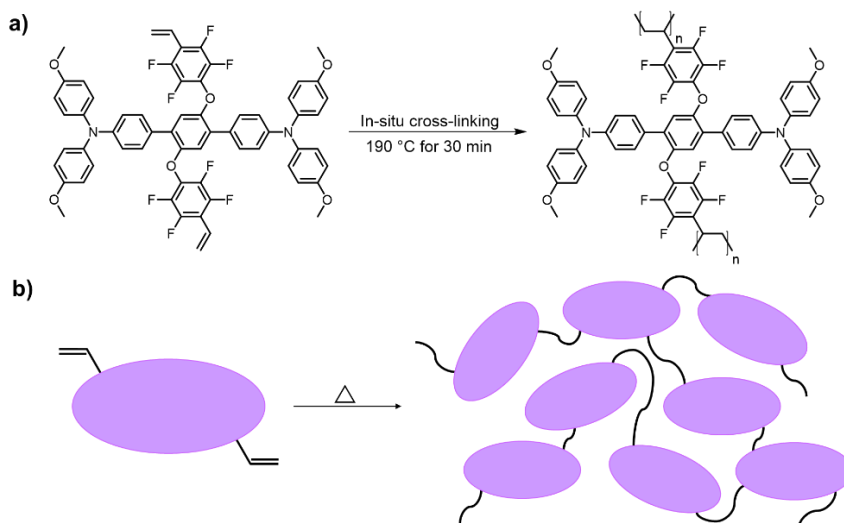
Figure 14. In-situ cross-linking polymerization of HTM-F under thermal conditions (a)[141], a schematic illustration of the formation of a continuous network polymer (b)

Shao et al. introduced a series of cross-linkable HTMs based on diphenylamine and fluorene derivatives[142]. The fabrication of inverted PSCs revealed that all in-situ thermally cross-linked HTLs positively influenced the efficiency of the devices when compared to the performance of the reference PEDOT:PSS-based PSCs (12.3 %). The highest PCE of 18.7 % was exhibited by a device containing HTM, empowered by methoxy groups and vinylbenzyl substituents, called VB-MeO-FDPA. Significantly improved device performance can be attributed to a better energy level alignment of VB-MeO-FDPA with the perovskite and high conductivity of the cross-linked layer. However, the replacement of methoxy groups with methyl groups (VB-Me-FDPA) resulted in a barely reduced efficiency of 17.9 %, whereas the incorporation of cross-linkable alkyl chains instead of vinylbenzyl substituents (DH-MeO-FDPA) decreased the PCE even more (15.9 %). Such results can be explained by high hole drift mobility values of VB-MeO-FDPA and VB-Me-FDPA, hence higher *FF* values. Recently, Zhang et al. presented carbazole-based in-situ cross-linkable compound MCz-VPOZ for hole transport in inverted PSCs, which demonstrated the highest reported performance (23.9 %) for non-PTAA HTMs so far[143]. Moreover, HTL of MCz-VPOZ showed an impressive chemical resistance to DMF and substantial defect passivation effect, resulting in a high-quality perovskite film and a decrease in recombination losses. Furthermore, the unencapsulated PSCs employed with cross-linked MCz-VPOZ HTL demonstrated an outstanding stability under several operational stressors for 2,500 h.

Table 4. Photovoltaic parameters of PSCs employed with cross-linkable HTMs

HTM	V_{OC} (V)	J_{SC} (mA/cm^2)	*FF*	PCE (%)	Reference PCE (%)[a]
VNPB[b,d]	1.11	19.0	0.81	16.5	14.0
HTM-F[b,c]	1.09	23.03	0.82	20.51	-
HTM-H[b,c]	1.05	22.7	0.80	19.07	-
VB-MeO-FDPA[b,c]	1.15	20.89	0.78	18.7	13.7
VB-Me-FDPA[b,c]	1.16	20.17	0.77	17.9	13.7
DH-MeO-FDPA[b,c]	1.09	19.54	0.75	15.9	13.7
MCz-VPOZ[b,c]	1.169	24.15	0.85	23.9	20.9

[a]Spiro-OMeTAD, PTAA, or PEDOT:PSS were used as a reference HTM, or compounds were compared with each other; [b]dopant-free composition, [c]p-i-n device structure, [d]n-i-p device structure.

2. REVIEW OF THE PUBLISHED ARTICLES

2.1. "Efficient and stable perovskite solar cells using low-cost aniline-based enamine hole-transporting materials" (scientific publication no. 1, Q1, 56 quotations)

This sub-chapter is based on the paper published in *Advanced Materials,* 2018, 30, 1803735 by D. Vaitukaityte, Z. Wang, T. Malinauskas, A. Magomedov, G. Bubniene, V. Jankauskas, V. Getautis, and H. J. Snaith[144].

As mentioned in the previous sections, cost-effective and stable HTMs are essential for ensuring further progress and scaling up of PSCs. Therefore, it is necessary to avoid the use of multi-step synthesis, metal catalysts, and a tedious sublimation step as the purification procedure. In the first publication, aniline was chosen as a backbone for the whole series of novel HTMs, since it is one of the most fundamental and commonly used precursors in the chemical industry. Surprisingly low price influences its availability and usability for the manufacture of various chemicals on a large scale[145]. In order to reduce the cost of aniline-based semiconductors even further, they were synthesized using a straightforward single-step condensation reaction, which is a transition-metal-catalyst-free synthesis; hence, the purification of HTMs is much less complicated, and often, a simple crystallization procedure is perfectly adequate.

In this work, four semiconductors were obtained by means of condensation between the amine group of aniline precursors and aldehyde group of 2,2-bis(4-methoxyphenyl)acetaldehyde in the presence of (+/−)camphor sulfonic acid (CSA). The synthesis of novel HTMs is presented in Scheme 6. Depending on the ratio of reactants, the enamines with two (**V1056**, **V1092**) or three (**V1091**, **V1102**) diphenylethenyl groups have been synthesized. In order to obtain **V1056**, aniline derivative with a methoxy group in the *p*-position, acting as an additional donor, was used as a precursor; correspondingly, for the synthesis of **V1102**, 3,5-dimethylaniline was used, which reportedly has a positive influence on the PV performance of devices[146].

The price of the reagents that are necessary for the synthesis was estimated using the procedure determined by Osedach et al. in order to evaluate the cost-effectiveness of new HTM series[147]. According to the calculations, the cost of **V1091** is approximately 16 \$/g, whereas 1 g of **V1056** can be synthesized for 8 \$, proving that enamines can be obtained at a significantly reduced rate compared to the reference spiro-OMeTAD (synthesis cost is 92 \$/g)[125].

In order to ascertain the thermal stability of aniline-based semiconductors, thermogravimetric analysis (TGA) was carried out; the results are demonstrated in Figure 15 and Table 5. The measurements showed that all four compounds possess superb thermal stability that was higher than 310 ºC, which is sufficient for regular device operation conditions. Additionally, the heating curves demonstrate rapid weight loss, indicating that HTMs sublime rather than thermally decompose, which implies that HTLs can be formed by vacuum deposition, further expanding the application of compounds.

a)

(4.5 eq.)
CSA, toluene, reflux, 6 h

V1091 (69 %)

(2.1 eq.)
CSA, toluene, reflux, 2 h

V1092 (72 %)

b)

(2.5 eq.)
CSA, toluene, reflux, 20 min

V1056 (46 %)

(6 eq.)
CSA, toluene, reflux, 2 h

V1102 (60 %)

V1056: R_1 = H; R_2 = -OCH$_3$
V1102: R_1 = -CH$_3$; R_2 = H
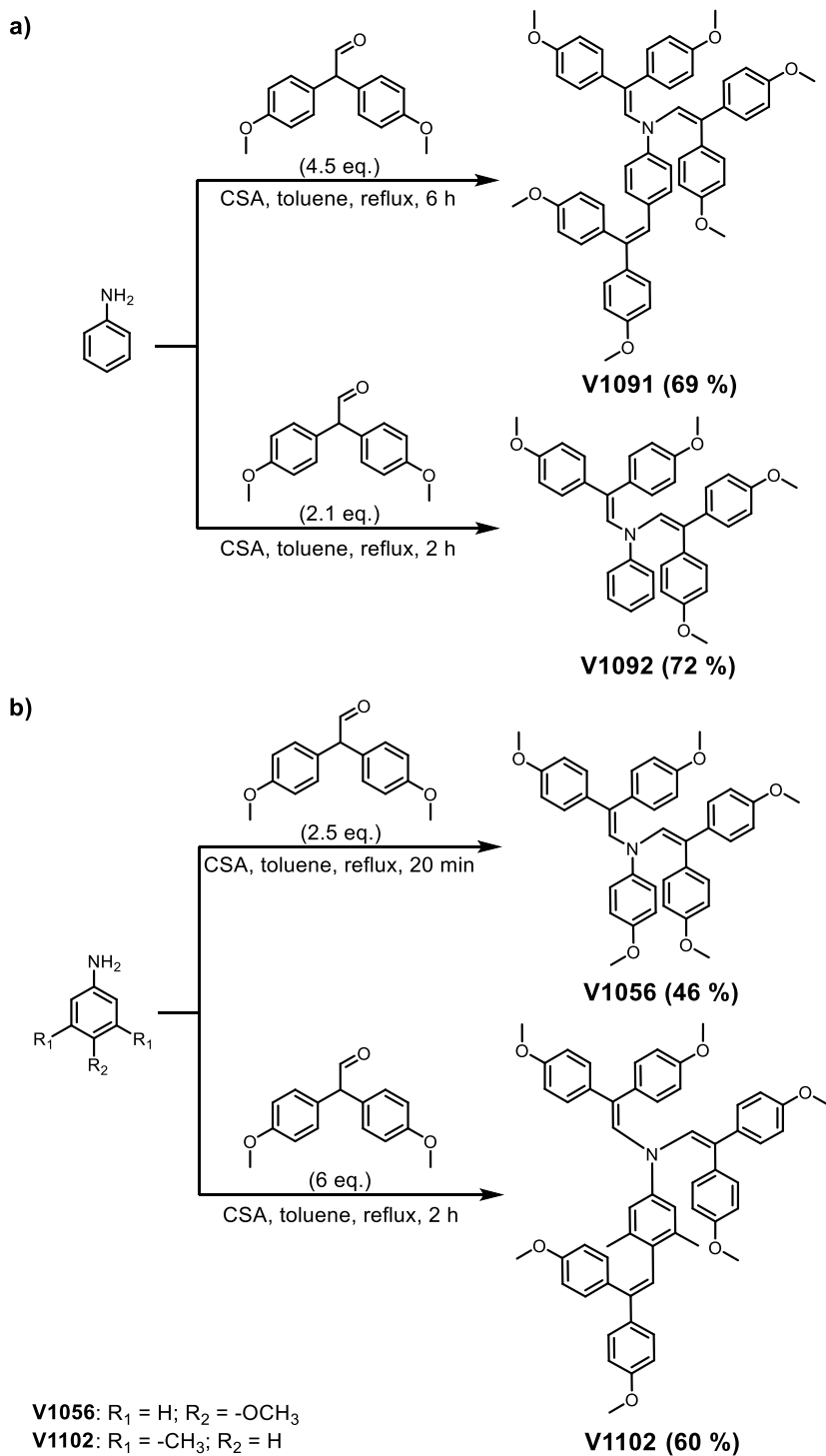
Scheme 6. Synthesis of aniline-based HTMs: a) **V1091**, **V1092**; b) **V1056**, **V1102**
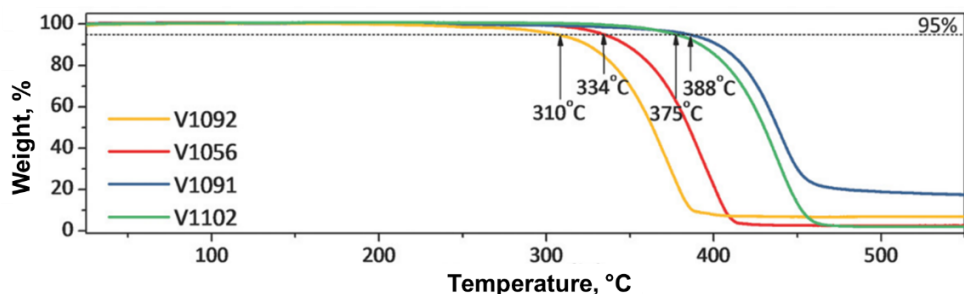
Figure 15. TGA heating curves of aniline-based HTMs (scan rate 10 K/min)

The thermal transitions of new HTMs were investigated by differential scanning calorimetry (DSC); detailed data is collected in Table 5. DSC analysis revealed that larger molecules, such as **V1091** and **V1102**, containing three diphenylethenyl moieties, show a lower tendency to crystallize than relatively smaller compounds **V1056** and **V1092**, including only two aforementioned moieties. The aniline derivative with the simplest structure of the series **V1092** presents a high melting temperature (T_m) at 251 °C, a glass transition (T_g) temperature at 80 °C, and a crystallization process at 129 °C. The incorporation of an additional methoxy group into the *para*-position of the phenyl ring **V1056** causes some disorder in the molecule, resulting in a significantly reduced T_m (190 °C) and the absence of the crystallization peak. The introduction of the third diphenylethenyl group in the mentioned position (**V1091**) interferes with the crystallization process even more; hence, the molecule gains a fully amorphous state. **V1102** shows similar behavior, but its T_g is lower, which can be explained by the steric hindrance of the molecule that occurred due to the addition of two methyl moieties.

Table 5. Thermal, optical, and photophysical properties of aniline-based HTMs and reference spiro-OMeTAD

ID	T_m (ºC)[a]	T_c (ºC)[a]	T_g (ºC)[a]	T_{dec} (ºC)[b]	λ_{abs} (nm)	I_p (eV)	μ_0 (cm²/Vs)[c]	μ (cm²/Vs)[d]
V1056	190	–	78	334	333 384	5.19	1.3×10^{-5}	7.8×10^{-4}
V1091	–	–	109	388	381	5.17	2.8×10^{-5}	1.7×10^{-2}
V1092	251	129	80	310	331 370	5.30	–	–
V1102	–	–	96	375	367	5.16	1.6×10^{-6}	1.5×10^{-4}
Spiro-OMeTAD	245	–	126	449	387	5.00	4.1×10^{-5}	5.0×10^{-4}

[a]Determined by DSC: scan rate 10 K/min, N_2 atmosphere, second run; [b]determined by TGA: scan rate 10 K/min, N_2 atmosphere; [c]mobility value at zero field strength; [d]mobility value at 6.4×10^5 V/cm field strength.

38

The optical properties of novel HTMs were inspected by the means of ultraviolet-visible (UV-vis) absorption. Figure 16 a shows the UV-vis spectra; the recorded absorption wavelengths are collected in Table 5.
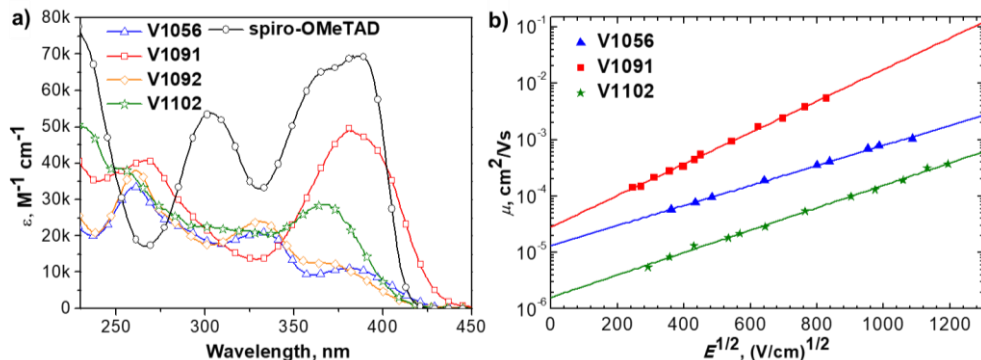
Figure 16. a) UV-vis absorption spectra of aniline-based HTMs and spiro-OMeTAD in THF ($c = 10^{-4}$ M), b) electric-field dependencies of the hole drift mobilities in films of **V1056**, **V1091**, and **V1102**

The UV-vis absorption spectra of **V1056** and **V1092**, containing two diphenylethenyl fragments, show that the incorporation of methoxy group has an insignificant influence on the π-conjugated system. Whereas the addition of the third fragment considerably expands the size of the system, demonstrating a bathochromic shift of ≈50 nm. In comparison, adding two methyl groups in the 3,5-positions of the phenyl ring (**V1102**) results in a ≈14 nm shift towards shorter wavelengths, which could be attributed to an enhanced steric hindrance at the *para*-position, twisting diphenylethenyl fragments out of the plane.

In order to investigate the energy levels of new semiconductors in the solid state, the ionization potential (I_p) was measured by the photoelectron spectroscopy in air (PESA) method; the results are summarized in Table 5. The highest I_p value of the series is demonstrated by **V1092**. The addition of electron donating moieties, such as diphenylethenyl (**V1091**) or methoxy (**V1056**), decreases the I_p value by approximately 0.1 eV, while two additional methyl groups (**V1102**) do not have any effect compared to the I_p of **V1092**. Although, the measured values of I_p of aniline-based HTMs are slightly higher than that one of spiro-OMeTAD, they are suitable for the application in PSCs, being in compliance with the VB of the perovskite absorbing layer[148].

The charge transport properties of synthesized enamines were studied by using the xerographic time-of-flight (XTOF) technique (Figure 16 b); the results are shown in Table 5. The hole drift mobility value of **V1056** is in the same order of magnitude at high electric fields as for spiro-OMeTAD (5.0×10^{-4} cm^2/Vs)[149], whereas the addition of the third diphenylethenyl fragment in **V1091** resulted in substantially increased mobility of 1.7×10^{-2} cm^2/Vs. However, the addition of two methyl groups to the phenyl ring in **V1102** has a negative impact on the charge transport properties at zero field strength due to the increased steric hindrance effect.

Table 6. Solar cell performance parameters extracted from the *J-V* curves

ID	V_{OC} (V)	J_{SC} (mA/cm^2)	*FF*	PCE (%)
V1056	1.07	22.1	0.79	18.7
V1091	1.11	22.5	0.81	20.2
V1102	1.13	22.7	0.68	17.6
Spiro-OMeTAD	1.12	22.6	0.80	20.2

Eventually, in order to test the performance of aniline derivatives as HTLs, planar perovskite solar cells with a device structure of FTO/SnO$_2$/perovskite/HTM/Au were fabricated. The *J-V* characteristics were collected under simulated solar illumination (AM 1.5G, 100 mW/cm^{-2}); the data is summarized in Table 6. The champion PCE of the prepared devices with enamine-based HTMs varies from 17.6 % for **V1102** to 20.2 % for **V1091**, reaching the same efficiency as a control device containing spiro-OMeTAD.
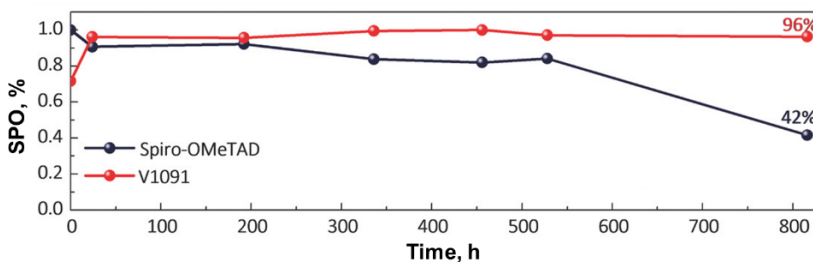
Figure 17. Decay of SPO of devices with spiro-OMeTAD and **V1091**

In Figure 17, the stability of the devices in ambient air with a relative humidity of 45 % without any encapsulation is reported for more than 800 h. The cells with **V1091** maintained even 96 % of their initial efficiency, while the stabilized power output (SPO) of the control device with spiro-OMeTAD decreased to 42 % after aging. The improvement in stability can be attributed to the enhanced molecular packing and a more hydrophobic surface of the **V1091** films.

2.2. "Cut from the same cloth: enamine-derived spirobifluorenes as hole transporters for perovskite solar cells" (scientific publication no. 2, Q1, 6 quotations)

This sub-chapter is based on the paper published in *Chemistry of Materials,* 2021, 33, 15, 6059–6067 by D. Vaitukaityte, C. Momblona, K. Rakstys, A. A. Sutanto, B. Ding, C. Igci, V. Jankauskas, A. Gruodis, T. Malinauskas, A. M. Asiri, P. J. Dyson, V. Getautis, and M. K. Nazeeruddin[150].

As previously discussed, spiro-OMeTAD is among the most extensively researched HTMs, but the synthetic and purification procedures are too complicated

and expensive to begin a large-scale production. However, the synthetic strategy of aniline-based enamines, introduced in the aforementioned section, has proven to be successful in regard to the simplified synthetic scheme and product workup, hence a considerably reduced cost of HTMs. Therefore, in the following publication, a combination of both strategies, spirobifluorene core and condensation reaction, has been used.

Herein, four novel HTMs with a differently substituted spirobifluorene core, containing from one to four enamine branches and mimicking the state-of-the-art spiro-OMeTAD, were obtained. Scheme 7 demonstrates the chemical structures of spirobifluorene-based semiconductors and synthesis route that are used to obtain such compounds. The calculations of a lab-scale synthesis cost of enamine-derived semiconductors showed that **V1307** (~37 \$/g) is much more inexpensive than a reference spiro-OMeTAD (~92 \$/g).

V1305 (49 %)

V1306 (58 %)

V1307 (33 %)

V1308 (42 %)

CSA, THF/toluene, reflux

V1305: R$_1$ = H; R$_2$ = NH$_2$; R$_3$ = H; R$_4$ = H
V1306: R$_1$ = H; R$_2$ = NH$_2$; R$_3$ = NH$_2$; R$_4$ = H
V1307: R$_1$ = NH$_2$; R$_2$ = NH$_2$; R$_3$ = NH$_2$; R$_4$ = NH$_2$
V1308: R$_1$ = NH$_2$; R$_2$ = NH$_2$; R$_3$ = H; R$_4$ = H
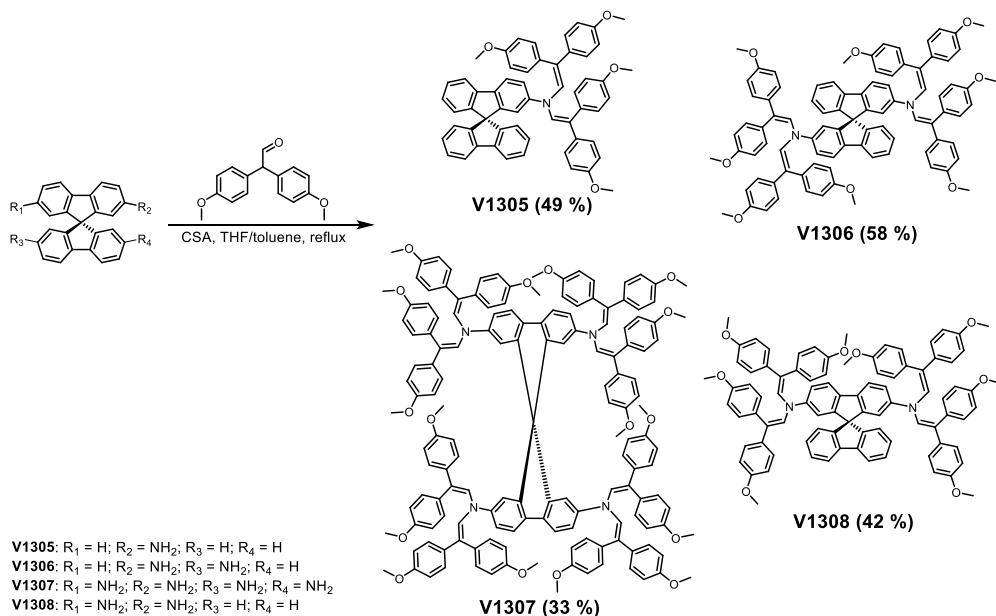
Scheme 7. Synthesis of spirobifluorene-based HTMs: **V1305**, **V1306**, **V1307**, **V1308**

The results of TGA and DSC of new condensation-based HTMs are summarized in Table 7. The decomposition temperature (T_{dec}), indicating a weight loss of 5 %, of all compounds from the series is approximately 400 °C, which implies very good thermal stability. DSC analysis indicated that three of four materials (**V1305**, **V1306**, **V1308**) tend to exist in both crystalline and amorphous states as well as spiro-OMeTAD[149]. However, a compound with a large structure and an enhanced molecular weight (**V1307**) has only an amorphous state and the highest T_g in the series (169 °C). Furthermore, all newly synthesized enamines have a higher glass transition temperature compared to spiro-OMeTAD (126 °C), indicating an improved morphological stability of the films.

Table 7. Thermal, optical, and photophysical properties of spiro-based HTMs

ID	T_m (°C)[a]	T_c (°C)[a]	T_g (°C)[a]	T_{dec} (°C)[a]	λ_{abs} (nm)[b]	I_P (eV)[c]	E_g (eV)[d]	E_{ea} (eV)[e]	μ_0 (cm²/Vs)[f]
V1305	243	-	131	380	267, 372	5.33	2.90	2.43	1.7×10^{-5}
V1306	294	226	154	402	267, 373	5.37	2.84	2.53	5.4×10^{-6}
V1307	-	-	169	401	263, 389, 408	5.46	2.83	2.63	6.4×10^{-4}
V1308	305	203	158	371	263, 388, 408	5.46	2.78	2.68	9.4×10^{-4}

[a]Observed from DSC and TGA (10 °C/min, N_2 atmosphere); [b]absorption spectra were measured in THF solutions (10^{-4} M); [c]ionization energies of the films measured using PESA; [d]E_g estimated from the intersection of absorption and emission spectra of solid films; [e]$E_{ea} = I_P - E_g$; [f]mobility value at zero field strength.

Figure 18 a shows the UV-vis absorption spectra of synthesized HTMs in THF solution. All four enamines exhibit π–π* transitions of the absorption band located around 260 nm, whereas even a stronger absorption band was observed in the 370–410 nm range, attributing to n−π* transitions. The differences in absorption spectra are due to a different number and the substitution position of diphenylethenyl moieties. The absorption shifts hyperchromically when the quantity of enamine fragments increases, whereas the substitution of fluorene on both sides (**V1307**, **V1308**) determines a red-shift of 35 nm. The optical bandgaps (E_g) estimated from the intersection of the absorption and emission spectra are in the range between 2.78 and 2.90 eV.
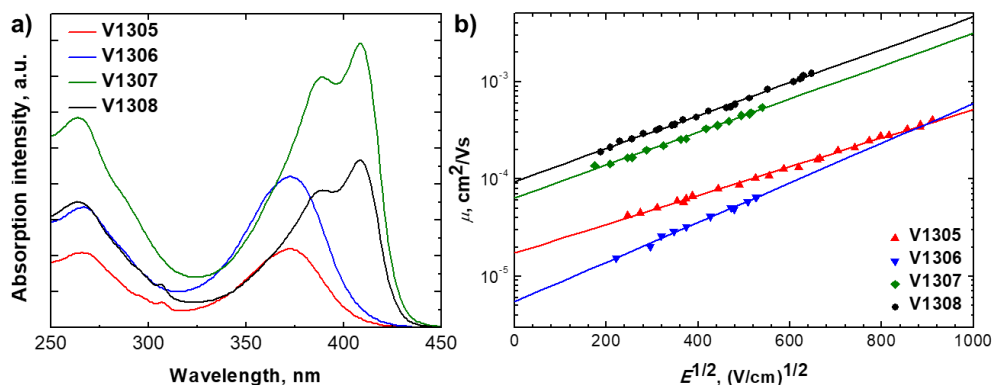
Figure 18. a) UV-vis absorption spectra of spiro-based HTMs in THF (10^{-4} M), b) electric field dependencies of the hole drift mobility in films of spiro-enamines

The solid-state I_P measurements demonstrate that the HOMO energy level of spiro-based HTMs is in the range of 5.33 and 5.46 eV, which is quite stabilized compared to spiro-OMeTAD (5.00 eV)[151]. The data mentioned above was used for the calculations of the electron affinities (E_{ea}), which were found to be between 2.43 and 2.68 eV. It is important to note that the E_{ea} values are smaller than the CB of the perovskite (−4.10 eV); thus, it should be possible to avoid the unwanted electron transfer from the perovskite to the electrode. The results of the I_P measurements and the calculations of the E_{ea} are summarized in Table 7.

Figure 18 b shows the hole drift mobility dependency on the electric field strength; the summarized data is provided in Table 7. The best charge transporting properties of the series were demonstrated by **V1308** and **V1307** with the μ_0 values of 9.4×10^{-4} and 6.4×10^{-4} cm^2/Vs, respectively; thus, both exceeded the mobility value of the reference spiro-OMeTAD ($\mu_0 = 1.3 \times 10^{-4}$ cm^2/Vs)[152]. Such results indicate that charge transporting abilities are strongly influenced by the molecular structure and particularly in this case, by a higher degree of conjugation in enamine branches of **V1307**[153–155].

Table 8. Solar cell performance parameters extracted from the *J-V* curves

ID	V_{OC} (V)	J_{SC} (mA/cm^2)	*FF*	PCE (%)
V1305	1.08	23.17	0.76	19.0
V1306	1.00	22.22	0.71	15.8
V1307	1.07	23.21	0.77	19.2
V1308	1.07	23.44	0.76	19.1
Spiro-OMeTAD	1.12	22.90	0.77	19.7

In order to reveal the influence of HTM with a different number and substitution position of enamine fragments on the performance of PSCs, n-i-p structured devices with a layout of FTO/c-TiO$_2$/m-TiO$_2$/SnO$_2$/perovskite/HTM/Au were fabricated. The data from the *J-V* curves is collected and summarized in Table 8. Three out of four devices containing **V1305**, **V1307**, and **V1308** showed similar efficiency values of 19.0 %, 19.2 %, and 19.1 %, respectively, which are on par with those of the traditional spiro-OMeTAD-based cells. In contrast, **V1306** presented the smallest PCE of the series (15.8 %), which can be attributed to the lowest value of hole mobility. In addition, a lower *FF* might be another element, which implies poor film quality of **V1306**-based devices, hence an unfavorable effect on the hole charge extraction and inadequate performance. The stability measurements of the unencapsulated devices revealed that enamine-based PSCs show results, comparable to those of the devices incorporated with a standard spiro-OMeTAD, for the same testing period.

2.3. "Molecular engineering of enamine-based hole-transporting materials for high-performing perovskite solar cells: influence of the central heteroatom" (scientific publication no. 3, Q1, 1 quotation)

This sub-chapter is based on the paper published in *Solar RRL*, 2022, 6, 11, 2200590 by D. Vaitukaityte, M. A. Truong, K. Rakstys, R. Murdey, T. Funasaki, T. Yamada, Y. Kanemitsu, V. Jankauskas, V. Getautis, A. Wakamiya[156].

According to the scientific literature, the replacement of the central core of a molecule can have different effects on the properties of HTM[157–159]. Furthermore, the presence of a different heteroatom in the structure has an impact on the electrochemical and photophysical properties of the material and the performance parameters of the device. The incorporation of heteroatoms, such as oxygen (O)[160,161], nitrogen (N)[162,163], and sulfur (S)[164–166], into the structure of the hole transporter is reported to result in the passivation of undercoordinated lead ions, while suppressing nonradiative losses at the perovskite/HTM interface. Moreover, the substitution of heteroatoms leads to suitably aligned energy levels regarding the VB of the perovskite, which may improve the performance of PSCs[118,170].

In this publication, the same one-step synthetic procedure, as it has been previously described, was used for the synthesis of a new series of compounds based on the incorporation of various central fragments, such as diphenyl ether (**V1433**), diphenyl sulfide (**V1434**), triphenylamine (**V1435**), and tetraphenylmethane (**V1431**), containing a different number of enamine branches (Scheme 8).
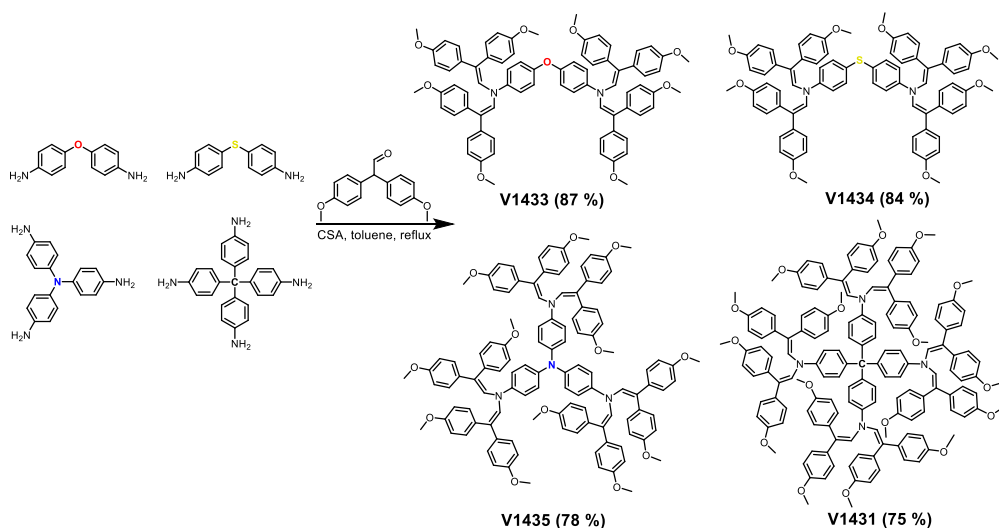
Scheme 8. Synthesis of HTMs **V1433**, **V1434**, **V1435**, and **V1431** with a different central heteroatom and a varying degree of enamine branches

The TGA analysis revealed that all newly synthesized semiconductors possess excellent thermal stability values of 413, 415, 409, and 413 °C for **V1431**, **V1435**, **V1433**, and **V1434**, respectively. The results of the DSC analysis showed that the C-cored compound **V1431** only has an endothermic peak at 339 °C, which implies about the melting process, whereas **V1433**, containing the oxygen core, presents T_g at 130 °C, followed by a cold crystallization at 270 °C and T_m at 295 °C, implying both crystalline and amorphous behavior. The other two molecules with N- and S-cores exhibited a reduced tendency to crystallize with glass transition temperatures at 130 °C for **V1435** and 125 °C for **V1434**, confirming their fully amorphous behavior. Detailed thermal features are summarized in Table 9.

Table 9. Thermal, optical, and photophysical properties of enamine-based HTMs

ID	T_m (°C)[a]	T_c (°C)[a]	T_g (°C)[a]	T_{dec} (°C)[a]	λ_{abs} (nm)[b]	I_P (eV)[c]	E_g (eV)[d]	E_{ea} (eV)[e]	μ_0 (cm^2/Vs)[f]
V1433	295	270	130	409	261, 344	5.37	2.97	2.40	3.0×10^{-6}
V1434	–	–	125	413	264, 357	5.52	2.99	2.53	3.5×10^{-6}
V1435	–	–	130	415	260, 373	5.27	2.88	2.39	2.0×10^{-5}
V1431	339	–	–	413	263, 347	5.54	3.02	2.52	5.0×10^{-6}

[a]Melting, crystallization, and glass transition temperatures observed from DSC; decomposition temperature observed from TGA, respectively (10 °C/min, N_2 atmosphere); [b]absorption spectra were measured in THF solutions (10^{-4} M); [c]ionization potentials of the films measured using PESA; [d]E_g estimated from the intersection of absorption and emission spectra of solid films; [e]$E_{ea} = I_P - E_g$; [f]hole drift mobility value at zero field strength.

The absorption spectra of enamines in the THF solution (Figure 19 a) display λ_{max} at 344, 347, 357, and 373 nm for **V1433**, **V1431**, **V1434**, and **V1435**, respectively, indicating a red-shift of approximately 20 nm for N-cored compound, which can be ascribed to an enhanced π-conjugation. Based on the intersection of absorption and emission spectra, the estimated bandgap values for all semiconductors from the series are similar at around 3.0 eV (Table 9).

The solid-state ionization potential measurements revealed that the HOMO energy level shifts deeper as the electron density of the central atom decreases; the I_P values of the compounds are presented in Table 9. LUMO energy level of novel compounds was estimated from the I_P and E_g values (-2.39, -2.40, -2.53, -2.52 eV for **V1435**, **V1433**, **V1434**, **V1431**, respectively), and it was found to be suitable for the application in PSCs[168].

The XTOF technique was used to estimate the charge transporting properties of undoped films of these new semiconductors; as demonstrated in Figure 19 b and Table 9, the best zero-field hole drift mobility value belongs to the N-cored **V1435**, showing one order of magnitude higher results than the rest of the compounds from the series.
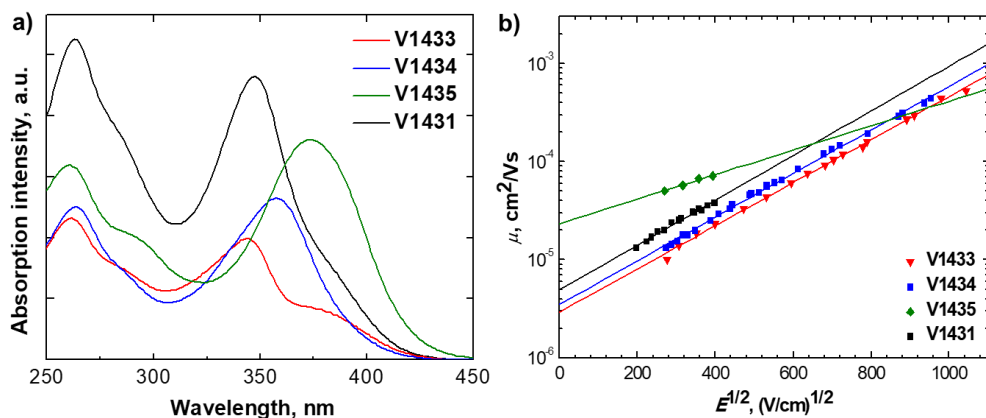
Figure 19. a) Absorption spectra of **V1433**, **V1434**, **V1435**, and **V1431** in THF solutions (10^{-4} M), b) electric field dependencies of the hole-drift mobility of enamines with a different central heteroatom

A new series of enamines containing various central heteroatoms was tested as HTLs in conventional n-i-p structured PSCs with the following device architecture: ITO-coated glass substrate/SnO$_2$/perovskite/HTM/gold. However, compound **V1433** with oxygen core did not show good solubility in 1,2-dichlorobenzene and chlorobenzene; therefore, the devices using this HTM could not be manufactured. In addition, a mixed-composition perovskite layer (Cs$_{0.05}$FA$_{0.87}$MA$_{0.08}$PbI$_{2.76}$Br$_{0.24}$) with a comparably deep VB level (-5.68 eV)[169] had to be chosen for the fabrication of these PSCs in order to match the HOMO energy level of new HTMs. The PV characteristics of the champion devices for each enamine-based HTM and a reference spiro-OMeTAD are summarized in Table 10.

Table 10. Solar cell performance parameters extracted from the *J-V* curves

ID	V_{OC} (V)	J_{SC} (mA/cm^2)	*FF*	PCE (%)
V1431	1.11	22.3	0.73	18.0
V1434	1.11	22.7	0.74	18.6
V1435	1.12	22.7	0.79	20.1
Spiro-OMeTAD	1.13	22.4	0.79	20.1

The best performance, as well as the highest hole drift mobility value, was demonstrated by **V1435**-based PSCs, reaching a PCE of 20.1 %, which was the same for the reference device. Other fabricated solar cells showed comparable performance results of 18.0 and 18.6 % for C- and S-core based HTLs.

2.4. "Enamine-based cross-linkable hole-transporting materials for perovskite solar cells" (scientific publication no. 4, Q1, 7 quotations)

This sub-chapter is based on the paper published in *Solar RRL*, 2021, 5, 1, 2000597 by D. Vaitukaityte, A. Al-Ashouri, M. Daskeviciene, E. Kamarauskas, J. Nekrasovas, V. Jankauskas, A. Magomedov, S. Albrecht, V. Getautis[170].

As mentioned earlier, high efficiency of PSCs is not the only goal: the longevity of these devices is an equally important criterion. One of the ways to improve the stability of devices is to avoid using dopants, which in most cases are responsible for the accelerated degradation of the perovskite, since lithium salts are hygroscopic and *t*BP tends to form complexes with PbI_2[171]. In order to enhance the longevity of p-i-n structured PSCs, it is necessary to use a solvent-resistant HTL that the polar solvents used for the formation of the perovskite layer could not wash away or etch the layer formed below the perovskite. One of the best options to fulfill these criteria is to take advantage of the characteristic of monomers containing vinyl groups to be thermally cross-linked and form 3D networks. In addition, such a strategy was combined with the aforementioned strategy for the synthesis of cost-effective enamine-based HTMs, and both were adapted and used in this publication.
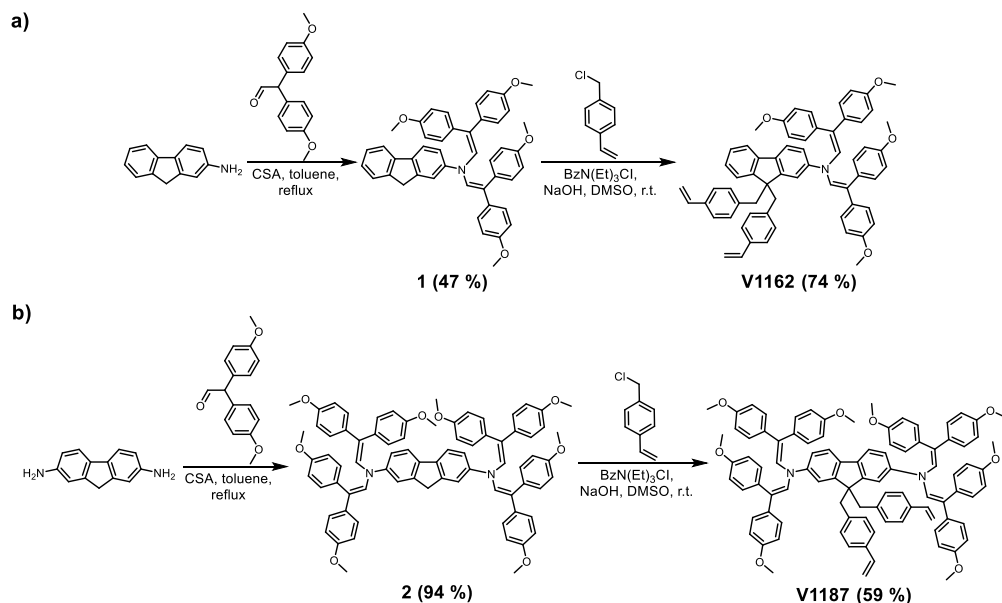
Scheme 9. Synthesis of cross-linkable HTMs: a) **V1162**, b) **V1187**

Firstly, for the preparation of enamines, the same synthetic approach as introduced before was followed, where two commercially available fluorene amines were chosen as starting materials. Secondly, in order to prepare the target molecules containing two vinyl groups, which are necessary for the thermal polymerization, a simple alkylation reaction was used in the presence of 4-vinylbenzylchloride, benzyltriethylammonium chloride, and sodium hydroxide in DMSO. During this synthetic procedure, two final compounds with one (**V1162**) and two (**V1187**) enamine branches were obtained (Scheme 9). Even though two-step synthesis was

used to prepare these semiconductors, the overall price of compounds was calculated to be 13.56 and 16.34 €/g for **V1162** and **V1187**, respectively, which is still extremely lower than the synthesis cost of one among the best performing polymeric HTMs for p-i-n devices, i.e., PTAA (500 $/g)[172].

A slightly different behavior of cross-linkable semiconductors can be observed from DSC curves (Figure 20 a, Table 11). During the first heating cycle, **V1162** presents a glass transition process at 100 °C, followed by a sharp endothermic peak corresponding to T_m at 228 °C, which indicates both crystalline and amorphous states that are inherent to this compound. An exothermic process appears right after the melting of the compound at 231 °C, indicating the thermal polymerization temperature (T_p). The absence of additional phase transitions during consecutive scans indicates the formation of the cross-linked polymer. In comparison, **V1187** shows a slightly higher T_g of 136 °C; moreover, the heating curves do not show the melting process, which is an indication of only amorphous state. The thermal polymerization starts at around 190 °C and reaches its peak at approximately 239 °C.
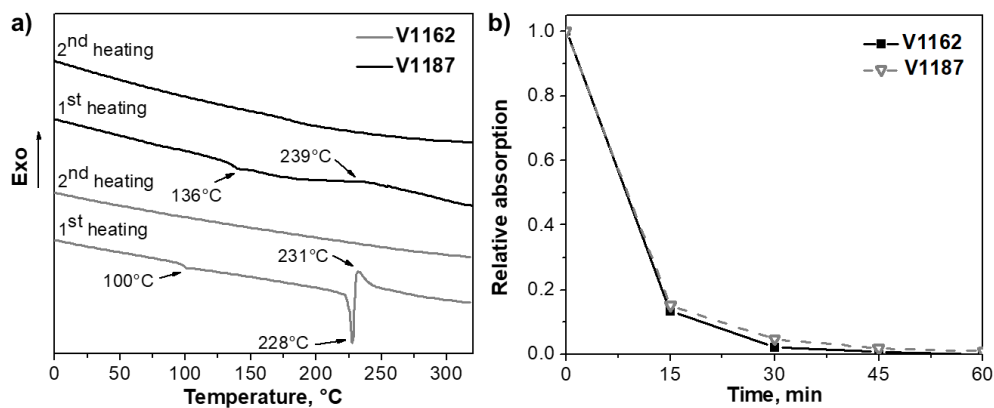
Figure 20. a) DSC curves for **V1162** and **V1187** (heating rate 10 °C/min), b) the cross-linking experiment of the films of **V1162** and **V1187**; the absorption of the solutions, prepared by dipping spin-coated HTM films into THF after heating at the required temperatures for the respective times, relative to the absorption of the solution, prepared by dipping of the non-cross-linked film

UV-vis spectra demonstrated that the absorption maximum of compound **V1162** is at 370 nm, whereas **V1187** shows a bathochromic shift of 36 nm, which can be attributed to a larger π-conjugated system, resulting from the addition of a second enamine branch. The results are summarized in Table 11.

The UV-vis spectroscopy was used for the evaluation of the cross-linking process of novel semiconductors. First, thin films of synthesized HTMs were formed by spin-coating, then the films were heated at 231 and 239 °C for **V1162** and **V1187**, respectively, for 1 hour. Afterwards, the layers were rinsed with THF, and the amount of washed material was analyzed by the absorption spectra. The results indicate that after 15 minutes of heating, the majority of both monomers were cross-linked into solvent-resistant 3D networks, while after 45 minutes, the thermal polymerization process was completed (Figure 20 b). In addition, Fourier-transform infrared

spectroscopy (FTIR) was previously reported to prove the completion of the cross-linking process[173,174]. The results show that the peaks of the vinyl groups at the 988–991 and 904–908 cm^{-1} disappear after heating.

Table 11. Thermal, optical, and photophysical properties of cross-linkable HTMs

ID	T_m (°C)[a]	T_p (°C)[a]	T_g (°C)[a]	T_{dec} (°C)[a]	λ_{abs} (nm)[b]	I_P (eV)[c]	μ (cm^2/Vs)[d]
V1162	228	231	100	396	370	5.26	8.6×10^{-4} (before cross-linking) 4.0×10^{-4} (after cross-linking)
V1187	–	239	136	393	406	5.11	5.0×10^{-3} (before and after cross-linking)

[a]Melting, polymerization, and glass transition temperatures observed from the DSC; decomposition temperature of cross-linked polymers observed from TGA, respectively (10 °C/min, N$_2$ atmosphere); [b]absorption spectra were measured in THF solutions (10^{-4} M); [c]ionization potentials of the films measured using PESA; [d]hole drift mobility value at strong electric fields.

I_P measurements revealed that the values recorded for both cross-linkable enamines are suitable for the use of these semiconductors in PSCs (5.11 and 5.26 eV for **V1187** and **V1162**, respectively).

Excellent charge transport properties at strong electric fields were demonstrated by enamine **V1187**, reaching 10^{-3} cm^2/Vs. More importantly, the hole drift mobility value of **V1187** did not change after the cross-linking process. In comparison, compound **V1162** with a smaller structure showed lightly worse mobility values before the polymerization, whereas mobility after heating became significantly lower. The results of charge transport properties in films are collected in Table 11 and presented in Figure 21 a.
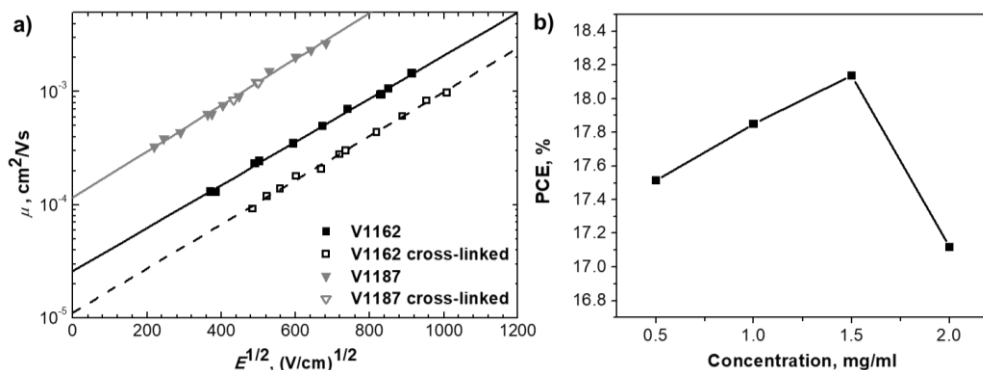
Figure 21. a) Electric-field dependencies of the hole drift mobilities in films of **V1162** and **V1187** before and after thermal polymerization, b) dependence of PCE on the concentration of the **V1187** solution

Table 12. Solar cell performance parameters extracted from the *J-V* curves

ID	V_{OC} (V)	J_{SC} (mA/cm^2)	*FF*	PCE (%)
V1162	0.878	21.60	0.76	14.49
V1162 cross-linked	1.077	21.51	0.64	14.71
V1187	0.932	20.73	0.80	15.51
V1187 cross-linked	1.069	21.40	0.73	16.77

The newly synthesized enamines were incorporated into p-i-n PSCs as HTLs (device architecture: ITO/HTM/perovskite/C60/bathocuproine (BCP)/Ag). The performance parameters of devices are summarized in Table 12. The data illustrate that PSCs containing neat films of **V1187** showed higher efficiency values (15.51 %) compared to **V1162** (14.49 %), which can be attributed to the higher hole drift mobilities. The same tendency is observed for the devices containing cross-linked films; furthermore, after the thermal polymerization, the efficiency of all PSCs increased, demonstrating promising results of 16.77 % for **V1187**-based devices. In addition, even higher PCE values for **V1187**-based PSCs were achieved by optimizing the concentration of HTM in a solution, which varied between 0.5 and 2 mg/mL. Detailed results can be found in Figure 21 b. Finally, the best performance was recorded to be 18.14 % for the devices with cross-linked films of **V1187** produced from 1.5 mg/mL solutions.

3. CONCLUSIONS

To conclude, this work presents a straightforward and cost-effective route of enamine synthesis by condensation reaction, which allows the elimination of palladium catalysts associated with excessive purification procedures, and the avoidance of inert atmosphere conditions, as a result, ensuring that such an approach is more appealing for the industrial applications in perovskite solar cells. In particular:

1. A new series of small organic enamine-based hole transporting materials containing aniline core were synthesized and investigated. It has been determined that:

    1.1. Synthesized aniline derivatives are thermally stable; the decomposition temperature of all compounds exceeds 310 ºC, which is sufficient for regular device operation conditions;

    1.2. The addition of a third diphenylethenyl fragment into the *p*-position of the phenyl ring expands π-conjugated system of a molecule and ensures a fully amorphous state of the compound;

    1.3. The developed *p*-type organic semiconductors show suitable values of ionization potential (5.16–5.30 eV) and excellent charge transport properties, reaching 10^{-2} cm^2/Vs at strong electric fields;

    1.4. The incorporation of aniline-based trisubstituted enamine **V1091** as hole transport layer in the fabricated perovskite solar cells allowed to reach an excellent champion power conversion efficiency exceeding 20 %, proving the potential of a novel class of compounds, while devices with spiro-OMeTAD showed identical efficiency results.

2. New hole transporting materials based on spirobifluorene core were synthesized, and their investigation revealed that:

    2.1. The addition of enamine fragments increases the glass transition temperature of the final compounds, determining their tendency to amorphousness and greater morphological stability;

    2.2. The best charge transporting properties (9.4×10^{-4} cm^2/Vs) were demonstrated by the compound **V1308** with the highest number of substituents;

    2.3. Three out of four semiconductors (**V1305**, **V1307**, **V1308**) in the series ensured a high performance of devices exceeding 19 %, which is on par with spiro-OMeTAD-based cells.

3. Novel hole transporting materials containing different central heteroatoms and a varying number of enamine branches were synthesized; the investigation of their properties has shown that:

    3.1. Thermal decomposition temperatures corresponding to 5 % weight loss of newly synthesized compounds exceeded 400 ºC, which indicate an excellent thermal stability of the series;

    3.2. The fully amorphous state of the materials was achieved only for the enamines containing triphenylamine and diphenyl sulfide central fragments;

3.3. An expanded π-conjugated system in the N-cored compound is responsible for a bathochromic shift of approximately 20 nm compared to the absorption maximum of the other molecules. In addition, this semiconductor demonstrated the best hole drift mobility value (2.0×10^{-5} cm^2/Vs) from the series;

3.4. The best maximum power conversion efficiency of more than 20 % was demonstrated by the devices with nitrogen-cored semiconductor, which helped to achieve one of the highest reported performances among enamine-based hole transporting materials.

4. A group of new fluorene-derived cross-linkable hole transporting materials were synthesized and investigated; moreover, a study of the influence of thermal polymerization was conducted. It has been found that:

4.1. The polymerization process of the compound with one enamine branch occurs at 231 ºC, while the compound containing two enamine branches has a slightly higher peak of polymerization temperature (239 ºC);

4.2. The enamine-based films form three-dimensional networks and become resistant to the organic solvents after approximately 45 minutes of heating;

4.3. Charge transporting properties of new enamines were not significantly affected by the in-situ cross-linking procedure; thus, cross-linkable layers are suitable for the application in p-i-n solar cells;

4.4. The concentration of solution of the hole transporting material appeared to have a notable influence on the performance of perovskite solar cells, and the cross-linking process positively affects the efficiency of the devices;

4.5. Optimized p-i-n structured perovskite solar cells containing a cross-linked hole transport layer of disubstituted enamine demonstrated promising efficiency results of over 18 %.

5. The synthesis cost of newly synthesized organic p-type photoconductors is 3 to 12 times lower compared to the well-known standard hole transporters (spiro-OMeTAD) that are typically used for efficient perovskite solar cells.

4. SUMMARY

4.1. Įvadas

XVIII a. viduryje prasidėjusi Pramonės revoliucija ne tik paskatino daugybę novatoriškų idėjų, išradimų, padėjo didinti pramoninės gamybos apimtis ir našumą, sukėlė gyventojų migraciją iš užmiesčio į miestus, bet taip pat pagerino darbuotojų darbo sąlygas ir leido užtikrinti geresnę sveikatos apsaugą. Tokie veiksniai sąlygojo didžiulį žmonių populiacijos augimą, ir ji šiandien yra beveik aštuonis kartus didesnė nei buvo prieš kelis šimtus metų. Industrializacija ir labai išaugęs gyventojų skaičius paskatino intensyvų iškastinio kuro naudojimą ir padidėjusį oro užterštumo lygį, o tai sukėlė energetikos ir aplinkosaugos krizes[1]. Dėl išaugusios svarbos šiandieniniame kontekste moksliniai tyrimai atsinaujinančių išteklių energetikos srityje yra plėtojami vis sparčiau. Tarp visų atsinaujinančių energijos šaltinių saulės energija yra viena iš paprasčiausiai išgaunamų ir plačiausiai paplitusių, per metus Žemę pasiekia apie 5×10^4 EJ energijos[2], o viso pasaulio suvartotas energijos kiekis 2021 m. buvo tik 595 EJ[3]. Tai įrodo, jog Saulė yra neišsenkantis energijos šaltinis, galintis visiškai patenkinti augantį žmonijos energijos poreikį, pasitelkiant reikiamas technologijas.

Siliciniai saulės elementai yra plačiausiai paplitę visoje fotovoltinių technologijų rinkoje dėl gerai žinomo gamybos proceso, plataus paties silicio paplitimo ir prietaisų ilgaamžiškumo. Tačiau tradicinių saulės elementų gamyba yra labai brangus ir daug energijos sąnaudų reikalaujantis procesas[4,5]. Be to, dėl savo kietumo, trapumo ir sunkumo šie prietaisai turi ribotas pritaikymo galimybes[6,7].

Žmonijai įsipareigojus kuo greičiau pasiekti nulinį šiltnamio efektą sukeliančių dujų emisijos lygį veiksmingesnių technologijų pritaikymas yra tiesiog neišvengiamas. Pastaruosius tris dešimtmečius plonasluoksnių, lanksčių fotovoltinių technologijų plėtra sukėlė nemažai susidomėjimo, kuris įrodo, jog naujausios kartos saulės elementai turi didžiulį potencialą pigiai ir paprastai gamybos technologijai, kartu sunaudojant nedidelį medžiagų kiekį[8,9].

Viena iš sparčiausiai tobulinamų ir daugiausiai žadančių technologijų yra organiniai-neorganiniai hibridiniai perovskitiniai saulės elementai (PSE), kurie 2009 m. literatūroje pirmą kartą buvo paminėti kaip šviesos energiją konvertuojantys prietaisai[10]. Ši technologija sulaukė tokio didelio susidomėjimo dėl nepaprastai greito prietaisų efektyvumo augimo, kiek ilgiau nei per dešimtmetį jų našumas pakilo nuo 3,8 % iki beveik 26 %[10,11]. Stulbinantis PSE efektyvumas, kuris šiandien lenkia komercinių iš silicio pagamintų saulės elementų efektyvumą, yra pagrįstas išskirtinėmis elektrinėmis ir optinėmis perovskito savybėmis[12,13].

Be absorbuojančio perovskito sluoksnio, kita ypatingai svarbi PSE sudedamoji dalis yra skyles transportuojantis sluoksnis, kuris atsakingas už skylių ištraukimą iš perovskito ir skyles transportuojančios medžiagos (STM) sandūros[14,15]. Šiam sluoksniui modifikuoti yra pasitelkiama organinė sintezė, kurios dėka STM gali įgyti atitinkamas savybes, nulemiančias efektyvių bei stabilių PSE gamybą ir sėkmingą jų įvedimą į rinką.

Darbo tikslas – ekonomiškų enaminų sintezė ir jų savybių ištyrimas bei pritaikymas skylių transportavimui perovskitiniuose saulės elementuose.

Disertacijos tikslui pasiekti buvo iškelti šie uždaviniai:

1. Mažamolekulių organinių junginių, turinčių anilino centrinį fragmentą bei difeniletenilgrupes ir tinkančių panaudojimui perovskitiniuose saulės elementuose, sintezė ir tyrimas.

2. Naujų skyles transportuojančių medžiagų, turinčių spirobifluoreno centrinį fragmentą ir difeniletenilgrupes, sintezė ir terminių, optinių bei fotofizikinių savybių tyrimas, taip pat perovskitinių saulės elementų fotovoltinių savybių vertinimas.

3. Naujų organinių puslaidininkių, besiskiriančių centriniu heteroatomu ir enamino fragmentų skaičiumi, sintezė, charakterizavimas ir pritaikymas skylių transportavimui perovskitiniuose saulės elementuose.

4. Fluoreno centrinį fragmentą turinčių ir tinklintis galinčių molekulių sintezė, charakterizavimas ir terminės polimerizacijos įtakos perovskitinių saulės elementų efektyvumui tyrimas.

5. Susintetintų skyles transportuojančių medžiagų sintezės kainos įvertinimas.

Darbo naujumas ir sąryšis tarp publikacijų:

Siekiant įvesti PSE į rinką, jie turi atitikti keletą reikalavimų: pasižymėti prieinama kaina, būti itin efektyvūs ir ilgai išlikti stabilūs. Nors visai neseniai buvo užfiksuotas naujas šių prietaisų efektyvumo pasaulinis rekordas (25,7 %)[16], tačiau tinkamų STM trūkumas vis dar neleidžia išnaudoti viso PSE potencialo. Geriausiai žinomas standartas, taikomas norint palyginti šias medžiagas, yra vadinamas spiro-OMeTAD. Nors ir buvo susintetintas daugiau nei prieš du dešimtmečius, šis organinis puslaidininkis net ir šiandien yra vienas dažniausiai naudojamų STM *n-i-p* tipo prietaisuose. Deja, vienas iš pagrindinių spiro-OMeTAD minusų yra sudėtinga šešių žingsnių sintezė, kuriai būtinos inertinės sąlygos ir agresyvių bei jautrių reagentų naudojimas, be to, šiam junginiui išgauti reikalingas ilgas ir komplikuotas gryninimo procesas. Tokie veiksniai labai padidina organinio puslaidininkio kainą, o tai apriboja jo pritaikymą pramonei. Todėl visose keturiose šios disertacijos autorės publikacijose aprašytos STM buvo susintetintos pasitelkus paprastą enaminų kondensacijos reakciją, kuriai nenaudojami brangūs katalizatoriai ir netaikomos sudėtingos gryninimo procedūros, ir tai nulėmė mažesnę organinių puslaidininkių savikainą.

Pirmojoje publikacijoje pristatoma serija junginių, susintetintų vienpakopės sintezės dėka, kaip pradinę medžiagą naudojant komercinį aniliną. Šiuos organinius junginius panaudojus PSE kaip skyles transportuojančius sluoksnius, prietaisai pademonstravo didesnį nei 20 % efektyvumą, o tuo metu, kai buvo publikuotas šis straipsnis, tai reiškė įspūdingus ir daug žadančius rezultatus. Be to, prietaisai, kuriuose panaudotas organinis puslaidininkis su padidinta konjuguota π dvigubųjų jungčių sistema, išlaikė net 96 % savo pradinio efektyvumo praėjus 800 valandų, o štai prietaisų su standartu spiro-OMeTAD efektyvumas praėjus tam pačiam laikui sumažėjo iki 42 %.

Antrojoje publikacijoje aprašoma spirobifluoreno-enaminų serija, kuri pasižymi patobulintu morfologiniu stabilumu ir išlaikytomis elektrinėmis savybėmis spirobifluoreno centrinio fragmento dėka. Puslaidininkinėms savybėms svarbią įtaką turi ir skirtingas enamino fragmentų skaičius, prijungtas prie spirobifluoreno centro. Didesnis pakaitų kiekis sąlygojo didesnę stiklėjimo temperatūrą, kuri ne tik padėjo gerinti morfologines medžiagų savybes, bet ir nulėmė stabilesnę amorfinę būseną. Dėl to PSE parodė didesnį nei 19 % efektyvumą, kurį galima prilyginti prietaisų su etalonu spiro-OMeTAD efektyvumui. Be to, STM, turinčios vieną ir du enamino fragmentus, leido pademonstruoti geriausius prietaisų stabilumo rezultatus lyginant su kitais šios serijos junginiais ar standartu spiro-OMeTAD.

Trečiojoje publikacijoje dėmesys taip pat skiriamas pigiai ir paprastai STM sintezei, joje pristatyta nauja enaminų serija su skirtingais centriniais heteroatomais (C, N, O bei S) ir atitinkamai kintančiu enamino fragmentų skaičiumi. Geriausias PSE efektyvumas buvo pasiektas panaudojus azoto heteroatomą turintį organinį puslaidininkį, kai prietaiso efektyvumas viršijo 20 %, o štai PSE su etalonu spiro-OMeTAD parodė identiškus efektyvumo rezultatus. Be to, STM su azoto ir anglies centriniais atomais užtikrino geresnį prietaisų terminį stabilumą lyginant su PSE, kuriuose buvo naudojama palyginamoji STM. Šie rezultatai patvirtina, kad taikant racionalią molekulių inžineriją net ir paprasta enaminų kondensacijos reakcija gali būti panaudota stabilių bei našių saulės elementų gamybai.

Paskutinėje publikacijoje dėmesys kreipiamas ne tik į nedidelę kainą ar gerą PSE efektyvumą, bet ir ypatingai koncentruojamasi į jų ilgaamžiškumą. Norint pagerinti organinių puslaidininkių elektrinį laidumą, tam yra naudojami legiruojantys priedai, tačiau dėl savo higroskopinės prigimties ir cheminio irimo jie neigiamai veikia prietaiso stabilumą, todėl šiai publikacijai buvo pagaminti *p-i-n* tipo prietaisai, kuriuose tokie priedai nenaudoti. Straipsnyje pristatomi fluoreno pagrindu susintetinti organiniai puslaidininkiai gali būti termiškai sutinklinami, šitaip suformuojamas tirpikliams atsparus STM sluoksnis, kuris padėjo PSE pasiekti didesnį nei 18 % efektyvumą, o tai įrodo pasiūlytos strategijos veiksmingumą tolimesniam STM tobulinimui.

4.2. Paskelbtų publikacijų apžvalga

4.2.1. Anilino pagrindu susintetintų enaminų panaudojimas skyles transportuojantiems sluoksniams efektyviuose ir stabiliuose perovskitiniuose saulės elementuose

Šis skyrius yra parašytas remiantis publikuotu straipsniu: *Advanced Materials,* **2018**, 30, 1803735, *D. Vaitukaitytė, Z. Wang, T. Malinauskas, A. Magomedov, G. Bubnienė, V. Jankauskas, V. Getautis, H. J. Snaith*[144]*; cituota 56 kartus.*

Kaip minėta ankstesniuose skyriuose, ekonomiškos ir stabilios STM yra būtinos norint užtikrinti tolimesnį progresą PSE gamybos ir jų komercializavimo srityje. Siekiant šio tikslo įgyvendinimo, labai svarbu vengti daugiapakopės sintezės, metalo katalizatorių ir sudėtingų gryninimo metodų, tokių kaip sublimacija, taikymo. Kadangi anilinas yra vienas paprasčiausių ir dažniausiai chemijos pramonėje naudojamų reagentų, jis buvo pasirinktas kaip pagrindas naujai STM serijai, aprašytai

pirmojoje publikacijoje. Stebėtinai maža anilino kaina sąlygoja šio junginio prieinamumą ir platų pritaikymą įvairioms cheminėms medžiagoms gaminti dideliais kiekiais[145]. Siekiant dar labiau sumažinti anilino pagrindu susintetintų puslaidininkių gamybos išlaidas, tam buvo pasirinkta vienpakopė kondensacijos reakcija, kuriai nereikalingi pereinamųjų metalų katalizatoriai, todėl tokių medžiagų gryninimas nėra sudėtingas, ir tam dažnai užtenka paprastos kristalizacijos procedūros.

Šiame straipsnyje buvo pristatyti keturi nauji organiniai puslaidininkiai, gauti kondensacijos reakcijos metu reaguojant anilino darinių amino grupei su 2,2-bis(4-metoksifenil)acetaldehido aldehido grupe, dalyvaujant katalizatoriui (+/−) kamparo sulfoninei rūgščiai (KSR). Naujų STM sintezė yra pateikta 1 schemoje. Pagal skirtingą reagentų santykį buvo susintetinti enaminai su dviem (**V1056**, **V1092**) arba trimis (**V1091**, **V1102**) difeniletenilgrupėmis. Anilino darinys, *p*-padėtyje turintis papildomą donorinę metoksigrupę, buvo panaudotas gauti **V1056**, atitinkamai, **V1102** sintezei buvo pasirinktas 3,5-dimetilanilinas, kuris gali turėti teigiamą įtaką fotovoltinių prietaisų veikimui[146].

Siekiant įvertinti naujos STM serijos ekonomiškumą, visų reagentų, reikalingų junginių sintezei, kainos buvo paskaičiuotos remiantis Osedach ir kt. pasiūlyta procedūra[147]. Paskaičiuota, kad junginio **V1091** kaina yra apie 16 $/g, o 1 g junginio **V1056** galima susintetinti už 8 $. Taigi šie enaminai yra žymiai pigesni nei gerai ištirtas standartas spiro-OMeTAD, kurio sintezės kaina 92 $/g[125].

Siekiant įvertinti terminį anilino pagrindu susintetintų puslaidininkių stabilumą buvo atlikta termogravimetrinė analizė (TGA), kurios rezultatai pateikti 1 paveiksle ir 1 lentelėje. Matavimai parodė, jog visiems keturiems junginiams yra būdingas puikus terminis stabilumas, didesnis nei 310 °C, kurio pakanka įprastomis prietaisų veikimo sąlygomis. Be to, termogravimetrinės kreivės demonstruoja gana staigius masės nuostolius, o tai reiškia, jog šie junginiai sublimuojasi, todėl skyles transportuojančių sluoksnių formavimui galima panaudoti ir vakuuminį nusodinimą, kuris išplečia šių junginių pritaikymo galimybes.
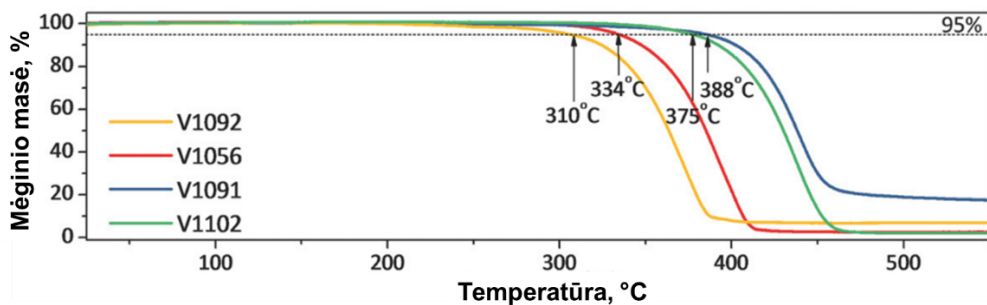
1 pav. Iš anilino ir jo darinių susintetintų organinių puslaidininkių termogravimetrinės kreivės (kaitinimo režimas 10 K/min)

a)

(4,5 ekv.)

KSR, toluenas, v. t., 6 val.

V1091 (69 %)

(2,1 ekv.)

KSR, toluenas, v. t., 2 val.

V1092 (72 %)

b)

(2,5 ekv.)

KSR, toluenas, v. t., 20 min

V1056 (46 %)

(6 ekv.)

KSR, toluenas, v. t., 2 val.

V1056: R_1 = H; R_2 = -OCH$_3$
V1102: R_1 = -CH$_3$; R_2 = H

V1102 (60 %)
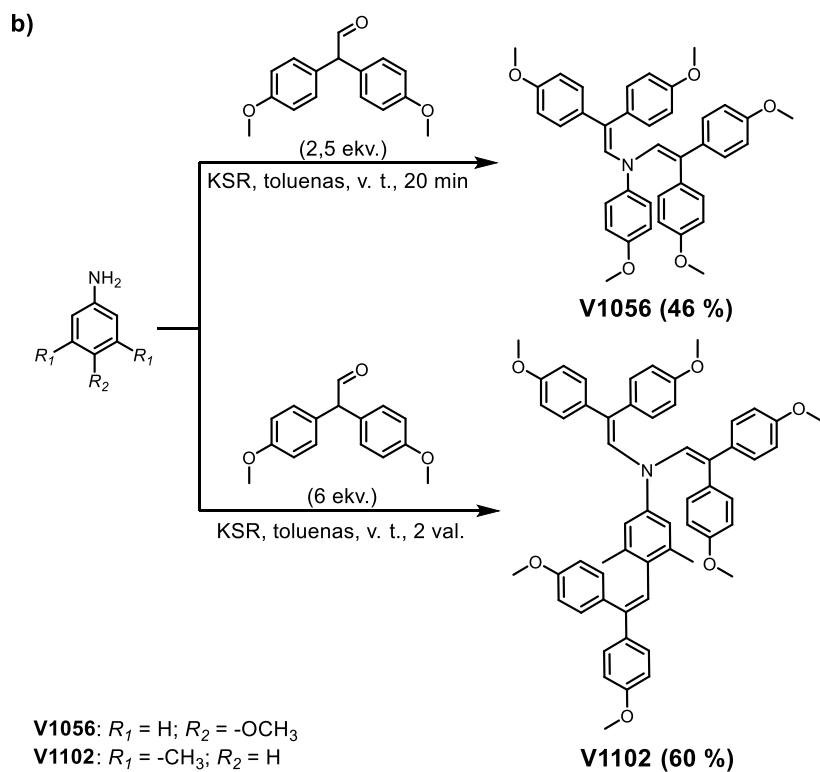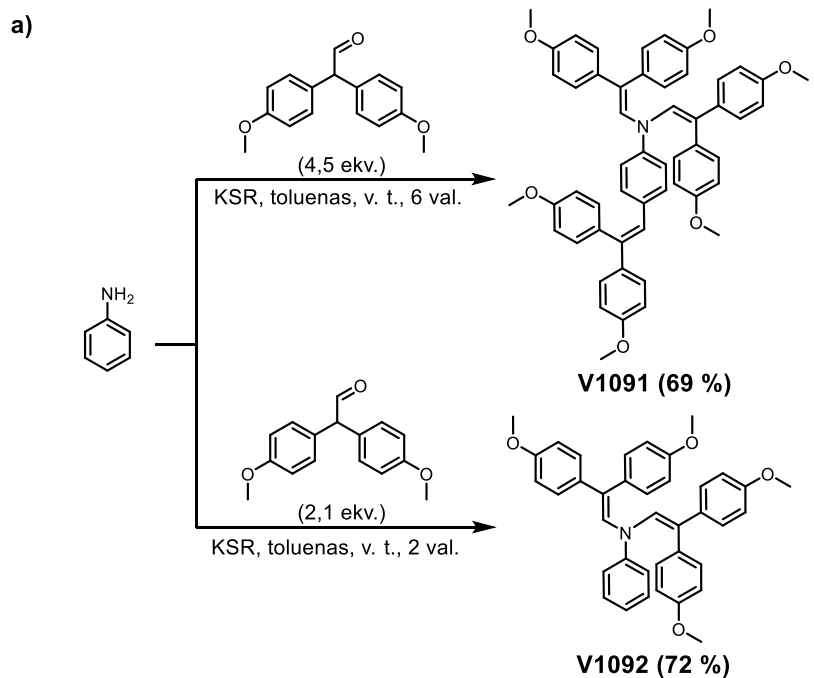
1 schema. Iš anilino ir jo darinių gautų STM sintezė: a) **V1091**, **V1092**; b) **V1056**, **V1102**

Naujai susintetintų STM morfologinės savybės buvo nustatytos naudojantis diferencine skenuojamąja kalorimetrija (DSK), išsamūs duomenys pateikti 1 lentelėje. DSK analizė parodė, jog didesnės molekulės **V1091** ir **V1102**, turinčios tris difeniletenilo fragmentus, yra labiau linkusios kristalizuotis lyginant su mažesniais junginiais **V1056** ir **V1092**, turinčiais tik du prieš tai minėtus fragmentus. Anilino darinys su pačia paprasčiausia struktūra **V1092** pademonstravo didelę lydymosi temperatūrą ($T_{lyd.}$) esant 251 °C, jo stiklėjimo temperatūra ($T_{st.}$) nustatyta ties 80 °C, o kristalizacijos procesas užfiksuotas esant 129 °C. Papildomos metoksigrupės įvedimas fenilo žiedo *p*-padėtyje (**V1056**) sukelia tam tikrą netvarką molekulės struktūroje, kuri lemia žymiai sumažėjusią $T_{lyd.}$ (190 °C) ir egzoterminės kristalizacijos smailės išnykimą. Trečio difeniletenilfragmento buvimas šioje padėtyje (**V1091**) dar labiau apsunkina kristalizacijos procesą, ir molekulė tampa visiškai amorfiška. **V1102** taip pat pasižymi visiška amorfine būsena, tačiau šio junginio $T_{st.}$ yra kiek žemesnė, o tai gali būti paaiškinta erdviniais trukdžiais, atsiradusiais dėl dviejų papildomų metilgrupių buvimo.

1 lentelė. Iš anilino bei jo darinių susintetintų STM ir standarto spiro-OMeTAD terminės, optinės ir fotofizikinės savybės

Junginys	$T_{lyd.}$ (°C)[a]	$T_{krist.}$ (°C)[a]	$T_{st.}$ (°C)[a]	$T_{5\% mas. nuost.}$ (°C)[b]	λ_{abs} (nm)	I_p (eV)	μ_0 (cm^2/Vs)[c]	μ (cm^2/Vs)[d]
V1056	190	–	78	334	333 384	5,19	$1,3\times10^{-5}$	$7,8\times10^{-4}$
V1091	–	–	109	388	381	5,17	$2,8\times10^{-5}$	$1,7\times10^{-2}$
V1092	251	129	80	310	331 370	5,30	–	–
V1102	–	–	96	375	367	5,16	$1,6\times10^{-6}$	$1,5\times10^{-4}$
Spiro-OMeTAD	245	–	126	449	387	5,00	$4,1\times10^{-5}$	$5,0\times10^{-4}$

[a]Nustatyta iš DSK matavimų: kaitinimo režimas 10 K/min, N_2 terpė; [b]nustatyta iš TGA: kaitinimo režimas 10 K/min, N_2 aplinka; [c]krūvininkų dreifinis judris esant nuliniam elektrinio lauko stipriui; [d]krūvininkų dreifinis judris, esant $6,4\times10^5$ V/cm stiprio elektriniam laukui.

Naujų junginių optinių savybių nustatymui buvo panaudoti ultravioletinės-regimosios šviesos (UV–RŠ) spinduliuotės sugerties spektrai (2a pav., 1 lent.). Junginių **V1056** ir **V1092**, turinčių du difeniletenilfragmentus, UV–RŠ absorbcijos spektruose matyti, kad papildomos metoksigrupės įvedimas neturi didelės įtakos konjuguotai π elektronų sistemai. O štai trečio difeniletenilfragmento atsiradimas žymiai praplečia konjuguotą sistemą, tai įrodo absorbcijos maksimumo, atitinkančio $\pi\rightarrow\pi^*$ elektronų perėjimus, batochrominis 50 nm poslinkis. Tačiau

dviejų metilgrupių buvimas 3-iojoje ir 5-ojoje fenilo žiedo padėtyse (**V1102**) sukelia 14 nm poslinkį į trumpesnių bangų pusę, kurį galima paaiškinti padidėjusiais erdviniais trukdžiais *p*-padėtyje, ir difeniletenilfragmentų pasisukimą plokštumos atžvilgiu.
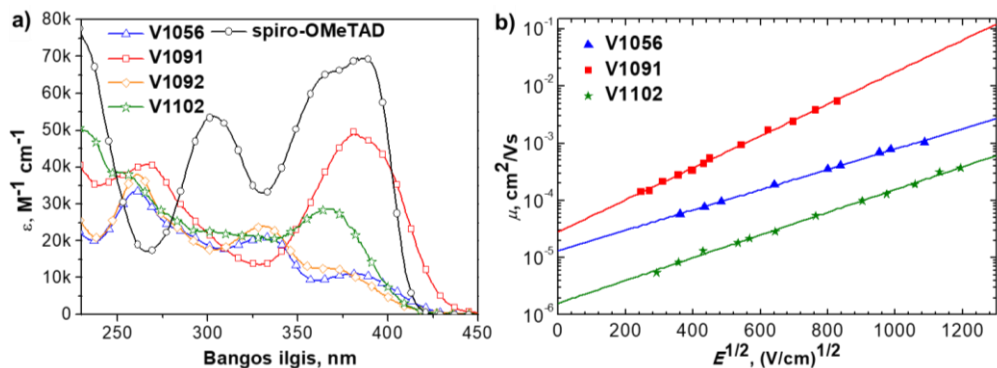
2 pav. a) Iš anilino bei jo darinių susintetintų STM ir spiro-OMeTAD UV–RŠ spinduliuotės sugerties spektrai (THF, $c = 10^{-4}$ M); b) junginių **V1056**, **V1091** ir **V1102** dreifinių judrių priklausomybė nuo elektrinio lauko stiprio

Siekiant nustatyti puslaidininkių energijos lygmenis buvo panaudotas jonizacijos potencialo (I_p) matavimas elektronų fotoemisijos ore metodu, rezultatai pateikti 1 lentelėje. Didžiausią I_p vertę parodė junginys **V1092**. Papildomų elektronų donorų, tokių kaip difeniletenil- (**V1091**) arba metoksigrupių (**V1056**), atsiradimas molekulėje sumažino jonizacijos potencialą maždaug 0,1 eV, o štai dviejų metilgrupių (**V1102**) įvedimas neturėjo jokios įtakos lyginant su puslaidininkio **V1092** I_p. Nors iš anilino bei jo darinių susintetintų STM I_p vertės kiek didesnės nei spiro-OMeTAD, šie junginiai yra tinkami naudoti PSE, kadangi jų HOMO lygmuo yra suderintas su perovskito sluoksnio valentine juosta[148].

Susintetintų enaminų krūvio pernašos greitis buvo išmatuotas kserografiniu laiko lėkio metodu (2b pav.), rezultatai pateikti 1 lentelėje. Junginio **V1056** skylių dreifinio judrio vertė stipriuose elektriniuose laukuose yra tos pačios eilės kaip ir standarto spiro-OMeTAD ($5,0 \times 10^{-4}$ cm²/Vs)[149], o štai trečio difeniletenilfragmento įvedimas (**V1091**) lemia žymiai padidėjusį judrį ($1,7 \times 10^{-2}$ cm²/Vs). Tačiau junginio **V1102**, turinčio tuos pačius tris difeniletenilfragmentus bei dvi papildomas metilgrupes prie fenilo žiedo, krūvio pernašos greitis silpnuose laukuose yra žymiai mažesnis, greičiausiai dėl didesnių erdvinių trukdžių atsiradimo.

Norint įvertinti anilino darinių kaip skyles transportuojančių sluoksnių panaudojimo efektyvumą buvo sukonstruoti *n-i-p* architektūros PSE (sandara: FTO (fluoru legiruotas alavo oksidas)/SnO₂/perovskitas/STM/Au). Duomenys, surinkti iš fotosrovės–įtampos (*J–V*) kreivių grafiko, susisteminti ir pateikti 2 lentelėje. Remiantis PSE fotovoltinėmis charakteristikomis galima teigti, jog prietaisų su nauja STM serija efektyvumas varijuoja nuo 17,6 % (**V1102**) iki 20,2 % (**V1091**), ir tai parodo, jog šie enaminai gali padėti pasiekti tokį patį efektyvumą, kaip ir etalonas spiro-OMeTAD.

2 lentelė. Saulės elementų našumo parametrai, gauti iš *J–V* kreivių

Junginys	V_{OC} (V)	J_{SC} (mA/cm^2)	*FF*	PCE (%)
V1056	1,07	22,1	0,79	18,7
V1091	1,11	22,5	0,81	20,2
V1102	1,13	22,7	0,68	17,6
Spiro-OMeTAD	1,12	22,6	0,80	20,2

3 paveiksle yra pavaizduotas neužsandarintų prietaisų stabilumas juos laikant ore ilgiau nei 800 valandų, esant 45 % drėgmei. Rezultatai rodo, jog PSE su junginiu **V1091** išlaikė net 96 % savo pradinio efektyvumo, o štai kontrolinio prietaiso su spiro-OMeTAD našumas nukrito iki 42 %. Toks stabilumo pagerinimas gali būti paaiškinamas kokybiškesniu molekulių išsidėstymu sluoksnyje ir didesniu **V1091** hidrofobiškumu.
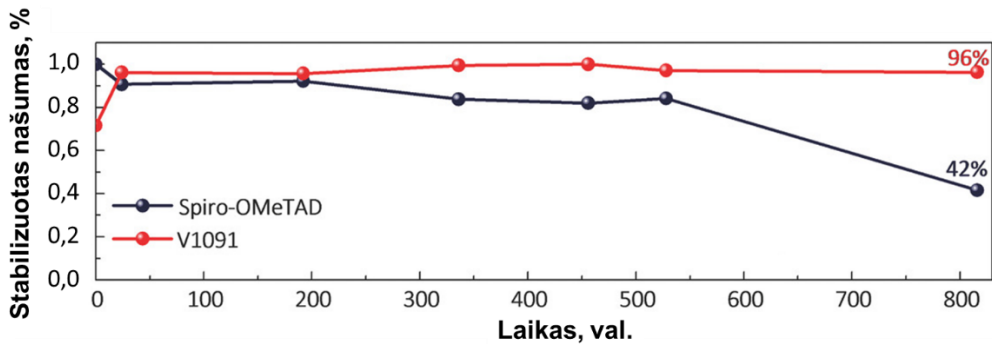
3 pav. PSE su **V1091** ir spiro-OMeTAD efektyvumo kitimas laike

4.2.2. Perovskitiniuose saulės elementuose skyles transportuojantys enaminai, turintys spirobifluoreno fragmentą

Šis skyrius yra parašytas remiantis publikuotu straipsniu: *Chemistry of Materials,* **2021**, 33, 15, 6059–6067, *D. Vaitukaitytė, C. Momblona, K. Rakštys, A. A. Sutanto, B. Ding, C. Igci, V. Jankauskas, A. Gruodis, T. Malinauskas, A. M. Asiri, P. J. Dyson, V. Getautis, and M. K. Nazeeruddin*[150]; *cituota 6 kartus.*

Kaip jau minėta anksčiau, spiro-OMeTAD yra viena labiausiai ištyrinėtų ir aprašytų STM, tačiau jos sintezės ir gryninimo procedūros yra per daug sudėtingos ir brangios norint pradėti gamybą pramoniniu mastu. O štai enaminų sintezės iš anilino bei jo darinių strategija, pristatyta ankstesniame poskyryje, įrodė esanti puiki alternatyva, pasižyminti supaprastinta sintezės schema ir paprastu produktų išskyrimu, žymiai sumažinančiu STM kainą. Todėl šioje publikacijoje pristatyta

abiejų minėtų strategijų, spirobifluoreno centrinio fragmento ir kondensacijos reakcijos, kombinacija.

Šiame straipsnyje buvo susintetintos keturios naujos STM su spirobifluoreno centru, turinčiu nuo vieno iki keturių enamino fragmentų, išsidėsčiusių taip, jog atkartotų etalono spiro-OMeTAD struktūrą. 2 schemoje pateiktos šių junginių struktūrinės formulės ir pavaizduotas sintezės kelias, naudotas šių puslaidininkių gavimui. Laboratorinės sintezės kainos skaičiavimai parodė, jog susintetinti puslaidininkiai, turintys tiek spirobifluoreno, tiek difeniletenil- fragmentų, yra žymiai pigesni: pavyzdžiui, 1 g junginio **V1307** kainuoja apie 37 $, o štai standarto spiro-OMeTAD kaina yra 92 $/g.

V1305 (49 %)

V1306 (58 %)

V1307 (33 %)

V1308 (42 %)

V1305: R_1 = H; R_2 = NH$_2$; R_3 = H; R_4 = H
V1306: R_1 = H; R_2 = NH$_2$; R_3 = NH$_2$; R_4 = H
V1307: R_1 = NH$_2$; R_2 = NH$_2$; R_3 = NH$_2$; R_4 = NH$_2$
V1308: R_1 = NH$_2$; R_2 = NH$_2$; R_3 = H; R_4 = H

KSR, THF/toluenas, v. t.
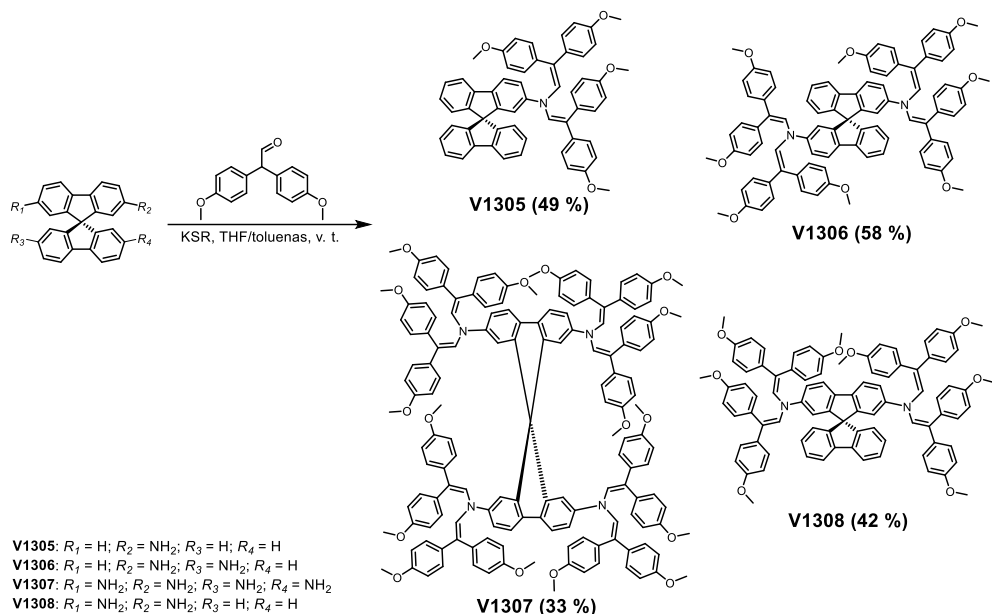
2 schema. Iš spirobifluoreno darinių susintetintų STM sintezė: **V1305**, **V1306**, **V1307**, **V1308**

Naujų, kondensacijos reakcijos metu susintetintų, STM TGA ir DSK matavimų rezultatai yra pateikti 3 lentelėje. 5 % masės nuostolių temperatūra šios serijos junginiams yra apie 400 °C, o tai rodo, jog jiems būdingas labai geras terminis stabilumas. DSK analizė rodo, kad trims iš keturių medžiagų (**V1305**, **V1306**, **V1308**) yra būdingos tiek kristalinė, tiek amorfinė būsenos, panašiai kaip ir spiro-OMeTAD[149]. Tačiau junginys **V1307**, turintis didžiausią struktūrą ir molekulinę masę, pasižymi vien tik amorfine būsena, be to, jam būdinga ir aukščiausia $T_{st.}$ iš visos junginių serijos (169 °C). Visi naujai susintetinti enaminai turi didesnę stiklėjimo temperatūrą lyginant su etalonu spiro-OMeTAD (124 °C), o tai įrodo geresnį sluoksnių morfologinį stabilumą.

3 lentelė. Iš spirobifluoreno darinių susintetintų STM terminės, optinės ir fotofizikinės savybės

Junginys	$T_{lyd.}$ (°C)[a]	$T_{krist.}$ (°C)[a]	$T_{st.}$ (°C)[a]	$T_{5\%}$ mas. nuost. (°C)[a]	λ_{abs} (nm)[b]	I_P (eV)[c]	E_g (eV)[d]	E_{ea} (eV)[e]	μ_0 (cm²/Vs)[f]
V1305	243	–	131	380	267; 372	5,33	2,90	2,43	$1,7 \times 10^{-5}$
V1306	294	226	154	402	267; 373	5,37	2,84	2,53	$5,4 \times 10^{-6}$
V1307	–	–	169	401	263; 389; 408	5,46	2,83	2,63	$6,4 \times 10^{-4}$
V1308	305	203	158	371	263; 388; 408	5,46	2,78	2,68	$9,4 \times 10^{-4}$

[a]Nustatyta iš DSK ir TGA matavimų (10 °C/min, N_2 terpė); [b]absorbcijos spektrai, užrašyti iš tirpalų THF (10^{-4} M); [c]jonizacijos potencialai, išmatuoti plėvelėse, taikant elektronų fotoemisijos ore metodą; [d]E_g, apskaičiuota iš absorbcijos ir emisijos spektrų susikirtimo vietos; [e]$E_{ea} = I_P - E_g$; [f]skylių dreifinio judrio vertės esant nuliniam elektrinio lauko stipriui.

4 paveiksle pavaizduoti susintetintų STM UV–RŠ absorbcijos spektrai. Visų keturių spirobifluoreno-enaminų sugerties spektruose pastebimas prie 260 nm esantis absorbcijos maksimumas, atsiradęs dėl π–π* valentinių elektronų šuolių molekulėse, o štai kitas sugerties maksimumas, būdingas n−π* elektronų šuoliams, užfiksuotas srityje nuo 370 nm iki 410 nm. Absorbcijos spektrų skirtumai gali būti paaiškinti skirtingu difeniletenilfragmentų skaičiumi ir padėtimi molekulėje. Didėjant enaminų fragmentų skaičiui stebimas λ_{abs} hiperchrominis poslinkis, o štai pakaitų buvimas abiejose fluoreno pusėse nulemia 35 nm aborbcijos maksimumo poslinkį raudonųjų bangų link. Draustinių energijų juostų (E_g) vertės buvo paskaičiuotos iš sugerties ir emisijos spektrų susikirtimo vietos, jos varijuoja nuo 2,78 eV iki 2,90 eV.
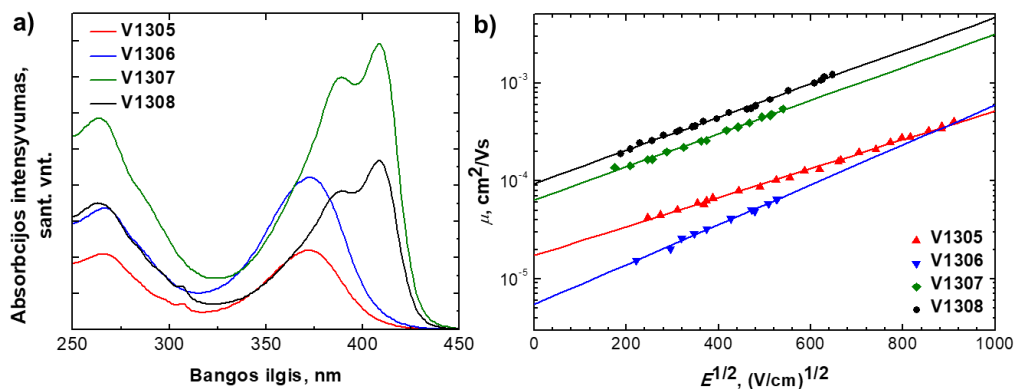
4 pav. a) Iš spirobifluoreno darinių susintetintų STM UV–RŠ absorbcijos spektrai (THF, 10^{-4} M); b) spirobifluoreno-enaminų dreifinio judrio priklausomybė nuo elektrinio lauko stiprio

Spirobifluoreno-enaminų jonizacijos potencialo matavimai parodė, kad HOMO energijos lygmens vertės yra pakankamai stabilizuotos tarp 5,33 eV ir 5,46 eV, lyginant su spiro-OMeTAD (5,00 eV)[151]. Remiantis šiais duomenimis buvo apskaičiuotos ir elektroninio giminingumo (E_{ea}) vertės, kurios yra intervale nuo 2,43 eV iki 2,68 eV. Svarbu paminėti, kad šios vertės taip pat nurodo ir LUMO energijos lygmenį, kuris turi būti mažesnis nei perovskito sluoksnio laidumo juosta (−4,10 eV), siekiant išvengti nepageidaujamos elektronų pernašos iš perovskito į elektrodą. Duomenys iš I_P matavimų ir E_{ea} skaičiavimų yra pateikti 3 lentelėje.

4b paveiksle pavaizduota skylių dreifinio judrio priklausomybė nuo elektrinio lauko stiprio, apibendrinti duomenys pateikti 3 lentelėje. Greičiausią krūvio pernašą esant nuliniam elektriniam laukui pademonstravo junginiai **V1308** ($9,4 \times 10^{-4}$ cm^2/Vs) ir **V1307** ($6,4 \times 10^{-4}$ cm^2/Vs), kurių dreifinio judrio vertės yra didesnės nei etalono spiro-OMeTAD ($\mu_0 = 1,3 \times 10^{-4}$ cm^2/Vs)[152]. Šie rezultatai rodo, jog krūvio pernašos savybes stipriai veikia molekulės struktūra, ypač didesnė konjugacija (**V1307**) esant didesniam enamino fragmentų skaičiui[153–155].

4 lentelė. Saulės elementų našumo parametrai, gauti iš *J–V* kreivių

Junginys	V_{OC} (V)	J_{SC} (mA/cm^2)	*FF*	PCE (%)
V1305	1,08	23,17	0,76	19,0
V1306	1,00	22,22	0,71	15,8
V1307	1,07	23,21	0,77	19,2
V1308	1,07	23,44	0,76	19,1
Spiro-OMeTAD	1,12	22,90	0,77	19,7

Norint nustatyti skyles transportuojančioje medžiagoje esančių enamino fragmentų skaičiaus ir padėties įtaką PSE efektyvumui buvo sukonstruoti *n-i-p* tipo prietaisai (sandara: FTO/c-TiO$_2$ (kompaktinis titano dioksidas)/m-TiO$_2$ (mezoporinis titano dioksidas)/SnO$_2$/perovskitas/STM/Au). Duomenys, surinkti iš *J–V* kreivių, susisteminti ir pateikti 4 lentelėje. PSE su trimis iš keturių STM iš naujos serijos parodė panašias prietaisų efektyvumo vertes, siekiančias 19 % (**V1305**, **V1307**, **V1308**, atitinkamai, 19,0 %, 19,2 %, 19,1 %). Kiek mažesnį našumą (15,8 %) pademonstravo PSE su junginiu **V1306**, to priežastis gali būti mažiausia šios STM dreifinio judrio vertė. Be to, prie mažesnio efektyvumo galėjo prisidėti ir mažesnis užpildymo faktorius (angl. *FF-fill factor*), kuris parodo prastą skyles transportuojančių sluoksnių kokybę. Prietaisų stabilumo matavimai pademonstravo, jog PSE su naujos serijos enaminais yra tokie pat stabilūs, kaip ir prietaisai su standartu spiro-OMeTAD.

4.2.3. Centrinio heteroatomo įtaka perovskitiniams saulės elementams skirtų skyles transportuojančių medžiagų savybėms

Šis skyrius yra parašytas remiantis publikuotu straipsniu: *Solar RRL*, **2022**, 6, 11, 2200590, *D. Vaitukaitytė, M. A. Truong, K. Rakštys, R. Murdey, T. Funasaki, T. Yamada, Y. Kanemitsu, V. Jankauskas, V. Getautis, A. Wakamiya*[156]*; cituota 1 kartą.*

Remiantis mokslinė literatūra, centrinio branduolio pakeitimas molekulėje stipriai paveikia ir keičia STM savybes[157–159]. Be to, skirtingų heteroatomų atsiradimas struktūroje turi įtaką ne tik elektrocheminėms ir fotofizikinėms medžiagų savybėms, bet ir prietaisų našumo parametrams. Deguonies (O)[160,161], azoto (N)[162,163] ir sieros (S)[164–166] heteroatomų įvedimas į skyles transportuojančią molekulę padeda pasyvuoti švino jonus, kartu mažinant rekombinacinius nuostolius perovskito/STM sandūroje. Tinkamo heteroatomo parinkimas taip pat lemia efektyvesnį junginių energetinių lygmenų suderinimą, kuris turi teigiamą poveikį pačių PSE našumui[118,170].

Šioje publikacijoje naujai organinių puslaidininkių serijai su įvairiais centriniais fragmentais (difenileteriu (**V1433**), difenilsulfidu (**V1434**), trifenilaminu (**V1435**) ar tetrafenilmetanu (**V1431**)) ir skirtingu enamino šakų skaičiumi gauti buvo panaudota ta pati vieno žingsnio sintezės procedūra, aprašyta anksčiau (3 schema).
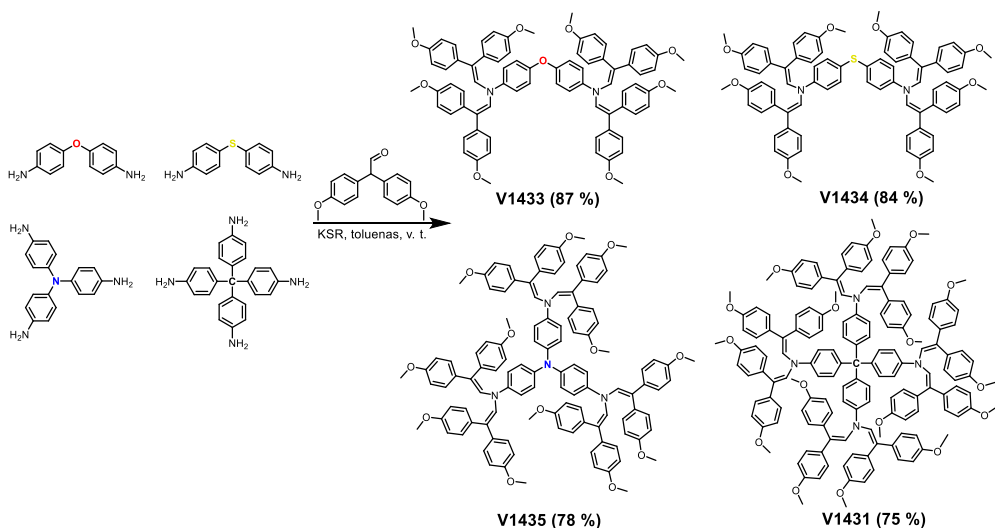
3 schema. Puslaidininkių **V1433**, **V1434**, **V1435** ir **V1431** su įvairiais centriniais heteroatomais ir skirtingu enamino fragmentų skaičiumi sintezė

TGA rezultatai atskleidė, jog visi naujai susintetinti puslaidininkiai pasižymi puikiu terminiu stabilumu, siekiančiu 413 (**V1431**, **V1434**), 415 (**V1435)** ir 409 °C (**V1433**). DSK analizė parodė, jog junginys su centriniu anglies atomu **V1431** turi tik endoterminę smailę esant 339 °C, kuri reiškia lydymosi procesą, o štai junginio **V1433**, turinčio deguonies centrą, termogramose užfiksuota tiek $T_{st.}$ esant 130 °C, tiek kristalizacija esant 270 °C, tiek lydymosi procesas esant 295 °C; tai rodo dviejų, kristalinės ir amorfinės, būsenų egzistavimą. Likusios molekulės su N- ir S-centrais

pademonstravo sumažėjusį polinkį kristalizacijai, kadangi jų termogramose užfiksuotos tik stiklėjimo temperatūros, esant 130 °C junginiui **V1435** ir esant 125 °C junginiui **V1434**, įrodančios amorfinės būsenos dominavimą. Išsamesnė terminių savybių informacija pateikta 5 lentelėje.

5 lentelė. STM su įvairiais centriniais heteroatomais terminės, optinės ir fotofizikinės savybės

Junginys	$T_{lyd.}$ (°C)[a]	$T_{krist.}$ (°C)[a]	$T_{st.}$ (°C)[a]	$T_{5\ \%\ mas.\ nuost.}$ (°C)[a]	λ_{abs} (nm)[b]	I_P (eV)[c]	E_g (eV)[d]	E_{ea} (eV)[e]	μ_0 (cm^2/Vs)[f]
V1433	295	270	130	409	261; 344	5,37	2,97	2,40	$3,0 \times 10^{-6}$
V1434	–	–	125	413	264; 357	5,52	2,99	2,53	$3,5 \times 10^{-6}$
V1435	–	–	130	415	260; 373	5,27	2,88	2,39	$2,0 \times 10^{-5}$
V1431	339	–	–	413	263; 347	5,54	3,02	2,52	$5,0 \times 10^{-6}$

[a]Lydymosi, kristalizacijos ir stiklėjimo temperatūros, užfiksuotos iš DSK matavimų; 5 % masės nuostolių temperatūra, užfiksuota TGA metu (10 °C/min, N_2 terpė); [b]absorbcijos spektrai, matuoti iš tirpalų THF (10^{-4} M); [c]jonizacijos potencialai, išmatuoti plėvelėse, taikant elektronų fotoemisijos ore metodą; [d]E_g, apskaičiuota iš absorbcijos ir emisijos spektrų susikirtimo vietos; [e]$E_{ea} = I_P − E_g$; [f]skylių dreifinio judrio vertės esant nuliniam elektrinio lauko stipriui.

Enaminų sugerties spektrai (5a pav.) rodo, jog absorbcijos maksimumai yra užfiksuoti prie 344 nm (**V1433**), 347 nm (**V1431**), 357 nm (**V1434**) ir 373 nm (**V1435**). Iš šių duomenų galima pastebėti, kad junginiui, centre turinčiam azoto atomą, yra būdingas 20 nm poslinkis raudonųjų bangų link, kuris gali būti paaiškintas padidėjusia konjuguota π dvigubųjų jungčių sistema. Pasinaudojus junginių sugerties ir emisijos spektrų susikirtimo vietomis buvo apskaičiuotos draustinių energijų juostų vertės, kurios visiems puslaidininkiams buvo panašios, apie 3,0 eV (5 lent.).

Jonizacijos potencialo matavimai medžiagoms esant kietosios būsenos atskleidė, jog HOMO energijos lygmuo gilėja centrinio atomo elektronų tankiui mažėjant, I_P vertės yra pateiktos 5 lentelėje. Naujų junginių LUMO energijos lygmuo buvo apskaičiuotas iš I_P ir E_g verčių (–2,39 eV, –2,40 eV, –2,53 eV, –2,52 eV junginiams **V1435**, **V1433**, **V1434**, **V1431**, atitinkamai); tai parodė, jog šios medžiagos yra tinkamos panaudojimui PSE[168].
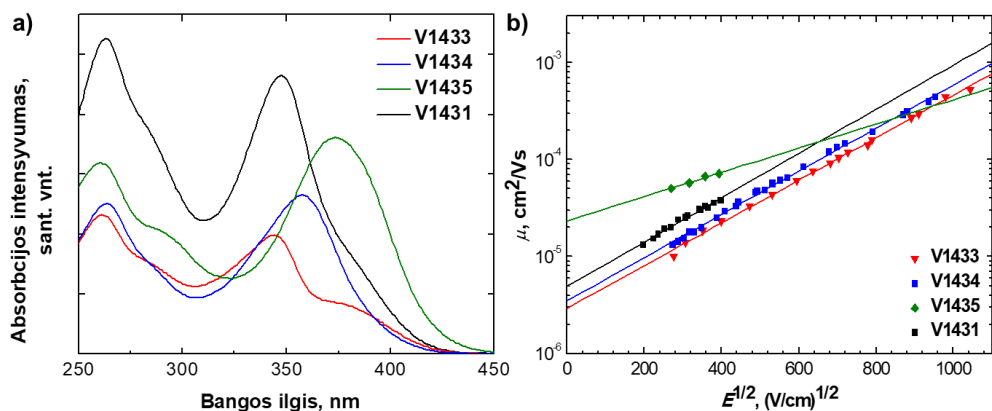
5 pav. a) Junginių **V1433**, **V1434**, **V1435** ir **V1431** absorbcijos spektrai (THF, 10^{-4} M); b) enaminų su skirtingu centriniu heteroatomu dreifinio judrio priklausomybė nuo elektrinio lauko stiprio

Pasitelkus kserografinį laiko lėkio metodą buvo nustatytos puslaidininkių krūvio pernašos savybės (5b pav., 5 lent.), iš kurių galima teigti, kad geriausiu krūvininkų dreifiniu judriu, esant nuliniam elektrinio lauko stipriui, pasižymi junginys **V1435** su N-centru, pademonstravęs viena eile aukštesnius rezultatus nei kiti junginiai iš šios serijos.

6 lentelė. Saulės elementų našumo parametrai, gauti iš *J–V* kreivių

Junginys	V_{OC} (V)	J_{SC} (mA/cm^2)	*FF*	*PCE* (%)
V1431	1,11	22,3	0,73	18,0
V1434	1,11	22,7	0,74	18,6
V1435	1,12	22,7	0,79	20,1
Spiro-OMeTAD	1,13	22,4	0,79	20,1

Nauja enaminų serija su skirtingais centriniais heteroatomais buvo išbandyta kaip skyles transportuojantys sluoksniai ir panaudota tradicinės *n-i-p* struktūros PSE gamybai (prietaiso sandara: ITO (indžio alavo oksidas)/SnO$_2$/perovskitas/STM/auksas). Deja, junginys **V1433**, turintis deguonies centrinį branduolį, nebuvo pakankamai tirpus nei 1,2-dichlorbenzene, nei chlorbenzene, todėl prietaisų su šiuo junginiu sukonstruoti nepavyko. Siekiant, kad naujai susintetintų STM HOMO energijos lygmuo gerai derėtų su perovskito valentine juosta, šiuo atveju teko pasirinkti mišrios kompozicijos perovskito sluoksnį (Cs$_{0,05}$FA$_{0,87}$MA$_{0,08}$PbI$_{2,76}$Br$_{0,24}$), kuris pasižymi kiek gilesniu valentinės juostos lygmeniu (–5,68 eV)[169]. Našiausių prietaisų su enaminais ir etalonu spiro-OMeTAD fotovoltinės charakteristikos yra pateiktos 6 lentelėje. Didžiausią, net 20,1 %,

efektyvumą pademonstravo PSE su junginiu, pasižyminčiu didžiausiu krūvio pernašos greičiu iš visos serijos, **V1435** (palyginamieji prietaisai su standartine STM parodė tokius pačius rezultatus). Saulės elementai, sukonstruoti su kitais enaminais, taip pat pademonstravo daug žadančius rezultatus, pasiekdami 18,0 % ir 18,6 % efektyvumą su atitinkamai anglies ir sieros centrinius fragmentus turinčiomis STM.

4.2.4. Enamino fragmentus turinčios ir tinklintis galinčios skyles transportuojančios medžiagos perovskitiniams saulės elementams

Šis skyrius yra parašytas remiantis publikuotu straipsniu: *Solar RRL*, **2021**, 5, 1, 2000597, *D. Vaitukaitytė, A. Al-Ashouri, M. Daškevičienė, E. Kamarauskas, J. Nekrasovas, V. Jankauskas, A. Magomedov, S. Albrecht, V. Getautis*[170]*; cituota 7 kartus.*

Kaip jau minėta anksčiau, didelis prietaisų efektyvumas nėra vienintelis tikslas siekiant komercializuoti PSE; kita taip pat svarbi savybė yra ilgaamžiškumas. Vienas iš būdų užtikrinti prietaiso stabilumą yra priedų, naudojamų skyles transportuojančių medžiagų laidumui pagerinti, atsisakymas. Žinoma, kad ličio druskos yra higroskopiškos, o 4-*tret*-butilpiridinas yra linkęs formuoti kompleksus kartu su PbI$_2$, ir tai lemia greitesnį paties perovskito skilimą[171]. Norint prailginti *p-i-n* tipo PSE veikimo trukmę būtina paruošti tirpikliams atsparius skyles transportuojančius sluoksnius, kurie neišsiplautų perovskito sluoksnio formavimo metu, kai naudojami stiprūs poliniai tirpikliai. Vienas geriausių variantų šiems kriterijams įgyvendinti yra pasinaudoti unikalia vinilgrupes turinčių monomerų savybe suformuoti trimatį tinklą, paveikus temperatūra. Be to, ši strategija buvo suderinta su jau minėta ekonomiškai efektyvių STM sintezės strategija ir abi jos pritaikytos šioje publikacijoje.
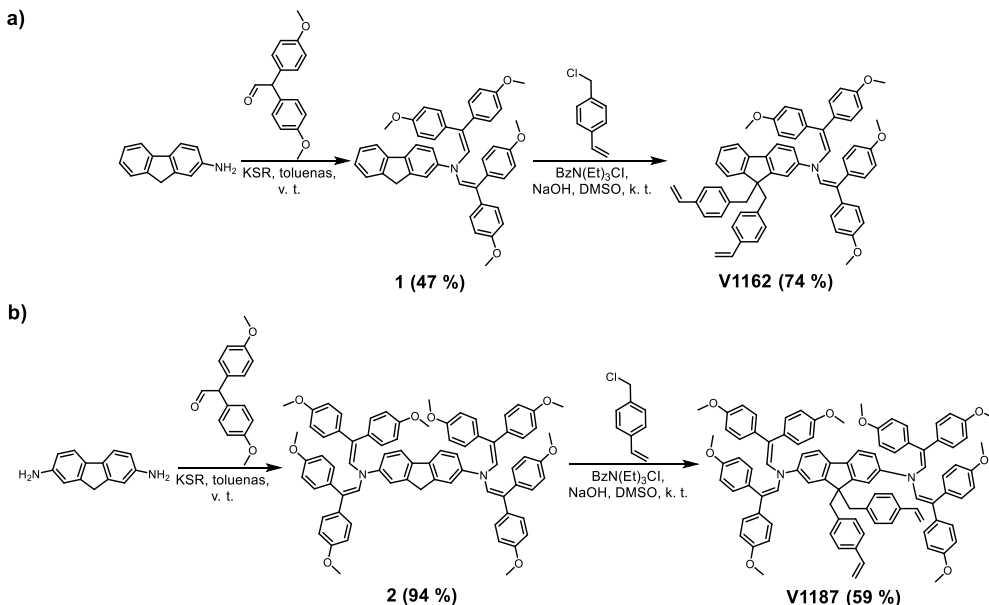
4 schema. Sutinklinamų STM sintezė: a) **V1162**; b) **V1187**

Pirmame STM sintezės žingsnyje buvo pritaikyta anksčiau minėta kondensacijos reakcija, kuriai komerciškai prieinami fluoreno aminai pasirinkti kaip pradinės medžiagos. Antroje sintezės stadijoje, siekiant įvesti terminei polimerizacijai reikalingas vinilgrupes, buvo pasitelkta alkilinimo reakcija su 4-vinilbenzilchloridu dimetilsulfokside, reakcijoje dalyvaujant benziltrietilamonio chloridui ir natrio hidroksidui. Šios sintezės metu buvo gauti du galutiniai junginiai su vienu (**V1162**) ir dviem (**V1187**) enamino fragmentais (4 schema). Nors šių puslaidininkių gavimui buvo reikalinga dviejų žingsnių sintezė, tačiau paskaičiuota jų savikaina (13,56 €/g ir 16,34 €/g, atitinkamai, **V1162** ir **V1187**) vis tiek yra žymiai mažesnė nei vienos efektyviausių polimerinių STM – PTAA, naudojamų invertuotos architektūros prietaisuose, sintezės kaina (500 $/g)[172].

Iš DSK matavimų nustatyta, kad sutinklinamiems puslaidininkiams būdingos skirtingos savybės (6 pav., 7 lent.). Pirmojo kaitinimo metu junginio **V1162** termogramoje esant 100 °C užfiksuotas stiklėjimo procesas, po kurio esant 228 °C užfiksuota endoterminė smailė, atitinkanti $T_{lyd.}$. Tai parodo, jog šiai medžiagai būdinga tiek kristalinė, tiek amorfinė būsenos. Be to, iš karto po lydymosi proceso, esant 231 °C pastebėtas egzoterminis procesas, nurodantis terminės polimerizacijos temperatūrą ($T_{pol.}$). Kadangi tiek aušinimo, tiek antrojo kaitinimo metu daugiau neužfiksuota jokių terminių virsmų, tai patvirtina sutinklinto trimačio polimero susiformavimą. O štai junginiui **V1187** būdinga kiek didesnė $T_{st.}$ (136 °C), bet lydymosi procesas termogramoje neužfiksuotas, tai parodo, jog ši medžiaga turi tik amorfinę būseną. Terminė polimerizacija prasideda esant 190 °C ir pasiekia maksimumą esant 239 °C.
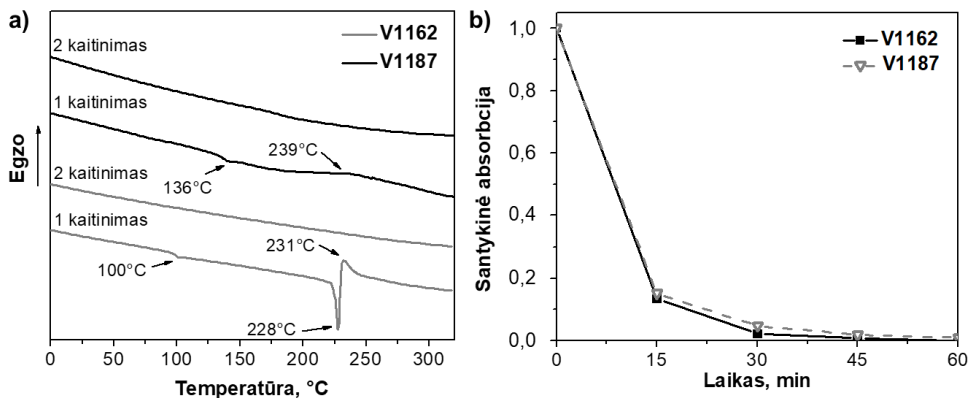
6 pav. a) Junginių **V1162** ir **V1187** DSK termogramos (kaitinimo režimas: 10 °C/min); b) junginių **V1162** ir **V1187** plėvelių sutinklinimo eksperimentas. Tirpalų, gautų po skirtingą laiką kaitintų plėvelių nuplovimo, absorbcijos palyginimas su tirpalų, paruoštų po nesutinklintų plėvelių nuplovimo, absorbcija

Iš UV–RŠ spektrų nustatyta, kad junginio **V1162** absorbcijos maksimumas yra ties 370 nm, o štai **V1187** maksimumui būdingas 36 nm batochrominis poslinkis, kurį galima paaiškinti didesne π konjuguota dvigubųjų jungčių sistema, atsiradusia dėl antrojo enamino fragmento buvimo molekulėje. Matavimų rezultatai pateikti 7 lentelėje.

**7 lentelė.** Terminės, optinės ir fotofizikinės sutinklinamų STM savybės

Junginys	$T_{lyd.}$ (°C)[a]	$T_{pol.}$ (°C)[a]	$T_{st.}$ (°C)[a]	$T_{5\ \%\ mas.\ nuost.}$ (°C)[a]	λ_{abs} (nm)[b]	I_P (eV)[c]	μ (cm^2/Vs)[d]
V1162	228	231	100	396	370	5,26	$8,6 \times 10^{-4}$ (prieš sutinklinimą)
							$4,0 \times 10^{-4}$ (po sutinklinimo)
V1187	–	239	136	393	406	5,11	$5,0 \times 10^{-3}$ (prieš ir po sutinklinimo)

[a]Lydymosi, polimerizacijos ir stiklėjimo temperatūros, užfiksuotos DSK metu; sutinklintų puslaidininkių 5 % masės nuostolių temperatūra, užfiksuota TGA metu (10 °C/min, N$_2$ terpė); [b]absorbcijos spektrai, matuoti iš tirpalų THF (10^{-4} M); [c]jonizacijos potencialai, išmatuoti plėvelėse, taikant elektronų fotoemisijos ore metodą; [d]skylių dreifinio judrio vertės esant stipriam elektriniam laukui.

UV–RŠ spektroskopija taip pat buvo pritaikyta puslaidininkių sutinklinimo procesui įvertinti. Visų pirma buvo suformuoti susintetintų STM sluoksniai, po to plėvelės buvo pakaitintos vieną valandą skirtingose temperatūrose (231 °C ir 239 °C, atitinkamai junginys **V1162** ir **V1187**). Vėliau, sluoksniai buvo nuplauti su tetrahidrofuranu, o nuplovimui naudotas tirpiklis išanalizuotas absorbcijos spektrais. Rezultatai parodė, jog didžioji dalis abiejų monomerų buvo supolimerinta į organiniams tirpikliams atsparias trimates (3D) struktūras jau po 15 kaitinimo minučių, o po 45 minučių terminės polimerizacijos procesas buvo visiškai baigtas (6b pav.). Sutinklinimo proceso įrodymui buvo pritaikyta ir Furjė transformacijos infraraudonųjų spindulių spektroskopija[173,174]. Tyrimų rezultatai parodė, kad vinilgrupių smailės, esančios prie 988–991 cm^{-1} ir 904–908 cm^{-1}, išnyksta po sluoksnių pakaitinimo atitinkamoje temperatūroje.

Jonizacijos potencialo matavimai pademonstravo, kad abiejų sutinklinamų enaminų I_P vertės yra tinkamos norint šiuos puslaidininkius pritaikyti PSE gamybai (5,11 eV ir 5,26 eV, atitinkamai junginiams **V1187** ir **V1162**).

Enaminas **V1187** parodė puikias krūvio pernašos savybes stipriuose elektriniuose laukuose, kai buvo pasiektos 10^{-3} cm^2/Vs vertės. Visgi dar svarbiau tai, kad **V1187** dreifinio judrio vertės nei kiek nesuprastėjo po sutinklinimo proceso. O štai junginys **V1162**, turintis mažesnę struktūrinę formulę, pasižymėjo kiek prastesniu krūvio pernašos greičiu nei **V1187**, ir po terminės polimerizacijos jo dreifinio judrio vertės sumažėjo kone dvigubai. Krūvio pernašos savybių plėvelėse duomenys pateikti 7 lentelėje ir 7a paveiksle.
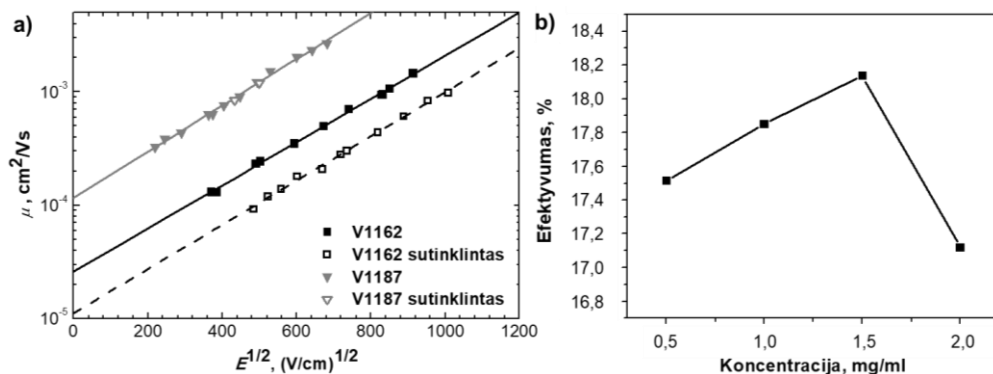
7 pav. a) Enaminų **V1162** ir **V1187** dreifinio judrio priklausomybė nuo elektrinio lauko stiprio prieš ir po terminės polimerizacijos; b) prietaisų efektyvumo kitimas esant skirtingai STM **V1187** tirpalo koncentracijai

Naujai susintetinti enaminai buvo panaudoti kaip skyles transportuojantys sluoksniai *p-i-n* tipo perovskitiniuose saulės elementuose (prietaiso struktūra: ITO/STM/perovskitas/C60/batokuproinas (BCP)/Ag), jų našumo parametrai pateikti 8 lentelėje.

8 lentelė. Saulės elementų našumo parametrai, gauti iš *J–V* kreivių

Junginys	V_{OC} (V)	J_{SC} (mA/cm²)	FF	PCE (%)
V1162	0,878	21,60	0,76	14,49
V1162 (sutinklintas)	1,077	21,51	0,64	14,71
V1187	0,932	20,73	0,80	15,51
V1187 (sutinklintas)	1,069	21,40	0,73	16,77

Duomenys rodo, kad prietaisai su nekaitintais **V1187** sluoksniais turi didesnį efektyvumą (15,51 %) palyginus su **V1162** (14,49 %); tam galėjo turėti įtakos greitesnė junginio **V1187** krūvių pernaša. Tokia pati tendencija yra stebima lyginant prietaisus su sutinklintais STM sluoksniais; be to, nustatyta, kad terminė polimerizacija teigiamai veikia ir jų efektyvumą, užfiksavus daug žadančius PSE rezultatus (16,77 %) su enaminu **V1187**. Visgi optimizavus šios STM koncentraciją tirpale, kuri varijavo nuo 0,5 mg/ml iki 2 mg/ml, buvo sukonstruoti dar našesni prietaisai, išsamūs rezultatai pateikti 7b paveiksle. Taigi po atliktų eksperimentų nustatyta, kad aukščiausias užfiksuotas PSE su sutinklintu enamino **V1187** sluoksniu efektyvumas yra 18,14 %, kuris buvo pasiektas esant 1,5 mg/ml STM tirpalo koncentracijai.

4.3. Išvados

Šiame darbe pristatytas nesudėtingas ir ekonomiškai patrauklus enaminų sintezės kelias pasitelkus kondensacijos reakciją, kuri leidžia visiškai atsisakyti medžiagų gryninimo procesą apsunkinančių paladžio katalizatorių ir išvengti inertinės aplinkos sąlygų naudojimo; tai užtikrina šios strategijos patrauklumą pramoninei perovskitinių saulės elementų gamybai. Darbo metu suformuluotos išvados:

1. Iš anilino ir jo darinių susintetinta ir ištirta nauja mažamolekulių organinių skyles transportuojančių junginių, turinčių enamino fragmentus, serija. Atlikus tyrimus nustatyta, kad:
   1.1. Gauti anilino darinių enaminai yra termiškai stabilūs, visų junginių 5 % masės nuostolių temperatūra yra didesnė nei 310 °C.
   1.2. Trečiojo difeniletenilo fragmento prijungimas fenilo žiedo p-padėtyje ne tik praplečia molekulės konjuguotą π dvigubųjų jungčių sistemą, bet ir užtikrina puslaidininkių amorfinę būseną.
   1.3. Šie puslaidininkiai turi tinkamas jonizacijos potencialo vertes (5,16– 5,30 eV) ir puikias skylių transportines savybes, stipriuose elektriniuose laukuose siekiančias 10^{-2} cm^2/Vs.
   1.4. Perovskitinių saulės elementų gamybai kaip skyles transportuojančius sluoksnius panaudojus šiuos anilino darinių enaminus, puslaidininkis, turintis tris enamino fragmentus (**V1091**) pademonstravo didesnį nei 20 % efektyvumą. Tokiomis pat sąlygomis etalonas spiro-OMeTAD parodė lygiai tokius pačius rezultatus.

2. Susintetinti skyles transportuojantys spirobifluoreno dariniai, turintys enamino fragmentų. Jų tyrimai atskleidė, kad:
   2.1. Enamino fragmentų buvimas molekulės struktūroje padidina junginių stiklėjimo temperatūrą, kuri nulemia geresnį morfologinį stabilumą.
   2.2. Geriausias krūvio pernašos savybes (9,4 × 10^{-4} cm^2/Vs) pademonstravo junginys **V1308**, turintis du enamino fragmentus viename fluoreno žiede.
   2.3. Trys iš keturių naujos serijos puslaidininkių (**V1305**, **V1307**, **V1308**) užtikrino didesnį nei 19 % prietaisų efektyvumą, kuris prilygsta saulės elementams su spiro-OMeTAD tomis pačiomis sąlygomis.

3. Susintetinta nauja skyles transportuojančių medžiagų serija, kurioje junginiai skiriasi centriniu heteroatomu ir enamino fragmentų skaičiumi. Šių medžiagų savybių tyrimai parodė, kad:
   3.1. Naujai susintetintų medžiagų 5 % masės nuostolių temperatūra yra aukštesnė nei 400 °C, ir tai įrodo puikų visos serijos terminį stabilumą.
   3.2. Visiškai amorfinė būsena yra būdinga tik dviem enaminams, kurie savo struktūros centre turi trifenilamino ir difenilsulfido centrinius fragmentus.
   3.3. Junginys su centriniu azoto heteroatomu turi didesnę konjuguotą π dvigubųjų jungčių sistemą, dėl kurios buvo užfiksuotas apie 20 nm batochrominis absorbcijos maksimumo poslinkis. Be to, šis puslaidininkis pademonstravo ir didžiausią iš visos serijos krūvininkų dreifinį judrį (2,0 × 10^{-5} cm^2/Vs);
   3.4. Prietaisai, kurių struktūroje buvo panaudotas puslaidininkis su azoto centriniu atomu, pademonstravo didesnį nei 20 % efektyvumą, o tai yra

vienas iš didžiausių publikuotų našumų tarp perovskitinių saulės elementų, kuriuose skyles transportuojantys junginiai turi enamino fragmentų.

4. Susintetinta grupė sutinklinamų ir skyles transportuojančių fluoreno darinių, turinčių enamino fragmentus. Atlikus šių junginių analizę ir terminės polimerizacijos poveikio jų savybėms tyrimą buvo nustatyta, kad:

   4.1. Vieną enamino fragmentą turinčio junginio polimerizacija užfiksuota esant 231 °C, o štai junginio su dviem fragmentais polimerizacija vyksta esant kiek didesnei temperatūrai (239 °C).

   4.2. Po maždaug 45 minučių kaitinimo iš enaminų plėvelių susiformuoja organiniams tirpikliams atsparūs trimačiai sutinklinti sluoksniai.

   4.3. *In-situ* sutinklinimo procesas neturi didelės įtakos naujųjų enaminų skylių transportinėms savybėms, todėl tokie sluoksniai gali būti pritaikyti *p-i-n* tipo perovskitiniuose saulės elementuose.

   4.4. Skyles transportuojančios medžiagos tirpalo koncentracija turi didelę įtaką perovskitinių saulės elementų efektyvumui, o pats sutinklinimo procesas prietaisų efektyvumą veikia teigiamai.

   4.5. Optimizavus prietaisus, turinčius sutinklintą skyles transportuojančios medžiagos su dviem enamino fragmentais sluoksnį, buvo pasiektas daug žadantis, didesnis nei 18 %, efektyvumas.

5. Susintetinti *p*-tipo organiniai fotopuslaidininkiai yra nuo 3 iki 12 kartų pigesni nei žinomi standartiniai puslaidininkiai (spiro-OMeTAD), naudojami efektyviems perovskitiniams saulės elementams gauti.

5. REFERENCES

1. Abram NJ, McGregor H V., Tierney JE, et al. Early onset of industrial-era warming across the oceans and continents. *Nat 2016 5367617*. 2016;536(7617):411-418. doi:10.1038/nature19082

2. Kabir E, Kumar P, Kumar S, Adelodun AA, Kim KH. Solar energy: Potential and future prospects. *Renew Sustain Energy Rev*. 2018;82(August 2017):894-900. doi:10.1016/j.rser.2017.09.094

3. Statista. https://www.statista.com/statistics/265598/consumption-of-primary-energy-worldwide/

4. Imamzai M, Aghaei M, Thayoob YH. A Review on Comparison between Traditional Silicon Solar Cells and Thin-Film CdTe Solar Cell. In: *Proceedings National Graduate Conference*. ; 2012:8-10.

5. Saga T. Advances in crystalline silicon solar cell technology for industrial mass production. *NPG Asia Mater 2010 23*. 2010;2(3):96-102. doi:10.1038/asiamat.2010.82

6. Polman A, Knight M, Garnett EC, Ehrler B, Sinke WC. Photovoltaic materials: Present efficiencies and future challenges. *Science (80-)*. 2016;352(6283). doi:10.1126/SCIENCE.AAD4424

7. Zhao L, Maynadier A, Nelias D. Stiffness and fracture analysis of photovoltaic grade silicon plates. *Int J Solids Struct*. 2016;97_98:355-369. doi:10.1016/J.IJSOLSTR.2016.07.013

8. T.S S, C.R K. New Materials for Thin Film Solar Cells. In: *Coatings and Thin-Film Technologies*. IntechOpen; 2019. doi:10.5772/intechopen.81393

9. Li F, Jen AKY. Interface Engineering in Solution-Processed Thin-Film Solar Cells. *Accounts Mater Res*. 2022;3(3):272-282. doi:10.1021/ACCOUNTSMR.1C00169

10. Kojima A, Teshima K, Shirai Y, Miyasaka T. Organometal halide perovskites as visible-light sensitizers for photovoltaic cells. *J Am Chem Soc*. 2009;131(17):6050-6051. doi:10.1021/ja809598r

11. Min H, Lee DY, Kim J, et al. Perovskite solar cells with atomically coherent interlayers on SnO2 electrodes. *Nature*. 2021;598(7881):444-450. doi:10.1038/s41586-021-03964-8

12. Assirey EAR. Perovskite synthesis, properties and their related biochemical and industrial application. *Saudi Pharm J*. 2019;27(6):817-829. doi:10.1016/J.JSPS.2019.05.003

13. Chang J, Chen H, Wang G, Wang B, Chen X, Yuan H. Electronic and optical properties of perovskite compounds MA 1Àa FA a PbI 3Àb X b (X ¼ Cl, Br) explored for photovoltaic applications. Published online 2019. doi:10.1039/c8ra08189a

14. Abd Mutalib M, Aziz F, Ismail AF, et al. Towards high performance perovskite solar cells: A review of morphological control and HTM development. *Appl Mater Today*. 2018;13:69-82. doi:10.1016/J.APMT.2018.08.006

15. Li S, Cao YL, Li WH, Bo ZS. A brief review of hole transporting materials commonly used in perovskite solar cells. *Rare Met*. 2021;40(10):2712-2729. doi:10.1007/S12598-020-01691-Z

16. NREL. https://www.nrel.gov/pv/assets/pdfs/cell-pv-eff-emergingpv-rev220630.pdf

17.   Brooks K. Perovskite. *Geol Today*. 2020;36(1):33-38. doi:10.1111/gto.12299

18.   Lee JW, Seo S, Nandi P, Jung HS, Park NG, Shin H. Dynamic structural property of organic-inorganic metal halide perovskite. *iScience*. 2021;24(1). doi:10.1016/J.ISCI.2020.101959

19.   Fakharuddin A, Gangishetty MK, Abdi-Jalebi M, et al. Perovskite light-emitting diodes. *Nat Electron*. 2022;5:203-216. doi:10.1038/s41928-022-00745-7

20.   Liu XK, Xu W, Bai S, et al. Metal halide perovskites for light-emitting diodes. doi:10.1038/s41563-020-0784-7

21.   Zhang K, Zhu N, Zhang M, Wang L, Xing J. Materials for optical, magnetic and electronic devices Opportunities and challenges in perovskite LED commercialization †. *J Mater Chem C*. 2021;9:3795. doi:10.1039/d1tc00232e

22.   Li C, Wang H, Wang F, et al. Ultrafast and broadband photodetectors based on a perovskite/organic bulk heterojunction for large-dynamic-range imaging. *Off J CIOMP*.:2047-7538. doi:10.1038/s41377-020-0264-5

23.   Li G, Wang Y, Huang L, Sun W. Research Progress of High-Sensitivity Perovskite Photodetectors: A Review of Photodetectors: Noise, Structure, and Materials. *ACS Appl Electron Mater*. 2022;4(4):1485–1505. doi:10.1021/acsaelm.1c01349

24.   Zhou Y, Qiu X, Wan Z, et al. Halide-exchanged perovskite photodetectors for wearable visible-blind ultraviolet monitoring. *Nano Energy*. 2022;100:107516. doi:10.1016/J.NANOEN.2022.107516

25.   Fu L, Li B, Li S, Yin L. Magnetic, Electronic, and Optical Properties of Perovskite Materials. Published online 2020:43-59. doi:10.1007/978-981-15-1267-4_2

26.   Hong Noh J, Hyuk Im S, Hyuck Heo J, Mandal TN, Il Seok S. Chemical Management for Colorful, Efficient, and Stable Inorganic− Organic Hybrid Nanostructured Solar Cells. Published online 2013. doi:10.1021/nl400349b

27.   Saliba M, Matsui T, Seo JY, et al. Cesium-containing triple cation perovskite solar cells: improved stability, reproducibility and high efficiency. *Energy Environ Sci*. 2016;9(6):1989-1997. doi:10.1039/c5ee03874j

28.   Zhou D, Zhou T, Tian Y, Zhu X, Tu Y. Perovskite-Based Solar Cells: Materials, Methods, and Future Perspectives. *J Nanomater*. 2018;2018:8148072. doi:10.1155/2018/8148072

29.   Warby J, Zu F, Zeiske S, et al. Understanding Performance Limiting Interfacial Recombination in pin Perovskite Solar Cells. *Adv Energy Mater*. 2022;12(12). doi:10.1002/AENM.202103567

30.   Ašmontas S, Čerškus A, Gradauskas J, et al. Photoelectric Properties of Planar and Mesoporous Structured Perovskite Solar Cells. *Materials (Basel)*. 2022;15(12). doi:10.3390/ma15124300

31.   Mali SS, Hong CK. p-i-n/n-i-p type planar hybrid structure of highly efficient perovskite solar cells towards improved air stability: synthetic strategies and the role of p-type hole transport layer (HTL) and n-type electron transport layer (ETL) metal oxides. *Nanoscale*. 2016;8(20):10528-10540. doi:10.1039/C6NR02276F

32.   Kim HS, Lee CR, Im JH, et al. Lead Iodide Perovskite Sensitized All-Solid-State Submicron Thin Film Mesoscopic Solar Cell with Efficiency Exceeding 9%. *Sci Rep*. 2012;2:591. doi:10.1038/srep00591

33. Lee MM, Teuscher J, Miyasaka T, Murakami TN, Snaith HJ. Efficient hybrid solar cells based on meso-superstructured organometal halide perovskites. *Science (80-)*. 2012;338(6107):643-647. doi:10.1126/science.1228604

34. Liu X, Cheng Y, Liu C, et al. 20.7% highly reproducible inverted planar perovskite solar cells with enhanced fill factor and eliminated hysteresis. *Energy Environ Sci*. 2019;12(5):1622-1633. doi:10.1039/C9EE00872A

35. Huang H, Cui P, Chen Y, et al. 24.8%-efficient planar perovskite solar cells via ligand-engineered TiO2 deposition. *Joule*. 2022;6(9):2186-2202. doi:10.1016/J.JOULE.2022.07.004

36. Mora-Seró I. How Do Perovskite Solar Cells Work? *Joule*. 2018;2(4):585-587. doi:10.1016/J.JOULE.2018.03.020

37. Jha A, Duan HG, Tiwari V, et al. Direct Observation of Ultrafast Exciton Dissociation in Lead Iodide Perovskite by 2D Electronic Spectroscopy. 2022;15:12. doi:10.1021/acsphotonics.7b01025

38. Fortunato E, Ginley D, Hosono H, Paine DC. Transparent conducting oxides for photovoltaics. *MRS Bull*. 2007;32(3):242-247. doi:10.1557/mrs2007.29

39. Ikhmayies SJ. Transparent conducting oxides for solar cell applications. In: *Mediterranean Green Buildings and Renewable Energy: Selected Papers from the World Renewable Energy Network's Med Green Forum*. Springer International Publishing; 2017:899-907. doi:10.1007/978-3-319-30746-6_70

40. Kaienburg P, Hartnagel P, Pieters BE, et al. How Contact Layers Control Shunting Losses from Pinholes in Thin-Film Solar Cells. *J Phys Chem C*. 2018;122(48):27263-27272. doi:10.1021/ACS.JPCC.8B09400

41. Valadi K, Gharibi S, Taheri-Ledari R, et al. Metal oxide electron transport materials for perovskite solar cells: a review. *Environ Chem Lett*. 2021;19:2185-2207. doi:10.1007/s10311-020-01171-x

42. Ali Said A, Xie J, Zhang Q, Said AA, Xie J, Zhang Q. Recent Progress in Organic Electron Transport Materials in Inverted Perovskite Solar Cells. *Small*. 2019;15(27):1900854. doi:10.1002/SMLL.201900854

43. Sauvé G, Fernando R. Beyond Fullerenes: Designing Alternative Molecular Electron Acceptors for Solution-Processable Bulk Heterojunction Organic Photovoltaics. *J Phys Chem Lett*. 2015;6(18):3770-3780. doi:10.1021/ACS.JPCLETT.5B01471

44. Nielsen CB, Holliday S, Chen HY, Cryer SJ, McCulloch I. Non-Fullerene Electron Acceptors for Use in Organic Solar Cells. *Acc Chem Res*. 2015;48(11):2803-2812. doi:10.1021/ACS.ACCOUNTS.5B00199

45. Jiang K, Wu F, Yu H, et al. A perylene diimide-based electron transport layer enabling efficient inverted perovskite solar cells. *J Mater Chem A*. 2018;6(35):16868-16873. doi:10.1039/C8TA06081A

46. Wang R, Jiang K, Yu H, Wu F, Zhu L, Yan H. Efficient inverted perovskite solar cells with truxene-bridged PDI trimers as electron transporting materials. *Mater Chem Front*. 2019;3(10):2137-2142. doi:10.1039/C9QM00329K

47. Said AA, Wagalgave SM, Xie J, et al. NDI-based small molecules as electron transporting layers in solution-processed planar perovskite solar cells. *J Solid State Chem*. 2019;270:51-57. doi:10.1016/J.JSSC.2018.10.045

48.   Kim H Il, Kim MJ, Choi K, et al. Improving the Performance and Stability of Inverted Planar Flexible Perovskite Solar Cells Employing a Novel NDI-Based Polymer as the Electron Transport Layer. *Adv Energy Mater*. 2018;8(16):1702872. doi:10.1002/AENM.201702872

49.   Gu PY, Wang N, Wu A, et al. An Azaacene Derivative as Promising Electron-Transport Layer for Inverted Perovskite Solar Cells. *Chem – An Asian J*. 2016;11(15):2135-2138. doi:10.1002/ASIA.201600856

50.   Gu PY, Wang N, Wang C, et al. Pushing up the efficiency of planar perovskite solar cells to 18.2% with organic small molecules as the electron transport layer. *J Mater Chem A*. 2017;5(16):7339-7344. doi:10.1039/C7TA01764B

51.   Lian J, Lu B, Niu F, Zeng P, Zhan X. Electron-Transport Materials in Perovskite Solar Cells. *Small Methods*. 2018;2(10):1800082. doi:10.1002/SMTD.201800082

52.   Wali Q, Iqbal Y, Pal B, Lowe A, Jose R. Tin oxide as an emerging electron transport medium in perovskite solar cells. *Sol Energy Mater Sol Cells*. 2018;179:102-117. doi:10.1016/J.SOLMAT.2018.02.007

53.   Zhang P, Wu J, Zhang T, et al. Perovskite Solar Cells with ZnO Electron-Transporting Materials. *Adv Mater*. 2018;30(3):1703737. doi:10.1002/ADMA.201703737

54.   Wang K, Olthof S, Subhani WS, et al. Novel inorganic electron transport layers for planar perovskite solar cells: Progress and prospective. *Nano Energy*. 2020;68:104289. doi:10.1016/J.NANOEN.2019.104289

55.   Kim M, Murakami TN, Kim TW, et al. Ultra-thin Cadmium Sulfide Electron-transporting Layer for Planar Perovskite Solar Cell. *Chem Lett*. 2018;47(11):1350-1353. doi:10.1246/CL.180616

56.   Ghosh P, Senthilarasu S, Nixon T, Krishnamurthy S. Influence of Nanostructures in Perovskite Solar Cells. *Ref Modul Mater Sci Mater Eng*. Published online January 1, 2016. doi:10.1016/B978-0-12-803581-8.04062-5

57.   Lin L, Jones TW, Chien T, et al. Inorganic Electron Transport Materials in Perovskite Solar Cells. *Adv Funct Mater*. 2021;31(5):2008300. doi:10.1002/ADFM.202008300

58.   Blackburn D, Routledge TJ, O'Kane M, et al. Low-Temperature, Scalable, Reactive Deposition of Tin Oxide for Perovskite Solar Cells. *Sol RRL*. 2022;6(8):2200263. doi:10.1002/SOLR.202200263

59.   Giorgi G, Yamashita K. Organic–inorganic halide perovskites: an ambipolar class of materials with enhanced photovoltaic performances. *J Mater Chem A*. 2015;3(17):8981-8991. doi:10.1039/C4TA05046K

60.   Endres J, Egger DA, Kulbak M, et al. Valence and Conduction Band Densities of States of Metal Halide Perovskites: A Combined Experimental-Theoretical Study. *J Phys Chem Lett*. 2016;7(14):2722-2729. doi:10.1021/ACS.JPCLETT.6B00946

61.   Gil-Escrig L, Momblona C, La-Placa MG, et al. Vacuum Deposited Triple-Cation Mixed-Halide Perovskite Solar Cells. *Adv Energy Mater*. 2018;8(14):1703506. doi:10.1002/AENM.201703506

62.   Li H, Zhou J, Tan L, et al. Sequential vacuum-evaporated perovskite solar cells with more than 24% efficiency. *Sci Adv*. 2022;8(28):7422. doi:10.1126/SCIADV.ABO7422

63. Chen Q, Zhou H, Hong Z, et al. Planar heterojunction perovskite solar cells via vapor-assisted solution process. *J Am Chem Soc*. 2014;136(2):622-625. doi:10.1021/JA411509G

64. Djurišić AB, Liu FZ, Tam HW, et al. Perovskite solar cells - An overview of critical issues. *Prog Quantum Electron*. 2017;53:1-37. doi:10.1016/J.PQUANTELEC.2017.05.002

65. Chen S, Xiao X, Chen B, et al. Crystallization in one-step solution deposition of perovskite films: Upward or downward? *Sci Adv*. 2021;7(4). doi:10.1126/SCIADV.ABB2412

66. Mehdi H, Mhamdi A, Hannachi R, Bouazizi A. MAPbBr3 perovskite solar cells via a two-step deposition process. *RSC Adv*. 2019;9(23):12906-12912. doi:10.1039/C9RA02036E

67. Chi W, Banerjee SK. Achieving Resistance against Moisture and Oxygen for Perovskite Solar Cells with High Efficiency and Stability. *Chem Mater*. 2021;33(12):4269-4303. doi:10.1021/ACS.CHEMMATER.1C00773

68. Singh R, Singh PK, Bhattacharya B, Rhee HW. Review of current progress in inorganic hole-transport materials for perovskite solar cells. *Appl Mater Today*. 2019;14:175-200. doi:10.1016/J.APMT.2018.12.011

69. Rajeswari R, Mrinalini M, Prasanthkumar S, Giribabu L. Emerging of Inorganic Hole Transporting Materials For Perovskite Solar Cells. *Chem Rec*. 2017;17(7):681-699. doi:10.1002/TCR.201600117

70. Xie F, Chen CC, Wu Y, et al. Vertical recrystallization for highly efficient and stable formamidinium-based inverted-structure perovskite solar cells. *Energy Environ Sci*. 2017;10(9):1942-1949. doi:10.1039/C7EE01675A

71. Arora N, Dar MI, Hinderhofer A, et al. Perovskite solar cells with CuSCN hole extraction layers yield stabilized efficiencies greater than 20%. *Science (80-)*. 2017;358(6364):768-771. doi:10.1126/SCIENCE.AAM5655

72. Chen Y, Yang Z, Wang S, et al. Design of an Inorganic Mesoporous Hole-Transporting Layer for Highly Efficient and Stable Inverted Perovskite Solar Cells. *Adv Mater*. 2018;30(52):1805660. doi:10.1002/ADMA.201805660

73. Bach U, Lupo D, Comte P, et al. Solid-state dye-sensitized mesoporous TiO2 solar cells with high photon-to-electron conversion efficiencies. *Nature*. 1998;395(6702):583-585. doi:10.1038/26936

74. Kasparavicius E, Magomedov A, Malinauskas T, Getautis V. Long-Term Stability of the Oxidized Hole-Transporting Materials used in Perovskite Solar Cells. *Chem - A Eur J*. 2018;24(39):9910-9918. doi:10.1002/CHEM.201801441

75. Saragi TPI, Spehr T, Siebert A, Fuhrmann-Lieker T, Salbeck J. Spiro compounds for organic optoelectronics. *Chem Rev*. 2007;107(4):1011-1065. doi:10.1021/cr0501341

76. Mattiello S, Lucarelli G, Calascibetta A, et al. Sustainable, Efficient, and Scalable Preparation of Pure and Performing Spiro-OMeTAD for Perovskite Solar Cells. *ACS Sustain Chem Eng*. 2022;10(14):4750-4757. doi:10.1021/ACSSUSCHEMENG.2C00493

77. Zhu G, Yang L, Zhang C, et al. Unveiling the Critical Role of Oxidants and Additives in Doped Spiro-OMeTAD toward Stable and Efficient Perovskite Solar Cells. *ACS Appl Energy Mater*. 2022;5(3):3595-3604. doi:10.1021/ACSAEM.1C04097

78. Wang S, Sina M, Parikh P, et al. Role of 4-tert-Butylpyridine as a Hole Transport Layer Morphological Controller in Perovskite Solar Cells. *Nano Lett*. 2016;16(9):5594-5600. doi:10.1021/acs.nanolett.6b02158

79. Noel NK, Abate A, Stranks SD, et al. Enhanced photoluminescence and solar cell performance via Lewis base passivation of organic-inorganic lead halide perovskites. *ACS Nano*. 2014;8(10):9815-9821. doi:10.1021/NN5036476

80. Wang S, Huang Z, Wang X, et al. Unveiling the Role of tBP-LiTFSI Complexes in Perovskite Solar Cells. *J Am Chem Soc*. 2018;140(48):16720-16730. doi:10.1021/JACS.8B09809

81. Schloemer TH, Christians JA, Luther JM, Sellinger A. Doping strategies for small molecule organic hole-transport materials: impacts on perovskite solar cell performance and stability. *Chem Sci*. 2019;10(7):1904-1935. doi:10.1039/C8SC05284K

82. Luo D, Yang W, Wang Z, et al. Enhanced photovoltage for inverted planar heterojunction perovskite solar cells. *Science (80-)*. 2018;360(6396):1442-1446. doi:10.1126/science.aap9282

83. Sigma Aldrich. https://www.sigmaaldrich.com/LT/en/product/aldrich/702471

84. Cameron J, Skabara PJ. The damaging effects of the acidity in PEDOT:PSS on semiconductor device performance and solutions based on non-acidic alternatives. *Mater Horizons*. 2020;7(7):1759-1772. doi:10.1039/C9MH01978B

85. Lyu B, Yang L, Luo Y, Zhang X, Zhang J. Counter electrodes for perovskite solar cells: materials, interfaces and device stability. *J Mater Chem C*. 2022;10(30):10775-10798. doi:10.1039/D2TC02182J

86. Liu Z, He H. *Counter Electrode Materials for Organic-Inorganic Perovskite Solar Cells*. Springer Berlin Heidelberg; 2019. doi:10.1007/978-3-662-59594-7_7

87. Uhl AR. *Metal Counter Electrodes for Perovskite Solar Cells*. John Wiley & Sons, Ltd; 2018. doi:10.1002/9783527813636.CH17

88. Liang L, Cai Y, Li X, Nazeeruddin MK, Gao P. All that glitters is not gold: Recent progress of alternative counter electrodes for perovskite solar cells. *Nano Energy*. 2018;52:211-238. doi:10.1016/J.NANOEN.2018.07.049

89. Svanström S, Jacobsson TJ, Boschloo G, Johansson EMJ, Rensmo H, Cappel UB. Degradation Mechanism of Silver Metal Deposited on Lead Halide Perovskites. *ACS Appl Mater Interfaces*. 2020;12(6):7212-7221. doi:10.1021/ACSAMI.9B20315

90. Que M, Zhang B, Chen J, Yin X, Yun S. Carbon-based electrodes for perovskite solar cells. *Mater Adv*. 2021;2(17):5560-5579. doi:10.1039/D1MA00352F

91. Muchuweni E, Martincigh BS, Nyamori VO. Perovskite Solar Cells: Current Trends in Graphene-Based Materials for Transparent Conductive Electrodes, Active Layers, Charge Transport Layers, and Encapsulation Layers. *Adv Energy Sustain Res*. 2021;2(9):2100050. doi:10.1002/AESR.202100050

92. International standard ISO 9845-1:2022. Published 2022. https://www.iso.org/obp/ui/#iso:std:iso:9845:-1:ed-2:v1:en

93. Shockley W, Queisser HJ. Detailed Balance Limit of Efficiency of p-n Junction Solar Cells. *J Appl Phys*. 2004;32(3):510. doi:10.1063/1.1736034

94. Rühle S. Tabulated values of the Shockley–Queisser limit for single junction solar cells. *Sol Energy*. 2016;130:139-147. doi:10.1016/J.SOLENER.2016.02.015

95. Sha WEI, Ren X, Chen L, Choy WCH. The efficiency limit of CH3NH3PbI3 perovskite solar cells. *Appl Phys Lett*. 2015;106(22):221104. doi:10.1063/1.4922150

96. Park NG, Segawa H. Research Direction toward Theoretical Efficiency in Perovskite Solar Cells. *ACS Photonics*. 2018;5(8):2970-2977. doi:10.1021/ACSPHOTONICS.8B00124

97. Chen B, Yang M, Priya S, Zhu K. Origin of J-V Hysteresis in Perovskite Solar Cells. *J Phys Chem Lett*. 2016;7(5):905-917. doi:10.1021/ACS.JPCLETT.6B00215

98. Wali Q, Aamir M, Ullah A, et al. Fundamentals of Hysteresis in Perovskite Solar Cells: From Structure-Property Relationship to Neoteric Breakthroughs. *Chem Rec*. 2022;22(1):e202100150. doi:10.1002/TCR.202100150

99. Rong Y, Hu Y, Ravishankar S, et al. Tunable hysteresis effect for perovskite solar cells. *Energy Environ Sci*. 2017;10(11):2383-2391. doi:10.1039/C7EE02048A

100. Nemnes GA, Besleaga C, Tomulescu AG, et al. How measurement protocols influence the dynamic J-V characteristics of perovskite solar cells: Theory and experiment. *Sol Energy*. 2018;173:976-983. doi:10.1016/J.SOLENER.2018.08.033

101. Singh R, Parashar M. *Soft-Matter Thin Film Solar Cells*. AIP Publishing LLCAIP PublishingMelville, New York; 2021. doi:10.1063/9780735422414_001

102. Zani L, Dessì A, Franchi D, Calamante M, Reginato G, Mordini A. Transition metal-catalyzed cross-coupling methodologies for the engineering of small molecules with applications in organic electronics and photovoltaics. *Coord Chem Rev*. 2019;392:177-236. doi:10.1016/J.CCR.2019.04.007

103. Nakka L, Cheng Y, Aberle AG, Lin F. Analytical Review of Spiro-OMeTAD Hole Transport Materials: Paths Toward Stable and Efficient Perovskite Solar Cells. *Adv Energy Sustain Res*. 2022;3(8):2200045. doi:10.1002/AESR.202200045

104. Usluer Ö, Abbas M, Wantz G, et al. Metal residues in semiconducting polymers: Impact on the performance of organic electronic devices. *ACS Macro Lett*. 2014;3(11):1134-1138. doi:10.1021/MZ500590D

105. Rombach FM, Haque SA, Macdonald TJ. Lessons learned from spiro-OMeTAD and PTAA in perovskite solar cells. *Energy Environ Sci*. 2021;14(10):5161-5190. doi:10.1039/D1EE02095A

106. Al-Zohbi F, Jouane Y, Benhattab S, et al. Simple carbazole-based hole transporting materials with fused benzene ring substituents for efficient perovskite solar cells. *New J Chem*. 2019;43(31):12211-12214. doi:10.1039/C9NJ03089A

107. Sutanto AA, Joseph V, Igci C, et al. Isomeric Carbazole-Based Hole-Transporting Materials: Role of the Linkage Position on the Photovoltaic Performance of Perovskite Solar Cells. *Chem Mater*. 2021;33(9):3286-3296. doi:10.1021/ACS.CHEMMATER.1C00335

108. Rakstys K, Paek S, Gao P, et al. Molecular engineering of face-on oriented dopant-free hole transporting material for perovskite solar cells with 19% PCE. *J Mater Chem A*. 2017;5(17):7811-7815. doi:10.1039/C7TA01718A

109. Wang B, Zeng Q, Sun Z, Xue S, Liang M. Molecularly engineering of truxene-based dopant-free hole-transporting materials for efficient inverted planar perovskite solar cells. *Dye Pigment*. 2019;165:81-89. doi:10.1016/J.DYEPIG.2019.01.052

110. Zhang F, Wang Z, Zhu H, Wang S, Li X. A low-cost thiophene-based hole transport material for efficient and stable perovskite solar cells. *Org Electron*. 2019;71:194-198. doi:10.1016/J.ORGEL.2019.05.024

111. Zhang F, Wang Z, Zhu H, et al. Over 20% PCE perovskite solar cells with superior stability achieved by novel and low-cost hole-transporting materials. *Nano Energy*. 2017;41:469-475. doi:10.1016/J.NANOEN.2017.09.035

112. Tepliakova M, Yakushenko IK, Romadina EI, et al. Strength of attraction: pyrene-based hole-transport materials with effective π–π stacking for dopant-free perovskite solar cells. *Sustain Energy Fuels*. 2021;5(1):283-288. doi:10.1039/D0SE01300E

113. Ge QQ, Shao JY, Ding J, et al. A Two-Dimensional Hole-Transporting Material for High-Performance Perovskite Solar Cells with 20 % Average Efficiency. *Angew Chemie Int Ed*. 2018;57(34):10959-10965. doi:10.1002/ANIE.201806392

114. Do K, Choi H, Lim K, et al. Star-shaped hole transporting materials with a triazine unit for efficient perovskite solar cells. *Chem Commun*. 2014;50(75):10971-10974. doi:10.1039/C4CC04550E

115. Lim K, Kang MS, Myung Y, et al. Star-shaped hole transport materials with indeno[1,2-b] thiophene or fluorene on a triazine core for efficient perovskite solar cells. *J Mater Chem A*. 2016;4(4):1186-1190. doi:10.1039/C5TA07369C

116. Jeon NJ, Lee HG, Kim YC, et al. O-methoxy substituents in spiro-OMeTAD for efficient inorganic-organic hybrid perovskite solar cells. *J Am Chem Soc*. 2014;136(22):7837-7840. doi:10.1021/JA502824C

117. Hammett LP. The Effect of Structure upon the Reactions of Organic Compounds. Benzene Derivatives. *J Am Chem Soc*. 1937;59(1):96-103. doi:10.1021/JA01280A022

118. Hu Z, Fu W, Yan L, et al. Effects of heteroatom substitution in spiro-bifluorene hole transport materials. *Chem Sci*. 2016;7(8):5007-5012. doi:10.1039/C6SC00973E

119. Xu B, Bi D, Hua Y, et al. A low-cost spiro[fluorene-9,9′-xanthene]-based hole transport material for highly efficient solid-state dye-sensitized solar cells and perovskite solar cells. *Energy Environ Sci*. 2016;9(3):873-877. doi:10.1039/C6EE00056H

120. Zhang J, Hua Y, Xu B, et al. The Role of 3D Molecular Structural Control in New Hole Transport Materials Outperforming Spiro-OMeTAD in Perovskite Solar Cells. *Adv Energy Mater*. 2016;6(19):1601062. doi:10.1002/AENM.201601062

121. Saliba M, Orlandi S, Matsui T, et al. A molecularly engineered hole-transporting material for efficient perovskite solar cells. 2016;1(2):1-7. doi:10.1038/nenergy.2015.17

122. Akin S, Bauer M, Uchida R, et al. Cyclopentadithiophene-Based Hole-Transporting Material for Highly Stable Perovskite Solar Cells with Stabilized Efficiencies Approaching 21%. *ACS Appl Energy Mater*. 2020;3(8):7456-7463. doi:10.1021/ACSAEM.0C00811

123. Cao Y, Li Y, Morrissey T, et al. Dopant-free molecular hole transport material that mediates a 20% power conversion efficiency in a perovskite solar cell. *Energy Environ Sci*. 2019;12(12):3502-3507. doi:10.1039/C9EE02983D

124. Wang J, Wu X, Liu Y, et al. Dopant-Free Hole-Transporting Material with Enhanced Intermolecular Interaction for Efficient and Stable n-i-p Perovskite Solar Cells. *Adv Energy Mater*. 2021;11(29):2100967. doi:10.1002/AENM.202100967

125. Petrus ML, Bein T, Dingemans TJ, Docampo P. A low cost azomethine-based hole transporting material for perovskite photovoltaics. *J Mater Chem A*. 2015;3(23):12159-12162. doi:10.1039/C5TA03046C

126. Petrus ML, Sirtl MT, Closs AC, Bein T, Docampo P. Hydrazone-based hole transporting material prepared via condensation chemistry as alternative for cross-coupling chemistry for perovskite solar cells. *Mol Syst Des Eng*. 2018;3(5):734-740. doi:10.1039/C8ME00023A

127. Petrus ML, Schutt K, Sirtl MT, et al. New Generation Hole Transporting Materials for Perovskite Solar Cells: Amide-Based Small-Molecules with Nonconjugated Backbones. *Adv Energy Mater*. 2018;8(32):1801605. doi:10.1002/AENM.201801605

128. Daskeviciene M, Paek S, Wang Z, et al. Carbazole-based enamine: Low-cost and efficient hole transporting material for perovskite solar cells. *Nano Energy*. 2017;32(January):551-557. doi:10.1016/J.NANOEN.2017.01.015

129. Daskeviciene M, Paek S, Magomedov A, et al. Molecular engineering of enamine-based small organic compounds as hole-transporting materials for perovskite solar cells. *J Mater Chem C*. 2019;7(9):2717-2724. doi:10.1039/C8TC06297H

130. Zhou S, Daskeviciene M, Steponaitis M, et al. Low-Cost Dopant-Free Carbazole Enamine Hole-Transporting Materials for Thermally Stable Perovskite Solar Cells. *Sol RRL*. 2022;6(1):2100984. doi:10.1002/SOLR.202100984

131. Elbohy H, Bahrami B, Mabrouk S, et al. Tuning Hole Transport Layer Using Urea for High-Performance Perovskite Solar Cells. *Adv Funct Mater*. 2019;29(47):1806740. doi:10.1002/ADFM.201806740

132. Ahmadi M, Hsiao YC, Wu T, et al. Effect of Photogenerated Dipoles in the Hole Transport Layer on Photovoltaic Performance of Organic–Inorganic Perovskite Solar Cells. *Adv Energy Mater*. 2017;7(4):1601575. doi:10.1002/AENM.201601575

133. Yaghoobi Nia N, Lamanna E, Zendehdel M, et al. Doping Strategy for Efficient and Stable Triple Cation Hybrid Perovskite Solar Cells and Module Based on Poly(3-hexylthiophene) Hole Transport Layer. *Small*. 2019;15(49):1904399. doi:10.1002/SMLL.201904399

134. Li S, He B, Xu J, et al. Highly efficient inverted perovskite solar cells incorporating P3CT-Rb as a hole transport layer to achieve a large open circuit voltage of 1.144 V. *Nanoscale*. 2020;12(6):3686-3691. doi:10.1039/C9NR08441J

135. Kim GW, Lee J, Kang G, Kim T, Park T. Donor–Acceptor Type Dopant-Free, Polymeric Hole Transport Material for Planar Perovskite Solar Cells (19.8%). *Adv Energy Mater*. 2018;8(4):1701935. doi:10.1002/AENM.201701935

136. Lee J, Kim GW, Kim M, Park SA, Park T. Nonaromatic Green-Solvent-Processable, Dopant-Free, and Lead-Capturable Hole Transport Polymers in Perovskite Solar Cells with High Efficiency. *Adv Energy Mater*. 2020;10(8):1902662. doi:10.1002/AENM.201902662

137. Wu X, Gao D, Sun X, et al. Backbone Engineering Enables Highly Efficient Polymer Hole-Transporting Materials for Inverted Perovskite Solar Cells. *Adv Mater*. Published online December 31, 2022:2208431. doi:10.1002/ADMA.202208431

138.   Magomedov A, Al-Ashouri A, Kasparavičius E, et al. Self-Assembled Hole Transporting Monolayer for Highly Efficient Perovskite Solar Cells. *Adv Energy Mater*. 2018;8(32):1801892. doi:10.1002/AENM.201801892

139.   Wang C, Hu J, Li C, et al. Spiro-Linked Molecular Hole-Transport Materials for Highly Efficient Inverted Perovskite Solar Cells. *Sol RRL*. 2020;4(3):1900389. doi:10.1002/SOLR.201900389

140.   Xu J, Voznyy O, Comin R, et al. Crosslinked Remote-Doped Hole-Extracting Contacts Enhance Stability under Accelerated Lifetime Testing in Perovskite Solar Cells. *Adv Mater*. 2016;28(14):2807-2815. doi:10.1002/ADMA.201505630

141.   Wu J, Hu M, zhang L, et al. Fluorinated Cross-linkable and Dopant-free hole transporting materials for efficient and stable perovskite solar cells. *Chem Eng J*. 2021;422:130124. doi:10.1016/J.CEJ.2021.130124

142.   Zhang Y, Kou C, Zhang J, et al. Crosslinked and dopant free hole transport materials for efficient and stable planar perovskite solar cells. *J Mater Chem A*. 2019;7(10):5522-5529. doi:10.1039/C8TA12060A

143.   Zhang C, Liao Q, Chen J, et al. Thermally Crosslinked Hole Conductor Enables Stable Inverted Perovskite Solar Cells with 23.9% Efficiency. *Adv Mater*. 2023;2209422:2209422. doi:10.1002/ADMA.202209422

144.   Vaitukaityte D, Wang Z, Malinauskas T, et al. Efficient and Stable Perovskite Solar Cells Using Low-Cost Aniline-Based Enamine Hole-Transporting Materials. *Adv Mater*. 2018;30(45):1803735. doi:10.1002/adma.201803735

145.   Yuan D, Tian L, Li Z, et al. Solar Thermo-coupled Electrochemical Oxidation of Aniline in Wastewater for the Complete Mineralization beyond an Anodic Passivation Film. *Sci Rep*. 2018;8(1):1-12. doi:10.1038/s41598-018-21473-z

146.   Matsui T, Petrikyte I, Malinauskas T, et al. Additive-Free Transparent Triarylamine-Based Polymeric Hole-Transport Materials for Stable Perovskite Solar Cells. *ChemSusChem*. 2016;9(18):2567-2571. doi:10.1002/CSSC.201600762

147.   Osedach TP, Andrew TL, Bulović V. Effect of synthetic accessibility on the commercial viability of organic photovoltaics. *Energy Environ Sci*. 2013;6(3):711-718. doi:10.1039/C3EE24138F

148.   Correa-Baena JP, Abate A, Saliba M, et al. The rapid evolution of highly efficient perovskite solar cells. *Energy Environ Sci*. 2017;10(3):710-727. doi:10.1039/C6EE03397K

149.   Malinauskas T, Tomkute-Luksiene D, Sens R, et al. Enhancing thermal stability and lifetime of solid-state dye-sensitized solar cells via molecular engineering of the hole-transporting material spiro-OMeTAD. *ACS Appl Mater Interfaces*. 2015;7(21):11107-11116. doi:10.1021/am5090385

150.   Vaitukaityte D, Momblona C, Rakstys K, et al. Cut from the Same Cloth: Enamine-Derived Spirobifluorenes as Hole Transporters for Perovskite Solar Cells. *Chem Mater*. 2021;33(15):6059-6067. doi:10.1021/acs.chemmater.1c01486

151.   Daskeviciute S, Momblona C, Rakstys K, et al. Fluorene-based enamines as low-cost and dopant-free hole transporting materials for high performance and stable perovskite solar cells. *J Mater Chem A*. 2021;9(1):301-309. doi:10.1039/d0ta08452b

152.   Rakstys K, Saliba M, Gao P, et al. Highly Efficient Perovskite Solar Cells Employing an Easily Attainable Bifluorenylidene-Based Hole-Transporting Material. *Angew Chemie Int Ed*. 2016;55(26):7464-7468. doi:10.1002/ANIE.201602545

153. Liao YL, Hung WY, Hou TH, Lin CY, Wong KT. Hole mobilities of 2,7- And 2,2-disubstituted 9,9′-spirobifluorene- based triaryldiamines and their application as hole transport materials in OLEDs. *Chem Mater*. 2007;19(25):6350-6357. doi:10.1021/CM702230E

154. Qiu J, Liu H, Li X, Wang S. Position effect of arylamine branches on pyrene-based dopant-free hole transport materials for efficient and stable perovskite solar cells. *Chem Eng J*. 2020;387:123965. doi:10.1016/J.CEJ.2019.123965

155. Liu P, Xu B, Hua Y, et al. Design, synthesis and application of a π-conjugated, non-spiro molecular alternative as hole-transport material for highly efficient dye-sensitized solar cells and perovskite solar cells. *J Power Sources*. 2017;344:11-14. doi:10.1016/J.JPOWSOUR.2017.01.092

156. Vaitukaityte D, Truong MA, Rakstys K, et al. Molecular Engineering of Enamine-Based Hole-Transporting Materials for High-Performing Perovskite Solar Cells: Influence of the Central Heteroatom. *Sol RRL*. 2022;6(11):1-8. doi:10.1002/solr.202200590

157. Pham HD, Xianqiang L, Li W, Manzhos S, Kyaw AKK, Sonar P. Organic interfacial materials for perovskite-based optoelectronic devices. *Energy Environ Sci*. 2019;12(4):1177-1209. doi:10.1039/C8EE02744G

158. Vasilopoulou M, Fakharuddin A, Coutsolelos AG, et al. Molecular materials as interfacial layers and additives in perovskite solar cells. *Chem Soc Rev*. 2020;49(13):4496-4526. doi:10.1039/C9CS00733D

159. Wang W, Zhou J, Tang W. Design of dopant-free small molecular hole transport materials for perovskite solar cells: a viewpoint from defect passivation. *J Mater Chem A*. 2022;10(3):1150-1178. doi:10.1039/D1TA10388A

160. Wang Y, Wu N, Zhang X, et al. Effects of Heteroatom and Extending the Conjugation on Linear Hole-Transporting Materials for Perovskite Solar Cells. *ACS Appl Energy Mater*. Published online 2022. doi:10.1021/ACSAEM.2C01267

161. García-Benito I, Zimmermann I, Urieta-Mora J, et al. Heteroatom Effect on Star-Shaped Hole-Transporting Materials for Perovskite Solar Cells. *Adv Funct Mater*. 2018;28(31):1801734. doi:10.1002/ADFM.201801734

162. Sun X, Li Z, Yu X, et al. Efficient Inverted Perovskite Solar Cells with Low Voltage Loss Achieved by a Pyridine-Based Dopant-Free Polymer Semiconductor. *Angew Chemie Int Ed*. 2021;60(13):7227-7233. doi:10.1002/ANIE.202016085

163. Chen W, Shi Y, Wang Y, et al. N-type conjugated polymer as efficient electron transport layer for planar inverted perovskite solar cells with power conversion efficiency of 20.86%. *Nano Energy*. 2020;68:104363. doi:10.1016/J.NANOEN.2019.104363

164. Zhang J, Sun Q, Chen Q, et al. Dibenzo[b,d]thiophene-Cored Hole-Transport Material with Passivation Effect Enabling the High-Efficiency Planar p–i–n Perovskite Solar Cells with 83% Fill Factor. *Sol RRL*. 2020;4(3):1900421. doi:10.1002/SOLR.201900421

165. Yang J, Huang J, Zhang C, et al. Isomeric Dithienothiophene-Based Hole Transport Materials: Role of Sulphur Atoms Positions on Photovoltaic Performance of Inverted Perovskite Solar Cells. *Adv Funct Mater*. 2022;32(41):2206311. doi:10.1002/ADFM.202206311

166. Li MH, Sun TG, Shao JY, Wang YD, Hu JS, Zhong YW. A sulfur-rich small molecule as a bifunctional interfacial layer for stable perovskite solar cells with efficiencies exceeding 22%. *Nano Energy*. 2021;79:105462. doi:10.1016/J.NANOEN.2020.105462

167. Zhang X, Liu X, Wu N, et al. Heteroatom engineering on spiro-type hole transporting materials for perovskite solar cells. *J Energy Chem*. 2022;67:19-26. doi:10.1016/j.jechem.2021.09.046

168. Urieta-Mora J, García-Benito I, Molina-Ontoria A, Martín N. Hole transporting materials for perovskite solar cells: a chemical approach. *Chem Soc Rev*. 2018;47(23):8541-8571. doi:10.1039/c8cs00262b

169. Zheng X, Hou Y, Bao C, et al. Managing grains and interfaces via ligand anchoring enables 22.3%-efficiency inverted perovskite solar cells. *Nat Energy 2020 52*. 2020;5(2):131-140. doi:10.1038/s41560-019-0538-4

170. Vaitukaitytė D, Al-Ashouri A, Daškevičienė M, et al. Enamine-Based Cross-Linkable Hole-Transporting Materials for Perovskite Solar Cells. *Sol RRL*. 2021;5(1):1-6. doi:10.1002/solr.202000597

171. Lee KM, Chiu WH, Tsai YH, Wang CS, Tao YT, Lin YD. High-performance perovskite solar cells based on dopant-free hole-transporting material fabricated by a thermal-assisted blade-coating method with efficiency exceeding 21%. *Chem Eng J*. 2022;427:131609. doi:10.1016/J.CEJ.2021.131609

172. Wang Y, Duan L, Zhang M, et al. PTAA as Efficient Hole Transport Materials in Perovskite Solar Cells: A Review. *Sol RRL*. 2022;6(8):2200234. doi:10.1002/SOLR.202200234

173. Li Z, Zhu Z, Chueh CC, Luo J, Jen AKY. Facile Thiol-Ene Thermal Crosslinking Reaction Facilitated Hole-Transporting Layer for Highly Efficient and Stable Perovskite Solar Cells. *Adv Energy Mater*. 2016;6(21). doi:10.1002/aenm.201601165

174. Abraham S, Ganesh GPT, Varughese S, Deb B, Joseph J. Cross-Linkable Fluorene-Diphenylamine Derivatives for Electrochromic Applications. *ACS Appl Mater Interfaces*. 2015;7(45):25424-25433. doi:10.1021/acsami.5b08218

6. CURRICULUM VITAE

Deimantė Vaitukaitytė
deimante.vaitukaityte@ktu.lt
Date of birth: 1994-11-19
Nationality: Lithuanian

Education:

2001–2011	Vilkaviškis primary school
2011–2013	Vilkaviškis "Aušra" gymnasium
2013–2017	Kaunas University of Technology, Bachelor's degree in Chemistry
2017–2019	Kaunas University of Technology, Master's degree in Chemistry
2019–present	Kaunas University of Technology, PhD in Chemistry

Work experience:

2017 02 01–2017 02 28	Ltd. "Cosmoway", Laboratory Trainee
2019 01 10–2019 04 11	Ltd. "Dirbtinis pluoštas", Laboratory Technician
2019 04 15–2019 06 07	Ltd. "Santonika", Quality Assurance Manager
2020 03 09–2022 12 31	Kaunas University of Technology, Project "2D perovskites for highly efficient 2D/3D perovskite solar cells with improved stability" Junior Researcher
2020 04 24–2023 04 30	Kaunas University of Technology, Project "Functional molecules for the new generation of solar cells: from synthesis to commercialization" Junior Researcher
2020 07 20–2023 08 31	Kaunas University of Technology, Project "Effective and sustainable charge transporting molecules for energy efficiency technologies" Junior Researcher

Scientific work:

2015, 2017, 2018	3 times participant of the Research Council of Lithuania project "Students scientific practice"
2016–present	Research work in Prof. Dr. Vytautas Getautis scientific group: synthesis and characterization of organic semiconductors for novel applications in perovskite solar cells

Languages:

Lithuanian (mother tongue), English (C1).

Awards:

2022 06 02	Woman in Renewable Energy (WiRE) Best Poster Award at EMRS (European Materials Research Society)

| 2023 03 23 | Laureate of the 11th conference of young scientists "Interdisciplinary research in physical and technological sciences" |

Scholarships:

2015	Rector's promotional scholarship for outstanding academic and study results
2016	Monthly faculty's incentive scholarship
2018–2019	University's talent scholarship for outstanding academic and study results, 2 times
2020–2022	KTU most active PhD student's scholarship, 3 times
2020	Lithuanian Research Council PhD student's scholarship for academic achievements

7. LIST OF AUTHOR'S PUBLICATIONS AND CONFERENCES

Publications in peer-reviewed journals

1. **Vaitukaityte, Deimante**; Truong, Minh Anh; Rakstys, Kasparas; Murdey, Richard; Funasaki, Tsukasa; Yamada, Takumi; Kanemitsu, Yoshihiko; Jankauskas, Vygintas; Getautis, Vytautas; Wakamiya, Atsushi. Molecular engineering of enamine-based hole-transporting materials for high-performing perovskite solar cells: influence of the central heteroatom // Solar RRL. Weinheim : Wiley. ISSN 2367-198X. 2022, vol. 6, iss. 11, art. no. 2200590, p. 1-8. DOI: 10.1002/solr.202200590. [Science Citation Index Expanded (Web of Science); Scopus] [IF: 9,173; AIF: 7,258; IF/AIF: 1,263; Q1 (2021, InCites JCR SCIE)] [M.kr.: N 003] [Indėlis: 0,100]

2. **Vaitukaityte, Deimante**; Momblona, Cristina; Rakstys, Kasparas; Sutanto, Albertus Adrian; Ding, Bin; Igci, Cansu; Jankauskas, Vygintas; Gruodis, Alytis; Malinauskas, Tadas; Asiri, Abdullah M.; Dyson, Paul J.; Getautis, Vytautas; Nazeeruddin, Mohammad Khaja. Cut from the same cloth: enamine-derived spirobifluorenes as hole transporters for Perovskite solar cells // Chemistry of materials. Washington, DC : American chemical society. ISSN 0897-4756. eISSN 1520-5002. 2021, vol. 33, iss. 15, p. 6059-6067. DOI: 10.1021/acs.chemmater.1c01486. [Science Citation Index Expanded (Web of Science); Scopus; MEDLINE] [IF: 10,508; AIF: 7,238; IF/AIF: 1,451; Q1 (2021, InCites JCR SCIE)] [M.kr.: N 003] [Indėlis: 0,088]

3. **Vaitukaitytė, Deimantė**; Al-Ashouri, Amran; Daškevičienė, Marytė; Kamarauskas, Egidijus; Nekrasovas, Jonas; Jankauskas, Vygintas; Magomedov, Artiom; Albrecht, Steve; Getautis, Vytautas. Enamine-based cross-linkable hole-transporting materials for perovskite solar cells // Solar RRL. Weinheim : Wiley-VCH. ISSN 2367-198X. 2021, vol. 5, iss. 1, art. no. 2000597, p. 1-6. DOI: 10.1002/solr.202000597. [Science Citation Index Expanded (Web of Science); Scopus] [IF: 9,173; AIF: 7,257; IF/AIF: 1,264; Q1 (2021, InCites JCR SCIE)] [M.kr.: N 003] [Indėlis: 0,112]

4. **Vaitukaityte, Deimante**; Wang, Zhiping; Malinauskas, Tadas; Magomedov, Artiom; Bubniene, Giedre; Jankauskas, Vygintas; Getautis, Vytautas; Snaith, Henry J. Efficient and stable perovskite solar cells using low-cost aniline-based enamine hole-transporting materials // Advanced materials. Weinheim : Wiley. ISSN 0935-9648. eISSN 1521-4095. 2018, vol. 30, iss. 45, art. no. 1803735, p. 1-7. DOI: 10.1002/adma.201803735. [Science Citation Index Expanded (Web of Science); Scopus; MEDLINE] [IF: 25,809; AIF: 5,477; IF/AIF: 4,712; Q1 (2018, InCites JCR SCIE)] [M.kr.: N 002, N 003] [Indėlis: 0,125]

List of conferences

1. Thermally Cross-Linkable Fluorene-Derived Hole Transporting Materials for the Application in Perovskite Solar Cells (poster presentation) // 15th International Conference on Hybrid and Organic Photovoltaics, June 12–14, 2023, London, United Kingdom.

2.   Molecular Engineering of Enamine-Based Hole Transporting Materials for Efficient Perovskite Solar Cells (oral presentation) // 11th conference of young scientists "Interdisciplinary research in physical and technological sciences", March 23rd, 2023, Vilnius, Lithuania.

3.   Molecular Engineering of Enamine-Based Hole Transporting Materials for High-Performing Perovskite Solar Cells: Influence of the Central Heteroatom (oral presentation) // Chemistry and chemical technology: proceedings of international scientific conference, October 14th, 2022, Kaunas, Lithuania.

4.   Engineering the Central Heteroatom of Hole Transporting Enamines for Efficient Perovskite Solar Cells (oral presentation) // 23rd International Conference on Photochemical Conversion and Storage Energy, August 2–5, 2022, Lausanne, Switzerland.

5.   Ambipolar charge transport in anthraquinone-based semiconductors (poster presentation) // Balticum organicum syntheticum [BOS] 2022: in memory of Prof. Victor Snieckus: July 3–6, 2022, Vilnius, Lithuania.

6.   Efficient Perovskite Solar Cells using Enamine-derived Hole Transporting Materials (poster presentation) // European Materials Research Society 2022 Spring Meeting, May 30–June 3, 2022, virtual conference.

7.   Engineering the Central Heteroatom of Hole Transporting Enamines for Efficient Perovskite Solar Cells (poster presentation) // International Conference on Hybrid and Organic Photovoltaics, May 19–26, 2022, Valencia, Spain.

8.   Enamine-based spirobifluorenes as hole transporting materials for perovskite solar cells (poster presentation) // European Materials Research Society Spring Meeting, May 31–June 4, 2021, virtual conference.

9.   Enamine-derived Spirobifluorenes as Stable Hole Transporters for Perovskite Solar Cells (poster presentation) // HOPV21 13th International Conference on Hybrid and Organic Photovoltaics, May 24–28, 2021, virtual conference.

10.   Enamine-derived spirobifluorenes as hole transporting materials for perovskite solar cells (oral presentation) // Open readings 2021: 64th international conference for students of physics and natural sciences, March 16–19, 2021, Vilnius, Lithuania.

11.   Cross-linkable fluorene-based enamines as hole transporting materials for perovskite solar cells (poster presentation) // Functional materials and nanotechnologies: [13th international conference], FM&NT-2020: virtual, November 23–26, 2020, Vilnius, Lithuania.

12.   Cross-linkable Fluorene-based Enamines as Hole Transporting Materials for Perovskite Solar Cells (poster presentation) // Online nanoGe Fall Meeting 20, October 20–23, 2020, virtual conference.

13.   Aniline-based Enamine Hole Transporting Materials for Efficient and Stable Perovskite Solar Cells (poster presentation) // HOPV20 12th International Conference on Hybrid and Organic Photovoltaics, May 26–29, 2020, virtual conference.

14.   Efficient cross-linkable fluorene-based enamines as hole transporting layers (poster presentation) // Open readings 2019: 62nd international conference for students of physics and natural sciences, March 19–22, 2019, Vilnius, Lithuania.

15. Efficient enamine hole transporting materials for perovskite solar cells from inexpensive aniline (oral presentation) // Chemistry & Chemical Technology, May 18th, 2018, Klaipeda, Lithuania.

16. Enamine based hole transporting materials obtained from aniline derivatives (oral presentation) // Mathematics and natural sciences: theory and applications, April 19th, 2018, Kaunas, Lithuania.

17. Enamine based hole transporting materials obtained from aniline derivatives (oral presentation) // Chemistry & Chemical Technology, April 27th, 2017, Kaunas, Lithuania.

8.   AUTHOR'S PUBLICATIONS

Efficient and Stable Perovskite Solar Cells Using Low-Cost Aniline-Based Enamine Hole-Transporting Materials

Deimante Vaitukaityte, Zhiping Wang,* Tadas Malinauskas, Artiom Magomedov, Giedre Bubniene, Vygintas Jankauskas, Vytautas Getautis,* and Henry J. Snaith*

Metal-halide perovskites offer great potential to realize low-cost and flexible next-generation solar cells. Low-temperature-processed organic hole-transporting layers play an important role in advancing device efficiencies and stabilities. Inexpensive and stable hole-transporting materials (HTMs) are highly desirable toward the scaling up of perovskite solar cells (PSCs). Here, a new group of aniline-based enamine HTMs obtained via a one-step synthesis procedure is reported, without using a transition metal catalyst, from very common and inexpensive aniline precursors. This results in a material cost reduction to less than 1/5 of that for the archetypal spiro-OMeTAD. PSCs using an enamine V1091 HTM exhibit a champion power conversion efficiency of over 20%. Importantly, the unsealed devices with V1091 retain 96% of their original efficiency after storage in ambient air, with a relative humidity of 45% for over 800 h, while the devices fabricated using spiro-OMeTAD dropped down to 42% of their original efficiency after aging. Additionally, these materials can be processed via both solution and vacuum processes, which is believed to open up new possibilities for interlayers used in large-area all perovskite tandem cells, as well as many other optoelectronic device applications.

During the past several years, perovskite solar cell (PSC) technology has evolved from a scientific curiosity to a major research subject in the field of photovoltaics. In that short period of time, they have gained recognition as one of the most promising photovoltaic technologies and managed to demonstrate

D. Vaitukaityte, Dr. T. Malinauskas, A. Magomedov, Dr. G. Bubniene, Prof. V. Getautis
Department of Organic Chemistry
Kaunas University of Technology
Radvilenu pl. 19, Kaunas 50254, Lithuania
E-mail: vytautas.getautis@ktu.lt
Dr. Z. Wang, Prof. H. J. Snaith
Clarendon Laboratory
Department of Physics
University of Oxford
Parks Road, Oxford OX1 3PU, UK
E-mail: zhiping.wang@physics.ox.ac.uk; henry.snaith@physics.ox.ac.uk
Dr. V. Jankauskas
Department of Solid State Electronics
Vilnius University
Sauletekio 9, Vilnius 10222, Lithuania

The ORCID identification number(s) for the author(s) of this article can be found under https://doi.org/10.1002/adma.201803735.

remarkable achievements in the power conversion efficiency (PCE) exceeding 22%[1] and rivaling other thin-film technologies as well as silicon photovoltaic devices.[2] The remarkable device performances can be attributed to excellent optoelectronic properties of metal halide perovskites, such as low exciton binding energy,[3] high charge carrier mobility,[4,5] high absorption coefficient,[6,7] and long carrier diffusion length.[8,9] To date, most of the high-efficiency negative(n)-intrinsic(i)-positive(p) structured PSCs are based on either 2,2′,7,7′-tetrakis(N,N-di-p-methoxyphenylamine)-9-9′-spirobifluorene (spiro-OMeTAD) or poly[bis(4-phenyl)(2,4,6-trimethylphenyl)amine] (PTAA) hole-transporting materials (HTMs), both of which are very expensive.[10–12] The generated high cost is mainly due to the following reasons: i) multistep synthesis; ii) complicated purification procedures[13]; iii) sublimation steps for purification; and iv) use of transition metal catalysts.

For step iv, tiny amount of the catalysts, i.e., palladium, would remain in the grained HTMs, which may serve as traps that deteriorate the charge-transporting properties of the synthesized HTMs and result in poor device performance.[14,15] To remove the catalyst residue, sophisticated purification procedures, such as sublimation or repeated column chromatography, are typically required, which would greatly reduce the material yield and therefore further increase the final costs.

Aniline, as one of the most basic and widely used precursors in chemical industry, has been used in synthesis of numerous chemicals and is extremely cheap and produced on a vast scale (over 7 million tons per year).[16] Use of such a low cost and readily available reagent as a starting material could be beneficial from both practical and commercial points of view.

Herein, we synthesize enamine-based HTMs using aniline precursors and further adopt a cost-effective single step, transition-metal-catalysts-free route which we established previously.[17] We demonstrate that PSCs with the synthesized HTMs exhibit comparable high efficiencies and greatly enhanced ambient-air stability in contrast to the cells with the state-of-the-art spiro-OMeTAD HTM.

We synthesize the HTMs by reacting the aniline precursor with 2,2-bis(4-methoxyphenyl)acetaldehyde in the presence of (+/−)camphor sulfonic acid (CSA). Depending on the ration

90

of the reagents, enamines with two (**V1092**) or three (**V1091**) diphenylethenyl groups have been isolated (**Scheme 1**a). Additionally, aniline derivatives with a methoxy group in the *para*-position (**V1056**) and 3,5-dimethyl-substituted analogue (**V1102**) were also used for the synthesis (Scheme 1b). The methoxy group serves as an additional donor and blocks the *para*-position of the phenyl ring. The 3,5-dimethylaniline was chosen due to its beneficial influence on device performance.[18] Different from the synthesis of the conventional HTMs used in PSCs,[19] we do not need any transition metal catalysts during

the synthesis of these enamines, and the problematic catalysts-residual-induced recombination[20–22] as mentioned above is no longer a major concern. Another advantage of the catalyst-free synthesis is that the purification of the HTMs is largely simplified and oftentimes a basic crystallization is sufficient. The detailed synthesis procedure and analysis can be found in the Supporting Information.

To assess the cost-effectiveness of the HTMs, we performed material cost estimations for the synthesis of **V1056** and **V1091** based on the procedure established by Osedach et al. (Tables S1 and S2, Supporting Information).[23] We estimate the material cost is ≈16 $ g^{-1} for **V1091** and ≈8 $ g^{-1} for **V1056** which are less than 1/5 of the cost of the reference spiro-OMeTAD (≈92 $ g^{-1}).[24]

To examine the thermal stability of the target materials, we applied thermogravimetric (TGA) measurement as we show the data in **Figure 1**, and give full characteristics in **Table 1**. We find that all the HTM molecules exhibit excellent thermal stability. Interestingly, we observe a rapid weight loss during TGA experiments, which indicates that the HTMs undergo sublimation rather than thermal decomposition. This suggests that the HTMs could also be processed by vacuum process which would further widen its applications.

Differential scanning calorimetry (DSC) analysis demonstrated that the relatively smaller molecules with two diphenylethenyl fragments (**V1056** and **V1092**) have a stronger tendency of crystallization than the larger analogues with three diphenylethenyl fragments (**V1091** and **V1102**). Aniline derivative **V1092** shows a relatively high melting temperature (T_m) of 251 °C (Figure 1b); during the second heating, a glass transition (T_g) is observed at 80 °C followed by recrystallization at 129 °C. The additional methoxy functional group in **V1056** introduces a certain degree of disorder into the molecule and lowers the melting temperature considerably to 190 °C. It also contributes to the stability of the amorphous state; the material no longer crystallizes during second heating and only T_g at 78 °C is observed (Figure 1c). The third diphenylethenyl moiety in the *para*-position of the phenyl ring in **V1091** even further hampers crystallization and molecule becomes fully amorphous; it also adds some additional structural bulk, increasing T_g to 109 °C (Figure 1d). Similar picture is observed for **V1102** (Figure 1e), although, glass transition temperature is lower, most likely methyl groups at the 3,5-positions of the phenyl ring contribute to the steric hindrance of the molecule.

The ultraviolet–visible (UV–vis) absorption spectra of the aniline-based enamines containing two diphenylethenyl groups (**V1056**, **V1092**) showed a bathochromic shift (≈50 nm) compared with the unsubstituted aniline (**Figure 2**a). The methoxy group in **V1056** has a negligible effect on the size of the π-conjugated system. A third diphenylethenyl group in **V1091**, however, noticeably increases its size, resulting in an ≈50 nm bathochromic shift. This confirms that the amine condensation with 2,2-bis(4-methoxy-phenyl)acetaldehyde offers a simple route toward enlarged conjugated system. In fact, the sizes of the π-conjugated system of the spiro-OMeTAD and tri-substituted aniline **V1091** are similar. With the addition of the methyl groups in the 3,5-positions of the phenyl ring, **V1102** shows significant changes in the overall size of the π-conjugated system as compared with **V1091**, resulting a hypsochromic shift of ≈14 nm. It is likely that the steric hindrance at the 4-position of the
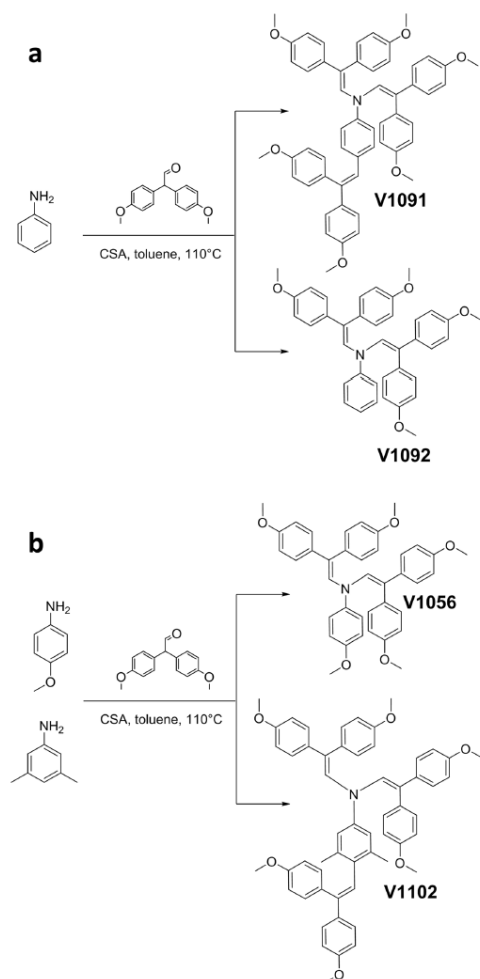
Scheme 1. A single-step synthesis of the HTMs: a) **V1091**, **V1092**; b) **V1056**, **V1102**.

91

ADVANCED
SCIENCE NEWS
www.advancedsciencenews.com

ADVANCED
MATERIALS
www.advmat.de
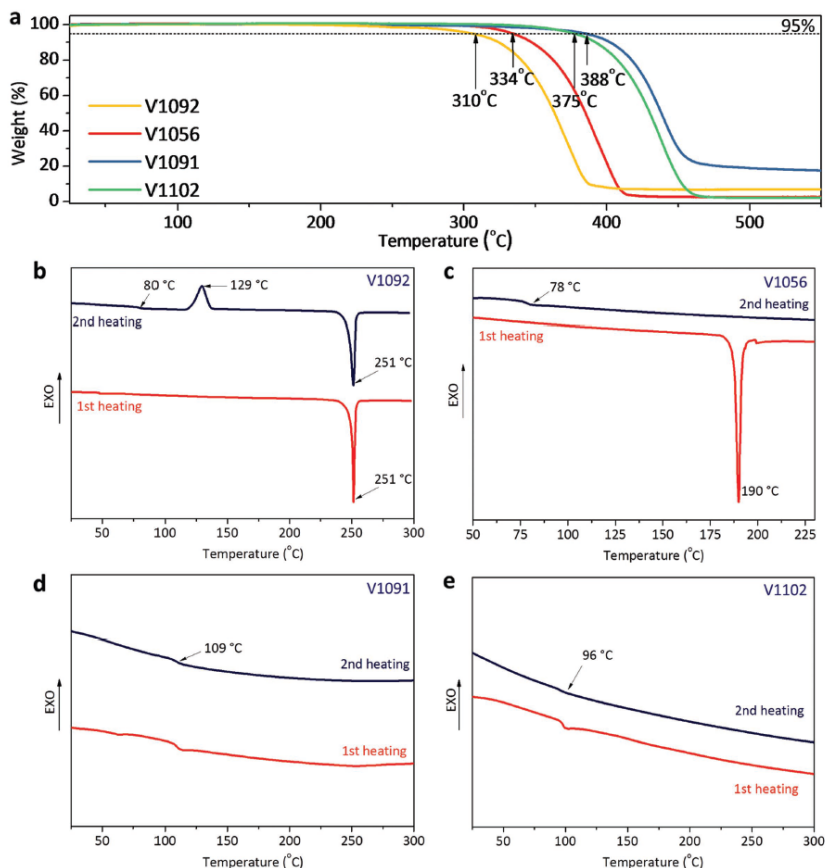
Figure 1. a) TGA heating curves of **V1092**, **V1056**, **V1091**, and **V1102** (heating rate 10 K min⁻¹). b–e) DSC heating curves of **V1092** (b), **V1056** (c), **V1091** (d), and **V1102** (e) (heating and cooling rate 10 K min⁻¹).

phenyl ring is increased by the presence of the methyl groups at the 3,5-positions. As a consequence, diphenylethenyl moiety becomes more twisted out of the plane.

Table 1. Thermal properties of synthesized HTMs and spiro-OMeTAD.

HTM	T_m [°C]	T_{recr} [°C]	T_g [°C][a]	T_{dec} [°C]
V1056	190	–	78	334
V1091	–	–	109	388
V1092	251	129	80	310
V1102	–	–	96	375
spiro-OMeTAD	245	–	126	449

[a]Determined by DSC: scan rate, 10 K min⁻¹; N₂ atmosphere; second run.

Photoelectron spectroscopy in air method was used to measure ionization potentials (I_p) of the investigated HTMs (Figure S1, Supporting Information; **Table 2**). Aniline derivative containing two diphenylethenyl groups (**V1092**) exhibits the highest I_p value among all HTMs investigated in this work. Additional electron donating dipheneylethenyl (**V1091**) or methoxy (**V1056**) group lowers the I_p values of the HTMs by ≈0.1 eV. With the addition of methyl groups at the 3,5-positions of the phenyl ring in **V1102**, we do not see an obvious change in I_p. On the whole, the I_p values of the synthesized HTMs are slightly higher than spiro-OMeTAD, but still suitable for hole extraction in PSCs.[2]

The charge-transport properties of the investigated HTMs were measured using xerographic time-of-flight (XTOF) technique (Figure 2b) and we show the results in Table 2. **V1056**, with

ADVANCED
SCIENCE NEWS
www.advancedsciencenews.com

ADVANCED
MATERIALS
www.advmat.de
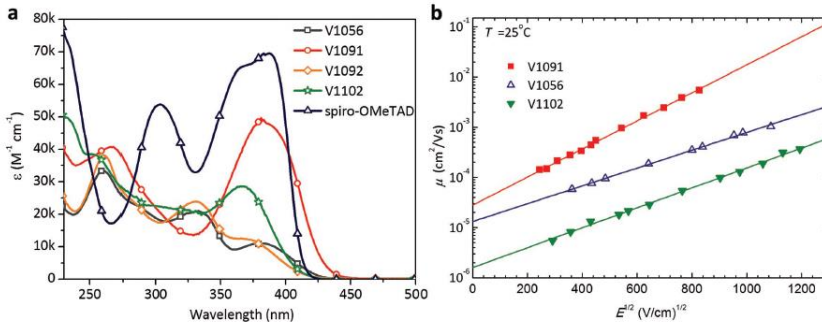
Figure 2. a) UV–vis absorption spectra of **V1056**, **V1091**, **V1092**, **V1102**, and spiro-OMeTAD in THF ($c = 10^{-4}$ M). b) Electric-field dependencies of the hole drift mobilities in films of **V1056**, **V1091**, and **V1102**.

the methoxy group at the *para*-position of a phenyl ring, shows a similar hole mobility as compared to spiro-OMeTAD. In contrast, **V1091**, containing three diphenylethenyl moieties, displays significantly better hole drift mobilities at high electric fields. The presence of the methyl groups at the 3,5-positions of the phenyl ring in **V1102** results in reduced charge mobility.

To study influence of the methyl groups on the geometry of the **V1102**, molecular geometries of the **V1091** and **V1102** were optimized via density functional theory (DFT) calculations with B3LYP/def2-SVP (vacuum) level of theory. Dihedral angle between phenyl plane of aniline and double bond increased from 24.6° in **V1091** to 58.6° in **V1102** after addition of two methyl groups (Figure 3). Generally, increased 3D structural complexity of organic molecules, i.e., decreased planarity, would disturb intermolecular π–π packing and leads to difficulties in intermolecular charge carrier hopping.[25–27] We, therefore, observed decreased mobility in the **V1102** as compared to **V1091**. This is also in good agreement with the DSC results where we observed a higher glass transition temperature for the **V1091** than the **V1102**. Furthermore, from highest occupied molecular orbital (HOMO) of the corresponding molecules (**Figure 3**), we see that a lower planarity hinders delocalization of the electrons in **V1102** over double bond and results in a smaller π-conjugated system as compared to the **V1091**. Therefore, we would expect a smaller absorption coefficient for the

V1102 than that for the **V1091**. This is consistent with the UV–vis absorption measurement (Figure 2a).

We now proceed to test the synthesized HTMs in planar heterojunction PSCs (with a device structure: fluorine-doped tin oxide (FTO)/SnO₂/perovskite/HTM/Au). A mixed-cation lead mixed-halide $FA_{0.83}Cs_{0.17}Pb(I_{0.9}Br_{0.1})_3$ perovskite was adopted as a photoactive layer.[28,29] The current-density–voltage (J–V) characteristics were measured under a simulated AM 1.5 G (100 mW cm⁻²) sunlight and results are presented in **Figure 4**a and **Table 3**, while device statistics can be seen
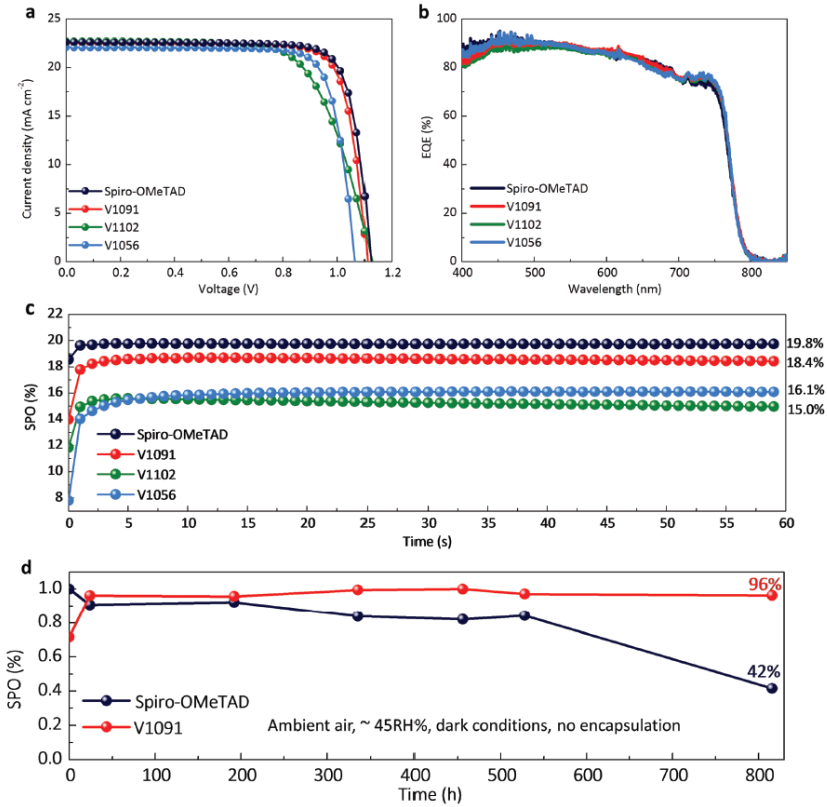
Table 2. UV–vis absorbance, I_p, and hole mobility investigated HTMs and spiro-OMeTAD.

ID	λ_{max}^{abs} [nm]	I_p [eV]	$\mu_0^{a)}$ [cm² V⁻¹ s⁻¹]	$\mu^{b)}$ [cm² V⁻¹ s⁻¹]	$\alpha^{c)}$ [cm^{1/2} V^{-1/2}]
V1056	333, 384	5.19	1.3×10^{-5}	7.8×10^{-4}	0.0041
V1091	381	5.17	2.8×10^{-5}	1.7×10^{-2}	0.0046
V1092	331, 370	5.30	–	–	–
V1102	367	5.16	1.6×10^{-6}	1.5×10^{-4}	0.0064
spiro-OMeTAD	387	5.00	4.1×10^{-5}	5.0×10^{-4}	0.0031

a)Mobility value at zero field strength; b)Mobility value at 6.4×10^5 V cm⁻¹ field strength; c)Poole–Frenkel parameter (α).
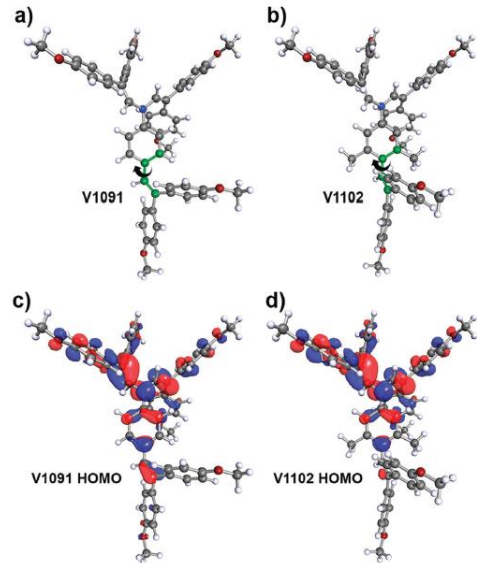
Figure 3. a,b) Optimized geometries of the **V1091** (a) and **V1102** (b). c,d) HOMO molecular orbitals of the **V1091** (c) and **V1102** (d).

**ADVANCED
SCIENCE NEWS**
www.advancedsciencenews.com

**ADVANCED
MATERIALS**
www.advmat.de

Figure 4. a) J–V characteristics of the best performing PSC devices using V1091, V1102, V1056, and spiro-OMeTAD. b) Corresponding EQE spectra as a function of the wavelength of monochromatic light. c) SPO over time of the devices containing investigated HTMs and spiro-OMeTAD. d) Decay of SPO of devices with spiro-OMeTAD (navy) and **V1091** (red). The device structure is FTO/SnO$_2$/perovskite/HTM/Au. The devices are in ambient air with a relative humidity of $\approx$ 45% under dark conditions without encapsulation.

Table 3. Summary of solar cell characteristics.

ID		J_{sc} [mA cm^{-2}]	V_{oc} [V]	FF	PCE [%]
spiro-OMeTAD	Average	22.6 ± 0.24	1.11 ± 0.03	0.75 ± 0.03	18.4 ± 1.0
	Champion	22.6	1.12	0.80	20.2
V1091	Average	22.0 ± 0.27	1.11 ± 0.05	0.77 ± 0.03	17.0 ± 2.5
	Champion	22.5	1.11	0.81	20.2
V1102	Average	22.0 ± 0.64	1.05 ± 0.07	0.59 ± 0.06	13.5 ± 2.5
	Champion	22.7	1.13	0.68	17.6
V1056	Average	22.1 ± 0.15	1.03 ± 0.03	0.78 ± 0.05	17.5 ± 1.2
	Champion	22.1	1.07	0.79	18.7

94

**ADVANCED
SCIENCE NEWS**
www.advancedsciencenews.com

**ADVANCED
MATERIALS**
www.advmat.de

in Figure S2 in the Supporting Information. As determined from the forward bias (FB) to short-circuit (SC) current–voltage scan, the device using the **V1102** and **V1056** shows a champion efficiency of 17.6% and 18.7%, respectively, which is slightly lower than the PCE of 20.2% for the control device using the spiro-OMeTAD. In contrast, the PSC using **V1091** exhibits a high efficiency of 20.2% with a J_{sc} of 22.5 mA cm^{-2}, a V_{oc} of 1.11 V, and a FF of 0.81. The devices containing investigated HTMs showed very similar external quantum efficiency (EQE) spectra to that of the spiro-OMeTAD device (Figure 4b), which is consistent with the similar J_{sc} observed in the J–V scans. Due to the hysteretic behavior of PSCs, a stabilized efficiency measurement was performed to accurately access the performance of the PSC (Figure 4c). By holding the cells at a fixed maximum power point FB voltage, we measure the stabilized power output (SPO) over time, achieving a stabilized efficiency of 19.8% for the control device and 18.4% for the **V1091** device. Furthermore, we find that device performance varies significantly with the thickness of the spiro-OMeTAD, as shown in Figure S6 in the Supporting Information. In contrast, the performance of the V1091 devices is less sensitive to the thickness of V1091. We note that when increasing the thickness of the V1091, we need a longer time for oxidation to reach the peak efficiency. Understanding and accelerating the oxidization process is a subject of ongoing study. On the whole, PSC containing **V1091** and spiro-OMeTAD showed comparable performance.

To access the device stability using the HTMs, we aged nonencapsulated high-efficiency devices with the **V1091** and spiro-OMeTAD hole-transporting layers in ambient air with a relative humidity of ≈45% under dark conditions and measured under an AM 1.5 G solar simulator at different time intervals, the decay of the SPO is shown in Figure 4d. The **V1091** device showed superior stability sustaining 96% of its original efficiency after 820 h. In contrast, the SPO of the control device dropped to 42% after aging. The Li-TFSI was used as a dopant for both the **V1091** and spiro-OMeTAD. Previous studies observed that devices using the Li-TFSI doped spiro-OMeTAD show moisture instability due to the hygroscopic nature of Li-TFSI,[28,30] which can be the reason for the observed fast decay of efficiency in the control device. Surprisingly, the **V1091** molecule seems to specifically resist this Li-TFSI-induced degradation. To better understand the stability enhancement, we measured the UV–vis absorption spectra of the HTMs in solutions and thin films, as we show the results in Figure S3 in the Supporting Information. Generally, the molecules in solution do not have a particular packing, which is random. For **V1091**, we observe a bathochromic shift of absorption maximum and broadening of the spectrum when comparing the thin films with the solution, which is indicative of aggregate formation in the film.[31–33] In contrast, we do not see noticeable change in the spectra of spiro-OMeTAD solution and thin films, suggesting its random molecular packing in the thin film (Figure S4, Supporting Information). Furthermore, we carried out contact angle (θ) measurement to assess the hydrophobicity of the HTMs (Figure S5, Supporting Information). We do not see an obvious change in θ between the pristine (undoped) spiro-OMeTAD and **V1091** films. However, we surprisingly discover that with the addition of Li-TFSI and tBP dopants, the

V1091 film displays a clearly more hydrophobic surface with a θ of 71.2° than the spiro-OMeTAD film with a θ of 65.4°. Both of the improved molecular packing and a more hydrophobic surface for the V1091 film would retard the ambient moisture ingression, which directly contributed to the improved stability.

In conclusion, we have developed a new group of aniline-based HTMs obtainable via a one-step synthetic procedure from low-cost aniline starting materials without the use of expensive and problematic oraganometallic catalysts. The material costs have been greatly reduced to less than 1/5 of that for spiro-OMeTAD. PSCs using these cheap HTMs show comparable efficiency to the cells using the expensive spiro-OMeTAD HTM. Importantly, PSCs using enamine **V1091** shows significantly enhanced ambient stability in contrast to the cells using spiro-OMeTAD. The cost-effective, efficient, and stable aniline-based enamines offer great opportunities for up-scaling PSCs. Furthermore, these materials can be processed via both solution and vacuum processes, which we believe would open up possibilities for the interlayers for large-area perovskite–perovskite tandem cells as well as many other opto-electronic device applications.

Supporting Information

Acknowledgements

Conflict of Interest

The authors declare no conflict of interest.

Keywords

[1] W. S. Yang, B.-W. Park, E. H. Jung, N. J. Jeon, Y. C. Kim, D. U. Lee, S. S. Shin, J. Seo, E. K. Kim, J. H. Noh, S. I. Seok, *Science* **2017**, *356*, 1376.

[2] J.-P. Correa-Baena, A. Abate, M. Saliba, W. Tress, T. J. Jacobsson, M. Grätzel, A. Hagfeldt, *Energy Environ. Sci.* **2017**, *10*, 710.

[3] S. Park, J. H. Heo, C. H. Cheon, H. Kim, S. H. Im, H. J. Son, *J. Mater. Chem. A* **2015**, *3*, 24215.

[4] O. Malinkiewicz, A. Yella, Y. H. Lee, G. M. Espallargas, M. Graetzel, M. K. Nazeeruddin, H. J. Bolink, *Nat. Photonics* **2014**, *8*, 128.

[5] S. Kazim, M. K. Nazeeruddin, M. Gratzel, S. Ahmad, *Angew. Chem., Int. Ed.* **2014**, *53*, 2812.

[6] H.-S. Kim, C.-R. Lee, J.-H. Im, K.-B. Lee, T. Moehl, A. Marchioro, S.-J. Moon, R. Humphry-Baker, J.-H. Yum, J. E. Moser, M. Gratzel, N.-G. Park, *Sci. Rep.* **2012**, *2*, 591.

[7] N.-G. Park, *J. Phys. Chem. Lett.* **2013**, *4*, 2423.

[8] S. D. Stranks, G. E. Eperon, G. Grancini, C. Menelaou, M. J. P. Alcocer, T. Leijtens, L. M. Herz, A. Petrozza, H. J. Snaith, *Science* **2013**, *342*, 341.

[9] G. Xing, N. Mathews, S. Sun, S. S. Lim, Y. M. Lam, M. Grätzel, S. Mhaisalkar, T. C. Sum, *Science* **2013**, *342*, 344.

[10] H. Tan, A. Jain, O. Voznyy, X. Lan, F. P. García de Arquer, J. Z. Fan, R. Quintero-Bermudez, M. Yuan, B. Zhang, Y. Zhao, F. Fan, P. Li, L. N. Quan, Y. Zhao, Z.-H. Lu, Z. Yang, S. Hoogland, E. H. Sargent, *Science* **2017**, *355*, 722.

[11] Z. Yu, L. Sun, *Adv. Energy Mater.* **2015**, *5*, 1500213.

[12] K. Him, K.-G. Lima, T.-W. Lee, *Energy Environ. Sci.* **2016**, *9*, 12.

[13] T. P. I. Saragi, T. Spehr, A. Siebert, T. Fuhrmann-Lieker, J. Salbeck, *Chem. Rev.* **2007**, *107*, 1011.

[14] A. Krishna, A. C. Grimsdale, *J. Mater. Chem. A* **2017**, *5*, 16446.

[15] M. P. Nikiforov, B. Lai, W. Chen, S. Chen, R. D. Schaller, J. Strzalka, J. Maser, S. B. Darling, *Energy Environ. Sci.* **2013**, *6*, 1513.

[16] D. Yuan, L. Tian, Z. Li, H. Jiang, C. Yan, J. Dong, H. Wu, B. Wang, *Sci. Rep.* **2018**, *8*, 3103.

[17] M. Daskeviciene, S. Paek, Z. Wang, T. Malinauskas, G. Jokubauskaite, K. Rakstys, K. T. Cho, A. Magomedov, V. Jankauskas, S. Ahmad, H. J. Snaith, V. Getautis, M. K. Nazeeruddin, *Nano Energy* **2017**, *32*, 551.

[18] T. Matsui, I. Petrikyte, T. Malinauskas, K. Domanski, M. Daskeviciene, M. Steponaitis, P. Gratia, W. Tress, J.-P. Correa-Baena, A. Abate, A. Hagfeldt, M. Grätzel, M. K. Nazeeruddin, V. Getautis, M. Saliba, *ChemSusChem* **2016**, *9*, 2567.

[19] L. Calió, S. Kazim, M. Grätzel, S. Ahmad, *Angew. Chem., Int. Ed.* **2016**, *55*, 14522.

[20] K. Rakstys, M. Saliba, P. Gao, P. Gratia, E. Kamarauskas, S. Paek, V. Jankauskas, M. K. Nazeeruddin, *Angew. Chem., Int. Ed.* **2016**, *55*, 7464.

[21] M. Degbia, M. Ben Manaa, B. Schmaltz, N. Berton, J. Boucle, R. Antony, F. Tran Van, *Mater. Sci. Semicond. Process.* **2016**, *43*, 90.

[22] O. Usluer, M. Abbas, G. Wantz, L. Vignau, L. Hirsch, E. Grana, C. Brochon, E. Cloutet, G. Hadziioannou, *ACS Macro Lett.* **2014**, *3*, 1134.

[23] T. P. Osedach, T. L. Andrew, V. Bulovic, *Energy Environ. Sci.* **2013**, *6*, 711.

[24] M. L. Petrus, T. Bein, T. J. Dingemans, P. Docampo, *J. Mater. Chem. A* **2015**, *3*, 12159.

[25] Z. Wang, Y. Zhou, T. Miyadera, M. Chikamatsu, Y. Yoshida, *ACS Appl. Mater. Interfaces* **2017**, *9*, 43893.

[26] Z. Wang, T. Miyadera, T. Yamanari, Y. Yoshida, *ACS Appl. Mater. Interfaces* **2014**, *6*, 6369.

[27] Z. Wang, Y. Uemura, Y. Zhou, T. Miyadera, R. Azumi, Y. Yoshida, M. Chikamatsu, *ACS Appl. Mater. Interfaces* **2015**, *7*, 10814.

[28] Z. Wang, D. P. McMeekin, N. Sakai, S. van Reenen, K. Wojciechowski, J. B. Patel, M. B. Johnston, H. J. Snaith, *Adv. Mater.* **2017**, *29*, 1604186.

[29] Z. Wang, Q. Lin, F. P. Chmiel, N. Sakai, L. M. Herz, H. J. Snaith, *Nat. Energy* **2017**, *2*, 17135.

[30] J.-W. Lee, D.-H. Kim, H.-S. Kim, S.-W. Seo, S. M. Cho, N.-G. Park, *Adv. Energy Mater.* **2015**, *5*, 1501310.

[31] M. Kasha, *Radiat. Res.* **1963**, *20*, 55.

[32] M. Más-Montoya, R. A. J. Janssen, *Adv. Funct. Mater.* **2017**, *27*, 1605779.

[33] Y. Ren, A. M. Hiszpanski, L. Whittaker-Brooks, Y.-L. Loo, *ACS Appl. Mater. Interfaces* **2014**, *6*, 14533.

Cut from the Same Cloth: Enamine-Derived Spirobifluorenes as Hole Transporters for Perovskite Solar Cells

Deimante Vaitukaityte, Cristina Momblona, Kasparas Rakstys,* Albertus Adrian Sutanto, Bin Ding, Cansu Igci, Vygintas Jankauskas, Alytis Gruodis, Tadas Malinauskas, Abdullah M. Asiri, Paul J. Dyson, Vytautas Getautis,* and Mohammad Khaja Nazeeruddin*

ABSTRACT: To attain commercial viability, perovskite solar cells (PSCs) have to be reasonably priced, highly efficient, and stable for a long period of time. Although a new record of a certified power conversion efficiency (PCE) value over 25% was achieved, PSC performance is limited by the lack of hole-transporting materials (HTMs), which extract positive charges from the light-absorbing perovskite layer and carry them to the electrode. Here, we report spirobifluorene-based HTMs with finely tuned energy levels, high glass-transition temperature, and excellent charge mobility and conductivity enabled by molecularly engineered enamine arms. HTMs are synthesized using simple condensation chemistry, which does not require costly catalysts, inert reaction conditions, and time-consuming product purification procedures. Enamine-derived HTMs allow the fabrication of PSCs reaching a maximum PCE of 19.2% and stability comparable to spiro-OMeTAD. This work demonstrates that simple enamine condensation reactions could be used as a universal path to obtain HTMs for highly efficient and stable PSCs.
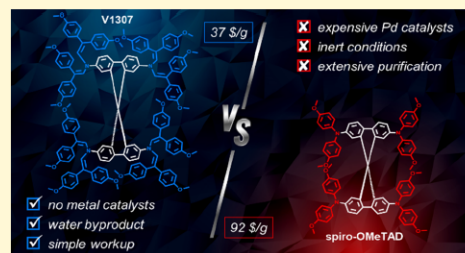
INTRODUCTION

The perovskite materials used in solar cells, i.e., perovskite solar cells (PSCs), and $APbX_3$ (A = methylammonium (MA), formamidinium (FA), caesium (Cs); X = Br, I) have remarkable properties, such as high absorption coefficients, long carrier diffusion lengths, small exciton binding energies, and high charge carrier mobilities.[1−7] Most highly efficient PSCs utilize an n-type layer of mesoporous TiO_2 and a p-type layer of spiro-OMeTAD in an n−i−p device configuration, where perovskite materials are used as light absorbers.[8] With the increased quality of perovskite films, further optimization of other layers to improve the overall solar cell performance is needed.[9,10] Specifically, there is a renewed interest in identifying hole-transporting materials (HTMs) other than spiro-OMeTAD that can yield high power conversion efficiency (PCE).

Since the first report of an HTM in solid-state dye-sensitized solar cells 2 decades ago, the organic semiconductor 2,2′,7,7′-tetrakis-(*N*,*N*′-di-*p*-methoxyphenylamine)-9,9′-spirobifluorene (spiro-OMeTAD) has revolutionized the field and has been selected as the state-of-the-art benchmark.[11] Two decades have passed, yet spiro-OMeTAD still prevails among other HTMs in the field of PSCs, and despite its high cost (~250 $/g), it is commonly used as a highly efficient reference material for research studies. The wide availability of spiro-OMeTAD due

to commercialization decades ago makes it one of the most researched materials, which is currently reported more than 4000 times in the scientific literature. However, the cost-effective industrial potential of spiro-OMeTAD toward practical applications is hardly probable due to its synthetic complexity and high-purity sublimation-grade requirement to obtain high-performance devices contributing more than 30% of the overall module price. Another key factor that plays a major role in the commercialization potential is the stability of the device. To match the necessary electrical conductivity, spiro-OMeTAD needs to be doped as pristine layers generally suffer from low PCE.[12,13]

Due to the success of spiro-OMeTAD, many research groups have focused on spiro-type compounds, expecting to improve the PCE with slight structural modifications.[14−16] The basic idea of the spiro concept is that the morphological stability is improved while retaining the electronic properties of connected π systems with identical or different functions via a
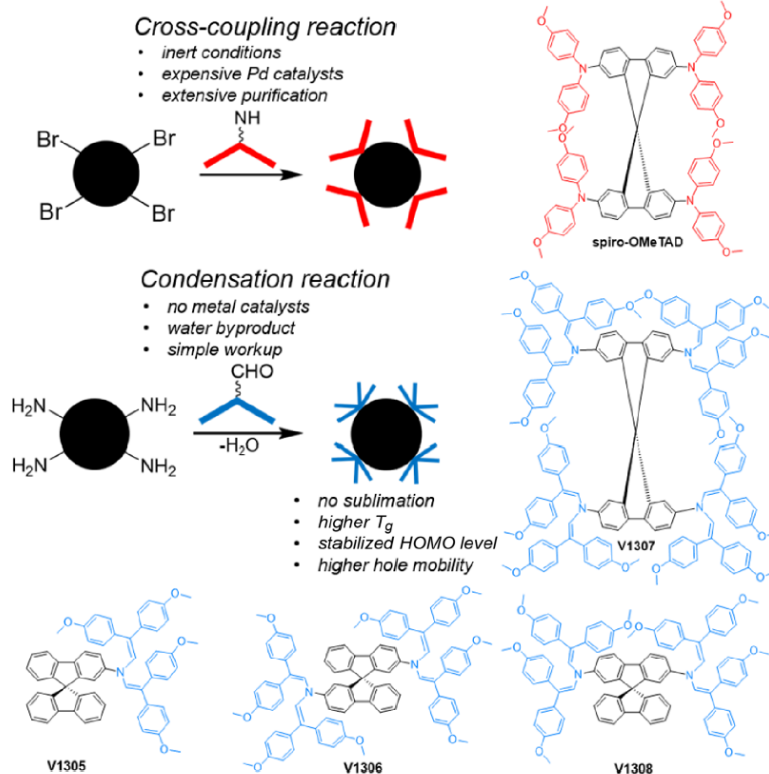
97
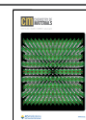
Figure 1. Schematic comparing cross-coupling and condensation reactions for the synthesis of spiro-OMeTAD and novel enamine HTMs.

common sp^3-hybridized atom.[17] Several groups have studied central 9,9′spirobifluorene-linked HTMs including dimethyl-fluorenyl-, ethylcarbazolyl-, and fluorinated methoxyphenyl-terminated compounds, which have been recently reported by Seo,[18] Chen,[19] and Yang,[20] respectively. However, the main focus is still directed on the development of new central spiro-cored structures such as spiro[fluorene-9,9′-xanthene],[21−25] spirobisacridine,[26] thiophene-containing spiro cores,[27−29] and other spiro-type derivatives.[30,31] However, the peripheral part is equally or of even more importance in fine tuning the properties of the HTM.[32,33] Generally, such spiro-centered HTMs are designed by linking prebrominated spiro core species with diphenylamine or borylated triphenylamine, both having electron-rich methoxy groups using C−N or C−C cross-coupling reactions, respectively. These reactions demand severe procedures that result in several disadvantages including inert reaction conditions, costly transition-metal catalysts, and time-consuming purification procedures due to the inherent formation of side products. Moreover, residues of metal catalysts remain in the HTL, which act as traps, deteriorating charge-transporting properties and negatively affecting the performance of the resulting devices.[34,35] Therefore, the hunt is now on for new organic semiconductors that are prepared by

simple, cost-effective, and green chemistry without sacrificing the efficiency.[36,37] In this sense, enamine condensation is promising to eliminate the use of palladium-catalyzed reactions since the only byproduct is water and cost-ineffective catalysts are not involved. In addition, greatly simplified product workup and purification significantly minimize the cost of the final product.[38−40]

Herein, we present a condensation-based spirobifluorene enamine family. The influence of different substitutions in the central spirobifluorene core going from single- to multiarmed enamines was revealed, showing that a higher degree of substitution has several advantages. First, the perpendicular arrangement of the two overcrowded enamine-based molecular halves leads to a high steric demand of the resulting rigid structure, efficiently suppressing molecular interactions. Furthermore, compound V1307 with a larger globular structure, higher molecular weight, and small intermolecular cohesion results in a high stability of the amorphous state. Comparing directly the dimethoxydiphenylamine- and bis-(dimethoxydiphenylenamine)-donating fragments of spiro-OMeTAD and V1307, respectively, it is found that the latter has some merits. First, bis(dimethoxydiphenylenamine) being a less strong donor results in the stabilized HOMO values.
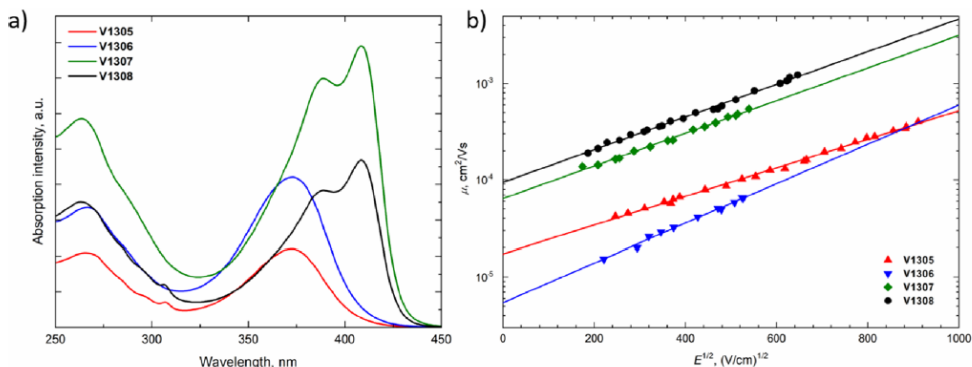
98

Figure 2. (a) UV−vis absorption spectra of **V1305**, **V1306**, **V1307**, and **V1308** in THF solutions (10^{-4} M). (b) Electric field dependencies of the hole drift mobility in spiro-enamines.

Second, the more pronounced and higher degree of conjugation in enamine arms results in the better charge transport through **V1307**, a more densely packed layer. These advantages made novel enamine-derived spirobifluorene HTMs promising candidates for their successful application in PSCs, reaching a photovoltaic performance of up to 19.2% with comparable stability. With this, we demonstrate the simple enamine condensation chemistry as a universal approach to obtain highly efficient and stable HTMs.

RESULTS AND DISCUSSION

Figure 1 presents the chemical structures of the parent spiro-OMeTAD and enamine-based analogues (**V1307**, **V1305**, **V1306**, and **V1308**). A series of four new HTMs containing a well-known spirobifluorene core with enamine arms were obtained simply by condensing aminated precursors with 2,2-bis(4-methoxyphenyl)acetaldehyde. The condensation reaction was carried out under ambient conditions, and the only byproduct is water, which is continuously separated using a Dean−Stark trap that accelerates the formation of the final product. Detailed synthetic protocols and full characterization of the compounds (NMR spectroscopy, mass spectrometry, and elemental analysis) are described in the Supporting Information. To assess the synthesis costs of the enamine condensation reaction in comparison with the regular cross-coupling reaction, we calculated the costs on a lab-scale synthesis (Table S1).[41] The evaluated cost of **V1307** is ∼37 $/g, which is much less than the cost of spiro-OMeTAD (∼92 $/g).[42]

Thermogravimetric analysis suggests that novel HTMs start to decompose at around 400 °C (Figure S1), which is far above the temperature for conventional device operation. Differential scanning calorimetry measurements (Figure S2) indicate that **V1305**, **V1306**, and **V1308** could exist in both crystalline and amorphous states similar to spiro-OMeTAD.[43] Interestingly, **V1307** is fully amorphous and has the highest glass-transition temperature (T_g) of 169 °C, which should result in the improved quality of the **V1307** layers. We also note that all synthesized HTMs have higher T_g than spiro-OMeTAD (124 °C), meaning that the introduction of enamine fragments improves the morphological stability.

Gaussian09 software[44] was used for simulation purposes to establish the most probable molecular geometries of **V1305**, **V1306**, **V1307**, and **V1308** with their corresponding absorption spectra. Ground state geometry optimization was performed by means of the density functional theory method with B3LYP and 6-31G basis sets without polarization functions, and the predicted molecular structures are presented in Figure S3. As expected, two fluorene core fragments (F1>C<F2) are connected through the carbon atom having a perpendicular orientation. Due to the presence of the double bonds in the enamine chain [>C=CH—N—CH=C<], orientation of substituents is chaotic and a large number of different possible positions are allowed. However, the most probable orientation is related to the V-shaped structure, when one methoxyphenyl fragment of F1 is oriented to the end of F2 (see Figure S3, **V1305**). Similar enamine branch orientations could be found in **V1306**, **V1307**, and **V1308**. Interestingly, comparing both four-armed **V1307** and spiro-OMeTAD, several differences in the molecular orientation are observed, i.e., well-ordered and dual-axed perpendicular symmetry of spiro-OMeTAD is damaged since the fluorenes in **V1307** are not completely perpendicular, and they are not flat anymore due to the chaotic arrangement of enamine substituents resulting in the fully amorphous morphology of **V1307**.

The ultraviolet−visible absorption (UV−vis) spectra in THF solutions of **V1305**, **V1306**, **V1307**, and **V1308** are shown in Figure 2a. All spiro-enamines possess two significant absorption bands at around 260 and 380 nm. The less intense absorption at shorter wavelengths corresponds to localized $\pi-\pi^*$ transitions. Longer wavelengths are observed for more intensive delocalization from the conjugated scaffold and are assigned to n−π^* transitions. The change in the number and the position of enamine arms in the system has significantly influenced the absorption. While the increasing number of enamine arms shifts the absorption hyperchromically (**V1305** < **V1306** = **V1308** < **V1307**), the increased conjugation in **V1307** and **V1308**, where fluorene is substituted on both sides, also resulted in the bathochromic shift around 35 nm. The optical gaps (E_g) were evaluated from the intersection of absorption and photoluminescence (PL) spectra of thin films and were estimated to be similar for all of the compounds at around 2.85 eV (Figure S6).

99

Table 1. Thermal, Optical, and Photophysical Properties of Newly Synthesized Enamines

ID	T_m [°C][a]	T_c [°C][a]	T_g [°C][a]	T_{dec} [°C][a]	λ_{abs} [nm][b]	I_P [eV][c]	E_g [eV][d]	E_{ea} [eV][e]	μ_0 [cm² V⁻¹ s⁻¹][f]	σ [S cm⁻¹][g]
V1305	243		131	380	267 and 372	5.33	2.90	2.43	1.7×10^{-5}	3.9×10^{-6}
V1306	294	226	154	402	267 and 373	5.37	2.84	2.53	5.4×10^{-6}	6.7×10^{-5}
V1307			169	401	263, 389, and 408	5.46	2.83	2.63	6.4×10^{-4}	1.4×10^{-3}
V1308	305	203	158	371	263, 388, and 408	5.46	2.78	2.68	9.4×10^{-4}	2.9×10^{-4}

[a]Melting (T_m), crystallization (T_c), glass transition (T_g), and decomposition (T_{dec}) temperatures observed from DSC and TGA (10 °C/min, N_2 atmosphere). [b]Absorption spectra were measured in THF solutions (10^{-4} M). [c]Ionization energies of the films measured using PESA. [d]E_g estimated from the intersection of absorption and emission spectra of solid films. [e]$E_{ea} = I_P - E_g$. [f]Mobility value at zero field strength. [g]Conductivity values.
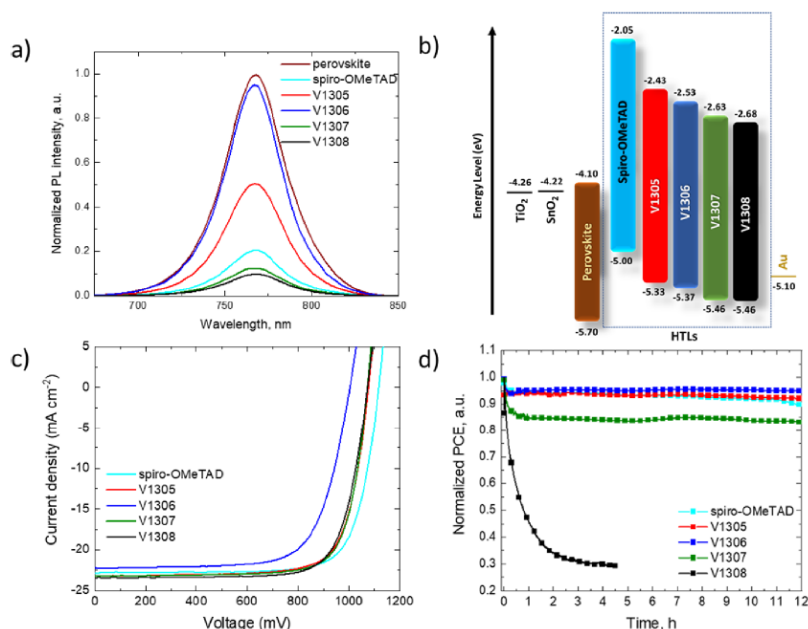
Figure 3. (a) PL spectra upon the 625 nm excitation wavelength of perovskite and perovskite/HTM samples deposited on glass with HTMs: spiro-OMeTAD, V1305, V1306, V1307, and V1308. PSCs with the FTO/c-TiO₂/m-TiO₂/SnO₂/perovskite/HTM/Au layout: (b) energy diagram of the device, (c) $J–V$ characteristics of the most efficient devices under 1 sun illumination measured in air, and (d) stability of unencapsulated devices under constant 1 sun illumination in the N₂ atmosphere.

The solid-state ionization potentials (I_P) of V1305, V1306, V1307, V1308, and spiro-OMeTAD were determined using photoemission spectroscopy in air (PESA) of the thin films to assess the HOMO energy level of spiro-enamine HTMs (Figure S7). I_P values of V1305, V1306, V1307, and V1308 were found to be 5.33, 5.37, 5.46, and 5.46 eV, respectively, which are significantly stabilized compared to those of spiro-OMeTAD (5.00 eV).[40] Based on the solid-state optical gap and I_P values, we calculated the electron affinities (E_{ea}) to be 2.43, 2.53, 2.63, and 2.68 eV for V1305, V1306, V1307, and V1308, respectively. Importantly, the electron affinities are smaller compared with the conduction band energy of the perovskite (−4.10 eV); therefore, effective electron blocking from the perovskite to the electrode should be ensured.

Xerographic time-of-flight measurements were used to determine the charge mobility of the V-series layers. Depend-

encies of hole drift mobility on the electric field strength are shown in Figure 2b. V1308 and V1307 exhibited the highest zero-field hole-drift mobility (μ_0) among the series with the values of 9.4×10^{-4} and 6.4×10^{-4} cm²/Vs, respectively, both outperforming spiro-OMeTAD ($\mu_0 = 1.3 \times 10^{-4}$ cm²/Vs).[34] In addition, the lateral thin film conductivity of the V-series layers was measured with organic field-effect transistors (OFETs) (Figure S8). Similar to the result of the hole mobility measurement, V1307 and V1308 showed a higher conductivity (1.4×10^{-3} and 2.9×10^{-4} S cm⁻¹, respectively) than V1305 (3.9×10^{-6} S cm⁻¹) and V1306 (6.7×10^{-5} S cm⁻¹). The conductivity of the doped spiro-OMeTAD as a reference was determined to be 1.0×10^{-3} S cm⁻¹. The conductivity trend obtained for the V-series was found to be directly correlated with the degree of conjugation of the molecules. The fact that V1307 has the higher hole mobility and

100

conductivity value between the V-series and spiro-OMeTAD can be attributed to the higher degree of conjugation in enamine arms of V1307.[45−47] The thermal, optical, and photoelectrical properties of the spiro-enamines are summarized in Table 1.

Steady-state PL was evaluated in samples with glass/perovskite and glass/perovskite/HTM layouts to determine their hole extraction properties in PSCs (Figure 3a). The PL spectra show that the hole transfer between V1307 and V1308 HTMs and perovskite is more efficient than that between V1305 and V1306. A slight quenching effect is observed in V1305 and V1306, which is in good agreement with the lowest hole drift mobility values (5.4×10^{-6} cm^2/Vs for V1305 and 1.7×10^{-5} cm^2/Vs for V1306). This quenching is enhanced with the use of spiro-OMeTAD, V1307, and V1308 HTMs that have higher hole mobility values (1.3×10^{-4}, 6.4×10^{-4}, and 9.4×10^{-4} cm^2/Vs) due to more efficient hole transfer between perovskite and the corresponding HTM.

Fabrication of n−i−p solar cells was carried out with the device layout FTO/c-TiO$_2$/m-TiO$_2$/SnO$_2$/perovskite/HTM/Au by spin-coating, except for the top electrode, deposited by thermal evaporation. The perovskite composition used was the triple-cation perovskite [(FAPbI$_3$)$_{0.87}$(MAPbBr$_3$)$_{0.13}$]$_{0.92}$(CsPbI$_3$)$_{0.08}$, and the HTM is doped with the bis(trifluoromethylsulfonyl)imide lithium salt (LiTFSI) and cobalt(III)-tris(bis(trifluoromethylsulfonyl)-imide). tert-Butylpyridine (tBP) was also added to the HTM solution to improve the HTM morphology and increase the LiTFSI solubility.[48] The energy diagram of the device is shown in Figure 3b, and the detailed preparation process is described in the Methods section. Cross-sectional and top-view scanning electron microscopy (SEM) images were obtained to determine the thickness and morphology of the HTM, respectively (Figures S9 and S10). The HTM thickness is 180 nm for spiro-OMeTAD-based devices; 80 nm for devices containing V1305, V1306, and V1307; and 140 nm for devices fabricated with V1308.

The current−voltage ($J−V$) characteristics of the most efficient devices are presented in Figure 3c, and their corresponding PV parameters are extracted and shown in Table 2. The most efficient devices containing V1305, V1307, and V1308 have similar PCE values of 19.0%, 19.2%, and 19.1%, respectively. The corresponding external quantum efficiency (EQE) and the integrated current density are shown in Figure S11. The analysis of the statistical data presented in Figure S12 and Table S4 confirms the correlation between hole-drift mobility and device performance, and being the most efficient, the devices containing the HTM with higher hole mobility values follow the order: V1306 < V1305 < V1308 ∼ V1307.[49]

Although the use of HTMs with deeper HOMO levels is, in principle, beneficial for the device performance due to larger V_{OC} values,[33,50] in our study, all the devices showed lower V_{OC} values. These values (∼1070 mV) are lower compared to those of the devices containing spiro-OMeTAD (∼1100 mV) in spite of their deeper HOMO values (5.33 eV for V1305, 5.37 eV for V1306, and 5.46 for V1307 and V1308) compared to spiro-OMeTAD (5.00 eV).[40] Therefore, the lower V_{OC} values might be due to a contact issue at the perovskite/HTM interface producing higher charge recombination in comparison to spiro-OMeTAD-based devices. The fill factor (FF) is similar for devices containing spiro-OMeTAD, V1305, V1307, and V1308, but this main parameter differs for V1306-based devices, indicating poor film quality, which will negatively affect the hole charge extraction. The analysis of the film by top-view high-magnification SEM demonstrates the presence of pinholes in devices fabricated with V1306 (Figure S13a). The appearance of these pinholes is also observed in the device fabricated with V1308 (Figure S13b). However, for V1308, the efficiency is not affected, but it does affect the long-term device stability. The hysteretic behavior of the devices was estimated from the $J−V$ curves collected by scanning the device from the forward bias (FB) to the short circuit (SC) followed by from SC to FB (Figure S14), and their PV parameters are reported in Table 2. The hysteresis index was calculated from the formulae previously reported,[51] and values of 0.036, 0.100, 0.259, 0.047, and 0.037 were estimated for the devices containing spiro-OMeTAD, V1305, V1306, V1307, and V1308, respectively.

The stability of the unencapsulated devices was measured under 1 sun illumination and under a N$_2$ atmosphere, as shown in Figure 3d. Devices containing V1305 and V1306 that have one and two enamine arms, respectively, are the most stable of the series and have a slightly better stability than devices that are composed of spiro-OMeTAD. However, the introduction of a second enamine moiety in the transconfigurated V1308 induces a fastest decay and is completely detrimental for the stability, which is in good agreement with the inhomogeneity observed in the top-view SEM images, where the highest pinhole density was observed. Interestingly, a slight initial decay in PCE of the tetra-substituted V1307 device was observed in the beginning of the measurement during the first hour followed by the similar trend to V1305, V1306, and spiro-OMeTAD during the remaining time. Similar dynamic mechanisms have been observed, demonstrating that a quick degradation is activated by the migration of metal electrode particles through HTM, resulting in the contact with the perovskite layer.[52,53] Stability measurements revealed that the number and position of enamine arms in the final HTM structure have a large impact on the stability of the final device.

■ CONCLUSIONS

In conclusion, a new series of spirobifluorene-based hole-transporting enamines were synthesized and systematically studied. Novel HTMs are obtained by a simple and straightforward condensation reaction, which in contrast to spiro-OMeTAD, do not require expensive palladium catalysts

Table 2. PV Parameters Extracted from the Corresponding Hysteresis $J−V$ Curves for the Best Performing Solar Cells[a]

ID		V_{OC} (mV)	J_{SC} (mA cm^{-2})	FF	PCE (%)
spiro-OMeTAD	REV	1118	22.90	0.77	19.7
	FWD	1104	22.89	0.75	19.0
V1305	REV	1077	23.17	0.76	19.0
	FWD	1043	23.15	0.71	17.1
V1306	REV	1004	22.22	0.71	15.8
	FWD	981	22.17	0.54	11.7
V1307	REV	1073	23.21	0.77	19.2
	FWD	1052	23.18	0.75	18.3
V1308	REV	1074	23.44	0.76	19.1
	FWD	1066	23.37	0.74	18.4

[a]REV, reverse bias; FWD, forward bias. Precondition: 2 s of light soaking. Illumination area through a shadow mask of 16 mm^2, a scan rate of 50 mV s^{-1}, and a voltage step of 10 mV.

101

and inert conditions, and water is the only byproduct obtained. In addition, simple product workup and purification result in significantly reduced synthesis costs. The impact of the different number and substitution of enamine fragments was revealed through the optical, electrochemical, photophysical, and photovoltaic measurements. It was found that enamine fragments increase the glass-transition temperature of final HTMs that are more amorphous and morphological stable. Moreover, synthesized enamine materials demonstrate a very high hole mobility and conductivity up to 9.4×10^{-4} cm^2/Vs and 1.4×10^{-3} S cm^{-1}, respectively. In summary, PSCs fabricated with the novel V1305 and V1307 HTMs present high-efficiency values exceeding 19%, with small hysteresis and stability being comparable to those of devices containing spiro-OMeTAD in the same testing period. This demonstrates that simple enamine condensation chemistry is a universal approach to obtain highly efficient and stable HTMs.

■ METHODS

Device Fabrication. Fluorine-doped tin oxide (FTO)-coated glass was laser scribed to avoid the direct contact between electrodes. The etched substrates were cleaned by the following procedure: 2% helmanex solution, deionized water, and ethanol were placed in an ultrasonic bath for 10 min and UV/O$_3$ treatment was performed for 15 min. Compact TiO$_2$ (c-TiO$_2$) (30 nm) was deposited by spray pyrolysis from titanium diisopropoxide bis(acetylacetonate) (Sigma-Aldrich) in isopropanol solution (1:15, v/v) and annealed at 450 °C for 30 min. The mesoporous TiO$_2$ (m-TiO$_2$) layers were prepared from a TiO$_2$ paste (Dyesol 30 NR-D) solution (1 g in 9 mL of ethanol dilution) by spin-coating at 5000 rpm (1000 rpm/s acceleration, 15 s). The layer was sintered on a hot plate at 500 °C for 30 min. Following this, a 20 nm SnO$_2$ layer was prepared by dissolving SnCl$_4$ (Acros) in deionized water (12 μL in 988 μL of water) and spin-coated at 3000 rpm for 30 s (1000 rpm/s acceleration), followed by annealing at 190 °C for 1 h. The [(FAP-bI$_3$)$_{0.87}$(MAPbBr$_3$)$_{0.13}$]$_{0.92}$(CsPbI$_3$)$_{0.08}$ perovskite solution was prepared by mixing 17.41 mg of MABr, 27.02 mg of CsI, 57.06 mg of PbBr$_2$, 178.94 mg of FAI, and 548.60 mg of PbI$_2$, and it was dissolved in 1 mL of DMF/DMSO (0.78:0.22, v/v). Then, the perovskite solution was spin-coated at 2000 rpm for 10 s, followed by 5000 rpm for 30 s. During spinning in the second step, the antisolvent chlorobenzene (110 μL) was dropped on the sample 15 s before finishing the process. The films were annealed at 100 °C for 1 h inside the glovebox. Once the samples were cooled down, the HTM was deposited on top of the perovskite layer by spin-coating at 4000 rpm for 30 s. The spiro-OMeTAD was deposited from a 60 mM solution in chlorobenzene with tBP, tris(2-(1H-pyrazol-1-yl)-4-tert-butylpyridine)cobalt(III) (FK209), and LiTFSI as additives. The concentration of V-series HTMs was 20 mM. The molar ratio of additives for spiro-OMeTAD and each doped HTM solution was 0.5 for LiTFSI from a 1.8 M stock solution in acetonitrile and 3.3 for tBP and 0.03 for FK209 from a 0.25 M stock solution in acetonitrile. Finally, a 70 nm Au film was thermally evaporated as the top electrode. The cross-sectional film morphology was investigated by using a high-resolution SEM (Merlin, Zeiss) equipped with a GEMINI II column and a Schottky Field Emission gun. Images were acquired with an In-Lens Secondary Electron Detector at 3 kV.

Thin Film and Device Characterization. Conductivity measurements of V1305, V1306, V1307, V1308, and spiro-OMeTAD were carried out using the OFET configuration with a two-contact electrical conductivity setup. The OFET substrates were purchased from Fraunhofer IPMS. The substrates were first prepared with 20 min of oxygen plasma cleaning and subsequent film deposition of HTMs and spiro-OMeTAD by spin-coating following the same procedure as in the device fabrication, at 4000 rpm for 30 s from a chlorobenzene solution (20 mM) chemically doped with FK-209, LiTFSI, and tBP as additives. The conductivity measurements were carried out on the 2.5 μm channel by sweeping from −10 to 10 V

(source−drain voltage) at a scan rate of 1 V s^{-1} with a Keithley 2612A (Figure S8). The data were recorded using the KickStart software program. The channel width and height are 10 mm and 40 nm, respectively, and the gate capacity is 15 nF. The conductivity was calculated from a linear fit of the current−voltage measurement and Ohm's law. The J−V characteristics were determined by using a 2400 Keithley system (scan rate: 50 mV s^{-1} and 10 mV voltage step) in combination with a Xe-lamp Oriel sol3A sun simulator (Newport Corporation), previously calibrated to AM1.5G standard conditions by using the reference cell Oriel 91150 V. The devices were measured with 2 s of light soaking, and the illumination area was defined through a shadow mask of 16 mm^2. EQE was measured with an IQE200B quantum efficiency measurement system (Oriel, Newport, UK). The stability test was performed as maximum power tracking under 100 mW cm^{-2} illumination with an LED power source. Note that during the stability test, the samples were placed in a measurement box purged continuously with nitrogen gas at 0% humidity to create an inert atmosphere. The box temperature was kept at 25 °C by a cooling system. A shadow mask of 16 mm^2 was used to define the illumination area during the long-term stability test. Top-view SEM images were recorded by an in-lens detector of the FEI Teneo Schottky field-emission SEM at a tension of 5 kV. The steady-state PL spectra of the glass/perovskite and glass/perovskite/HTM thin films were measured and recorded using a Fluorolog-3-22 spectrofluorometer. The spectra were recorded upon excitation at 625 nm with the sample illuminated from the front side (perovskite or the HTM side).

■ ASSOCIATED CONTENT

Ⓢ Supporting Information

The Supporting Information is available free of charge at https://pubs.acs.org/doi/10.1021/acs.chemmater.1c01486.

> Tables S1−S4 and Figures S1−S25; experimental section; detailed synthetic procedures; TGA data; DSC; optimized geometry of frontier molecular orbital diagrams; electronic absorption spectra; electronic excitation; V1305, V1306, V1307, and V1308 distributions; UV−vis/PL spectra of thin films; photoemission in air spectra; current−voltage measurements; ^{1}H and ^{13}C NMRs; MALDI-TOF-MS spectra; PESA; conductivity; SEM images; photovoltaic parameter statistics; J−V curves; EQE (PDF)

■ AUTHOR INFORMATION

Corresponding Authors

Kasparas Rakstys − Department of Organic Chemistry, Kaunas University of Technology, Kaunas 50254, Lithuania; Email: kasparas.rakstys@ktu.lt

Vytautas Getautis − Department of Organic Chemistry, Kaunas University of Technology, Kaunas 50254, Lithuania; ⓘ orcid.org/0000-0001-7695-4677; Email: vytautas.getautis@ktu.lt

Mohammad Khaja Nazeeruddin − Institute of Chemical Sciences and Engineering, École Polytechnique Fédérale de Lausanne, CH-1951 Sion, Switzerland; ⓘ orcid.org/0000-0001-5955-4786; Email: mdkhaja.nazeeruddin@epfl.ch

Authors

Deimante Vaitukaityte − Department of Organic Chemistry, Kaunas University of Technology, Kaunas 50254, Lithuania

Cristina Momblona − Institute of Chemical Sciences and Engineering, École Polytechnique Fédérale de Lausanne, CH-1951 Sion, Switzerland; ⓘ orcid.org/0000-0003-2953-3065

102

Albertus Adrian Sutanto − *Institute of Chemical Sciences and Engineering, École Polytechnique Fédérale de Lausanne, CH-1951 Sion, Switzerland;* ● orcid.org/0000-0002-9413-2789

Bin Ding − *Institute of Chemical Sciences and Engineering, École Polytechnique Fédérale de Lausanne, CH-1951 Sion, Switzerland*

Cansu Igci − *Institute of Chemical Sciences and Engineering, École Polytechnique Fédérale de Lausanne, CH-1951 Sion, Switzerland*

Vygintas Jankauskas − *Institute of Chemical Physics, Vilnius University, Vilnius 10257, Lithuania*

Alytis Gruodis − *Institute of Chemical Physics, Vilnius University, Vilnius 10257, Lithuania*

Tadas Malinauskas − *Department of Organic Chemistry, Kaunas University of Technology, Kaunas 50254, Lithuania;* ● orcid.org/0000-0002-5478-6550

Abdullah M. Asiri − *Center of Excellence for Advanced Materials Research (CEAMR), King Abdulaziz University, 21589 Jeddah, Saudi Arabia;* ● orcid.org/0000-0001-7905-3209

Paul J. Dyson − *Institute of Chemical Sciences and Engineering, École Polytechnique Fédérale de Lausanne, CH-1951 Sion, Switzerland;* ● orcid.org/0000-0003-3117-3249

Complete contact information is available at:
https://pubs.acs.org/10.1021/acs.chemmater.1c01486

Author Contributions

D.V. conducted the synthesis and structural characterization of the compounds and carried out UV−vis and PL measurements. C.M. and B.D. contributed to film preparation and device fabrication and testing. K.R. conceived the idea, K.R. and C.M. wrote the initial manuscript. C. I. contributed to the conductivity measurements and analysis. A.A.S. contributed to the SEM measurements and analysis. V.J. carried out the charge mobility measurements. A.G. performed computational simulations. T.M., A.M.A., and P.J.D. analyzed data. V.G. and M.K.N. supervised the research. All authors contributed to writing and reviewing this paper. This manuscript was written through contributions of all authors. All authors have given approval to the final version of the manuscript.

Notes

The authors declare no competing financial interest.

■ REFERENCES

(1) Oga, H.; Saeki, A.; Ogomi, Y.; Hayase, S.; Seki, S. Improved Understanding of the Electronic and Energetic Landscapes of Perovskite Solar Cells: High Local Charge Carrier Mobility, Reduced Recombination, and Extremely Shallow Traps. *J. Am. Chem. Soc.* **2014**, *136*, 13818−13825.

(2) Stranks, S. D.; Eperon, G. E.; Grancini, G.; Menelaou, C.; Alcocer, M. J. P.; Leijtens, T.; Herz, L. M.; Petrozza, A.; Snaith, H. J. Electron-Hole Diffusion Lengths Exceeding 1 Micrometer in an Organometal Trihalide Perovskite Absorber. *Science* **2013**, *342*, 341−344.

(3) Burschka, J.; Pellet, N.; Moon, S. J.; Humphry-Baker, R.; Gao, P.; Nazeeruddin, M. K.; Grätzel, M. Sequential Deposition as a Route to High-Performance Perovskite-Sensitized Solar Cells. *Nature* **2013**, *499*, 316−319.

(4) Jeon, N. J.; Noh, J. H.; Yang, W. S.; Kim, Y. C.; Ryu, S.; Seo, J.; Seok, S. I. Compositional Engineering of Perovskite Materials for High-Performance Solar Cells. *Nature* **2015**, *517*, 476−480.

(5) Saliba, M.; Matsui, T.; Seo, J. Y.; Domanski, K.; Correa-Baena, J. P.; Nazeeruddin, M. K.; Zakeeruddin, S. M.; Tress, W.; Abate, A.; Hagfeldt, A.; Grätzel, M. Cesium-Containing Triple Cation Perovskite Solar Cells: Improved Stability, Reproducibility and High Efficiency. *Energy Environ. Sci.* **2016**, *9*, 1989−1997.

(6) Wehrenfennig, C.; Eperon, G. E.; Johnston, M. B.; Snaith, H. J.; Herz, L. M. High Charge Carrier Mobilities and Lifetimes in Organolead Trihalide Perovskites. *Adv. Mater.* **2014**, *26*, 1584−1589.

(7) Lee, M. M.; Teuscher, J.; Miyasaka, T.; Murakami, T. N.; Snaith, H. J. Efficient Hybrid Solar Cells Based on Meso-Superstructured Organometal Halide Perovskites. *Science* **2012**, *338*, 643−647.

(8) Zhao, Y.; Zhu, K. Organic-Inorganic Hybrid Lead Halide Perovskites for Optoelectronic and Electronic Applications. *Chem. Soc. Rev.* **2016**, *45*, 655−689.

(9) Liu, M.; Johnston, M. B.; Snaith, H. J. Efficient Planar Heterojunction Perovskite Solar Cells by Vapour Deposition. *Nature* **2013**, *501*, 395−398.

(10) Jeon, N. J.; Noh, J. H.; Kim, Y. C.; Yang, W. S.; Ryu, S.; Seok, S. I. Solvent Engineering for High-Performance Inorganic-Organic Hybrid Perovskite Solar Cells. *Nat. Mater.* **2014**, *13*, 897−903.

(11) Bach, U.; Lupo, D.; Comte, P.; Moser, J. E.; Weissörtel, F.; Salbeck, J.; Spreitzer, H.; Grätzel, M. Solid-State Dye-Sensitized Mesoporous TiO2 Solar Cells with High Photon-to-Electron Conversion Efficiencies. *Nature* **1998**, *395*, 583−585.

(12) Jiang, K.; Wu, F.; Zhang, G.; Zhu, L.; Yan, H. Efficient Perovskite Solar Cells Based on Dopant-Free Spiro-OMeTAD Processed With Halogen-Free Green Solvent. *Sol. RRL* **2019**, *3*, No. 1900061.

(13) Luo, W.; Wu, C.; Wang, D.; Zhang, Z.; Qi, X.; Guo, X.; Qu, B.; Xiao, L.; Chen, Z. Dopant-Free Spiro-OMeTAD as Hole Transporting Layer for Stable and Efficient Perovskite Solar Cells. *Org. Electron.* **2019**, *74*, 7−12.

(14) Rakstys, K.; Igci, C.; Nazeeruddin, M. K. Efficiency: Vs. Stability: Dopant-Free Hole Transporting Materials towards Stabilized Perovskite Solar Cells. *Chem. Sci.* **2019**, *10*, 6748−6769.

(15) Hawash, Z.; Ono, L. K.; Qi, Y. Recent Advances in Spiro-MeOTAD Hole Transport Material and Its Applications in Organic−Inorganic Halide Perovskite Solar Cells. *Adv. Mater. Interfaces* **2018**, *5*, No. 1700623.

(16) Gangala, S.; Misra, R. Spiro-Linked Organic Small Molecules as Hole-Transport Materials for Perovskite Solar Cells. *J. Mater. Chem. A* **2018**, *6*, 18750−18765.

103

(17) Saragi, T. P. I.; Spehr, T.; Siebert, A.; Fuhrmann-Lieker, T.; Salbeck, J. Spiro Compounds for Organic Optoelectronics. *Chem. Rev.* 2007, 107, 1011−1065.

(18) Jeon, N. J.; Na, H.; Jung, E. H.; Yang, T. Y.; Lee, Y. G.; Kim, G.; Shin, H. W.; Il Seok, S.; Lee, J.; Seo, J. A Fluorene-Terminated Hole-Transporting Material for Highly Efficient and Stable Perovskite Solar Cells. *Nat. Energy* 2018, 3, 682−689.

(19) Chen, C. C.; Deng, Z.; He, M.; Zhang, Y.; Ullah, F.; Ding, K.; Liang, J.; Zhang, Z.; Xu, H.; Qiu, Y.; Xie, Z.; Shan, T.; Chen, Z.; Zhong, H. Design of Low Crystallinity Spiro-Typed Hole Transporting Material for Planar Perovskite Solar Cells to Achieve 21.76% Efficiency. *Chem. Mater.* 2021, 33, 285−297.

(20) Jeong, M.; Choi, I. W.; Go, E. M.; Cho, Y.; Kim, M.; Lee, B.; Jeong, S.; Jo, Y.; Choi, H. W.; Lee, J.; Bae, J. H.; Kwak, S. K.; Kim, D. S.; Yang, C. Stable Perovskite Solar Cells with Efficiency Exceeding 24.8% and 0.3-V Voltage Loss. *Science* 2020, 369, 1615−1620.

(21) Bi, D.; Xu, B.; Gao, P.; Sun, L.; Grätzel, M.; Hagfeldt, A. Facile Synthesized Organic Hole Transporting Material for Perovskite Solar Cell with Efficiency of 19.8%. *Nano Energy* 2016, 23, 138−144.

(22) Xu, B.; Bi, D.; Hua, Y.; Liu, P.; Cheng, M.; Grätzel, M.; Kloo, L.; Hagfeldt, A.; Sun, L. A Low-Cost Spiro[Fluorene-9,9′-Xanthene]-Based Hole Transport Material for Highly Efficient Solid-State Dye-Sensitized Solar Cells and Perovskite Solar Cells. *Energy Environ. Sci.* 2016, 9, 873−877.

(23) Zhang, J.; Xu, B.; Yang, L.; Ruan, C.; Wang, L.; Liu, P.; Zhang, W.; Vlachopoulos, N.; Kloo, L.; Boschloo, G.; Sun, L.; Hagfeldt, A.; Johansson, E. M. J. The Importance of Pendant Groups on Triphenylamine-Based Hole Transport Materials for Obtaining Perovskite Solar Cells with over 20% Efficiency. *Adv. Energy Mater.* 2018, 8, No. 1701209.

(24) Xu, B.; Zhang, J.; Hua, Y.; Liu, P.; Wang, L.; Ruan, C.; Li, Y.; Boschloo, G.; Johansson, E. M. J.; Kloo, L.; Hagfeldt, A.; Jen, A. K. Y.; Sun, L. Tailor-Making Low-Cost Spiro[Fluorene-9,9′-Xanthene]-Based 3D Oligomers for Perovskite Solar Cells. *Chem.* 2017, 2, 676−687.

(25) Chiykowski, V. A.; Cao, Y.; Tan, H.; Tabor, D. P.; Sargent, E. H.; Aspuru-Guzik, A.; Berlinguette, C. P. Precise Control of Thermal and Redox Properties of Organic Hole-Transport Materials. *Angew. Chem., Int. Ed.* 2018, 57, 15529−15533.

(26) Drigo, N.; Roldan-Carmona, C.; Franckevičius, M.; Lin, K. H.; Gegevičius, R.; Kim, H.; Schouwink, P. A.; Sutanto, A. A.; Olthof, S.; Sohail, M.; Meerholz, K.; Gulbinas, V.; Corminboeuf, C.; Paek, S.; Nazeeruddin, M. K. Doped but Stable: Spirobisacridine Hole Transporting Materials for Hysteresis-Free and Stable Perovskite Solar Cells. *J. Am. Chem. Soc.* 2020, 142, 1792−1800.

(27) Saliba, M.; Orlandi, S.; Matsui, T.; Aghazada, S.; Cavazzini, M.; Correa-Baena, J. P.; Gao, P.; Scopelliti, R.; Mosconi, E.; Dahmen, K. H.; De Angelis, F.; Abate, A.; Hagfeldt, A.; Pozzi, G.; Graetzel, M.; Nazeeruddin, M. K. A Molecularly Engineered Hole-Transporting Material for Efficient Perovskite Solar Cells. *Nat. Energy* 2016, 1, 15017.

(28) Rakstys, K.; Paek, S.; Sohail, M.; Gao, P.; Cho, K. T.; Gratia, P.; Lee, Y.; Dahmen, K. H.; Nazeeruddin, M. K. A Highly Hindered Bithiophene-Functionalized Dispiro-Oxepine Derivative as an Efficient Hole Transporting Material for Perovskite Solar Cells. *J. Mater. Chem. A* 2016, 4, 18259−18264.

(29) Gao, K.; Xu, B.; Hong, C.; Shi, X.; Liu, H.; Li, X.; Xie, L.; Jen, A. K. Y. Di-Spiro-Based Hole-Transporting Materials for Highly Efficient Perovskite Solar Cells. *Adv. Energy Mater.* 2018, 8, No. 1800809.

(30) Zhu, X. D.; Ma, X. J.; Wang, Y. K.; Li, Y.; Gao, C. H.; Wang, Z. K.; Jiang, Z. Q.; Liao, L. S. Hole-Transporting Materials Incorporating Carbazole into Spiro-Core for Highly Efficient Perovskite Solar Cells. *Adv. Funct. Mater.* 2019, 29, No. 1807094.

(31) Wang, X.; Zhang, J.; Yu, S.; Yu, W.; Fu, P.; Liu, X.; Tu, D.; Guo, X.; Li, C. Lowering Molecular Symmetry To Improve the Morphological Properties of the Hole-Transport Layer for Stable Perovskite Solar Cells. *Angew. Chem.* 2018, 130, 12709−12713.

(32) Truong, M. A.; Lee, J.; Nakamura, T.; Seo, J. Y.; Jung, M.; Ozaki, M.; Shimazaki, A.; Shioya, N.; Hasegawa, T.; Murata, Y.; Zakeeruddin, S. M.; Grätzel, M.; Murdey, R.; Wakamiya, A. Influence of Alkoxy Chain Length on the Properties of Two-Dimensionally Expanded Azulene-Core-Based Hole-Transporting Materials for Efficient Perovskite Solar Cells. *Chem. − Eur. J.* 2019, 25, 6741−6752.

(33) Rakstys, K.; Abate, A.; Dar, M. I.; Gao, P.; Jankauskas, V.; Jacopin, G.; Kamarauskas, E.; Kazim, S.; Ahmad, S.; Grätzel, M.; Nazeeruddin, M. K. Triazatruxene-Based Hole Transporting Materials for Highly Efficient Perovskite Solar Cells. *J. Am. Chem. Soc.* 2015, 137, 16172−16178.

(34) Rakstys, K.; Saliba, M.; Gao, P.; Gratia, P.; Kamarauskas, E.; Paek, S.; Jankauskas, V.; Nazeeruddin, M. K. Highly Efficient Perovskite Solar Cells Employing an Easily Attainable Bifluorenylidene-Based Hole-Transporting Material. *Angew. Chem., Int. Ed.* 2016, 55, 7464−7468.

(35) Usluer, Ö.; Abbas, M.; Wantz, G.; Vignau, L.; Hirsch, L.; Grana, E.; Brochon, C.; Cloutet, E.; Hadziioannou, G. Metal Residues in Semiconducting Polymers: Impact on the Performance of Organic Electronic Devices. *ACS Macro Lett.* 2014, 3, 1134−1138.

(36) Petrus, M. L.; Music, A.; Closs, A. C.; Bijleveld, J. C.; Sirtl, M. T.; Hu, Y.; Dingemans, T. J.; Bein, T.; Docampo, P. Design Rules for the Preparation of Low-Cost Hole Transporting Materials for Perovskite Solar Cells with Moisture Barrier Properties. *J. Mater. Chem. A* 2017, 5, 25200−25210.

(37) Petrus, M. L.; Schutt, K.; Sirtl, M. T.; Hutter, E. M.; Closs, A. C.; Ball, J. M.; Bijleveld, J. C.; Petrozza, A.; Bein, T.; Dingemans, T. J.; Savenije, T. J.; Snaith, H.; Docampo, P. New Generation Hole Transporting Materials for Perovskite Solar Cells: Amide-Based Small-Molecules with Nonconjugated Backbones. *Adv. Energy Mater.* 2018, 8, 1−11.

(38) Daskeviciene, M.; Paek, S.; Wang, Z.; Malinauskas, T.; Jokubauskaite, G.; Rakstys, K.; Cho, K. T.; Magomedov, A.; Jankauskas, V.; Ahmad, S.; Snaith, H. J.; Getautis, V.; Nazeeruddin, M. K. Carbazole-Based Enamine: Low-Cost and Efficient Hole Transporting Material for Perovskite Solar Cells. *Nano Energy* 2017, 32, 551−557.

(39) Vaitukaityte, D.; Wang, Z.; Malinauskas, T.; Magomedov, A.; Bubniene, G.; Jankauskas, V.; Getautis, V.; Snaith, H. J. Efficient and Stable Perovskite Solar Cells Using Low-Cost Aniline-Based Enamine Hole-Transporting Materials. *Adv. Mater.* 2018, 30, 1−7.

(40) Daskeviciute, S.; Momblona, C.; Rakstys, K.; Sutanto, A. A.; Daskeviciene, M.; Jankauskas, V.; Gruodis, A.; Bubniene, G.; Getautis, V.; Nazeeruddin, M. K. Fluorene-Based Enamines as Low-Cost and Dopant-Free Hole Transporting Materials for High Performance and Stable Perovskite Solar Cells. *J. Mater. Chem. A* 2021, 9, 301−309.

(41) Osedach, T. P.; Andrew, T. L.; Bulović, V. Effect of Synthetic Accessibility on the Commercial Viability of Organic Photovoltaics. *Energy Environ. Sci.* 2013, 6, 711−718.

(42) Petrus, M. L.; Bein, T.; Dingemans, T. J.; Docampo, P.; Low Cost, A. Azomethine-Based Hole Transporting Material for Perovskite Photovoltaics. *J. Mater. Chem. A* 2015, 3, 12159−12162.

(43) Malinauskas, T.; Tomkute-Luksiene, D.; Sens, R.; Daskeviciene, M.; Send, R.; Wonneberger, H.; Jankauskas, V.; Bruder, I.; Getautis, V. Enhancing Thermal Stability and Lifetime of Solid-State Dye-Sensitized Solar Cells via Molecular Engineering of the Hole-Transporting Material Spiro-OMeTAD. *ACS Appl. Mater. Interfaces* 2015, 7, 11107−11116.

(44) Additional Citation Recommendations. Gaussian 09 Citation Gaussian.com, https://gaussian.com/g09citation/ (accessed 2020-05-15).

(45) Liao, Y. L.; Hung, W. Y.; Hou, T. H.; Lin, C. Y.; Wong, K. T. Hole Mobilities of 2,7- And 2,2-Disubstituted 9,9′-Spirobifluorene-Based Triaryldiamines and Their Application as Hole Transport Materials in OLEDs. *Chem. Mater.* 2007, 19, 6350−6357.

(46) Qiu, J.; Liu, H.; Li, X.; Wang, S. Position Effect of Arylamine Branches on Pyrene-Based Dopant-Free Hole Transport Materials for Efficient and Stable Perovskite Solar Cells. *Chem. Eng. J.* 2020, 387, No. 123965.

104

(47) Liu, P.; Xu, B.; Hua, Y.; Cheng, M.; Aitola, K.; Sveinbjörnsson, K.; Zhang, J.; Boschloo, G.; Sun, L.; Kloo, L. Design, Synthesis and Application of a Π-Conjugated, Non-Spiro Molecular Alternative as Hole-Transport Material for Highly Efficient Dye-Sensitized Solar Cells and Perovskite Solar Cells. *J. Power Sources* **2017**, *344*, 11−14.

(48) Wang, S.; Sina, M.; Parikh, P.; Uekert, T.; Shahbazian, B.; Devaraj, A.; Meng, Y. S. Role of 4-Tert-Butylpyridine as a Hole Transport Layer Morphological Controller in Perovskite Solar Cells. *Nano Lett.* **2016**, *16*, 5594−5600.

(49) Daskeviciene, M.; Paek, S.; Magomedov, A.; Cho, K. T.; Saliba, M.; Kizeleviciute, A.; Malinauskas, T.; Gruodis, A.; Jankauskas, V.; Kamarauskas, E.; Nazeeruddin, M. K.; Getautis, V. Molecular Engineering of Enamine-Based Small Organic Compounds as Hole-Transporting Materials for Perovskite Solar Cells. *J. Mater. Chem. C* **2019**, *7*, 2717−2724.

(50) Urbani, M.; De La Torre, G.; Nazeeruddin, M. K.; Torres, T. Phthalocyanines and Porphyrinoid Analogues as Hole-and Electron-Transporting Materials for Perovskite Solar Cells. *Chem. Soc. Rev.* **2019**, *48*, 2738−2766.

(51) Habisreutinger, S. N.; Noel, N. K.; Snaith, H. J. Hysteresis Index: A Figure without Merit for Quantifying Hysteresis in Perovskite Solar Cells. *ACS Energy Lett.* **2018**, *3*, 2472−2476.

(52) Guarnera, S.; Abate, A.; Zhang, W.; Foster, J. M.; Richardson, G.; Petrozza, A.; Snaith, H. J. Improving the Long-Term Stability of Perovskite Solar Cells with a Porous Al2O3 Buffer Layer. *J. Phys. Chem. Lett.* **2015**, *6*, 432−437.

(53) Domanski, K.; Correa-Baena, J. P.; Mine, N.; Nazeeruddin, M. K.; Abate, A.; Saliba, M.; Tress, W.; Hagfeldt, A.; Grätzel, M. Not All That Glitters Is Gold: Metal-Migration-Induced Degradation in Perovskite Solar Cells. *ACS Nano* **2016**, *10*, 6306−6314.

105

Molecular Engineering of Enamine-Based Hole-Transporting Materials for High-Performing Perovskite Solar Cells: Influence of the Central Heteroatom

Deimante Vaitukaityte, Minh Anh Truong, Kasparas Rakstys,* Richard Murdey, Tsukasa Funasaki, Takumi Yamada, Yoshihiko Kanemitsu, Vygintas Jankauskas, Vytautas Getautis,* and Atsushi Wakamiya*

Stabilizing the high-performing perovskite solar cells (PSCs) with low-cost and simply affordable hole-transporting materials (HTMs) has been identified as an ongoing ambitious challenge. Herein, a series of enamine-based HTMs having different central heteroatoms (C, N, O, and S) and a number of enamine branches is designed and synthesized. The impact of varied central heteroatom cores is investigated in-depth including thermal, photophysical, and photovoltaic properties. Importantly, molecularly engineered HTMs are obtained by a single condensation reaction without the need for expensive catalysts, inert reaction conditions, or tedious product purification. PSCs with a power conversion efficiency (PCE) of over 20% can be realized with the triphenylamine core HTM (V1435), a result comparable with spiro-OMeTAD. HTMs based on tetraphenylmethane (V1431) and diphenyl sulfide (V1434) cores give a slightly lower performance under similar device fabrication conditions. This work demonstrates how rational molecular engineering of a simple condensation approach can produce HTMs for high-performing PSCs without sacrificing the PCE.

1. Introduction

Organic–inorganic metal halide perovskites are employed as efficient light absorbing materials due to their high absorption coefficient, long carrier diffusion length, small exciton binding energy, and high charge carrier mobility.[1–8] The remarkable power conversion efficiency (PCE) of perovskite solar cells (PSCs) of 25.8% has been achieved.[9] In a conventional n–i–p device, a perovskite light-absorbing layer is sandwiched between an electron-transporting material (ETM) and a hole-transporting material (HTM). HTMs facilitate photogenerated hole transport toward the counter electrode and block electron transfer back from the perovskite layer.[10,11] They can also prevent water ingress into the hygroscopic perovskite layer.[12] Accordingly, the proper incorporation of an appropriate HTM can significantly improve the stability of PSC devices.[13,14] The most common HTM used in PSCs is 2,2′,7,7′-tetrakis-(N,N-di-p-methoxyphenylamine)-9,9′-spirobifluorene (spiro-OMeTAD). This compound combines high solubility, good film-forming ability, and suitable frontier molecular orbitals energy levels, resulting in excellent performance and ease of use.[15–17] However, the synthesis of spiro-OMeTAD is expensive and its purification is tedious, which limits its application to the large-scale fabrication of PSCs.[18,19] Although many HTMs with comparable performance with spiro-OMeTAD have been reported, multistep synthetic procedures are still required in most cases.[20–22] More work is, therefore, needed to develop truly low-cost and efficient HTMs needed for the commercialization of PSCs.

Among the HTMs which have been reported to date, star-shaped molecules with their nonplanar structures and relatively large molecular volumes exhibit higher stability of the amorphous state compared with those of linear molecules[23,24] and, as a result, have consistently demonstrated better performance in PSCs.[22] Triphenylamine is one of the most well-known building blocks for efficient star-shaped HTMs because of its low ionization potential, excellent charge transport properties, and desirable thin-film morphology.[25–27] In addition, four-fold symmetrical tetraphenylmethane has also been reported to be an effective skeleton for improving thermal properties and providing good contact with different layers in organic solar cells[28] or PSCs.[29]

Many studies have shown that the properties of HTMs can be improved through modification of the central group.[30–35]

D. Vaitukaityte, K. Rakstys, V. Getautis
Department of Organic Chemistry
Kaunas University of Technology
50254 Kaunas, Lithuania
E-mail: kasparas.rakstys@ktu.lt; vytautas.getautis@ktu.lt

M. A. Truong, R. Murdey, T. Funasaki, T. Yamada, Y. Kanemitsu,
A. Wakamiya
Institute for Chemical Research
Kyoto University
Kyoto 611-0011, Japan
E-mail: wakamiya@scl.kyoto-u.ac.jp

V. Jankauskas
Institute of Chemical Physics
Vilnius University
Vilnius 10257, Lithuania

However, HTMs are typically assembled by connecting prebrominated central units to diphenylamine or borylated triphenylamine via Buchwald–Hartwig C–N or Suzuki–Miyaura C–C cross-coupling chemistry. Such coupling reactions require inert reaction conditions, expensive transition metal catalysts, and time-consuming purification procedures—including sublimation or repeated column chromatography—due to the inherent formation of side products. Moreover, residues of the metal catalyst may act as charge carrier-trapping sites and negatively affect the performance of the resulting PSC devices.[36,37] Therefore, efficient HTMs, which can be prepared by simple, cost-effective, and green chemistry, are required.[14,38,39] In this sense, enamine condensation has several advantages over transition metal-catalyzed reactions; first, expensive catalysts are not required, and second, water is the only side product. Moreover, simple product workup and purification may significantly reduce the cost of the final product.[18,40,41]

Herein, a new series of the enamine-based HTMs was prepared in a simple condensation reaction from commercially available materials without the use of expensive transition metal catalysts. The new HTMs comprise different central heteroatom and enamine branches. Oxygen (O),[42,43] sulfur (S),[44–46] and nitrogen (N)[47,48] heteroatoms in the HTM structure are reported to efficiently passivate the undercoordinated Pb^{2+}, suppressing nonradiative losses at the perovskite/HTM interface and improving the open-circuit voltage (V_{oc}) and overall efficiency of the PSC devices. Also, heteroatom substitution can modify the frontier orbital energy, leading to more effective alignment with the perovskite valence band (VB).[49–51] It was found that among the synthesized enamine-based compounds, the N-core-based V1435 has the highest glass transition temperature and hole drift mobility and the most suitable ionization potential. PCEs over 20% were achieved in PSCs fabricated using V1435. This is the highest efficiency among previously published enamine-based HTMs.[40,41,52] These results demonstrate that effective modification of the enamine-based HTMs with selected heteroatoms leads to highly efficient devices with strong potential as low-cost semiconductors for large-scale commercial fabrication.

2. Results and Discussion

Figure 1 shows the chemical structures containing modulated central fragments of diphenyl ether, diphenyl sulfide, triphenylamine, and tetraphenylmethane equipped with the different numbers of enamine arms coded V1433, V1434, V1435, and V1431, respectively. Four HTMs were synthesized by simply condensing aminated precursors with 2,2-bis(4-methoxyphenyl) acetaldehyde.[52] The enamine condensation reaction was performed under ambient conditions and water is the only side-product, being separated using a Dean–Stark trap that accelerates the formation of the final products. Detailed synthesis and molecular characterization are described in Supporting Information. The chemical structures were verified by NMR spectroscopy, mass spectrometry, and elemental analysis.
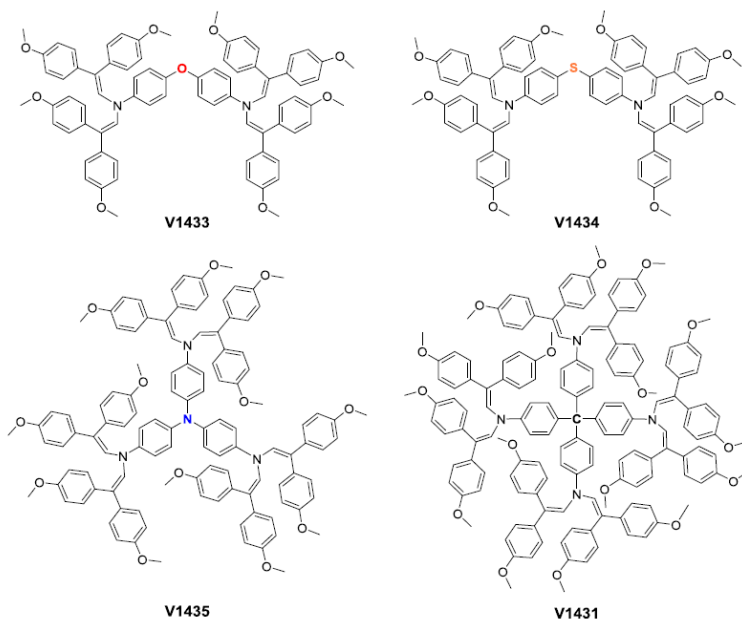

Figure 1. Chemical structures of HTMs containing different central heteroatoms and degree of enamine branches.

Thermal properties of enamine-based HTMs were evaluated by thermogravimetric analysis (TGA) and differential scanning calorimetry (DSC) in nitrogen atmosphere at a heating rate of 10 °C min^{-1}. The results are shown in **Figure** 2a, and S1, Supporting Information, and summarized in **Table** 1. The thermal decomposition temperatures (T_{dec}) corresponding to 5% weight loss of V1431, V1435, V1433, and V1434 were estimated to be 413, 415, 409, and 413 °C, respectively, indicating that all synthesized HTMs possess sufficient thermal stability for the typical processing conditions of PSCs. During the second heating

scan of the DSC measurement, C-cored V1431 shows only one endothermic peak corresponding to a melting process at a temperature of 339 °C, while O-cored V1433 exhibits a complex thermal behavior with three continuous processes: a glass transition (T_g) at 130 °C, followed by a cold crystallization at 270 °C and melting at 295 °C. In contrast, for N- and S-cored HTMs (V1435, V1434), only the glass transition was observed at 130 and 125 °C, respectively. The T_g of these HTMs is slightly higher than that of spiro-OMeTAD (124 °C)[53] and should result in improved film morphology.
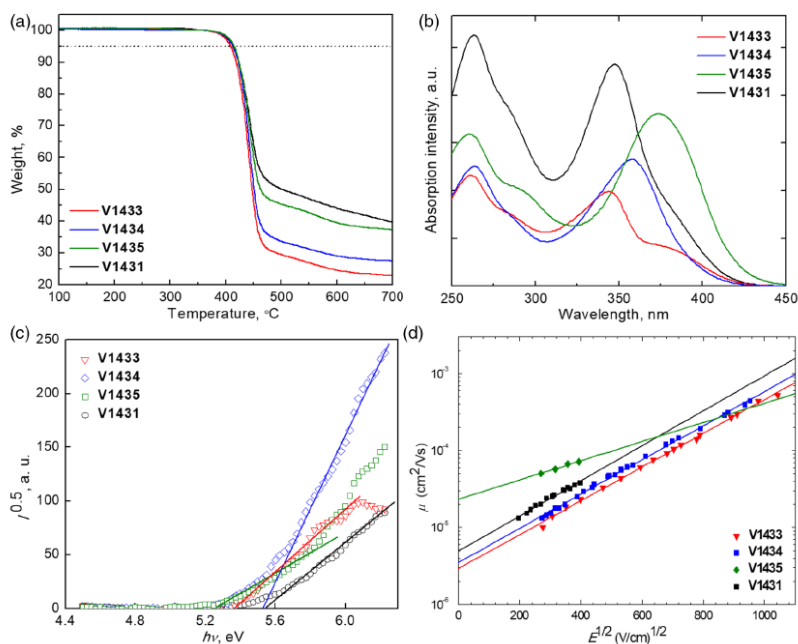
Figure 2. a) TGA data (heating rate of 10 °C min^{-1}, N$_2$ atmosphere); b) Absorption spectra in THF solutions (10^{-4} M); c) the PESA spectra; and d) electric field dependencies of the hole-drift mobility of V1433, V1434, V1435, and V1431.

Table 1. Thermal, optical, and photophysical properties of enamine-based compounds.

HTM	T_m [°C][a]	T_c [°C][a]	T_g [°C][a]	T_{dec} [°C][a]	λ_{max} [nm][b]	I_P [eV][c]	E_g [eV][d]	E_{ea} [eV][e]	μ_0 [cm^2 V^{-1} s^{-1}][f]
V1433	295	270	130	409	261, 344	5.37	2.97	2.40	3.0 × 10^{-6}
V1434	–	–	125	413	264, 357	5.52	2.99	2.53	3.5 × 10^{-6}
V1435	–	–	130	415	260, 373	5.27	2.88	2.39	2.0 × 10^{-5}
V1431	339	–	–	413	263, 347	5.54	3.02	2.52	5.0 × 10^{-6}

[a]Melting (T_m), crystallization (T_c), and glass transition (T_g) temperatures were observed from the second heating scan of DSC. Decomposition (T_{dec}) temperatures were observed from TGA measurements (10 °C min^{-1}, N$_2$ atmosphere). [b]Absorption spectra were measured in THF solutions (10^{-4} M). [c]Ionization potentials of the films were measured using the PESA. [d]E_g was estimated from the intersection of absorption and emission spectra of solid films. [e]$E_{ea} = I_P - E_g$. [f]Hole drift mobility value at zero field strength.

Ultraviolet–visible (UV–vis) absorption spectra were measured for the compounds in THF solution. The spectra are shown in Figure 2b and the related data are summarized in Table 1. The absorption maximum (λ_{max}) was observed at 344, 347, 357, and 373 nm for V1433, V1431, V1434, and V1435, respectively. A bathochromic shift of around 20 nm is observed for the N-cored V1435 in comparison with the other molecules due to enhanced π-conjugation. The optical gaps (E_g) were calculated from the intersection of absorption and photoluminescence spectra of thin films and were found to be similar for all the compounds at around 3.0 eV (Figure S2, Supporting Information). To interpret the absorption spectra of these molecules, time-dependent density functional theory (TD-DFT) calculations at the CAM-B3LYP/6-31G(d)//B3LYP/6-31G(d) level of theory were performed (see Table S1–S4, Figure S3–S6, Supporting Information). The singlet-excited electronic states were labeled as S_n. For C-cored V1431, an intense absorption band at 347 nm was ascribed to the electronic transition $S_0 \rightarrow S_4$, whereas the shoulder at around 390 nm was attributed to the electronic transitions to lower excited states ($S_0 \rightarrow S_n$, $n = 1, 2$, and 3). Similarly, in case of N-cored V1435, it was found that electronic transitions to highly excited states ($S_0 \rightarrow S_n$, $n = 4, 5$) were associated with an intense absorption band at 373 nm. However, the $S_0 \rightarrow S_n$ ($n = 1, 2$, and 3) transitions have very low oscillator strength; thus, they cannot be observed in the absorption band of V1435. In contrast, for O- and S-cored HTM (V1433, V1434), the broad band in the 325–400 nm range could be attributed to electronic transitions $S_0 \rightarrow S_n$ ($n = 1, 2$, and 3).

The solid-state ionization potentials (I_P) of V1435, V1433, V1434, and V1431 were measured using photoelectron spectroscopy in air (PESA). As shown in Figure 2c, the highest occupied molecular orbital (HOMO) energy levels of V1435, V1433, V1434, and V1431 was determined to be −5.27, −5.37, −5.52, and −5.54 eV, respectively. The HOMO energy level is shifted to be deeper as the electron density of the central atom is reduced. The lowest unoccupied molecular orbital (LUMO), calculated from the optical gap and ionization potential, is −2.39, −2.40, −2.53, and −2.52 eV for V1435, V1433, V1434, and V1431, respectively. These HOMO and LUMO energy levels of these enamine derivatives are suitable for the application in the PSCs.[21]

To evaluate the charge transporting properties, the hole drift mobilities of the undoped films were measured by xerographic time of flight (XTOF). As shown in Figure 2d and Table 1, the zero-field hole drift mobility (μ_0) of V1435 is 2.0×10^{-5} cm^2 V^{-1} s^{-1}, one order of magnitude higher than those of the other compounds and similar to that of spiro-OMeTAD reported elsewhere.[19]

The reorganization energies (λ_{reorg}) of these enamine-based molecules and spiro-OMeTAD, which represent their relaxation after oxidation (Figure S7, Supporting Information), were calculated using the B3LYP/6-31 G(d) level of theory and are summarized in Table S5, Supporting Information. Generally, according to the Marcus theory, small reorganization energy implies a fast hole transfer rate. As shown in Table S5, Supporting Information, the reorganization energies of V1431, V1434, V1433, V1435, and spiro-OMeTAD are 74, 125, 132, 170, and 145 meV, respectively. Thus, the hole mobility of C-cored V1431 might be expected to be superior to the S- and O-cored molecules (V1434, V1433). While the high mobility of V1431 was confirmed by the XTOF experiments, N-cored V1435 with $\lambda_{reorg} = 170$ meV also shows high mobility. In this case, the high mobility could be explained by strong electronic coupling between neighboring V1435 molecules.

To evaluate the potential use of the new enamine-based HTMs in PSCs, the conventional n–i–p structure was used. The device stack is indium tin oxide (ITO)-coated glass substrate/SnO$_2$/perovskite/HTM/gold electrode (Figure 3a). Reference devices using spiro-OMeTAD as the HTMs were prepared with the same fabrication process for comparison. The fabrication process for PSC devices is provided in the SI. HTMs were dissolved in chlorobenzene (0.02 M for the enamine-based HTM and 0.06 M for spiro-OMeTAD), together with the following dopants and additives: an oxidizing agent tris(2-(1 H-pyrazol-1-yl)-4-tert-butylpyridine)cobalt(III) tri[bis(trifluoromethane)sulfonimide] (Co(III) TFSI, 0.15 equiv), lithium bis(trifluoromethanesulfonyl)imide (LiTFSI, 0.54 equiv), and 4-tert-butylpyridine (tBP, 3.3 equiv). The water contact angle of V1433, V1434, V1431, and V1435 was estimated to be 82°, 76°, 74°, and 72°, respectively (Figure S8, Supporting Information), indicating similar wettability to that of spiro-OMeTAD (76°).[12] Unfortunately, V1433 did not form a smooth film due to its poor solubility in either chlorobenzene or 1,2-dichlorobenzene (Figure S9, Supporting Information). Therefore, PSC devices based on V1433 could not be fabricated. As we already reported previously,[54] efficient hole extraction from the perovskite layer requires that the
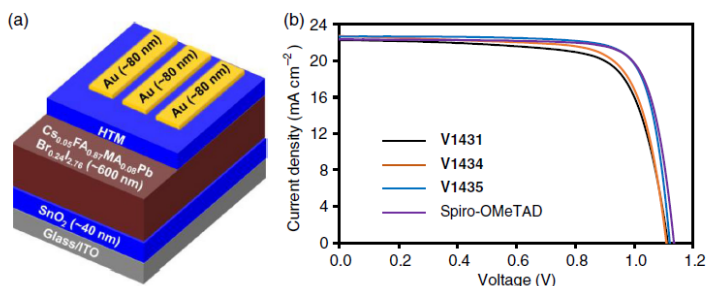

Figure 3. a) The solar cell structure used in this study. b) The forward scan J–V curves of the champion devices fabricated using different HTMs.

109

HOMO energy level of the HTM be at least 0.1 eV higher than the VB of perovskite. Therefore, considering that the HOMO energy level of these enamine-based HTMs is in the range of -5.27 to $5.54\,eV$, a mixed-composition $Cs_{0.05}FA_{0.87}MA_{0.08}PbBr_{0.24}I_{2.76}$ perovskite material with a relatively deep VB level of $-5.68\,eV$ was used as the absorber layer in the PSCs prepared in this work.[55]

The HTM layer plays an important role in both transporting holes to the counter electrode and preventing direct contact between the perovskite layer and the electrode. While a thin HTM layer could facilitate hole transport, it might reduce the uniformity of coverage. In contrast, a thicker HTM layer would uniformly cover the perovskite surface but retard hole transport due to the low hole mobility of HTM. Therefore, the thickness of the HTM layer needs to be carefully optimized to obtain full coverage of the perovskite layer without sacrificing the hole transporting ability.[56] The thickness of the HTM films was optimized for PSC performance by adjusting the speed during spin coating. Cross-sectional and top-view scanning electron microscopy (SEM) images were measured to determine the thickness, coverage, and morphology of the HTM layers (Figure S10–S17, Supporting Information). The detailed results for HTM thickness optimization are provided in Figure S18–S21, and Table S6–S9, Supporting Information. All the thickness-optimized HTM films were observed to uniformly cover the perovskite layer. Although a thick layer of spiro-OMeTAD ($\approx$200 nm) is typically required to obtain high-performance PSCs with high reproducibility,[57] we found that devices using enamine-based HTMs could achieve comparable performance with thinner HTM layers. The optimal thickness of V1431, V1434, and V1435 was estimated to be around 160, 55, and 130 nm, respectively.

The performance of the PSC devices was evaluated under AM1.5 G simulated sunlight. The current density–voltage (J–V) curves in the forward scan of the champion devices for each HTM are shown in Figure 3b, and the photovoltaic parameters are summarized in Table 2.

The best PCE for V1435, V1434, and V1431 obtained from the forward scan was 20.1%, 18.6%, and 18.0%, respectively. The average forward scan PCE was calculated to be 19.3%, 17.4%, and 17.6% for V1435, V1434, and V1431, respectively. All devices show small hysteresis. The hysteresis index of V1431, V1434,

V1435, and spiro-OMeTAD-based devices was calculated to be -0.028, -0.022, -0.046, and -0.020, respectively. It is noted that the obtained result for V1435 is the highest performance compared with previously published enamine-based HTMs.[40,41,52] The performance drop is mainly due to the loss of fill factor (V1435: 0.79, V1434: 0.74, and V1431: 0.73). The high fill factor of V1435 can be explained by its high hole mobility.

The J_{SC} values estimated from the J–V curves are consistent with the integrated current densities derived from the incident photon-to-current efficiency (IPCE) measurements (Figure S18–S21, Supporting Information). Overall, the performance of the devices using the enamine-based HTMs was comparable with the spiro-OMeTAD-based devices (Figure S22, Supporting Information). The HTMs with N- and C-central atoms (V1435, V1431) showed slightly better performance than the S-cored variant (V1434).

While HTMs with deeper HOMO levels are expected to align more effectively with the perovskite VB and result in higher V_{OC} values, this trend was not observed in our study. The V_{OC} of V1431 and V1434 are both 1.11 V; these values are slightly lower than those of V1435 and the devices with spiro-OMeTAD (V1435:1.12 V, spiro-OMeTAD: 1.13 V) despite their deeper HOMO values. The absence of a correlation between the HOMO energy levels of HTMs and the V_{OC} of the corresponding devices may be due to high variability in the quality of the perovskite/HTM interface for different materials.[58,59] Any dependence on the energy-level offset would be obscured if the charge recombination is dominated by a strongly variable interface trap density.

Complex impedance plots for devices with V1431, V1434, V1435, and spiro-OMeTAD HTM taken under AM1.5 G are shown in Figure S23, Supporting Information. Impedance measurements can reveal differences in the electrical characteristics of the device and materials that may not be readily apparent in the experimental J–V curves, which are all closely comparable. The data are analyzed with a simple equivalent circuit with series and parallel resistances and a single-capacitive element. Under low applied voltage, the parallel resistance reflects leakage or recombination currents, larger values indicating either superior quality of the perovskite layer or more efficient charge extraction from the perovskite absorber into the transport layers. The estimated

Table 2. Photovoltaic parameters of PSCs using different HTMs derived from J–V measurements.

HTM[a]	Scan[b]	J_{sc} [mA cm^{-2}][c]	V_{oc} [V][c]	FF[c]	PCE [%][c]	HI[d]
V1431	Forward	22.3 (22.1 ± 0.2)	1.11 (1.11 ± 0.01)	0.73 (0.72 ± 0.02)	18.0 (17.6 ± 0.3)	−0.028
	Reverse	22.2 (22.0 ± 0.2)	1.12 (1.11 ± 0.01)	0.71 (0.69 ± 0.02)	17.5 (16.7 ± 0.5)	
V1434	Forward	22.7 (22.6 ± 0.1)	1.11 (1.09 ± 0.04)	0.74 (0.70 ± 0.03)	18.6 (17.4 ± 1.1)	−0.022
	Reverse	22.3 (22.3 ± 0.2)	1.09 (1.10 ± 0.03)	0.74 (0.72 ± 0.03)	18.2 (17.7 ± 1.3)	
V1435	Forward	22.7 (22.2 ± 0.3)	1.12 (1.12 ± 0.01)	0.79 (0.78 ± 0.01)	20.1 (19.3 ± 0.5)	−0.046
	Reverse	22.6 (22.2 ± 0.3)	1.12 (1.11 ± 0.01)	0.76 (0.74 ± 0.01)	19.2 (18.3 ± 0.5)	
Spiro-OMeTAD	Forward	22.4 (22.2 ± 0.1)	1.13 (1.13 ± 0.01)	0.79 (0.78 ± 0.01)	20.1 (19.6 ± 0.2)	−0.020
	Reverse	22.3 (22.2 ± 0.1)	1.13 (1.12 ± 0.01)	0.78 (0.77 ± 0.01)	19.7 (19.2 ± 0.3)	

[a]HTM concentration: 0.02 M for V1431, V1434, and V1435, 0.06 M for spiro-OMeTAD. The optimal thickness is 160, 55, 130, and 215 nm for V1431, V1434, V1435, and spiro-OMeTAD, respectively. [b]Forward and reverse indicate the scan direction from J_{SC} to V_{OC} and from V_{OC} to J_{SC}, respectively. [c]The average and standard deviation values were calculated from nine devices. [d]Hysteresis index (HI) = $(PCE_{Reverse} - PCE_{Forward})/PCE_{Reverse}$.

110
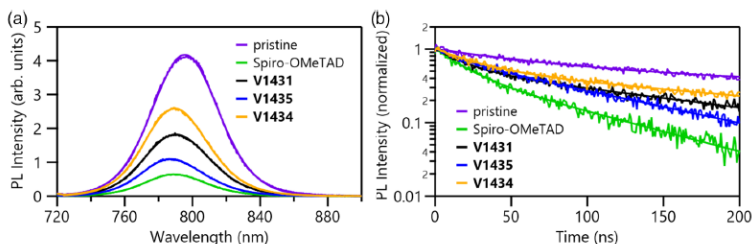
Figure 4. a) Steady-state PL spectra and b) time-resolved PL spectra of the pristine perovskite ($Cs_{0.05}FA_{0.87}MA_{0.08}PbBr_{0.24}I_{2.76}$) and perovskite/HTM films excited at 688 nm with an excitation fluence of 100 nJ cm^{-2}.

parallel resistances of V1431 (98 Ω cm^2), V1434 (44 Ω cm^2), and V1435 (87 Ω cm^2) are all lower than spiro-OMeTAD (157.5 Ω cm^2). While this is consistent overall with the lower measured PCE realized with the newly synthesized HTMs, no correlations could be drawn between the parallel resistance value and any feature of the experimental J–V curves. The series resistance for the V1431, V1434, V1435, and spiro-OMeTAD devices was estimated at 2.0, 1.2 1.1, and 1.0 Ω cm^2 respectively. Here, we can clearly differentiate between the V1434, V1435 HTMs, which have comparable conductance to the spiro-OMeTAD reference, and the V1431 HTM, which has a substantially lower conductance. The higher series resistance of the V1431 HTM can explain the slightly lower fill factor (FF) observed for the corresponding devices (see Table 2).

Following the impedance measurements, the operational stability of the devices was assessed by running them at the maximum power point under AM1.5G for 10 h. The results are shown in Figure S24, Supporting Information. The stability of the V1431- and V1435-based devices is comparable with spiro-OMeTAD and higher than that of the V1434-based devices.

As stability is important for PSCs, a thermal durability test on the unencapsulated devices with different HTMs was performed under ambient atmosphere (room humidity = 55%) (Figure S25, Supporting Information). After heating the devices at 100 °C for 1 h, the efficiency of the device using V1431 is largely unchanged. In contrast, under the same conditions, the efficiency of the devices using V1435, spiro-OMeTAD, and V1434 drops to 86%, 68%, and 47% of the initial efficiency, respectively. The higher thermal stability of V1431- and V1435-based devices is a result of the more stable amorphous phase of these materials compared with V1434 and spiro-OMeTAD.

The hole extraction properties of the HTMs were further investigated by performing steady-state photoluminescence (PL) quenching measurements on quartz/perovskite and quartz/perovskite/HTM samples.[60] The PL peak of the pristine perovskite film was observed at 795 nm. After fabricating HTMs on perovskite layers, the PL peak intensity was reduced to 62%, 44%, 26%, and 15% for V1434, V1431, V1435, and spiro-OMeTAD, respectively (**Figure 4**a). The strong PL quenching indicated that hole extraction into V1435 proceeds more efficiently than with V1431 and V1434. The higher V_{OC} and FF of the corresponding devices can be rationalized in terms of the improved hole extraction.

The trend was further confirmed by time-resolved PL (TRPL) decay measurements. The PL lifetime for the pristine perovskite film was 192 ns and in the perovskite/HTM films decreased to 130, 96, 76, and 47 ns for V1434, V1431, V1435, and spiro-OMeTAD, respectively (Figure 4b).

3. Conclusion

A new series of enamine-based HTMs was designed and synthesized via a simple condensation reaction. The influence of heteroatoms in the enamine core was systematically investigated by thermal, photophysical, and photovoltaic measurements. It was found that compared with the hydrocarbon compound (V1431) or the variant with sulfur heteroatom (V1434), the enamine-based HTM with nitrogen heteroatom (V1435) resulted in a higher glass transition temperature, more suitable ionization potential for perovskite applications, and higher hole drift mobility. The maximum PCE of devices using V1435 as the HTM exceeded 20%. To the best of our knowledge, this is the highest reported performance for enamine-based HTMs. The performance and stability of V1435 were similar to spiro-OMeTAD reference devices fabricated under the same conditions. This study demonstrates that the combination of the finely tuned core structure and simple enamine condensation chemistry is a beneficial approach to afford HTMs for high-performing and stable PSCs.

111

Conflict of Interest

The authors declare no conflict of interest.

Data Availability Statement

The data that support the findings of this study are available on request from the corresponding author. The data are not publicly available due to privacy or ethical restrictions.

Keywords

[1] A. Kojima, K. Teshima, Y. Shirai, T. Miyasaka, *J. Am. Chem. Soc.* **2009**, *131*, 6050.

[2] H. Oga, A. Saeki, Y. Ogomi, S. Hayase, S. Seki, *J. Am. Chem. Soc.* **2014**, *136*, 13818.

[3] S. D. Stranks, G. E. Eperon, G. Grancini, C. Menelaou, M. J. P. Alcocer, T. Leijtens, L. M. Herz, A. Petrozza, H. J. Snaith, *Science* **2013**, *342*, 341.

[4] J. Burschka, N. Pellet, S. J. Moon, R. Humphry-Baker, P. Gao, M. K. Nazeeruddin, M. Grätzel, *Nature* **2013**, *499*, 316.

[5] N. J. Jeon, J. H. Noh, W. S. Yang, Y. C. Kim, S. Ryu, J. Seo, S. Il Seok, *Nature* **2015**, *517*, 476.

[6] M. Saliba, T. Matsui, J. Y. Seo, K. Domanski, J. P. Correa-Baena, M. K. Nazeeruddin, S. M. Zakeeruddin, W. Tress, A. Abate, A. Hagfeldt, M. Grätzel, *Energy Environ. Sci.* **2016**, *9*, 1989.

[7] C. Wehrenfennig, G. E. Eperon, M. B. Johnston, H. J. Snaith, L. M. Herz, *Adv. Mater.* **2014**, *26*, 1584.

[8] M. M. Lee, J. Teuscher, T. Miyasaka, T. N. Murakami, H. J. Snaith, *Science* **2012**, *338*, 643.

[9] H. Min, D. Y. Lee, J. Kim, G. Kim, K. S. Lee, J. Kim, M. J. Paik, Y. K. Kim, K. S. Kim, M. G. Kim, T. J. Shin, S. Il Seok, *Nature* **2021**, *598*, 444.

[10] J. Seo, J. H. Noh, S. Il Seok, *Acc. Chem. Res.* **2016**, *49*, 562.

[11] L. Calió, S. Kazim, M. Grätzel, S. Ahmad, *Angew. Chem. Int. Ed.* **2016**, *55*, 14522.

[12] M. Jeong, I. W. Choi, E. M. Go, Y. Cho, M. Kim, B. Lee, S. Jeong, Y. Jo, H. W. Choi, J. Lee, J. H. Bae, S. K. Kwak, D. S. Kim, C. Yang, *Science* **2020**, *369*, 1615.

[13] M. Jeong, I. W. Choi, K. Yim, S. Jeong, M. Kim, S. J. Choi, Y. Cho, J. H. An, H. B. Kim, Y. Jo, S. H. Kang, J. H. Bae, C. W. Lee, D. S. Kim, C. Yang, *Nat. Photonics* **2022**, *16*, 119.

[14] S. Daskeviciute-Geguziene, Y. Zhang, K. Rakstys, G. Kreiza, S. B. Khan, H. Kanda, S. Paek, M. Daskeviciene, E. Kamarauskas, V. Jankauskas, A. M. Asiri, V. Getautis, M. K. Nazeeruddin, *Angew. Chem. Int. Ed.* **2022**, *61*, e202113207.

[15] T. Bu, J. Li, H. Li, C. Tian, J. Su, G. Tong, L. K. Ono, C. Wang, Z. Lin, N. Chai, X. L. Zhang, J. Chang, J. Lu, J. Zhong, W. Huang, Y. Qi, Y. B. Cheng, F. Huang, *Science* **2021**, *372*, 1327.

[16] F. M. Rombach, S. A. Haque, T. J. Macdonald, *Energy Environ. Sci.* **2021**, *14*, 5161.

[17] J. Jeong, M. Kim, J. Seo, H. Lu, P. Ahlawat, A. Mishra, Y. Yang, M. A. Hope, F. T. Eickemeyer, M. Kim, Y. J. Yoon, I. W. Choi, B. P. Darwich, S. J. Choi, Y. Jo, J. H. Lee, B. Walker, S. M. Zakeeruddin, L. Emsley, U. Rothlisberger, A. Hagfeldt, D. S. Kim, M. Grätzel, J. Y. Kim, *Nature* **2021**, *592*, 381.

[18] D. Vaitukaityte, Z. Wang, T. Malinauskas, A. Magomedov, G. Bubniene, V. Jankauskas, V. Getautis, H. J. Snaith, *Adv. Mater.* **2018**, *30*, 1803735.

[19] P. Gratia, A. Magomedov, T. Malinauskas, M. Daskeviciene, A. Abate, S. Ahmad, M. Grätzel, V. Getautis, M. K. Nazeeruddin, *Angew. Chem. Int. Ed.* **2015**, *54*, 11409.

[20] K. Rakstys, C. Igci, M. K. Nazeeruddin, *Chem. Sci.* **2019**, *10*, 6748.

[21] J. Urieta-Mora, I. García-Benito, A. Molina-Ontoria, N. Martín, *Chem. Soc. Rev.* **2018**, *47*, 8541.

[22] X. Yin, Z. Song, Z. Li, W. Tang, *Energy Environ. Sci.* **2020**, *13*, 4057.

[23] M. W. An, B. S. Wu, S. Wang, Z. C. Chen, Y. Su, L. L. Deng, S. H. Li, Z. A. Nan, H. R. Tian, X. L. Liu, D. Q. Yun, Q. Zhang, S. Y. Xie, L. S. Zheng, *Cell Rep. Phys. Sci.* **2021**, *2*, 100662.

[24] Y. Shirota, H. Kageyama, *Chem. Rev.* **2007**, *107*, 953.

[25] C. G. Zhan, J. A. Nichols, D. A. Dixon, *J. Phys. Chem. A* **2003**, *107*, 4184.

[26] A. N. Sobolev, V. K. Belsky, I. P. Romm, N. Y. Chernikova, E. N. Guryanova, *Acta Crystallogr. Sect. C Cryst. Struct. Commun.* **1985**, *41*, 967.

[27] F. Liu, F. Wu, W. Ling, Z. Tu, J. Zhang, Z. Wei, L. Zhu, Q. Li, Z. Li, *ACS Energy Lett.* **2019**, *4*, 2514.

[28] H. Lin, S. Chen, H. Hu, L. Zhang, T. Ma, J. Y. L. Lai, Z. Li, A. Qin, X. Huang, B. Tang, H. Yan, *Adv. Mater.* **2016**, *28*, 8546.

[29] X. Liu, F. Kong, T. Cheng, W. Chen, Z. Tan, T. Yu, F. Guo, J. Chen, J. Yao, S. Dai, *ChemSusChem* **2017**, *10*, 968.

[30] H. D. Pham, L. Xianqiang, W. Li, S. Manzhos, A. K. K. Kyaw, P. Sonar, *Energy Environ. Sci.* **2019**, *12*, 1177.

[31] Z. Shariatinia, *Renew. Sustain. Energy Rev.* **2020**, *119*, 109608.

[32] M. Vasilopoulou, A. Fakharuddin, A. G. Coutsolelos, P. Falaras, P. Argitis, A. R. B. M. Yusoff, M. K. Nazeeruddin, *Chem. Soc. Rev.* **2020**, *49*, 4496.

[33] W. Wang, J. Zhou, W. Tang, *J. Mater. Chem. A* **2022**, *10*, 1150.

[34] W. Yan, D. Sui, Y. Yang, M. Chang, *Dye. Pigment.* **2022**, *200*, 110102.

[35] F. Wang, Y. Cao, C. Chen, Q. Chen, X. Wu, X. Li, T. Qin, W. Huang, *Adv. Funct. Mater.* **2018**, *28*, 1803753.

[36] K. Rakstys, M. Saliba, P. Gao, P. Gratia, E. Kamarauskas, S. Paek, V. Jankauskas, M. K. Nazeeruddin, *Angew. Chem. Int. Ed.* **2016**, *55*, 7464.

[37] Ö. Usluer, M. Abbas, G. Wantz, L. Vignau, L. Hirsch, E. Grana, C. Brochon, E. Cloutet, G. Hadziioannou, *ACS Macro Lett.* **2014**, *3*, 1134.

[38] M. L. Petrus, A. Music, A. C. Closs, J. C. Bijleveld, M. T. Sirtl, Y. Hu, T. J. Dingemans, T. Bein, P. Docampo, *J. Mater. Chem. A* **2017**, *5*, 25200.

[39] M. L. Petrus, K. Schutt, M. T. Sirtl, E. M. Hutter, A. C. Closs, J. M. Ball, J. C. Bijleveld, A. Petrozza, T. Bein, T. J. Dingemans, T. J. Savenije, H. Snaith, P. Docampo, *Adv. Energy Mater.* **2018**, *8*, 1801605.

[40] M. Daskeviciene, S. Paek, Z. Wang, T. Malinauskas, G. Jokubauskaite, K. Rakstys, K. T. Cho, A. Magomedov, V. Jankauskas, S. Ahmad, H. J. Snaith, V. Getautis, M. K. Nazeeruddin, *Nano Energy* **2017**, *32*, 551.

[41] S. Daskeviciute, C. Momblona, K. Rakstys, A. A. Sutanto, M. Daskeviciene, V. Jankauskas, A. Gruodis, G. Bubniene, V. Getautis, M. K. Nazeeruddin, *J. Mater. Chem. A* **2021**, *9*, 301.

112

[42] Y. Guo, L. He, J. Guo, Y. Guo, F. Zhang, L. Wang, H. Yang, C. Xiao, Y. Liu, Y. Chen, Z. Yao, L. Sun, *Angew. Chem. Int. Ed.* **2022**, *61*, e202114341.

[43] Q. Cao, Y. Li, H. Zhang, J. Yang, J. Han, T. Xu, S. Wang, Z. Wang, B. Gao, J. Zhao, X. Li, X. Ma, S. M. Zakeeruddin, W. E. I. Sha, X. Li, M. Grätzel, *Sci. Adv.* **2021**, *7*, 633.

[44] J. Zhang, Q. Sun, Q. Chen, Y. Wang, Y. Zhou, B. Song, X. Jia, Y. Zhu, S. Zhang, N. Yuan, J. Ding, Y. Li, *Sol. RRL* **2020**, *4*, 1900421.

[45] M. H. Li, T. G. Sun, J. Y. Shao, Y. D. Wang, J. S. Hu, Y. W. Zhong, *Nano Energy* **2021**, *79*, 105462.

[46] K. Jiang, J. Wang, F. Wu, Q. Xue, Q. Yao, J. Zhang, Y. Chen, G. Zhang, Z. Zhu, H. Yan, L. Zhu, H. L. Yip, *Adv. Mater.* **2020**, *32*, 1908011.

[47] X. Sun, Z. Li, X. Yu, X. Wu, C. Zhong, D. Liu, D. Lei, A. K. Y. Jen, Z. Li, Z. Zhu, *Angew. Chem. Int. Ed.* **2021**, *60*, 7227.

[48] W. Chen, Y. Shi, Y. Wang, X. Feng, A. B. Djurišić, H. Y. Woo, X. Guo, Z. He, *Nano Energy* **2020**, *68*, 104363.

[49] X. Zhang, X. Liu, N. Wu, R. Ghadari, M. Han, Y. Wang, Y. Ding, M. Cai, Z. Qu, S. Dai, *J. Energy Chem.* **2022**, *67*, 19.

[50] I. García-Benito, I. Zimmermann, J. Urieta-Mora, J. Aragó, J. Calbo, J. Perles, A. Serrano, A. Molina-Ontoria, E. Ortí, N. Martín, M. K. Nazeeruddin, *Adv. Funct. Mater.* **2018**, *28*, 1801734.

[51] Z. Hu, W. Fu, L. Yan, J. Miao, H. Yu, Y. He, O. Goto, H. Meng, H. Chen, W. Huang, *Chem. Sci.* **2016**, *7*, 5007.

[52] D. Vaitukaityte, C. Momblona, K. Rakstys, A. A. Sutanto, B. Ding, C. Igci, V. Jankauskas, A. Gruodis, T. Malinauskas, A. M. Asiri,

P. J. Dyson, V. Getautis, M. K. Nazeeruddin, *Chem. Mater.* **2021**, *33*, 6059.

[53] T. Malinauskas, D. Tomkute-Luksiene, R. Sens, M. Daskeviciene, R. Send, H. Wonneberger, V. Jankauskas, I. Bruder, V. Getautis, *ACS Appl. Mater. Interfaces* **2015**, *7*, 11107.

[54] H. Nishimura, N. Ishida, A. Shimazaki, A. Wakamiya, A. Saeki, L. T. Scott, Y. Murata, *J. Am. Chem. Soc.* **2015**, *137*, 15656.

[55] X. Zheng, Y. Hou, C. Bao, J. Yin, F. Yuan, Z. Huang, K. Song, J. Liu, J. Troughton, N. Gasparini, C. Zhou, Y. Lin, D. J. Xue, B. Chen, A. K. Johnston, N. Wei, M. N. Hedhili, M. Wei, A. Y. Alsalloum, P. Maity, B. Turedi, C. Yang, D. Baran, T. D. Anthopoulos, Y. Han, Z. H. Lu, O. F. Mohammed, F. Gao, E. H. Sargent, O. M. Bakr, *Nat. Energy* **2020**, *5*, 131.

[56] G.-W. Kim, D. V. Shinde, T. Park, *RSC Adv.* **2015**, *5*, 99356.

[57] M. Saliba, J. P. Correa-Baena, C. M. Wolff, M. Stolterfoht, N. Phung, S. Albrecht, D. Neher, A. Abate, *Chem. Mater.* **2019**, *31*, 8576.

[58] I. Gelmetti, N. F. Montcada, A. Pérez-Rodríguez, E. Barrena, C. Ocal, I. García-Benito, A. Molina-Ontoria, N. Martín, A. Vidal-Ferran, E. Palomares, *Energy Environ. Sci.* **2019**, *12*, 1309.

[59] A. Abdulimu, R. Sandoval-Torrientes, I. Zimmermann, J. Santos, M. K. Nazeeruddin, N. Martín, *J. Mater. Chem. A* **2020**, *8*, 1386.

[60] T. Handa, D. M. Tex, A. Shimazaki, A. Wakamiya, Y. Kanemitsu, *J. Phys. Chem. Lett.* **2017**, *8*, 954.

113

Enamine-Based Cross-Linkable Hole-Transporting Materials for Perovskite Solar Cells

Deimantė Vaitukaitytė, Amran Al-Ashouri, Marytė Daškevičienė, Egidijus Kamarauskas, Jonas Nekrasovas, Vygintas Jankauskas, Artiom Magomedov, Steve Albrecht, and Vytautas Getautis*

The development of the simple synthesis schemes of organic semiconductors can have an important contribution to the advancement of related technologies. In particular, one of the fields where the high price of the hole-transporting materials may become an obstacle toward successful commercialization is perovskite solar cells. Herein, enamine-based materials that are capable of undergoing cross-linking due to the presence of two vinyl groups are synthesized. It is shown that new compounds can be thermally polymerized, making the films resistant to organic solvents. This can allow the use of a wet-coating process for the deposition of the perovskite absorber film, without the need for orthogonal solvents. Cross-linked films are used in perovskite solar cells, and, upon optimization of the film thickness, the highest power conversion efficiency of 18.1% is demonstrated.

1. Introduction

Perovskite solar cells (PSCs) have recently demonstrated efficiencies comparable to those of the best Si-based technologies.[1] Among other things, further advancement of PSCs depends on the development of novel materials that can serve as efficient hole transporters.[2] However, the choice of organic hole-transporting materials (HTMs) that are able to deliver competitive performance

is still limited. Therefore, it is important to search for promising new organic materials.

As an additional constraint, to keep the transition from lab to fab as fast as possible, it is advantageous to maintain the simplicity of the organic materials as one of the highest priorities. It is thus necessary to use simple and short synthesis pathways because it was recently shown that multistep schemes lead to extremely high materials costs.[3] In addition, it is better to avoid the use of metal-catalyzed reactions, as metal traces are known to have detrimental effects on the performance of optoelectronic devices,[4] and therefore additional purification processes (e.g., sublimation[5]) are required, which further increases the price of the final material. In this context, condensational chemistry is giving possibilities to increase the π-conjugated system of the molecules in a simple way, with water as the only byproduct. The simplicity of the synthesis and purification can promote wider application of such materials.

One of the semiconducting material classes that fulfill the aforementioned requirements is enamines. Typically, they are synthesized from aromatic amine and aromatic ketone/aldehyde. First studies of their charge-transporting abilities were reported in the 1980s,[6–8] and since then they have been successfully incorporated in electrophotographic devices[9] and organic light-emitting diodes,[10] and recently they have been reported to show good performance in PSCs.[11–13]

Depending on the order of the layers in the final device, PSCs are commonly divided into two large groups. Currently, the highest certified efficiency, published in peer-reviewed journals (22.7%), was achieved in a so-called regular or n–i–p configuration, where the HTM is deposited on top of the perovskite absorber layer.[14] As an alternative, in recent years, also p–i–n (or "inverted") configuration of PSCs was established, with efficiencies getting close to those of the best PSCs (highest published certified value of 22.3%),[15] and in addition, having advantages in tandem applications.[16,17] In the case of p–i–n devices, solution processing of the perovskite absorber layer adds additional constraints on the choice of HTMs, as it usually should withstand a mixture of polar dimethylformamide: dimethyl sulfoxide (DMF:DMSO) solvents. The perovskite precursor solution has significantly lower ability to dissolve organic HTMs (Table S1, Supporting Information); however, it is enough to reduce the scope of the applicable materials. Therefore, so far

D. Vaitukaitytė, Dr. M. Daškevičienė, Dr. A. Magomedov, Prof. V. Getautis
Department of Organic Chemistry
Kaunas University of Technology
Radvilenu pl. 19, Kaunas LT-50254, Lithuania
E-mail: vytautas.getautis@ktu.lt

A. Al-Ashouri, Prof. S. Albrecht
Young Investigator Group Perovskite Tandem Solar Cells
Helmholtz-Zentrum Berlin
Kekuléstraße 5, 12489 Berlin, Germany

Dr. E. Kamarauskas, J. Nekrasovas, Dr. V. Jankauskas
Institute of Chemical Physics
Vilnius University
Sauletekio al. 3, Vilnius LT-10257, Lithuania

Prof. S. Albrecht
Faculty of Electrical Engineering and Computer Science
Technical University Berlin
Marchstraße 23, 10587 Berlin, Germany

ⓘ The ORCID identification number(s) for the author(s) of this article can be found under https://doi.org/10.1002/solr.202000597.

the most popular choice of organic HTMs for such devices is polymers, such as poly[bis(4-phenyl)(2,4,6-trimethylphenyl) amine][18] and poly(3,4-ethylenedioxythiophene) polystyrene sulfonate.[19] Recently, different small-molecule HTMs for p–i–n have been reported, such as MPA-BTTI,[20] BTF4,[21] and BDPSO;[22] however, their number is still rather limited due to the aforementioned restriction. Therefore, as an alternative, several strategies have been reported, e.g., change of the perovskite precursor solvent,[23] use of self-assembled monolayers,[24] and use of soluble precursors that are subsequently transformed into insoluble films.[25] In addition, recently cross-linkable HTMs were introduced into inverted devices, resulting in relatively high performance.[26] However, it was achieved using palladium-catalyzed reactions.

In this work, enamine-based cross-linkable HTMs, containing two vinyl groups, were synthesized and investigated. We show that new materials can undergo thermal polymerization, forming solvent-resistant films. The polymerization process has a negligible effect on the electrical properties of the materials. As a proof of concept, PSCs of p–i–n configuration were constructed, and devices with polymerized V1187 showed a promising power conversion efficiency (PCE) of 18.14%, showing the great potential of the presented class of dopant-free organic HTMs.

2. Results and Discussion

For the target materials to undergo in situ cross-linking, it is required to incorporate at least two groups that can undergo polymerization into the structure of the final compounds. To do so, commercially available fluorene amines were chosen as the starting compounds, and following a simple two-step reaction scheme (Scheme S1 and S2, Supporting Information), two final compounds V1162 and V1187 were obtained (**Figure 1**). Detailed synthesis procedures are reported in the Supporting Information. In brief, during the first step, starting amines were condensed with 2,2-bis(4-methoxyphenyl)acetaldehyde, following a previously published procedure,[11] and intermediate compounds 1 and 2 were isolated via crystallization in 47% and 94% yields, respectively. During the second step, intermediate compounds were alkylated by 4-vinylbenzylchloride, to obtain final compounds V1162 and V1187 with good yields (74% and 59%, respectively). Structures of the synthesized compounds were confirmed by means of NMR and elemental analysis.

Following a previously published procedure,[3] the costs of the materials used for the synthesis were evaluated (detailed calculations can be found in the Supporting Information). The calculated price of the materials is 13.56 and 16.34€ g^{-1} for V1162 and V1187, respectively, which is somewhat higher than the lowest reported costs of organic HTMs (e.g., V950 ≈6€ g^{-1}[11] and EDOT–amide–TPA ≈5$ g^{-1}[27]); however, it is significantly lower than that of the most popular HTM Spiro-OMeTAD (93$ g^{-1}[28]).

To evaluate the optical properties of the synthesized compounds, UV–vis and photoluminescence (PL) spectra were recorded from the solutions, and the results are shown in Figure S2, Supporting Information. The enamine V1162 has an absorption maximum (λ_{max}) in the UV range at 370 nm, with only negligible absorption in the visible range of electromagnetic
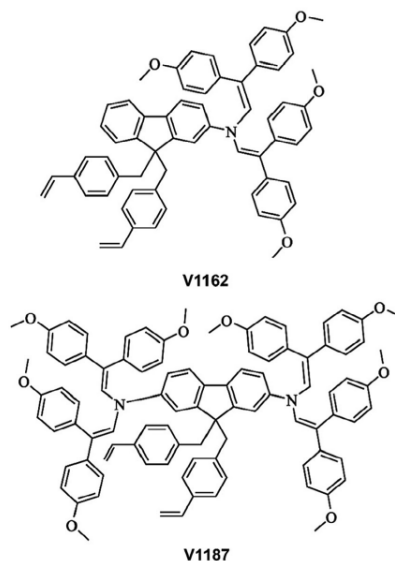

Figure 1. Molecular structures of the synthesized cross-linkable HTMs V1162 and V1187.

radiation. The compound V1187 with its additional enamine branch has a bathochromically shifted λ_{max} of 406 nm due to the larger π-conjugated electrons system, giving a slightly stronger light absorption in the visible range. This might reduce the performance of the p–i–n PSC, where the light first passes through the HTM layer; however, if the film thickness is small, the drop in J_{sc} should not be significant. In addition, from the PL spectra, it can be seen that the emission of the V1187 is slightly redshifted by 7 nm, compared to that of V1162, which is consistent with the increased π-conjugated electron system.

For the evaluation of the thermal stability of the materials and their ability to undergo a cross-linking process, thermal properties were studied by means of differential scanning calorimetry (DSC) and thermogravimetric analysis (TGA). For the V1162, during the first DSC heating cycle (**Figure 2**), the glass transition process was detected at 100 °C, followed by a melting process at 228 °C, showing that the material after purification has a mixture of amorphous and crystalline states. Directly after melting, an exothermic process was detected at 231 °C, suggesting that thermal polymerization occurs at this temperature. During the second heating cycle, no phase transitions were observed, confirming formation of the cross-linked polymer. For V1187, with higher molecular weight, a slightly higher T_g of 136 °C was detected and no melting process was observed, suggesting that V1187 was isolated as an amorphous material. The cross-linking process started at ≈190 °C, with a peak at around 239 °C. Again, during the second heating cycle, no phase transitions were detected. In addition, both compounds showed excellent thermal stability, with a T_d of 396 °C for V1162 and

115
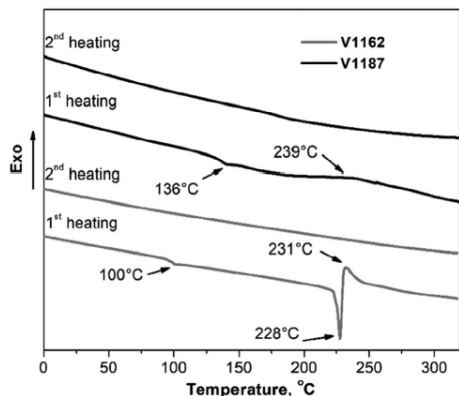
Figure 2. First and second scan heating curves of V1162 and V1187 (heating rate 10 °C min^{-1}; the y-axis is showing a heat flux).

393 °C for V1187, as can be seen from TGA analysis (Figure S1, Supporting Information).

To evaluate the cross-linking ability of the thin films of the new HTMs, they were analyzed by evaluating the amount of washed material from the spin-coated film, by means of UV–vis spectroscopy (detailed cross-linking procedure can be found in the Supporting Information). The results are shown in **Figure 3**. After heating the HTM films at 231 °C, already after 15 min the majority of the monomer was cross-linked into an insoluble polymer. A very similar behavior was observed for both the V1162 and V1187 materials, and the process of cross-linking was complete roughly after 45 min of heating. The cross-linked films have shown to be resistant to the DMF:DMSO (4:1)
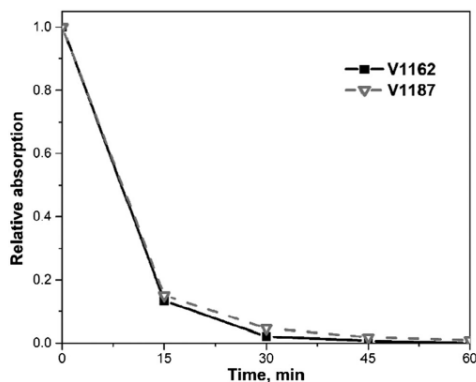
Figure 3. Cross-linking experiment of the V1162 and V1187 films. The absorption (at 370 nm for V1162 and at 406 nm for V1187) of the solutions, prepared by dipping spin-coated HTM films into THF after heating at 231 °C for the respective times, relative to the absorption of the solution, prepared by dipping of the non-cross-linked film.

solvents, as after exposure to them the UV–vis absorption spectra of the films remained almost the same (Figure S4 and S5, Supporting Information). As an additional indication of the conversion of the vinyl groups, fourier-transform infrared spectroscopy were recorded (Figure S6, Supporting Information). After annealing, the characteristic peaks of the vinyl groups at the 988–991 and 904–908 cm^{-1} disappeared, which were previously reported to show a complete cross-linking.[29,30] Next, to study the electrical properties of the synthesized HTMs, the hole drift mobility was measured with the xerographic time-of-flight (XTOF) technique (**Figure 4**). V1187 showed very good charge-transporting properties, reaching 10^{-3} cm^2 V^{-1} s^{-1} at strong electrical fields. The simpler compound V1162 showed slightly lower hole drift mobilities, yet still comparable to those of popular HTMs for PSCs. As the cross-linking process does not affect the chromophoric system of the HTMs, it had only a minor influence on the hole drift mobility. For V1187, the value stayed virtually the same, whereas for V1162 after cross-linking mobility became roughly two times lower (Figure 4). In addition to charge-transporting properties, ionization potentials were measured through photoelectron spectroscopy in air (PESA). The values were 5.11 and 5.26 eV for V1187 and V1162, respectively. Such values are consistent with the values reported for other HTMs used in PSCs.

To evaluate the performance of the materials acting as hole-selective layers in PSCs, devices with the p–i–n architecture were fabricated and characterized. As an absorber material, triple-cation perovskite was used,[31] with a nominal precursor solution composition of Cs$_{0.05}$(FA$_{0.83}$MA$_{0.17}$)$_{0.95}$Pb(I$_{0.83}$Br$_{0.17}$)$_3$ (see Figure S8, Supporting Information, for the top-view and cross-section scanning electron microscopy images of the best device). The films of the organic HTMs were prepared by spin coating from toluene, and afterward, they were annealed in a nitrogen atmosphere at 230 °C for 45 min for the cross-linking, as was determined previously. The J/V curves are reported in reverse (from open to short circuit) direction, as the devices have shown only a minor hysteresis (Figure S11, Supporting Information). A detailed description of the fabrication and
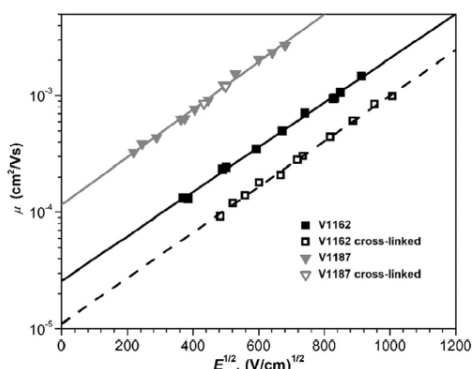
Figure 4. Electric-field dependencies of the hole drift mobilities in films of V1162 and V1187 before and after thermal cross-linking.
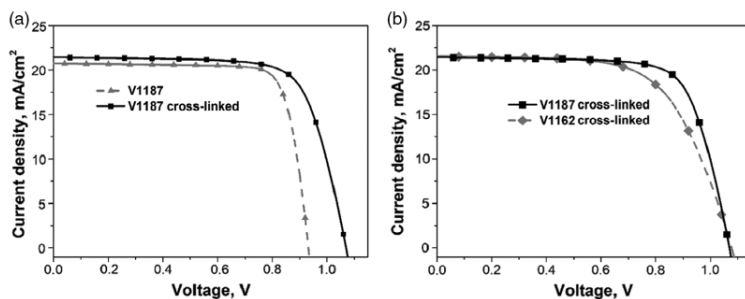
Figure 5. J/V measurements of the PSCs prepared with the new HTMs (reverse scan, from open to short circuit). a) Comparison of the devices, prepared with the neat HTM versus cross-linked HTM; b) comparison of the performances of the two cross-linked HTMs.

Table 1. Average performance parameters of the PSCs with new HTMs (prepared from 2 mg mL^{-1} in toluene). Data extracted from J/V scans, including the standard errors and the best performance parameters (in brackets). The statistics are based on six to ten cells on different substrates.

Compound	J_{sc} [mA cm^{-2}]	V_{oc} [V]	FF [%]	PCE [%]
V1162	21.19 ± 0.12 (21.60)	0.846 ± 0.013 (0.878)	75.8 ± 0.2 (76.4)	13.60 ± 0.25 (14.49)
V1162 cross-linked	21.55 ± 0.14 (21.51)	1.036 ± 0.014 (1.077)	61.7 ± 0.8 (63.5)	13.78 ± 0.35 (14.71)
V1187	21.34 ± 0.16 (20.73)	0.891 ± 0.020 (0.932)	79.3 ± 0.4 (80.3)	15.08 ± 0.35 (15.51)
V1187 cross-linked	21.95 ± 0.15 (21.40)	1.040 ± 0.012 (1.069)	71.1 ± 1.8 (73.3)	16.21 ± 0.35 (16.77)
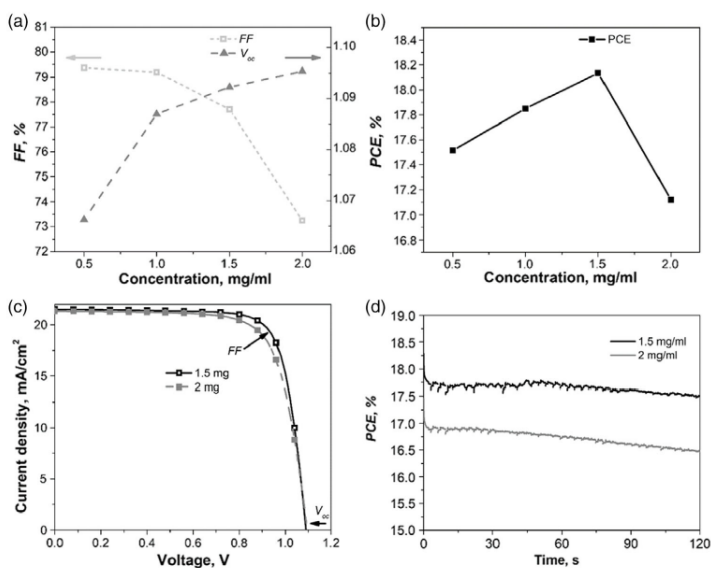
Figure 6. PSC analysis of cross-linked V1187 films. a) Dependence of the FF and V_{oc} and b) PCE on the concentration of the V1187 solution. c) Comparison of representative J/V characteristics (reverse scan, from open to short circuit) of V1187-based devices prepared from solutions with different concentrations and d) respective maximum power point tracking.

Table 2. Average performance parameters of the PSCs with the V1187 films, prepared from solutions with different concentrations. Data extracted from J/V scans, including the standard errors and the best performance parameters (in brackets). The statistics are based on six to ten cells on different substrates.

Compound	Concentration [mg mL^{-1}]	J_{sc} [mA cm^{-2}]	V_{oc} [V]	FF [%]	PCE [%]
V1187 cross-linked	0.5	20.98 ± 0.09 (21.18)	1.039 ± 0.013 (1.066)	73.3 ± 2.1 (79.4)	15.95 ± 0.47 (17.51)
	1.0	21.42 ± 0.12 (21.64)	1.057 ± 0.014 (1.070)	72.7 ± 3.4 (79.2)	16.48 ± 0.88 (17.74)
	1.5	21.39 ± 0.09 (21.61)	1.075 ± 0.009 (1.092)	71.4 ± 2.5 (77.7)	16.44 ± 0.68 (18.14)
	2.0	21.31 ± 0.10 (21.67)	1.077 ± 0.007 (1.095)	69.2 ± 1.2 (73.2)	15.88 ± 0.33 (17.12)

characterization of the devices can be found in the Supporting Information.

First, to check the influence of the cross-linking on the performance of the devices, we compared thermally cross-linked HTM films with the neat films. Via profilometry, we measured no significant surface morphology differences after the cross-linking process (Figure S3, Supporting Information). As shown in **Figure 5** and **Table 1**, both V1162 and V1187 devices with monomer films showed low open-circuit voltages (V_{oc}) (0.85 V for V1162 and 0.89 V for V1187 on average). It can be attributed to the formation of a direct contact between the perovskite and indium tin oxide (ITO), due to the damage of the HTM film during solution processing of the perovskite film. This in turn leads to increased interfacial recombination, which reduces V_{oc}.[32,33] In contrast, for both materials after thermal polymerization, V_{oc} was significantly improved up to 1.04 V on average. Quite a different trend can be observed for the full factor (FF), where higher values were obtained for neat films (75.8% for V1162 and 79.3% for V1187 on average), which can be attributed to the high conductivity of the ITO, and as a consequence fast transport of charges. This result is supporting the previous statement that after cross-linking the HTM films have improved resistance against solvents.

V1187 allowed for higher FFs than V1162 (Figure 5), and as a consequence, the highest PCE of 16.8%. As the films are used without oxidizing dopants, such improvement can be attributed to the higher values of the hole drift mobilities,[34] and as a result better transport of the charges through the film.

To further optimize the HTM film, the concentration of the V1187 starting solution was varied from 2 mg mL^{-1} down to 0.5 mg mL^{-1} in toluene. As expected, the lower concentration led to the improved FF, but at the cost of reduced V_{oc} (**Figure 6, Table 2**). Steady-state PL measurements of the perovskite films on this concentration series revealed a reduced intensity of the emission with lower concentration (Figure S9, Supporting Information). As the extraction abilities of the material should be independent of the concentration, such a behavior can be attributed to insufficient coverage of the ITO substrate and increased direct contact between the perovskite and ITO.[35] As a result of increased interface recombination, the reduction in V_{oc} is observed. Overall, an optimized PCE of 18.1% for the cross-linked films prepared from the 1.5 mg mL^{-1} solutions was achieved.

3. Conclusion

In conclusion, in this work, two new enamine-based HTMs were synthesized and investigated. Due to the presence of two vinyl groups, materials V1162 and V1187 are able to undergo thermal cross-linking during heating at 230 °C. After ≈45 min, the deposited films became resistant toward organic solvents. It was further shown that polymerization leads only to minor changes in hole drift mobilities; therefore, the materials are suitable for application in p–i–n PSCs. As a result, devices with the thermally cross-linked films have shown advantageous performance, mainly due to the higher open-circuit voltage. After further optimization of the concentration of the V1187 solution, PSCs have shown over 18% power conversion efficiency, demonstrating the great promise of the presented strategy.

Conflict of Interest

The authors declare no conflict of interest.

[1] Best Research-Cell Efficiency Chart, https://www.nrel.gov/pv/cell-efficiency.html (accessed: August 2020).
[2] A. K. Jena, A. Kulkarni, T. Miyasaka, *Chem. Rev.* **2019**, *119*, 3036.
[3] T. P. Osedach, T. L. Andrew, V. Bulović, *Energy Environ. Sci.* **2013**, *6*, 711.
[4] C. Bracher, H. Yi, N. W. Scarratt, R. Masters, A. J. Pearson, C. Rodenburg, A. Iraqi, D. G. Lidzey, *Org. Electron.* **2015**, *27*, 266.

118

[5] K. Rakstys, M. Saliba, P. Gao, P. Gratia, E. Kamarauskas, S. Paek, V. Jankauskas, M. K. Nazeeruddin, *Angew. Chem., Int. Ed.* **2016**, *55*, 7464.

[6] S. L. Rice, R. D. Balanson, R. Wingard, *J. Imaging Sci.* **1985**, *29*, 7.

[7] J. A. Sinicropi, J. R. Cowdery-Corvan, E. H. Magin, P. M. Borsenberger, *Chem. Phys.* **1997**, *218*, 331.

[8] Y. Morishita, Y. Sugimoto, H. Ishikawa, S. Hayashida, T. Okamoto, N. Hayashi, *Synth. Met.* **1991**, *41*, 1231.

[9] A. Matoliukstyte, E. Burbulis, J. V. Grazulevicius, V. Gaidelis, V. Jankauskas, *Synth. Met.* **2008**, *158*, 462.

[10] R. Paspirgelyte, R. Zostautiene, G. Buika, J. V. Grazulevicius, S. Grigalevicius, V. Jankauskas, C. C. Chen, Y. C. Chung, W. B. Wang, J. H. Jou, *Synth. Met.* **2010**, *160*, 162.

[11] M. Daskeviciene, S. Paek, Z. Wang, T. Malinauskas, G. Jokubauskaite, K. Rakstys, K. T. Cho, A. Magomedov, V. Jankauskas, S. Ahmad, H. J. Snaith, V. Getautis, M. K. Nazeeruddin, *Nano Energy* **2017**, *32*, 551.

[12] D. Vaitukaityte, Z. Wang, T. Malinauskas, A. Magomedov, G. Bubniene, V. Jankauskas, V. Getautis, H. J. Snaith, *Adv. Mater.* **2018**, *30*, 1803735.

[13] M. Steponaitis, M.-G. La-Placa, İ. C. Kaya, G. Bubniene, V. Jankauskas, M. Daskeviciene, M. Sessolo, T. Malinauskas, H. J. Bolink, V. Getautis, *Sustainable Energy Fuels* **2020**, *4*, 5017.

[14] E. H. Jung, N. J. Jeon, E. Y. Park, C. S. Moon, T. J. Shin, T. Y. Yang, J. H. Noh, J. Seo, *Nature* **2019**, *567*, 511.

[15] X. Zheng, Y. Hou, C. Bao, J. Yin, F. Yuan, Z. Huang, K. Song, J. Liu, J. Troughton, N. Gasparini, C. Zhou, Y. Lin, D. J. Xue, B. Chen, A. K. Johnston, N. Wei, M. N. Hedhili, M. Wei, A. Y. Alsalloum, P. Maity, B. Turedi, C. Yang, D. Baran, T. D. Anthopoulos, Y. Han, Z. H. Lu, O. F. Mohammed, F. Gao, E. H. Sargent, O. M. Bakr, *Nat. Energy* **2020**, *5*, 131.

[16] J. Xu, C. C. Boyd, Z. J. Yu, A. F. Palmstrom, D. J. Witter, B. W. Larson, R. M. France, J. Werner, S. P. Harvey, E. J. Wolf, W. Weigand, S. Manzoor, M. F. A. M. Van Hest, J. J. Berry, J. M. Luther, Z. C. Holman, M. D. McGehee, *Science* **2020**, *367*, 1097.

[17] Y. Hou, E. Aydin, M. De Bastiani, C. Xiao, F. H. Isikgor, D. J. Xue, B. Chen, H. Chen, B. Bahrami, A. H. Chowdhury, A. Johnston, S. W. Baek, Z. Huang, M. Wei, Y. Dong, J. Troughton, R. Jalmood, A. J. Mirabelli, T. G. Allen, E. Van Kerschaver, M. I. Saidaminov, D. Baran, Q. Qiao, K. Zhu, S. De Wolf, E. H. Sargent, *Science* **2020**, *367*, 1135.

[18] M. Stolterfoht, C. M. Wolff, J. A. Márquez, S. Zhang, C. J. Hages, D. Rothhardt, S. Albrecht, P. L. Burn, P. Meredith, T. Unold, D. Neher, *Nat. Energy* **2018**, *3*, 847.

[19] W. Nie, H. Tsai, R. Asadpour, J. C. Blancon, A. J. Neukirch, G. Gupta, J. J. Crochet, M. Chhowalla, S. Tretiak, M. A. Alam, H. L. Wang, A. D. Mohite, *Science* **2015**, *347*, 522.

[20] Y. Wang, W. Chen, L. Wang, B. Tu, T. Chen, B. Liu, K. Yang, C. W. Koh, X. Zhang, H. Sun, G. Chen, X. Feng, H. Y. Woo, A. B. Djurišić, Z. He, X. Guo, *Adv. Mater.* **2019**, *31*, 1902781.

[21] X. Sun, Q. Xue, Z. Zhu, Q. Xiao, K. Jiang, H. L. Yip, H. Yan, Z. Li, *Chem. Sci.* **2018**, *9*, 2698.

[22] R. Shang, Z. Zhou, H. Nishioka, H. Halim, S. Furukawa, I. Takei, N. Ninomiya, E. Nakamura, *J. Am. Chem. Soc.* **2018**, *140*, 5018.

[23] C. Wang, J. Hu, C. Li, S. Qiu, X. Liu, L. Zeng, C. Liu, Y. Mai, F. Guo, *Sol. RRL* **2019**, *4*, 1900389.

[24] A. Magomedov, A. Al-Ashouri, E. Kasparavičius, S. Strazdaite, G. Niaura, M. Jošt, T. Malinauskas, S. Albrecht, V. Getautis, *Adv. Energy Mater.* **2018**, *8*, 1801892.

[25] K. Rakstys, M. Stephen, J. Saghaei, H. Jin, M. Gao, G. Zhang, K. Hutchinson, A. Chesman, P. L. Burn, I. Gentle, P. E. Shaw, *ACS Appl. Energy Mater.* **2020**, *3*, 889.

[26] Y. Zhang, C. Kou, J. Zhang, Y. Liu, W. Li, Z. Bo, M. Shao, *J. Mater. Chem. A* **2019**, *7*, 5522.

[27] M. L. Petrus, K. Schutt, M. T. Sirtl, E. M. Hutter, A. C. Closs, J. M. Ball, J. C. Bijleveld, A. Petrozza, T. Bein, T. J. Dingemans, T. J. Savenije, H. Snaith, P. Docampo, *Adv. Energy Mater.* **2018**, *8*, 1801605.

[28] M. L. Petrus, T. Bein, T. J. Dingemans, P. Docampo, *J. Mater. Chem. A* **2015**, *3*, 12159.

[29] Z. Li, Z. Zhu, C.-C. Chueh, J. Luo, A. K.-Y. Jen, *Adv. Energy Mater.* **2016**, *6*, 1601165.

[30] S. Abraham, G. P. T. Ganesh, S. Varughese, B. Deb, J. Joseph, *ACS Appl. Mater. Interfaces* **2015**, *7*, 25424.

[31] M. Saliba, T. Matsui, J.-Y. Seo, K. Domanski, J.-P. Correa-Baena, M. K. Nazeeruddin, S. M. Zakeeruddin, W. Tress, A. Abate, A. Hagfeldt, M. Grätzel, *Energy Environ. Sci.* **2016**, *9*, 1989.

[32] M. Stolterfoht, P. Caprioglio, C. M. Wolff, J. A. Márquez, J. Nordmann, S. Zhang, D. Rothhardt, U. Hörmann, Y. Amir, A. Redinger, L. Kegelmann, F. Zu, S. Albrecht, N. Koch, T. Kirchartz, M. Saliba, T. Unold, D. Neher, *Energy Environ. Sci.* **2019**, *12*, 2778.

[33] J. P. Correa-Baena, W. Tress, K. Domanski, E. H. Anaraki, S. H. Turren-Cruz, B. Roose, P. P. Boix, M. Grätzel, M. Saliba, A. Abate, A. Hagfeldt, *Energy Environ. Sci.* **2017**, *10*, 1207.

[34] W. Zhou, Z. Wen, P. Gao, *Adv. Energy Mater.* **2018**, *8*, 1702512.

[35] E. M. Hutter, T. Kirchartz, B. Ehrler, D. Cahen, E. Von Hauff, *Appl. Phys. Lett.* **2020**, *116*, 100501.

119

9. ACKNOWLEDGMENTS